Downloaded from orbit.dtu.dk on: Apr 25, 2024

DTU Library

Design, modelling, and fabrication of a ferrite magnet axial flux in-wheel motor

Fasil, Muhammed

Publication date:
2018

Document Version
Publisher's PDF, also known as Version of record

Link back to DTU Orbit

Citation (APA):
Fasil, M. (2018). *Design, modelling, and fabrication of a ferrite magnet axial flux in-wheel motor*. Technical University of Denmark.

General rights
Copyright and moral rights for the publications made accessible in the public portal are retained by the authors and/or other copyright owners and it is a condition of accessing publications that users recognise and abide by the legal requirements associated with these rights.

- Users may download and print one copy of any publication from the public portal for the purpose of private study or research.
- You may not further distribute the material or use it for any profit-making activity or commercial gain
- You may freely distribute the URL identifying the publication in the public portal

If you believe that this document breaches copyright please contact us providing details, and we will remove access to the work immediately and investigate your claim.

Technical University of Denmark

Muhammed Fasil P.V.

Design, modelling, and fabrication of a ferrite magnet axial flux in-wheel motor

PhD Thesis

February 2018

DTU Electrical Engineering
Department of Electrical Engineering

Muhammed Fasil P.V.

Design, modelling, and fabrication of a ferrite magnet axial flux in-wheel motor

PhD Thesis

February 2018

Design, modelling, and fabrication of a ferrite magnet axial flux in-wheel motor

This report was prepared by
Muhammed Fasil P.V.

Supervisors
Nenad Mijatovic
Joachim Holbøll
Bogi Bech Jensen

Funding
EU-FP7 NANOPYME Project, No. 310516 (2/3)
Technical University of Denmark (1/3)

PhD school
Department of Electrical Engineering

Department of Electrical Engineering
Centre for Electric Power and Energy (CEE)
Technical University of Denmark
Elektrovej 325
DK-2800 Kgs. Lyngby
Denmark

www.cee.dtu.dk
Tel: (+45) 45 25 35 00
Fax: (+45) 45 88 61 11
E-mail: cee@elektro.dtu.dk

Release date:	TBD
Class:	1 (public)
Edition:	1
Comments:	This report is a part of the requirements to achieve the PhD degree at the Technical University of Denmark.
Rights:	©DTU Electrical Engineering, 2018

Preface

Rare-earth magnets have a high performance to size ratio and it is the preferred choice when a space constrained application requires a machine with high-efficiency. However, supply uncertainty, price fluctuation, and no influence on the production of rare-earth metals creates a huge disadvantage to European industries and is a concern for the European Union. The European Commission 2012 Work Programme highlights "Substituting magnetic materials and/or reducing the use of critical raw materials." There are many permanent magnet applications exist, where rare-earth magnets are used only because of lack of alternative magnet materials in the energy density band of 38 kJ/m^3 to 100 kJ/m^3. Some of these applications are wind generators, motors for automotive applications, photovoltaic cells, and compressor motor used in refrigeration. The NanoPyme project was proposed with a goal to create novel magnets with no rare-earth content and with a larger energy product than currently used ferrites targeting the applications at the lower end of the energy density band 38 kJ/m^3 to 100 kJ/m^3.

The NanoPyme consortium had eleven partners and they are IMDEA Nanociencia, Spanish Council for Scientific Research, Instituto de Magnetismo Aplicado, and Ingenieria Magnetica Aplicada S.L.from Spain, Technical University of Denmark and Aarhus University from Denmark, Institute Jozef Stefan and Magneti from Slovenia, Institute for Energy Technology from Norway, INSTM from Italy, and Innovant at first and General Numerics later from Germany. DTU role in the project was demonstrating the use of ferrite magnets as a substitute to rare-earth magnets in a real world application.

Besides the research, the DTU PhD program consists a course work for 30 ECTS, external research stay for up to six months, and compulsory work of up to six months covering teaching and dissemination. This thesis describes the research activities carried out to develop a ferrite magnet in-wheel motor for

an electric scooter. The research started with a study of present scenario of light electric vehicles. This was followed by a survey of to identify a suitable motor topology for a ferrite magnet in-wheel motors. Subsequently, a design program, as well as a dynamic model of the identified motor topology, was developed. The next stage focused on design and fabrication of motors. Finally, the motors have been tested, and a comparative study of the test results is carried out.

Even though the PhD work started in March 2013, the research methodology and many concepts presented in the research was formed during my work at Global R&D Centre of Crompton Greaves Ltd Mumbai and Masters program at IIT Delhi. DTU, Department of Electrical Engineering, and Centre for Electric Power and Energy all created an excellent atmosphere and world-class facilities to execute my ideas, and I am very thankful for that. Further, I would like to acknowledge that this research is partially funded by the European Community through the Seventh Framework Programme under grant agreement no. 310516.

I would like to thank my supervisor Nenad Mijatovic for guidance, his continued presence, unmatched enthusiasm, and efforts in making sure that I have all I need to complete the project successfully. I would like to thank Bogi Bech Jensen for recruiting me for this wonderful opportunity and for continuing as co-supervisor for this research. I would like to thank Joachim Holbøll for his immense support and help in many critical moments. I would like to express my gratitude to Jens Huusfeldt, Jens Christian Jensen, Flemming Juul Petersen, and Per Munch Jakobsen of PowerlabDK for all their help in building prototypes and test bench. I would like to thank partners of NanoPyme consortium for their help in completing this project. I would like to thank my present, and past colleagues Stig Högberg, Walid Ziad El-Khatib, Xiaowei Song, Matthew Lee Henriksen, Stephan Vogel, Alexandros Skrimpas, Pranshu Upadhayay, and Vinay Patwardhan for their support.

I would like to thank my wife Noorjahan, my son Halim Abu-Bakr, my daughter Aathiya Zuhara Maimoon, my parents, and my brothers for all their support and encouragement.

Muhammed Fasil
February 10, 2018

Abstract

The uncertainty in the availability and the price of rare-earth (RE) metals required to produce high-energy density magnets prompted the search for RE free high-efficiency machines. This work investigates the suitability of ferrite magnet machine as a substitute to RE magnet machine in an electric two-wheeler application. The two-wheeler selected for this work is an electric scooter used for the city commute, which belongs to a group of vehicles known as light electric vehicles (LEV). The objective of the work is to develop a ferrite magnet direct drive in-wheel motor for an electric two-wheeler and compare its performance with RE magnet in-wheel motors.

Currently, an electric scooter costs twice the internal combustion engine (ICE) vehicle of similar class. The existing LEV mostly use a powertrain with a lithium-ion battery as the power source and a motor using RE magnets like NdFeB as the energy converter to meet the range and the performance of ICE counterparts, and these two parts accounts the major share of the cost of the vehicle. When comparing a ferrite magnet and an NdFeB magnet of same dimensions, the ferrite magnet produces around one-fourth of the flux, and it can be demagnetized by a much lower demagnetizing field. Motor designers workaround the inherent deficiencies of ferrite magnets by selecting a motor topology that allows placing more magnets and ensuring that the motor field poles are not exposed to an armature field of magnitude that can cause demagnetization.

After reviewing many motor types and topologies, a permanent magnet brushless DC (PMBLDC) motor with a segmented armature torus (SAT) topology is selected for developing the ferrite magnet in-wheel motor. The SAT motor topology is a variation of axial flux motor and offers advantages such as high torque per unit mass, high-efficiency, and a dual rotor structure to accommodate more magnets. A finite element (FE) based design-synthesis program

is developed and the program is used to generate designs of a ferrite magnet motor and a bonded RE magnet motor. A non-linear dynamic model of PMBLDC motor that includes the core loss calculation has been developed to simulate the system performance of the designs. The operating characteristics of ferrite magnets vary considerably with temperature, and therefore, the performance variation of the designed ferrite magnet motor with the operating temperature is studied using the dynamic model. From the results of dynamic analysis, it is concluded that the presented design will meet the tractive force requirement of the electric two-wheeler over the expected magnet operating temperature variation.

The dual airgap assembly of SAT motor topology could present constructional difficulties, especially maintaining the proper airgap lengths. Two different assembly designs are considered for SAT motor prototypes. The first design is used in the construction of the bonded RE magnet motor, and the assembled motor has issues such as stator flexing and limited space for terminal connections. The second assembly of SAT motor addresses limitations of the first prototype, and it is used in the fabrication of the ferrite magnet motor. The operation of the first prototype is found to be restricted by its weak structure, and therefore, only the second prototype is installed in the electric two-wheeler. The ferrite magnet motor has been tested to measure back EMF, efficiency, and energy consumption when used as the powertrain of the prototype vehicle.

The ferrite magnet SAT PMBLDC motor delivered a peak efficiency of 96.6 % when tested using constant torque loads in a test bench. Further, the energy consumption of the ferrite magnet motor as in-wheel powertrain of the scooter is evaluated using the basic urban driving cycle, and the result is compared to the results of two market sourced vehicles. It is found that the ferrite magnet powertrain consumes less energy to complete the test sequence, however, has 70 % more acceleration time. The structural optimisation of the ferrite magnet motor prototype could bring down the mass of motor and reduce the gap in acceleration time between the prototype vehicle and the market sourced vehicles.

The development of a high-efficiency ferrite magnet motor for traction application and its positive test results provide a platform to expand the use of ferrite magnets in higher rated applications than the one covered in this work.

Dansk Resumé

Det var usikkerheden i forsyningen af sjældne jordarter og den høje pris påat bygge magneter med høj energidensitet der igangsatte jagten påhøjtydende maskiner uden brug af sjældne jordarter. Dette værk undersøger anvendeligheden af maskiner med ferritmagneter som et substitut for maskiner med magneter af sjældne jordarter anvendt påfx vindturbiner, bådmotorer og elektriske køretøjer, som er kendetegnet ved høj momenttæthed og lav hastighed.

Der er valgt en el-scooter anvendt til bykørsel, et køretøj der tilhører kategorien Light Electic Vehicles (LEV). Målet med dette værk er at udvikle en ferritmagnetbaseret, gearløs hjulnavsmonteret elektromotor til anvendelse i en tohjulet el-scooter og sammenligne ydelsen med en tilsvarende motor bygget med sjælden-jordartsmagnet.

I dag koster en el-scooter det dobbelte af en tilsvarende, konventionel scooter med forbrændingsmotor. For at opnåen ydeevne der svarer til en konventionel scooter bruger el-scooteren i dag typisk en drivlinje med lithiumionbatteri som energikilde og en motor med sjælden-jordartsmagnet såsom NdFeB til konvertering, og disse komponenter udgør hovedparten af køretøjets produktionspris.

Når man sammenligner en ferrit- og en neodyniummagnet af samme dimensioner produceres der kun en fjerdedel flux i ferritmagneten, og den kan afgmanetiseres af et meget mindre afmagnetiseringsfelt. Motordesignere omgår ferritmagnetens indbyggede ulemper ved at anvende en topologi som gør plads til flere magneter og ved at sikre at motorens feltpoler ikke er eksponeret for "an armature field of magnitude" der kan afmagnetisere.

Der vælges en motor med permanent, børsteløs jævnstrømsmagnet (PM-BLDC) med en Segmented Armature Torus (SAT)-magnet til udvikling af en ferritmagnet-hjulnavsmotor. SAT-motorens opbygning er en variant af en "aksialflux-motor" og nyder godt af en gunstigt momenttæthed, høj effektivitet og en

dobbeltrotor der kan rumme flere magneter. Et "finite element (FE) based design synthesis" program udvikles for at simulere systemets ydelse, og programmet bruges til at generere et motordesign med ferritmagnet motor og en "bonded" sjælden-jordartsmagnet-motor.

En ikke-lineær, dynamisk model af en PMBLDC-motor med beregninger for kernetab er blevet udviklet med det formål at simulere designets ydeevne, når det testes i et system. Ferritmagneternes karakteristika viser store udsving indbyrdes ved forskellige temperaturer, og variationen i ydelsen for den her udviklede ferritmagnet-motor analyseres gennem den dynamiske model. Påbaggrund af analysen konkluderes, at det i afhandlingen præsenterede design kan efterkomme kravet om trækkraft til el-scooteren inden for de forventede temperaturudsving i magneten under drift.

"Dual airgap assembly of SAT motor topology" kan være en problem når motoren bygges, navnlig at holde den korrekte afstand mellem segmenterne. Der vurderes to forskellige konstruktioner for prototyper påSAT-motorer. Det første design bruges i konstruktionen af den bundne neodym-magnetmotor, og motoren har problemer med at stator bøjer sig under drift og begrænset plads til terminaler. Den næste prototype af SAT-motoren løser de førnævnte problemer og bliver brugt i konstruktionen af ferritmagnet-motoren. Det konstateres at den første prototype i drift er begrænset af dens svage struktur, og det er derfor kun den anden prototype, som installeres i el-scooteren.

Ferritmagnet-motoren er testet for at måle EMF, effektivitet og forbrug som drivlinje. Motoren med ferritmagnet topper ved 96.6 % effektivitet når den testes ved et konstant moment i laboratoriet. Endvidere evaluereres feriitmagnetmotorens energiforbrug, når den anvendes som hjulmonteret drivlinje i scooteren, med anvendelse af et kørselsmønster for bykørsel og dette resultat sammenlignes med to andre markedsførte og indkøbte el-scootere. Det konstateres at ferritmagnetmotorens drivlinje forbruger mindre energi for at gennemkøre testkørslen i forhold til kontrollen, men til gengæld er accelerationstiden 70 % længere. Gennem optimering af motorkonstruktionen kunne massen nedbringes, og dermed reducere spændet i accelerationstid, når man sammenligner med de kommercielle køretøjer.

Udviklingen af en høj-effektiv ferritmagnetmotor til anvendelse som trækkraft, og de positive testresultater giver grundlag for at udvide brugen af ferritmagner til mere avancerede anvendelsesområder end de, som er behandlet i dette værk.

Contents

Preface i

Abstract iii

Dansk Resumé v

Contents vii

Nomenclature xi

List of Figures xvii

List of Tables xxiii

1 Introduction 1

1.1 Background of PhD Project 1
1.2 Problem definition 4
1.3 Scope of the study 4
1.4 Main contributions 5
1.5 Guide to the readers 6

2 Light electric vehicles and their powertrains 9

2.1 Introduction 9
2.2 Present scenario of light electric vehicles 9
2.2.1 Classification of electric vehicles 10
2.2.2 Advantage of LEV in urban context 12
2.2.3 Hindering factors to the growth of EV 12
2.2.4 Favourable factors for EV growth in future 13
2.2.5 System architecture and components of LEV 14
2.3 Traction motors for electric vehicles 15
2.4 Ferrite magnet traction motors 17

2.5 Selecting a traction motor for an electric two-wheeler 20
2.6 Operating principle of PMBLDC motor drives 21
2.7 Conclusion 22

3 The powertrain rating of electric two-wheeler 25
3.1 Introduction 25
3.2 Powertrain of a vehicle 25
3.2.1 The forces acting on a vehicle in motion 26
3.2.2 Characteristics of electric powertrain 27
3.2.3 Equations of electric vehicle in motion 28
3.3 Estimation of the rating of an electric drive based powertrain . 29
3.4 Powertrain specification of an electric two-wheeler for city use . 30
3.5 Conclusions 32

4 Design of segmented armature torus PMBLDC motors 33
4.1 Introduction 33
4.2 Finite element based design-synthesis program 34
4.2.1 Design variables of SAT PMBLDC motor 34
4.2.2 Finite element model based design tool 35
4.2.3 Search program 40
4.3 Design of bonded RE magnet and ferrite magnet motors 40
4.3.1 Results of design synthesis 45
4.3.2 Comparison of designs 49
4.4 Conclusions 51

5 Non-linear dynamic model of PMBLDC drive based system 53
5.1 Introduction 53
5.2 The core losses in SAT PMBLDC motors 56
5.2.1 FE model for extracting parameters of core loss model . 58
5.2.2 Core losses in stator tooth-tip 58
5.2.3 Core losses in stator tooth 62
5.2.4 Core losses in solid rotor yoke 62
5.3 Dynamic model of PMBLDC motor drives 68
5.3.1 Three-phase PMBLDC motor model 68
5.3.2 Power electronic converter model 71
5.3.3 Load model 72
5.4 Calculation of dynamic performance of the designed motors . . 73
5.4.1 Modelling the effect of armature reaction on back EMF . 73

5.4.2 Cogging torque in 18-slot 16-pole SAT PMBLDC motor . 76
5.4.3 Core loss modelling 77
5.4.4 Calculation of phase self-inductance 78
5.4.5 Constants of dynamic model 79
5.4.6 Results of dynamic simulation 80
5.5 Revision of design-synthesis program of SAT PMBLDC motors . 84
5.5.1 Revised design-synthesis program 84
5.5.2 Revised designs of SAT PMBLDC motor 86
5.5.3 Comparison of revised designs of SAT PMBLDC motors . 90
5.5.4 Performance of revised designs of SAT PMBLDC motors . 91
5.6 Performance variation of ferrite magnet motor with temperature 96
5.6.1 Measured BH characteristics of ferrite magnet 97
5.6.2 Estimation of demagnetization level of ferrite magnet . . 99
5.6.3 Effect of temperature on motor performance 100
5.7 Conclusions 103

6 Fabrication of prototype in-wheel motors 105
6.1 Introduction 105
6.2 Mechanical assembly of SAT PMBLDC in-wheel motor 106
6.2.1 The stator assembly of SAT PMBLDC in-wheel motor . . 106
6.2.2 The rotor assembly of SAT PMBLDC in-wheel motor . . . 109
6.2.3 Whole assembly of in-wheel motor 110
6.3 Construction of bonded RE magnet motor 112
6.4 Revised of mechanical assembly of SAT PMBLDC motor 115
6.5 Construction of ferrite magnet motor 119
6.6 Installation of SAT PMBLDC motor in electric two-wheeler . . . 123
6.7 Conclusions 123

7 Experimental results 125
7.1 Introduction 125
7.2 Experimental setup for testing of in-wheel motors 126
7.3 Thermal performance evaluation of in-wheel motors 128
7.3.1 FE thermal model of radial flux PMBLDC motor 129
7.3.2 FE thermal model of SAT PMBLDC motor 133
7.4 Performance evaluation of in-wheel motors 135
7.4.1 Back EMF testing of motors 135
7.4.2 Performance testing of motors 136
7.5 Evaluation of energy consumption of electric two-wheelers . . . 138

7.6 Conclusions 141

8 Discussion on design, modelling, and experimental validation 143

8.1 Introduction 143
8.2 Evolution of SAT PMBLDC motor from design to prototype . . . 144
8.3 Comparison of results of dynamic modelling and testing 146
8.3.1 Testing and modelling with constant torque load. 146
8.3.2 Testing and modelling with vehicle load. 151
8.4 Conclusions 153

9 Conclusions and future work 155

9.1 Conclusions 155
9.2 Future work 158

References 159

Appendices 177

A Derivations of formulae 179

A.1 Expression for slot area 179

B Implementation of design program 181

B.1 Overview of design program 181
B.2 Matlab implementation of design optimisation 182
B.3 Objective function of optimisation 183
B.4 Functions implemented in Excel VBA 183

C Measurements from the test bench evaluation of motors 201

C.1 Sintered rare-earth magnet PMBLDC hub motor 201
C.2 Ferrite magnet SAT PMBLDC hub motor 205

D Basic urban driving cycle as per ISO 13064-1:2012 209

E Fabrication drawing of components of prototype motors 211

E.1 Rare-earth magnet SAT PMBLDC motor 211
E.2 Ferrite magnet magnet SAT PMBLDC motor 222

F Published and submitted papers 233

Abbreviations and Symbols

Abbreviations

Abbreviations	Description
3D	Three-dimensional
AC	Alternating current
AFM	Axial flux machines
BEV	Battery electric vehicles
BRE-V1	Bonded RE magnet motor initial design
BRE-V2	Bonded RE magnet motor revised design
CAD	Computer-aided design
CNC	Computer numerical control
DC	Direct current
EDM	Electrical discharge machining
EMF	Electromotive force
EV	Electric vehicles
EU	European Union
FE	Finite element
Fe-V1	Ferrite magnet motor initial design
Fe-V2	Ferrite magnet motor revised design
GHG	Green house gas
ICE	Internal combustion engines
IPM	Interior permanent magnet
LEV	Light electric vehicles
Li-ion	Lithium-ion
NanoPyme	Nanocrystalline permanent magnets based on hybrid metal-ferrites
NdFeB	Neodymium iron boron

NiMH	Nickel-metal-hydride
PM	Permanent magnet
PMBLDC	Permanent magnet brushless DC
PMSM	Permanent magnet synchronous motor
PWM	Pulse width modulation
RE	Rare-earth
RM	Reluctance motor
RMS	Root of mean of squares
SAT	Segmented armature torus
SLA	Sealed lead-acid
SmCo	Samarium cobalt
SRM	Switched reluctance motor

Symbols

Symbol	Units	Description
α		A constant obtained from curve fitting of sine wave core loss data
α_{t}	rad−elec	Phase conduction angle of BLDC motor
α_{ta}	rad−elec	Stator tooth arc
α_{tt}	rad−elec	Mean pole transition angle
A_{f}	m^2	Frontal area of vehicle
A_{ry}	m^2	Area of the rotor yoke face
β		A constant obtained from curve fitting of sine wave core loss data
β_{m}	rad−elec	Rotor pole arc
B	T	Magnetic flux density
B_{g0}	T	Airgap flux density
B_{g0}	T	Airgap flux density during an intermediate stage of design iteration
B_{ttm}	T	Peak tooth tip flux density
C_{d}		The coefficient of drag of the vehicle
δ	m	Skin depth
D_{is}	mm	Inner diameter of stator
D_{os}	mm	Outer diameter of stator
$\frac{d}{dt}$	1/s	Time differential
ϵ		Predefined error value for convergence of design iteration
e, e_{a}, e_{b}, e_{c}	V	The instantaneous values of back EMF of phases
E	V	Line-line back EMF
f	Hz	Frequency
f_{a}	N	Force required to accelerate the vehicle
f_{aero}	N	Aerodynamic drag force
f_{road}	N	Road load
f_{roll}	N	Rolling friction
g	m/s^2	Gravitational acceleration constant
η_{max}	%	Maximum efficiency
H	A/m	Magnetizing field

i	A	Instantaneous currents
i		Harmonic order
$i_{\mathrm{a,b,c}}$	A	Instantaneous phase currents
I_{ph}	A	RMS phase current
I_{fl}	A	Rated full load phase current
J	A/mm^2	Maximum current density of winding
k_1	N	Constant of motive force equation
k_2	N s^2/m^2	Constant of motive force equation
k_{m}		Coefficient of rotational inertia
K_{e}		A constant obtained from curve fitting of sine wave core loss data
K_{h}		A constant obtained from curve fitting of sine wave core loss data
K_{p}		Pole arc to pole pitch ratio of rotor
K_{sff}		Gross slot fill factor
K_{E}	V s/rad	EMF constant
λ	m	Wavelength
l_{g}	mm	Axial length of airgap
L	mH	The phase self-inductance
L_{a}	mm	Axial length of motor
L_{m}	mm	Depth of magnet
L_{sl}	mm	Depth of slot lip
L_{sm}	mm	Depth of slot mouth
L_{t}	mm	Axial length of tooth
L_{yr}	mm	Depth of rotor yoke
μ_{Fe}	H/m	Average permeability of iron
m	kg	Total mass of vehicle including load
m		Number of phases of machine
n	rps	Rotational speed
n_{y}		Number of rotor yokes in the motor
N_{c}		Number of turns per coil
N_{r}	rpm	Rated speed
N_{s}		Number of stator slot
p		Number of pole pair
p	bar	Tire pressure
p_{et}	W	Eddy current loss in stator tooth per unit mass
p_{ey}	W	Eddy current loss in stator yoke per unit mass

p_{h}	W	Hysteresis loss per unit mass
p_{tt}	W	Tooth-tip core loss per unit mass
P	W	Output power of a machine
P		Number of rotor poles
P_{Lrye}	W	Eddy current loss in rotor yoke
P_{r}	W	Rated output power of a machine
θ	rad	Rotor position
θ_{grad}	%	Percentage slope of the riding surface
ρ_{air}	kg/m^3	Density of air
ρ_{Fe}	Ω m	Resistivity of iron
R	Ω	Phase resistance
R_{Ymean}	m	Mean radius of the rotor yoke
θ_{rise}	rad	Angle of movement of rotor corresponding to rise time of phase current
t_{f}	s	Acceleration time of a vehicle to reach the top speed
ΔT	s	Rise time of phase current
T_{cg}	N m	Cogging torque
T_{em}	N m	Instantaneous electro-magnetic torque
T_{r}	N m	Rated torque of machine
v	km/h	Velocity
$v_{\mathrm{a,b,c}}$	V	Applied voltage across phases
v_{r}	km/h	Rated speed
v_{m}	km/h	Top speed
V_{r}	V	Rated voltage
ω	rad/s	Angular velocity of rotor
ω_{r}	rad/s	Rated angular velocity of rotor
W_{so}	mm	Width of slot opening
W_{t}	mm	Width of stator tooth
ψ	Wb−turns	Flux linkage
ψ'	Wb−turns	Flux linkage derivative

List of Figures

1.1 Price history of RE metals. 2
1.2 The average daily travel distance and time in US and UK. 3

2.1 Classifications of electric vehicles. 10
2.2 System layout of a battery electric vehicle. 11
2.3 System layout of a series hybrid electric vehicle. 11
2.4 System layout of a parallel hybrid electric vehicle. 12
2.5 System architecture of light electric vehicles. 14
2.6 A classification of traction motors for electric vehicles. 16
2.7 A comparison of properties of different types of magnet. 17
2.8 Rotor of a spoke type interior permanent magnet motor. 18
2.9 The separated pole piece type IPM topology. 18
2.10 Spoke-type IPM with segmented wing-shaped poles. 19
2.11 An AF motor with circumferential and axial magnets. 19
2.12 Segmented armature torus permanent magnet motor. 21
2.13 Block diagram of a PMBLDC motor drive. 22
2.14 Ideal voltage and current waveforms of a PMBLDC motor. . . . 23

3.1 The forces acting on a vehicle moving at constant speed. 26
3.2 Torque and power variation of an electric motor drive. 28
3.3 The output power vs. acceleration time for vehicle-1. 31
3.4 The output power to maintain the top speed vs. gradients. . . . 31
3.5 The varaition of acclerating time with mass of vehicle. 32

4.1 Variables defining the geometry of the SAT PMBLDC motor . . . 35
4.2 Flowchart of design tool 37
4.3 Flowchart for calculating axial length of stator tooth 38
4.4 Flowchart for calculating coil dimensions 39

4.5 The maximum available space for motors in vehicle-1 frame. . . 41
4.6 Alternate tooth concentrated winding of 18-slot 16-pole SAT PMBLDC motor. 42
4.7 The FE model of SAT PMBLDC motor used in the design synthesis. 44
4.8 Results of design synthesis of in-wheel motors 45

5.1 Equivalent circuit representation of a PMBLDC motor. 54
5.2 Core losses, causes, and components with core losses. 57
5.3 FE model for extracting parameters of core loss model 58
5.4 The flux density distribution on tooth faces of SAT PMBLDC motor 59
5.5 Flux density distribution on stator tooth faces. 59
5.6 Peak tooth-tip flux density vs. armature current 60
5.7 Tooth-tip flux density variation with rotor position. 61
5.8 The simplified tooth-tip flux density variation. 61
5.9 Tooth flux density variation with rotor position. 62
5.10 No-load rotor yoke flux density variation with rotor position. . . 63
5.11 Rotor yoke flux density of SAT PMBLDC motor 64
5.12 The airgap flux density harmonics of SAT PMBLDC motor . . . 65
5.13 Block diagram of the dynamic model of SAT PMBLDC motor. . . 68
5.14 The model of voltage equation of a three-phase PMBLDC motor. 69
5.15 The model of the torque equation of a three-phase PMBLDC motor. 70
5.16 The core loss model of a PMBLDC motor. 71
5.17 The model of a basic controller and converter of PMBLDC motor. 72
5.18 The constant torque load model. 72
5.19 The FE model of motor used to calculate flux-linkage-derivative. 74
5.20 Two stage armature reaction modelling of PMBLDC motor . . . 74
5.21 Flux linkage variation of designed motors. 75
5.22 Flux derivative variation of the designed motors. 76
5.23 The cogging torque variation of a reduced size machine. 77
5.24 The peak tooth-tip flux density vs. armature current. 78
5.25 The yoke eddy current loss function vs. armature current. . . . 78
5.26 The simulated performance of the designed motors. 81
5.27 Simulated waveforms the bonded RE magnet motor. 83
5.28 The revised flowchart to calculate the coil diamensions. 85
5.29 Results of revised design synthesis of in-wheel motors. 87
5.30 Flux linkage variaiton of revised designs with rotor position. . . 92
5.31 Flux-linkage-derivative variaiton of revised designs. 93

5.32 The peak tooth-tip flux density variations of revised designs. . . 93
5.33 Variations of yoke eddy current loss function of revised designs. 94
5.34 Simulated performance of BRE-V1, Fe-V1, BRE-V2, and Fe-V2. . 95
5.35 Measured demagnetization characteristics of magnets. 98
5.36 Variation of differential permeability of ferrite magnet. 99
5.37 Demagnetizing field distribution for an armature current of 20 A. 100
5.38 Demagnetizing field distribution for an armature current of 200 A.100
5.39 The variation of EMF constant with armature current and magnet temperatures. 101
5.40 The temperature variation of performance of design Fe-V2. . . . 102

6.1 The stator assembly of SAT PMBLDC in-wheel motor. 107
6.2 Assembly of shaft and spider of SAT PMBLDC motor. 108
6.3 The stator tooth assembly of SAT PMBLDC motor. 108
6.4 Assembly of segmented stator tooth and spider. 108
6.5 The rotor assembly of SAT PMBLDC in-wheel motor. 109
6.6 The fabrication guidline of the rotor yoke and pole assembly. . . 110
6.7 The exploded view of the rotor assembly of SAT PMBLDC motor. 111
6.8 Mechanical assembly of SAT PMBLDC in-wheel motor. 111
6.9 Estimating deflection of tooth holder of SAT PMBLDC motor. . . 112
6.10 The segmented stator tooth with and without coil. 113
6.11 The finished shaft of the bonded magnet SAT PMBLDC motor. . 113
6.12 The stator assembly of the bonded RE magnet motor. 113
6.13 Bonded RE magnet poles and rotor yoke. 113
6.14 The bonded RE magnet motor during assembly. 114
6.15 Applying resin to the aligned stator. 114
6.16 The prototype of bonded RE magnet SAT PMBLDC motor. . . . 115
6.17 The assembly of a segmented stator tooth and hub. 117
6.18 The exploded view of the revised assembly for mounting tooth. 117
6.19 Threaded holes to ease the assembling and the dismantling. . . 118
6.20 The exploded view of the revised assembly of SAT motor. 118
6.21 Estimated defelction of revised tooth holder. 118
6.22 The stator tooth of the ferrite magnet SAT PMBLDC motor. . . . 120
6.23 The wound stator tooth of the ferrite magnet motor. 120
6.24 The shaft, the hub, and a tooth holder of the ferrite magnet motor.120
6.25 Assembling the stator of the ferrite magnet SAT PMBLDC motor. 121
6.26 The completed stator assembly of the ferrite magnet motor. . . 121

6.27 Machining hall sensor slots on the stator. 121
6.28 Hall sensors on the stator surface of the ferrite magnet motor. . 121
6.29 The ferrite magnet poles and rotor yoke assembly. 121
6.30 Uneven surface variation of ferrite magnet rotor 121
6.31 The end cover of the ferrite magnet motor with attached rotor. . 122
6.32 The rotor wheel of the ferrite magnet motor with end cover. . . 122
6.33 The ferrite magnet SAT PMBLDC motor during assembly. 122
6.34 The fabricated prototype of ferrite magnet motor. 122
6.35 The ferrite magnet motor installed in an electric-two wheeler. . 123

7.1 Experimental setup for testing hub motors. 127
7.2 Hub motor test setup under operation. 127
7.3 Exploded view of the motor removed from vehicle-1. 129
7.4 The FE thermal model of the radial flux PMBLDC hub motor. . . 130
7.5 Internal convective heat transfer regions of the radial flux motor. 130
7.6 The steady-state temperature variation of radial flux hub motor. 131
7.7 The temperature variation of radial flux motor with time. . . . 132
7.8 The surface temperature variation of the radial flux motor. . . . 132
7.9 FE thermal model of the ferrite magnet SAT PMBLDC motor. . . 134
7.10 Temperature distribution of the ferrite magnet motor. 134
7.11 Line-to-line back EMF waveforms obtained from back EMF tests. 135
7.12 Efficiency map obtained from test bench evaluation of motors. . 137
7.13 Data acquisition unit for recording data during driving cycle test. 138
7.14 The results from driving cycle tests of electric two-wheelers. . . 140

8.1 Flux-linkage-derivative of ferrite magnet motor prototype. . . . 147
8.2 Test and simulated line back EMF of the ferrite magnet motor. . 147
8.3 Comparison of peak tooth-tip flux densities of the prototype and design Fe-V2. 148
8.4 Comparison of rotor yoke eddy current loss function of the prototype and design Fe-V2. 148
8.5 The test and simulated phase current waveforms of the ferrite magnet motor. 149
8.6 The test and simulated efficiency map of the ferrite magnet motor. 150
8.7 Block diagram of the dynamic model of an electric scooter. . . . 151
8.8 The two-wheeler load model. 152

8.9 The controller model used in the simulation of an electric two-wheeler. 152
8.10 Comparison of results of simulation and testing of vehicle-3. . . 153

B.1 An overview of implementation of design program 181
B.2 Sheet-1 of Excel file used in the design program 184
B.3 Sheet-2 of Excel file used in the design program 184

D.1 The composition of test sequence based on the urban driving cycle. 210

List of Tables

1.1 Names of the vehicles used in the work 7

2.1 Comparison of battery technologies for electric vehicles. 15

3.1 Specification of vehicle-1. 30
3.2 The value of material properties, geometrical dimensions, and constants used to estimate the power rating of traction motors. 31
3.3 The powertrain specification of vehicle-2 and vehicle-3. 32

4.1 Classification of variables used to define the SAT motor geometry. 36
4.2 The performance and electrical specification of powertrains for vehicle-2 and vehicle-3. 41
4.3 Properties of the bonded RE magnet and ferrite magnet used in the design of motors. 43
4.4 Independent variables and their values of SAT PMBLDC motor, excluding optimisation variables. 43
4.5 The outer diameters of the bonded RE magnet motor and the ferrite magnet motor. 44
4.6 independent variables used as optimisation variables in design-synthesis of SAT PMBLDC motors and their range. 44
4.7 Results from the design synthesis of the bonded RE magnet motor. 47
4.8 Results from the design synthesis of the ferrite magnet motor. . 48
4.9 Summary of selected designs of the bonded RE magnet motor and the ferrite magnet motor. 50
4.10 Mass of active materials of the designed SAT PMBLDC traction motors. 51
4.11 Comparison of designs of the bonded magnet and the ferrite magnet SAT PMBLDC traction motors. 51

5.1 The dynamic model parameters with same value for both the bonded RE magnet and ferrite magnet motors. 79
5.2 The dynamic model parameters of the bonded RE magnet and the ferrite magnet motors. 80
5.3 The revised outer diameters of the bonded RE magnet motor and the ferrite magnet motor. 86
5.4 Results from the design synthesis of the bonded RE magnet motor using the revised design program. 88
5.5 Results from the design synthesis of the ferrite magnet motor using the revised design program. 89
5.6 Summary of the revised designs of SAT PMBLDC traction motors. 90
5.7 Mass of active materials of the revised designs of SAT PMBLDC traction motors. 91
5.8 Comparison of the revised designs of SAT PMBLDC traction motors. 91
5.9 The dynamic model parameters of revised designs 94
5.10 Properties of the bonded RE magnet and the ferrite magnet used in the designs. 98

6.1 The materials used in the fabrication of the stator components of SAT PMBLDC motor prototype. 107
6.2 The materials used in the fabrication of the rotor components of bonded magnet SAT PMBLDC motor prototype. 109
6.3 The specification of battery of the electric two wheeler. 123

7.1 Lists of tests performed on the group of motors used in the study 126

8.1 Comparison of designs and prototype of the bonded RE magnet SAT PMBLDC traction motors. 145
8.2 Comparison of designs and prototype of the ferrite magnet SAT PMBLDC traction motors. 145
8.3 The dynamic model parameters of prototype electromagnetic structure and design Fe-V2. 148

C.1 The performance measurement data of the sintered rare-earth magnet PMBLDC hub motor corresponding to a load torque of 5 N m. 201

C.2 The performance measurement data of the sintered rare-earth magnet PMBLDC hub motor corresponding to a load torque of 7.5 N m. 202
C.3 The performance measurement data of the sintered rare-earth magnet PMBLDC hub motor corresponding to a load torque of 10 N m. 202
C.4 The performance measurement data of the sintered rare-earth magnet PMBLDC hub motor corresponding to a load torque of 12.5 N m. 203
C.5 The performance measurement data of the sintered rare-earth magnet PMBLDC hub motor corresponding to a load torque of 15 N m. 203
C.6 The performance measurement data of the sintered rare-earth magnet PMBLDC hub motor corresponding to a load torque of 17.5 N m. 204
C.7 The performance measurement data of the sintered rare-earth magnet PMBLDC hub motor corresponding to a load torque of 20 N m. 204
C.8 The performance measurement data of the ferrite magnet SAT PMBLDC motor corresponding to a load torque of 5 N m. 205
C.9 The performance measurement data of the ferrite magnet SAT PMBLDC motor corresponding to a load torque of 7.5 N m. . . . 205
C.10 The performance measurement data of the ferrite magnet SAT PMBLDC motor corresponding to a load torque of 10 N m. . . . 206
C.11 The performance measurement data of the ferrite magnet SAT PMBLDC motor corresponding to a load torque of 12.5 N m. . . 206
C.12 The performance measurement data of the ferrite magnet SAT PMBLDC motor corresponding to a load torque of 15 N m. . . . 207
C.13 The performance measurement data of the ferrite magnet SAT PMBLDC motor corresponding to a load torque of 17.5 N m. . . 207
C.14 The performance measurement data of the ferrite magnet SAT PMBLDC motor corresponding to a load torque of 20 N m. . . . 208

D.1 Basic urban drive cycle as per ISO 13064-1:2012 209

Chapter 1

Introduction

1.1 Background of PhD Project

The high-energy density rare-earth (RE) magnets, especially Neodymium-Iron-Boron (NdFeB), are the preferred choice for all high-performance machines since the commercialisations of these magnets in the Eighties. There were very few efforts to find alternatives to the RE magnets or to develop high-efficiency electrical machines without using the RE magnets. Over the years, China became the largest producer of RE metals in the world, and in 2010, China was handling nearly all of the worldwide production of RE metals [1]–[4]. In 2011, the concern over the availability and the export restrictions caused the price of RE metals to increase considerably [5], [6]. The price variation of Neodymium, Dysprosium, and Samarium from 2001 to 2014 is shown in Figure 1.1, and although the price of the RE metals came down, the price fluctuations and the uncertainty in their supply is a concern for governments and manufacturers around the world [6], [7].

There are many permanent magnet applications where low-energy density bonded RE magnets are used only because of lack of alternative magnet materials in the energy density band of 38 kJ/m^3 to 100 kJ/m^3 [8]. Some of these applications are wind generators, motors for automotive applications, photovoltaic cells, and compressor motor used in refrigeration [8]. The energy density of ferrite magnets lies around the lower limit of the energy density band of 38 kJ/m^3 to 100 kJ/m^3. The ferrite materials are abundant, cost around $5 per kg, and represent about one-third of the worldwide permanent magnet market [9].

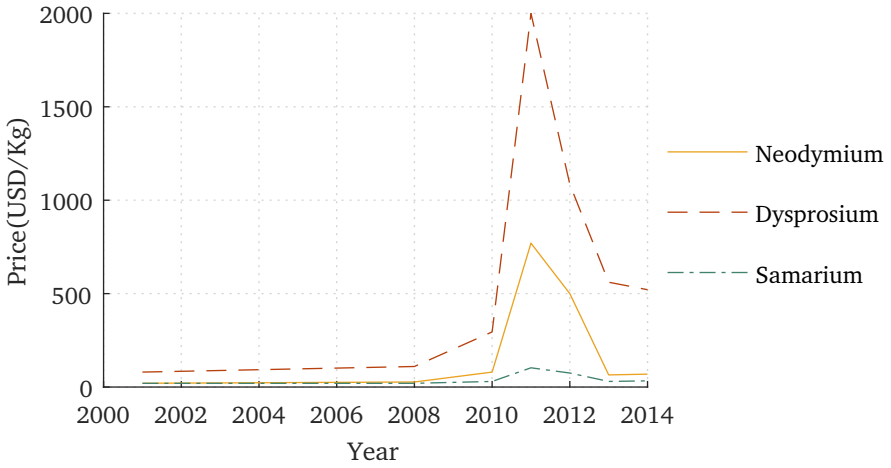

Figure 1.1: Price history of RE metals Neodymium, Dysprosium, and Samarium [5], [6].

The development of permanent magnets without or with reduced amounts of RE magnet, but showing a comparable performance to the low energy RE magnets, is crucial to allow technological companies in European Union (EU) to be competitive in the global market [7]. The NanoPyme (nanocrystalline permanent magnets based on hybrid metal-ferrites) consortium was formed[1] to create novel RE free magnets with an improved energy product than the currently used ferrites, and consequently, substitute the use of some of the low-energy density bonded RE magnet [10]. The PhD work was conceived as a part of the NanoPyme project with the aim of demonstrating the use of existing ferrite magnets as a substitute to RE magnets in a low-speed high-torque real world application.

After a review of permanent magnet machine applications, a direct drive traction motor for a city commuter electric two-wheeler is selected as the real world application for this work. The city commuter electric two-wheeler belongs to a group of vehicles known as light electric vehicles (LEV). The population of cities around the world is increasing, and consequently, mass transportation facilities are being severely stressed [11]. The situation contributes to an increased use of privately owned vehicles, and it adds to pollution and congestion. A comparison of travel characteristics of USA and UK is shown in Figure 1.2 highlights the congestion issues faced by the later country [12].

[1] The NanoPyme consortium was partially funded by the European Community through the Seventh Framework Programme under grant agreement no. 310516

The average distance travelled per day per individual in the UK is less than

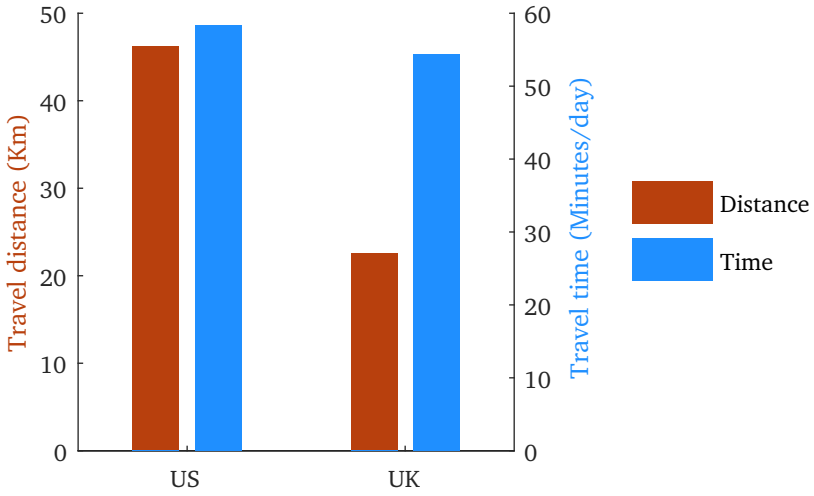

Figure 1.2: The average daily travel distance and time in US and UK [12].

half of that of USA. However, daily time spent on travel are nearly same in both countries. The modern powertrain and battery technologies are capable of developing LEV that can meet the average daily travel distance of people living in cities and their suburbs. Currently, a LEV costs twice compared to a similar vehicle with internal combustion engine (ICE). The LEV mostly use a powertrain with a lithium-ion (Li-ion) battery as the power source and a RE magnet motor as the energy converter to meet the range and the performance of ICE counterparts, and these two parts constitutes the major share of the cost of the vehicle. The battery prices are expected to reach $150 per kW h, goal for commercialisation, around the year 2020 [13], and a low-cost powertrain could help to price LEV competitively to ICE counterparts.

Though the PhD work started with the aim of using magnets developed by NanoPyme consortium, the technological challenges faced during the project meant that there was not enough material to produce the NanoPyme magnets for the machine design considered in the work. Therefore, a commercial ferrite magnet is used in this work.

1.2 Problem definition

This PhD study investigates the suitability of ferrite magnet machines as a substitute for RE magnet machines in an electric two-wheeler used for city commute. A ferrite magnet direct drive in-wheel motor will be developed for an electric two-wheeler, and additionally, a low-energy density bonded RE magnet in-wheel motor will be developed using the same design principle. A comparative study of design and performance of both the motors will be carried out. Further, the prototype vehicles with the ferrite magnet machine and the bonded RE magnet machine will be compared against the two vehicles of the same vehicle class purchased from the market.

1.3 Scope of the study

The scope of the work covers

1. A study of the significance of LEV in modern urban transportation context and the present market scenario of LEV.
2. Identification of a suitable type and topology of the motor for a ferrite magnet based electric two-wheeler powertrain.
3. Estimation of the rating of a direct drive motor used in an electric powertrain of a city commuter two-wheeler.
4. Development of a design-synthesis program of the identified motor topology.
5. Designing a bonded RE magnet motor and a ferrite magnet motor to use as traction motors of electric two-wheelers.
6. Development of a dynamic model of the motor topology incorporating the core losses to simulate the vehicle performance.
7. Development of mechanical assembly of the in-wheel motors.
8. Fabrication of the bonded RE magnet motor and the ferrite magnet motor.
9. Experimental evaluation of the fabricated motors on a test bench and as a powertrain of electric two-wheelers.

10. Assessment of the design program and the dynamic model using the experimental results.

1.4 Main contributions

The major contributions of this work are

1. **A simplified expression for calculating the motive force of a moving vehicle:** The proposed modification makes it easier to incorporate the equations of motion of a vehicle into numerical solving techniques.

2. **Finite element (FE) based design-synthesis program for segmented armature torus (SAT) motors:** When developing a design program for newer machine topologies, the use of FE models helps to avoid the time required for development of lumped parameter or analytical models. The developed FE design synthesis program generates a number of designs that satisfy a set of performance criteria and the designer can later select a design based on comparing parameters that are critical to the application for which the motor will be used. The presented approach makes it easier to define constraints for a design synthesis problem. A detailed description of the setting up of a FE based design synthesis problem, starting from the definition of design variables, FE model of the machine, how the design synthesis is carried out, and to, how a design is finalised from a set of designs that satisfy performance criteria, is included in this thesis. The usefulness of the proposed synthesis program is demonstrated by designing two SAT permanent magnet brushless DC (PMBLDC) traction motors.

3. **Nonlinear dynamic model of PMBLDC motor considering core losses:** The phase variable model is used commonly when simulating a motor drive system with a three-phase PMBLDC motor. The phase variable model neglects core losses and this affects its accuracy when modelling fractional-slot machines. The inaccuracy of phase variable model of fractional-slot machines can be attributed to considerable armature flux harmonics, which causes an increased core loss. This study proposes a nonlinear phase variable model of PMBLDC motor that considers

core losses induced in the stator and the rotor. The core loss model is developed based on the detailed analysis of the flux path and the variation of flux in different components of the machine.

4. **A study on the effect of temperature on the performance of ferrite magnet PMBLDC motor:** The influence of temperature on BH characteristics of ferrite magnets differ considerably from that of rare earth magnets and hence, requires a different approach when deciding the operating point of ferrite magnets in a machine. A detailed analysis is carried out to ensure that, the designed ferrite magnet motor is capable of delivering the specified torque throughout the operating temperature, without any irreversible demagnetization of magnets. The study concluded that the maximum speed of the ferrite magnet PMBLDC motor for a given load torque decreases as the magnet temperature drops.

5. **A novel mechanical assembly of SAT PMBLDC motor:** A mechanically stable, easy to assemble and dismantle, repair and recycle friendly assembly of SAT motor has been proposed and demonstrated.

6. **Development of a high-efficiency ferrite magnet based electric powertrain for two-wheelers:** A high-efficiency ferrite magnet based electric powertrain for two-wheelers has been developed and incorporated into a prototype vehicle. The performance of the prototype is tested against two market sourced electric two-wheelers with rare-earth magnet based motor. From the test data, it is found that the ferrite magnet powertrain consumes less energy to drive the driving cycle stated in ISO 13064-1:2012, however, has 70 % more acceleration time.

1.5 Guide to the readers

This report has nine chapters. Chapter 1 is the introduction to the report and presents the background of research, the problem definition, the scope of the work, and the main contributions from the work.

Chapter 2 explains the present scenario of LEV, traction motor choices for EV, the past works in the area of ferrite magnet traction motors, and concludes by selecting a motor topology for the ferrite magnet in-wheel motor.

Chapter 3 discusses the concept of a powertrain of a vehicle, a method to estimate the powertrain rating, and calculation of powertrain rating of the

prototype vehicles planned to build as a part of this work.

Chapter 4 covers the design-synthesis program of SAT PMBLDC motor, the design of the bonded RE magnet in-wheel motor, and the design of the ferrite magnet in-wheel motor.

Chapter 5 presents a non-linear dynamic model of PMBLDC motor that considers core losses in the machine. Further, the chapter discusses a revision of the design program of SAT PMBLDC motor based on the results of dynamic analysis and presents a study of performance variation of the designed ferrite magnet motor with the temperature of the magnet.

Chapter 6 discusses the mechanical assembly design of SAT motors, and documents the fabrication of both the bonded RE magnet motor and the ferrite magnet motor.

Chapter 7 covers tests done on prototype motor, prototype vehicle, and vehicles purchased from the market.

Chapter 8 discusses how the motors evolved through the different stages of product development starting from an initial design to a fabricated prototype. Further, the chapter also covers an assessment of theoretical models presented in this work.

Chapter 9 concludes the study and proposes future research directions for the concepts presented in this work.

In this work, the author refers direct drive traction motor built into the wheel of a vehicle as hub motor and in-wheel motor. Further, two-wheeler is also addressed as scooter and motor is also called as machine. This work uses two electric scooters purchase from the market, Matra emo and Yamaha EC-03. The vehicle chassis of Matra emo allows change of the controller and the traction motor, and hence it is used to test the prototype motors. The vehicles used in the study have been named as listed in Table 1.1.

Matra emo scooter	Vehicle-1
Matra emo chassis and bonded RE magnet motor	Vehicle-2
Matra emo chassis and ferrite magnet motor	Vehicle-3
Yamaha EC-03 scooter	Vehicle-4

Table 1.1: Names of the vehicles used in the work

Chapter 2

Light electric vehicles and their powertrains

2.1 Introduction

Light electric vehicles are designed for the use in populated urban centres. They are designed with a top speed that matches the city speed limit and therefore, not intended for the use on highways. LEV include diverse set of personal mobility solutions such as stand-on scooters, pedelecs, mopeds, scooters, motorcycles, and three-wheeled cargo bikes [14].

This chapter presents a digest of existing literature on electric vehicles (EV), light electric vehicles, the role of LEV in current and future urban transportation, and the system architecture of LEV. Further, different types of traction motors and their topologies are examined to identify a suitable motor, which will be used as the ferrite magnet direct-drive electric two-wheeler powertrain.

2.2 Present scenario of light electric vehicles

The search for an alternative to ICE powered vehicle has been around since the 1970s [15]. The interest of general public, government, and industries fluctuates depending on the oil price, environmental causes, and the need for energy independence [16]. Since 2010, several manufacturers, both existing as well as new entrants, launched EV in many countries around the

world [17]. First modern LEV launched in Japan by Yamaha in 1993, and they were not popular until 2001 [18]. World wide sales started climbing since 2001 and in 2011, Chinese market crossed thirty million, Japan has four hundred thousand, Europe has one million, and around eighty thousand in the USA [18]. Unlike China, European sales are dominated by pedelecs and the sale of higher-powered moped, scooters, and bikes was limited to 15,000 units in 2011 [18].

EV transportation, when coupled with renewable energy, has ultra low emission from well to wheel along with low cost of running. This section discusses different types of EV, hindering factors and challenges faced by EV, the expected favourable conditions in coming decade, and technological choices for LEV components.

2.2.1 Classification of electric vehicles

The EV coexisted with ICE vehicles at the beginning of 20th century [15]. The developments in ICE vehicle such as starter motor coupled with the short range of EV made ICE technology completely dominate the powered transportation [19]. The end of the 20th century saw return of EV with improved range and performance. The new generation of EV are powered from one or more power sources and are classified according to their powertrain configuration as shown in Figure 2.1.

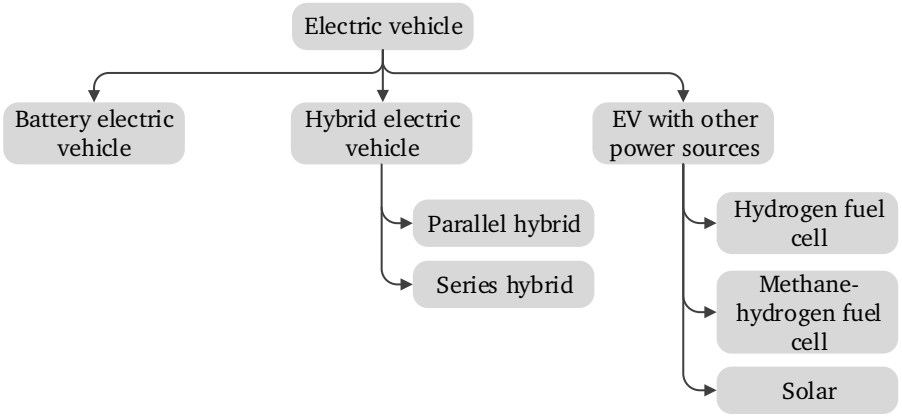

Figure 2.1: Classifications of electric vehicles.

The EV that uses rechargeable cells as their sole power source is known as battery electric vehicles (BEV). The layout of BEV is shown in Figure 2.2. The

battery will be supplying power to the traction motor via a power electronic converter. The power from the motor will be transmitted to the wheels either directly or via a transmission. The motor controllers can be configured to operate the drive in the four-quadrant mode to include regenerative breaking; thus extending the range of BEV.

Figure 2.2: System layout of a battery electric vehicle.

The short range of BEV and lack of wide availability of charging network has led to the development of hybrid electric vehicle with more than one power source. Toyota prius® is an example of hybrid vehicle, where a combination of an IC engine and an electric motor propels the vehicle. In most hybrid vehicles, the motor will be powered by a smaller capacity battery compared to BEV and the presence of the motor allows IC engine to operate in its maximum efficiency band by load sharing. Hybrid vehicles are classified as series and parallel depending on how the power is transferred to the wheels [19]. In series hybrid vehicles, an IC engine drives a generator, which in turn supplies power to one or more motor connected to the drive shaft. The layout of a configuration of the series hybrid vehicle is shown in Figure 2.3. In parallel

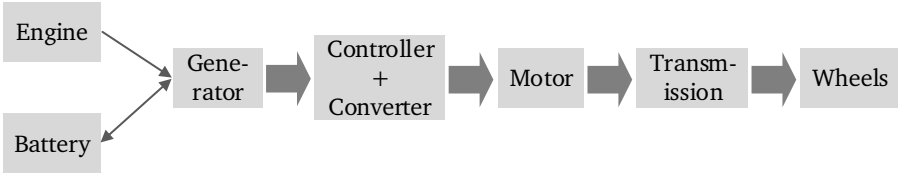

Figure 2.3: System layout of a series hybrid electric vehicle.

hybrid electric vehicles, both IC engine and motor can independently propel the vehicle. The layout of a parallel hybrid vehicle configuration is shown in Figure 2.4. Both the motor and the IC engine are mechanically coupled to the transmission of the vehicle, and the vehicle controller will decide the load ratio between the power sources based on driving mode.

In addition to the described types, there are EV technologies which are currently in technology demonstration stage such as fuel cell vehicles and solar-powered vehicles [19].

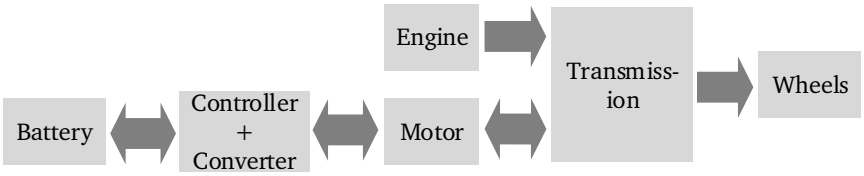

Figure 2.4: System layout of a parallel hybrid electric vehicle.

2.2.2 Advantage of LEV in urban context

LEV offer many benefit in an urban context as the major cities around the world are facing heavy traffic congestion and air pollution from automotive exhausts [20], [21]. The LEV can help to solve congestion and air pollution because they require less space on the road and for parking, have low running costs, and ultra low emission. At present, EV are available for the entire passenger class[2] and most of the modern EV will meet the daily commuting distance of the majority of the people living in cities and their suburbs [12], [18], [22].

2.2.3 Hindering factors to the growth of electric vehicles

The major factors affecting the growth of EV are following

1. Energy density of EV battery: The consumers are expecting a similar performance of ICE vehicles such as range, acceleration, and top speed from EV. At present, the battery technology is yet to evolve to have a similar energy density as that of hydrocarbon fuels. For example, petrol has a specific energy of around 1800 W h/kg after accounting the efficiency of ICE powertrain, which is around 20 %, and practical value of specific energy of the latest Li-ion battery is around 200 W h/kg [19], [23], [24]. Therefore, powertrain performance of LEV need to be optimized for the maximum range.

2. Cost of Li-ion battery: The cost of battery dominates the manufacturing cost of EV. The production cost of Li-ion battery, preferred battery choice for EV, is expected to remain high even after considering the economics

[2] The road transport vehicles are classified as passenger and commercial. The passenger vehicle category includes two-wheelers, three-wheelers, and cars. The commercial vehicle category includes delivery bikes, vans, light and heavy trucks, and buses.

of scale and will reach a realistic mass production value of $150 per kW h only around the year 2020 [13].

3. Charging time and infrastructure: The number of easily accessible charging stations and the time required to charge the battery are present concerns of a potential EV customer. Moreover, without an increased contribution from emission-free power generation, such as renewable and nuclear, to total electricity production, the reduction of well to wheel emission by EV will be marginal [25].

2.2.4 Favourable factors for electric vehicle growth in future

The following are the main driving factors behind the electrification of transportation

1. Cost of developing low emission ICE powered vehicles: Carbon dioxide (CO_2) is a greenhouse gas (GHG), and transportation is a major contributor of CO_2 emissions [22]. In Western Europe, 24 % all CO_2 emission are from transport and in that, more than 90 % is contributed by road transport [26]. A case study of mileage and emission in Germany from 1960 to 2010 is shown that continuously increasing mileage over years has not reduced CO_2 emission [22]. In 2009, EU Parliament introduced new laws aiming to reduce CO_2 emission to 95 g/km by 2020 with intermediate targets [16], [27]. Manufacturers who exceed the limit need to pay a penalty of €95 per gram for every gram that exceeds the limit from 2019 onwards [27]. Achieving the proposed low emission level can offset the cost benefit that ICE vehicles currently have over EV.

2. City traffic regulations: A study on two-wheeler emission in Europe for a period 1999-2012 estimated that these vehicles emit more than 7 % and 20 % of total road transport carbon monoxide and hydrocarbon emission respectively [20]. Even though NO_x and CO_2 emission from two-wheelers are negligible, the considerable growth of two-wheelers in urban areas is a concern and authorities are either considering or introducing regulatory measures restricting the use of vehicles with emission inside city limits [28], [29]. The 30 km/h speed limit in 80 % of roads in Amsterdam city is an example and the low speed limits make LEV faster by 50 % on intracity trips [11].

2.2.5 System architecture and components of light electric vehicles

The system architecture of LEV is shown in Figure 2.5. It consists of a pow-

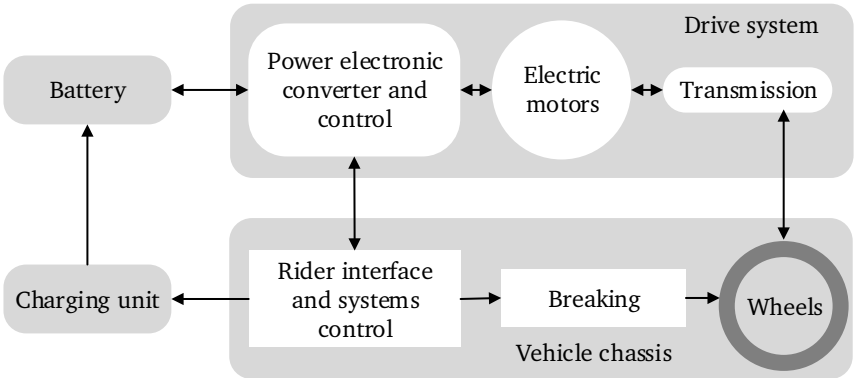

Figure 2.5: System architecture of light electric vehicles.

ertrain and chassis of the vehicle. The powertrain produces tractive force at the wheels by drawing the power from the battery. Besides the battery, the powertrain consists of a controller, a power electronic converter, an electric motor, and a transmission. The user inputs via the rider interface will control the operation of powertrain as well as braking. The rider interface consists of a throttle, brake levers, and switchgear for signalling and lighting. The charging unit charges the battery and the vehicle control systems monitors and regulates the rate of charging. Further, the rider interface in an LEV will have a display showing the information about the available range, the vehicle speed, and the status of different instruments of the vehicle. The vehicle performance and ease of usage parameters such as the maximum speed, hill climbing speed, range, rider position, and gross weight along with the production cost will decide the selection of components [14]. A brief overview of components of an LEV is described in the remaining parts of this section.

Until recently, the most commonly used batteries for EV were sealed lead acid (SLA) battery with gel as electrolyte [19]. The main drawback SLA battery is their low energy density, which makes EV using them considerably heavier. SLA batteries are easier to charge, and they are charged by applying a constant voltage. In modern EV, either Nickel-metal-hydride (NiMH) batteries or Lithium-ion (Li-ion) batteries substitute SLA batteries. The NiMH batteries have much higher energy density than SLA, and they can be charged con-

Parameter	SLA	NiMH	Li-ion
Specific energy (W h/kg)	40	50-80	80-190
Power density (W/kg)	250	200	300 to 1500
Full/partial recharge time (h)	8/1 for 90 %	1/0.33 for 60 %	3/1 for 80 %
Number of life cycles with 80 % of original capacity still available	800	1000	> 1000

Table 2.1: Comparison of battery technologies for electric vehicles [14], [19].

siderably faster. However, NiMH batteries get heated up quickly, and larger capacity requires integrated cooling solutions [19]. The Li-ion batteries offer the highest energy and power densities among commercialized battery technologies. Moreover, Li-ion batteries can be operated over a wide temperature range. Besides being the most expensive, Li-ion batteries require accurate voltage control for charging [19]. A comparison of the three battery technologies is shown in Table 2.1.

The power electronic converter uses MOSFETs or IGBTs as switching devices. The commonly used EV traction motors are induction motor, permanent magnet synchronous motor (PMSM), reluctance motor (RM), PMBLDC motor, or switched reluctance motor (SRM) [30]. The manufacturers have adopted the existing chassis used in ICE vehicles for LEV. The use of lightweight materials have not been widely adopted because the battery makes LEV costlier than comparable ICE vehicles, and the use of material such as carbon fibre could make LEV a niche product. EV in general uses specially developed low rolling resistance tires to reduce the frictional losses. The breaking system in LEV uses regenerative braking alongside mechanical or hydraulic brakes to improve overall range.

2.3 Traction motors for electric vehicles

A classification of electric motors used in commercially available EV or technology demonstration EV are shown in Figure 2.6 [30]. An electric motor can be a DC motor or an AC motor based on the operating field. The DC machine has a stationary field while AC machine has a rotating field.

In DC machines, the stator has wound field coils and the rotor has a brush-commutator arrangement to direct the current in the armature winding in such a way that a consistent unidirectional torque is produced. The brush-

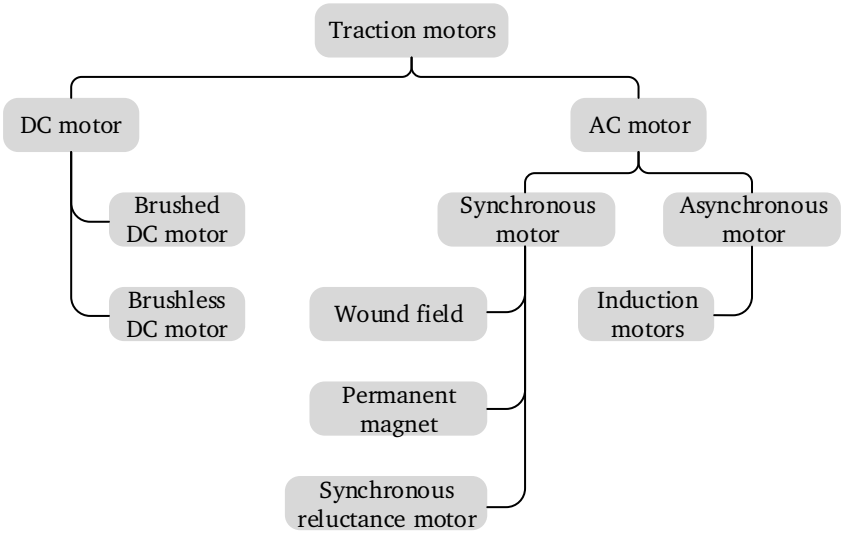

Figure 2.6: A classification of traction motors for electric vehicles.

commutator set up has disadvantages such as they require regular maintenance and they produce sparks that interfere with communication networks [31]. The developments in permanent magnet materials and power electronics allowed to replace the field coils in the stator with permanent magnet poles placed in the rotor [31]–[33]. Consequently, the armature is moved to the stator, and electronic switches control the magnitude and the direction of armature current based on the rotor position. The DC motors with permanent magnet poles on the rotor and electronically commutated armature on the stator are called permanent magnet brushless DC motor.

There are two types of AC motors and they are synchronous motors and asynchronous motors. In synchronous motors, the rotor will rotate at the same speed as that of stator field. Examples of commonly used synchronous motors are wound field synchronous motor, PMSM, and RM. In an asynchronous motor, the rotor will rotate at a speed different from that of the stator field, and the speed difference is the cause of rotating torque. The induction motor is an asynchronous motor that is extensively used in EV [30].

In addition, researchers are exploring the use of motors such as SRM, doubly-salient permanent magnet motor, flux-reversal permanent magnet motor, flux-switching permanent magnet motor, hybrid excited permanent magnet motor, flux-mnemonic permanent magnet motor, and vernier permanent magnet motor as traction motors for EV [30], [34]–[36].

Selecting a type of motor as a traction motor for an electric vehicle is decided based on many factors such as cost of the raw materials, cost of fabrication and assembly, efficiency, power per unit mass, torque per unit mass, cost of the maintenance, ease of repair, and recyclability of the motor components after service life. However, years of research in EV established few trends. Selecting permanent magnet motors with a high energy density RE magnet results in compact and very high efficiency motors [37], [38]. Choosing magnet-less motors such as induction motors and synchronous reluctance motor will lead to a low-cost electric powertrain at the cost of efficiency and compactness [39]. This work explores traction motors with low energy density magnets, specifically ferrite magnets, which costs considerably less than high-energy RE magnets.

2.4 Ferrite magnet traction motors

A comparison of remanence and coercivity of ferrite magnets and three RE magnet classes is shown in Figure 2.7. The ferrite magnets have nearly one-

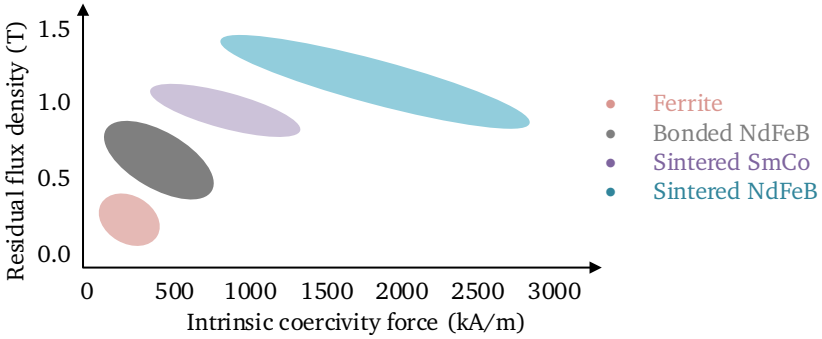

Figure 2.7: A comparison of magnetic properties of ferrite, bonded RE, samarium cobalt (SmCo), and neodymium iron boron magnets.

fourth residual flux density and a considerably lower coercivity compared to sintered NdFeB magnets. Therefore, when comparing a ferrite magnet and an NdFeB magnet of same dimensions, the ferrite magnet produces one-fourth of the flux generated by the NdFeB magnet, and could be demagnetized by a much lower demagnetizing field than the field required to demagnetize the NdFeB magnet. Motor designers tackle the inherent deficiencies of ferrite magnets by selecting a motor topology that allows placing more magnets and en-

suring that the motor field poles are not exposed to an armature field of magnitude that can cause demagnetization. However, it is important to emphasis that the ferrite motors are only suitable in applications where the performance reduction can be overreached by the cost reduction, and hence, not suitable in applications where high performance is critical.

Many motor topologies and modifications to motor geometry have been proposed to enhance the airgap flux density of ferrite magnet machines. The spoke-type topology of the interior permanent magnet (IPM) motor, shown in Figure 2.8, is favoured for ferrite magnet based drives, because the flux

Figure 2.8: Rotor of a spoke type IPM motor using ferrite magnet [40]. © 2016 IEEE.

concentration allows a higher flux density in the airgap than the residual flux density of the magnet [40], [41]. In [42], the authors fabricated and tested a separated-pole-piece type ferrite magnet IPM with multi-layered overhang. The separated-pole-piece type motor topology is shown in Figure 2.9, and the

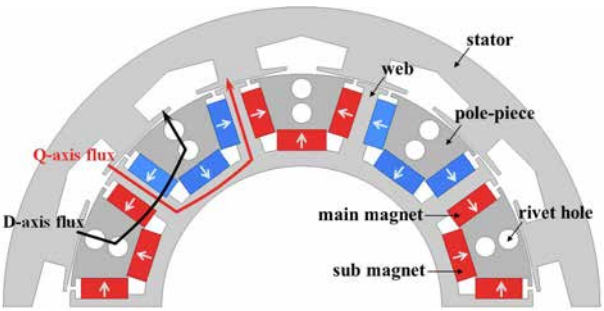

Figure 2.9: The separated pole piece type IPM topology [42]. © 2015 IEEE.

rotor is a modification of the spoke-type rotor. In [43], the authors proposed a modified spoke type IPM with segmented wing shaped poles. The topology, shown in Figure 2.10, uses smaller magnets to enhance the flux of the main

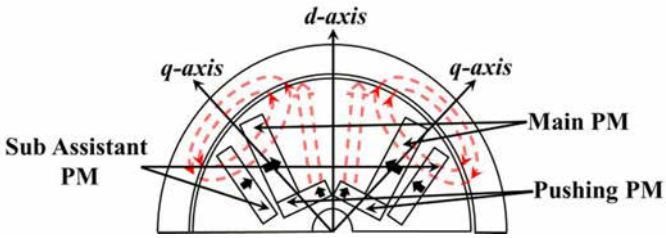

Figure 2.10: Spoke-type IPM with segmented wing-shaped poles [43]. © 2014 IEEE.

magnet pole.

In [44], the authors analysed two axial flux ferrite magnet in-wheel motors with stators made of soft magnetic composite and found that providing semi-closed slots instead of open slots allowed increasing the power rating by 50 %. In [45], the authors used a dual stator yokeless axial flux topology to develop an in-wheel ferrite magnet motor for an electric city commuter. In [46], the authors proposed an axial flux dual rotor motor topology for ferrite magnet motor, shown in Figure 2.11, with circumferentially magnetised magnets sandwiched in the stator that enhances the airgap flux density considerably more than the spoke type IPM motor topology.

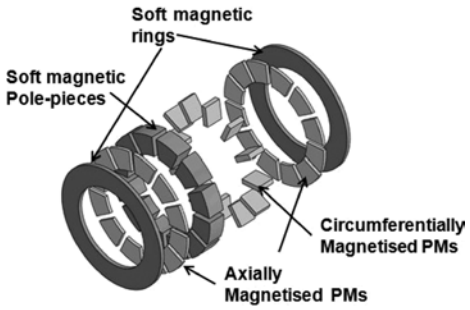

Figure 2.11: A dual rotor disk type motor with circumferentially and axially magnetized permanent magnets [46]. © 2012 IEEE.

Many works have explored trade-offs of opting for a ferrite magnet motor as a substitute to RE magnets in permanent magnet machines. In [47], the authors studied the relationship between magnet type and machine performance with the help of multi-objective optimisation and concluded that a lower energy density magnet can meet some of the performance indices such as high efficiency, high torque density, etc. of higher energy density magnets if appropriately optimised. In [48], the authors found that for an 80 kW traction

motor, the ferrite magnet machine is 2 % less efficient and torque per unit mass is 26 % lower compared to an NdFeB magnet motor of the same rating. However, the reduction in the cost of active material per kW was 30 %. In [49], the authors concluded that if efficiencies were comparable the ferrite magnet traction motor would have a lesser environmental impact than the RE magnet traction motor. In [50], the authors compared high-speed traction motors with different grades of dysprosium-free sintered NdFeB magnets and a ferrite magnet grade. The design of a motor that uses sintered NdFeB magnet with dysprosium is used as a baseline. The study concluded that the ferrite magnet motor was longer by 65 % and heavier by 31 %. However, the motor has better efficiency at higher operating speeds due to lower flux levels.

2.5 Selecting a traction motor topology for a city commuter electric two-wheeler

A survey of city commuter electric two-wheelers available in the European market found that they use either 13 inch or 14 inch wheels. Therefore, the maximum rotational speed of wheels of this vehicle at a top speed of 30 km/h will be below 400 rpm. The low wheel spinning speed of city electric two-wheelers allows using a direct-drive powertrain. The direct-drive motors offer simplicity by removing the gears and thus increasing the reliability. The permanent magnet motors offer many benefits over induction motors and SRM considering the limited space available in LEV such as higher efficiency due to low losses in rotating parts, higher torque per unit mass, and low torque ripple with fractional-slot configurations [31], [48].

The outer rotor motor is a commonly used configuration of direct-drive in-wheel motors [38], [51]–[54]. An outer rotor motor is preferred especially when the motor uses low energy density magnets as they allow placing a structurally simpler rotor outside and a more complex stator inside resulting an increased airgap volume where the electromagnetic force is produced in the motor. Further, the external rotor structure allows a direct structural link between the wheel rim and the rotor casing, thus avoiding the need for a drive shaft.

Theoretically, all permanent magnet brushless machines can be run either as a PMBLDC motor or as a PMSM [55]. The in-wheel motor for the city electric two-wheeler is a low-speed application, and there is no need to operate

the machine in the field weakening high-speed mode. A PMBLDC motor drive is more suitable for a low-speed high-torque application like LEV because it is more torque dense and their controllers and rotor position sensors are cheaper than the ones used PMSM [55]–[57].

Radial flux and axial flux are the two major configurations of permanent magnet machines. Axial flux machines (AFM) offer higher torque density compared to radial flux motors for low-speed application such as an in-wheel motor for electric two-wheelers, where the available axial length of the machine is limited [58]–[60]. The disc shapes of the stator and the rotor of AFM allows several topological variations by arranging the multiple units of stators and rotors [61]–[63]. Among all AFM topologies, the segmented armature torus topology, shown in Figure 2.12, was found to be most promising one

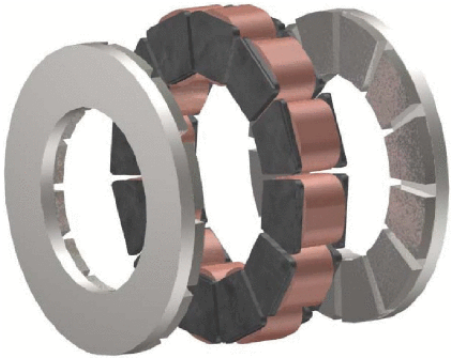

Figure 2.12: Segmented armature torus permanent magnet motor [64]. © 2007 IEEE.

for a ferrite magnet in-wheel motor [64]–[66]. The SAT motor topology is a variation of north-south type torus slotted AFM described by authors in [61] and has no stator yoke. The magnetically separated teeth can be wound separately before assembling the stator, and this ensures high fill factor and short end turn resulting in an efficiency improvement [67]. Moreover, a dual rotor AFM topology allows placing more magnets and helps to compensate the use of low-energy magnets.

2.6 Operating principle of PMBLDC motor drives

The block diagram of a three-phase PMBLDC motor drive is shown in Figure 2.13. A three-phase PMBLDC motor drive consists of a three-phase inverter, a PMBLDC motor with built-in position sensors, and a controller. A

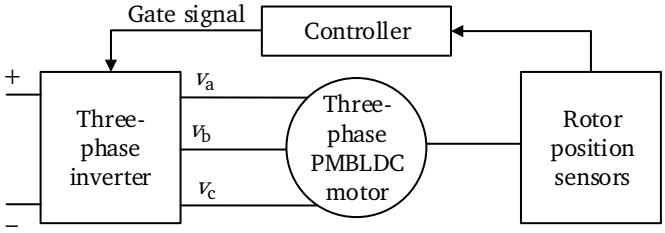

Figure 2.13: Block diagram of a PMBLDC motor drive.

set of three hall sensors, either fixed inside slot openings or on a separate mount attached to the stator frame, is used for the rotor position sensing. In a three-phase star connected PMBLDC motor, only two phases will be part of the electromagnetic torque production at any instant. The controller decides the active phases of the machine based on the sensed rotor position.

The operation of a three-phase PMBLDC motor can be explained with the help of a two-pole three-slot machine shown in Figure 2.14(a). The variations of idealised back EMF(electromotive force), current, and hall sensor outputs of the motor with rotor position is shown in Figure 2.14(b). In Figure 2.14(a), the rotor is positioned at 0°. Each phase conducts in two 120° electrical segments when the magnitude of back EMF of the conducting phase is at its maximum and this excitation pattern ensures the generation of the maximum output power. The controller will initiate the conduction for each phase at an instant when the hall sensor corresponding to that phase has a different state from the other two phases and turns off the phase when the state of that hall sensor changes. The direction of phase currents is decided by the state of hall sensors.

2.7 Conclusion

The electric propulsion offers unique solutions to the present and future transportation requirements of cities and their suburbs without GHG and pollutant emissions and has a low running cost. Additionally, LEV can reduce traffic congestion, and they require minimal parking spaces. The market studies highlight the growth potential of LEV and some of the markets like China and Europe already showing promise. The currently available LEV have the range to meet the daily commuting distance of the majority of the targeted customers and the main challenge is in bringing down their price to the cost of comparable ICE vehicles. A low-cost traction motor without RE magnets and the

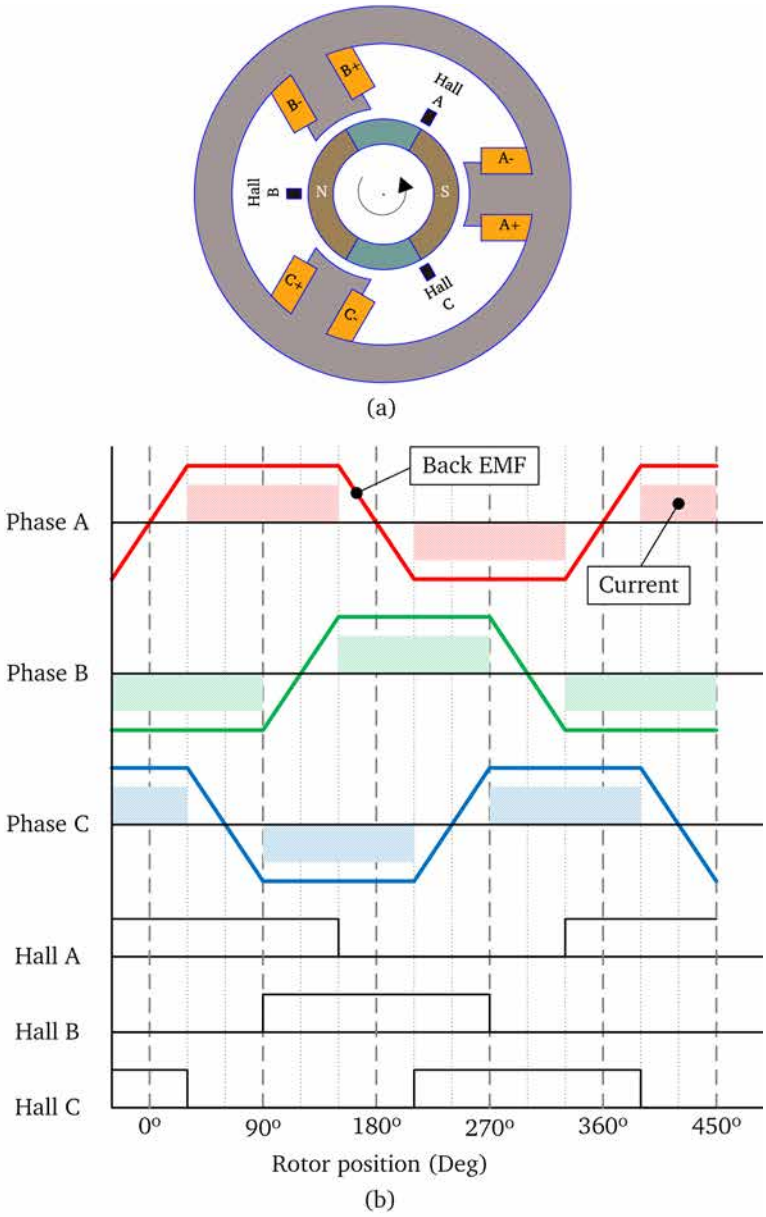

Figure 2.14: (a) A 2-pole three-phase PMBLDC motor with rotor positioned at 0°. (b) Ideal voltage, ideal current, and hall sensor output variations with rotor position.

expected price drop of Li-ion batteries in coming years could help to price the LEV competitively to ICE powered counterparts. The next chapter will discuss the calculation of the rating of an electric powertrain for a two-wheeler.

Chapter 3

The powertrain rating of electric two-wheeler

3.1 Introduction

This chapter discusses the powertrain of a vehicle, the method of calculating the rating of powertrain, and at the end, calculates the rating of the powertrain for an electric two-wheeler for city use.

3.2 Powertrain of a vehicle

The powertrain is the component of the vehicle that converts onboard stored energy into kinetic energy. The powertrain rating is the specification of power converter used to propel the vehicle. The power converter can be an internal combustion engine and a transmission, electric motor and a transmission, or electric motor alone in the case of a direct drive powertrain. The rating of the powertrain is decided based on the performance requirements such as the time required for accelerating to top speed and the capacity to maintain the top speed over different road condition such as ascents and headwind. This section discusses the forces acting on a moving vehicle and characteristics of the electric drive that power an electric vehicle.

3.2.1 The forces acting on a vehicle in motion

The motion of a vehicle consists of acceleration, maintaining a set speed, deceleration or coasting, and braking. When a vehicle moves, the bulk of the power is required during acceleration and a smaller quantity during constant speed running [19]. The power can be recovered back when the vehicle decelerates or brakes, if the vehicle is equipped with regenerative braking. During acceleration, the powertrain has to overcome the inertia of the vehicle that includes both linear and rotational components along with rolling and aerodynamic frictional forces. While moving along a gradient, the gravitational force component on vehicle mass along the gradient also appears. The forces acting on a vehicle moving at a constant speed are shown in Figure 3.1 and they are rolling friction, gravitational force, and aerodynamic drag force. The rolling

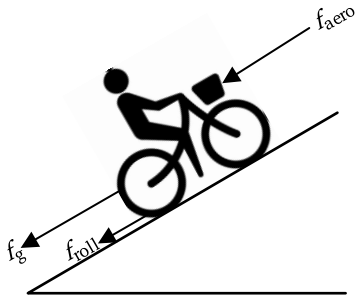

Figure 3.1: The forces acting on a vehicle moving at constant speed.

friction, f_{roll} is calculated as [52]

$$f_{\mathrm{roll}} = \left(0.0085 + \frac{0.01}{p} + \frac{2 \cdot 10^{-5} \cdot v^2}{p}\right) mg \tag{3.1}$$

where, p is the tire pressure in bar, v is the speed of vehicle, m is the total mass of vehicle, and g is the gravitational acceleration constant. The aerodynamic drag force is calculated as [52]

$$f_{\mathrm{aero}} = 0.5 C_{\mathrm{d}} \rho_{\mathrm{air}} A_{\mathrm{f}} v^2 \tag{3.2}$$

where, C_{d} is the coefficient of drag of the vehicle, ρ_{air} is the density of air, and A_{f} is frontal area of vehicle. The gravitation force when moving up a gradient is calculated as

$$f_{\mathrm{g}} = mg \sin\left[\tan^{-1}\left(\frac{\theta_{\mathrm{grad}}}{100}\right)\right] \tag{3.3}$$

where, θ_{grad} is the percentage slope of the riding surface. The total opposing force, named as road load, is therefore

$$f_{\text{r}} = \left(0.0085 + \frac{0.01}{p} + \frac{2 \cdot 10^{-5} \cdot v^2}{p}\right) mg + 0.5 C_{\text{d}} \rho_{\text{air}} A_{\text{f}} v^2 + mg \sin\left[\tan^{-1}\left(\frac{\theta_{\text{grad}}}{100}\right)\right] \tag{3.4}$$

The above equation can be rearranged as

$$f_{\text{r}} = \left\{0.0085 + \frac{0.018}{p} + \sin\left[\tan^{-1}\left(\frac{\theta_{\text{grad}}}{100}\right)\right]\right\} mg + \left(0.5 C_{\text{d}} \rho_{\text{air}} A_{\text{f}} + \frac{2 \cdot 10^{-5}}{p}\right) v^2 \tag{3.5}$$

While grouping speed dependant and independent terms, the road load can be expressed as

$$f_{\text{r}} = k_1 + k_2 v^2 \tag{3.6}$$

where, k_1 and k_2 are speed independent constants. The force required to accelerate the total mass of vehicle is given by

$$f_{\text{a}} = k_{\text{m}} m \frac{dv}{dt} \tag{3.7}$$

where, k_{m} is coefficient to correct rotational inertia. The total motive force, f_{m} required to accelerate the vehicle can be obtained from Eq. (3.6) and Eq. (3.7) as

$$f_{\text{m}} = k_1 + k_2 v^2 + k_{\text{m}} m \frac{dv}{dt} \tag{3.8}$$

3.2.2 Characteristics of electric powertrain

The electric powertrain consists of a controller, a converter, an electric motor, and in some cases a transmission to amplify the torque by reducing the speed of rotation. The powertrain delivers necessary tractive force based on the user inputs and the design of powertrain targets to supply the expected vehicle performance from a limited on-board energy storage, generally an electrochemical battery. Figure 3.2 shows the variation of output power and torque of an electric motor drive with speed of a vehicle. An electric motor can deliver the rated torque only up to its rated speed, v_{r} and at the rated speed, the power output will be equal to the rated power. Beyond the rated speed, a motor oper-

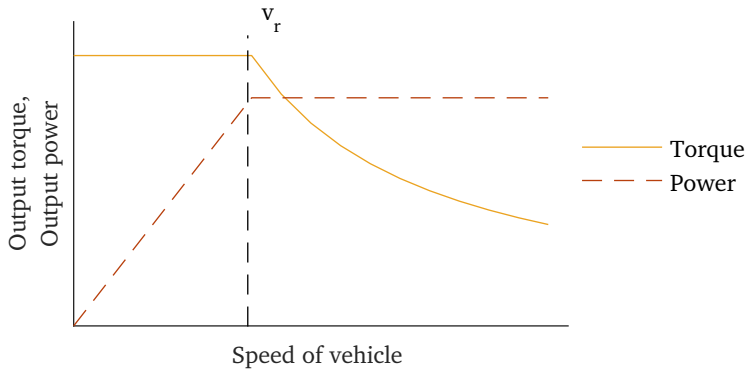

Figure 3.2: Torque and power variation of an electric motor drive with speed of the vehicle.

ates in constant power region and the output torque is inversely proportional to the speed.

3.2.3 Equations of electric vehicle in motion

In an electric vehicle, a motor drive with the torque curve as shown in Figure 3.2 will be driving a load governed by Eq. (3.8). The different powered stages in a vehicle movement are acceleration and constant speed running.

Acceleration of vehicle

The acceleration profile of a vehicle can be obtained by solving Eq. (3.8) for the motor drive torque-speed curve shown in Figure 3.2. The Eq. (3.8) has to be solved separately for the constant torque region and the constant power region because of the discontinuity in the torque vs. speed curve of the motor drive. For the constant torque region,

$$\frac{\mathrm{P_r}}{\mathrm{v_r}} = k_1 + k_2 v^2 + k_\mathrm{m} m \frac{dv}{dt} \tag{3.9}$$

where, $\mathrm{P_r}$ is the rated power of the electric drive. The Eq. (3.9) can be solved numerically until the speed is equal to the rated speed of the motor, and this velocity and the corresponding time will be the initial condition while solving the constant power region. In the constant power region Eq. (3.8) can be written as

$$\frac{\mathrm{P_r}}{v} = k_1 + k_2 v^2 + k_\mathrm{m} m \frac{dv}{dt} \tag{3.10}$$

All quantities in the above equations have to be converted to either rotational or linear equivalent values.

Constant speed operation

When a vehicle is moving with a constant speed, the powertrain has to deliver only a force equal to the road load as per Eq. (3.6). This force will be less than the force required during the acceleration.

3.3 Estimation of the rating of an electric drive based powertrain

The performance of a vehicle as perceived by consumers is the time required to reach the top speed, $\mathrm{v_m}$. The top speed, especially in city driving conditions, is regulated by traffic rules and traffic conditions. It is assumed that $\mathrm{v_m}$ is greater than $\mathrm{v_r}$ to generalise the formulation. The expression for the motive force given by Eq. (3.8) can be rearranged as

$$\frac{dv}{dt} = \frac{f_\mathrm{m} - (k_1 + k_2 v^2)}{k_\mathrm{m} m} \tag{3.11}$$

The time required to accelerate to the maximum velocity can be obtained from Eq. (3.11) as

$$t_\mathrm{f} = \int_0^{\mathrm{v_m}} dt = \int_0^{\mathrm{v_m}} \frac{k_\mathrm{m} m}{f_\mathrm{m} - (k_1 + k_2 v^2)} dv \tag{3.12}$$

The Eq. (3.12) can be modified, to consider the discontinuity of the torque-speed curve of the electric motor drive, as

$$t_\mathrm{f} = \int_0^{\mathrm{v_r}} \frac{k_\mathrm{m} m}{\frac{P}{\mathrm{v_r}} - (k_1 + k_2 v^2)} dv + \int_{\mathrm{v_r}}^{\mathrm{v_m}} \frac{k_\mathrm{m} m}{\frac{P}{v} - (k_1 + k_2 v^2)} dv \tag{3.13}$$

where, P is the power. The power required to accelerate to the maximum velocity in a period, t_f can be found by numerically solving the Eq. (3.13) for the variable P [68]. The initial value of P at the start of the iteration should be more than the power required to run the vehicle at a constant speed of $\mathrm{v_m}$.

3.4 Powertrain specification of an electric two-wheeler for city use

This section discusses the steps involved in finalising the powertrain rating of vehicle-2 and vehicle-3. The power rating of the PMBLDC motors designed for vehicle-2 and vehicle-3 is calculated based on the specifications of vehicle-1, and the data obtained by driving it. Table 3.1 lists these specifications and their values. The top speed of the vehicle is limited to 30 km/h because, the

Specification	Value
Rated voltage	48 V
Rated power	750 W
Peak power	1200 W
Loaded mass of vehicle	130 kg
Top speed of vehicle	30 km/h
Maximum speed of rotation of the motor	340 rpm
0 to 30 km/h time	10 s

Table 3.1: Specification of vehicle-1.

two-wheeler is designed for city use and it will be using a cycle path. Besides, the powertrain uses direct-drive motor configuration and therefore, the application demands a low-speed high-torque motor. Based on these considerations, it is decided not to use the constant power operation of the PMBLDC motor drive. Hence, the maximum speed of rotation is selected as the rated speed of the motor drive.

The material properties, geometrical dimensions, and constants used in the calculation is listed in Table 3.2, and these values are either measured from vehicle-1 or collected from the previously published data [14].

The power required to accelerate vehicle-1 to the top speed, calculated using Eq. (3.13), for different acceleration time is plotted in Figure 3.3. The low energy density of the magnets planned to use coupled with the limited space availability, because of using the same wheel size and the axle length of vehicle-1, will cap the power output of the motors used in vehicle-2 and vehicle-3. Therefore, the prototype motors are designed with an output power of 700 W. Vehicle-1 is using its peak power capability to accelerate to the top speed in 10 s, which is confirmed by the results shown in Figure 3.3. If the output power of the vehicle is limited to 700 W, it takes 20 s to accelerate to

Parameter	Value
Rotational inertia coefficient	1.09
Tire pressure	2.5 bar
Coefficient of drag	1.05
Vehicle frontal area	0.625 m
Wheel radius	0.2350 m
Density of air	1.225 kg/m^3

Table 3.2: The value of material properties, geometrical dimensions, and constants used to estimate the power rating of traction motors.

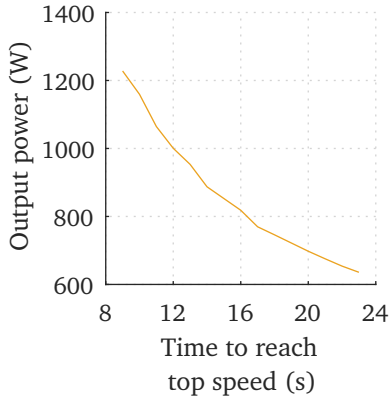

Figure 3.3: The power required to accelerate vehicle-1 to the top speed for different acceleration time.

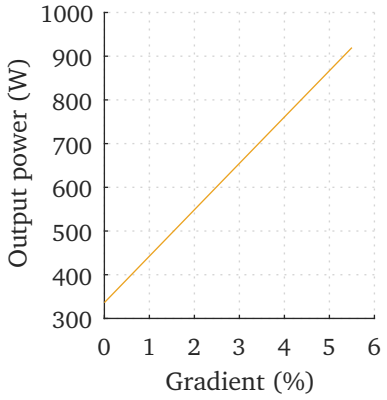

Figure 3.4: The output power required to maintain the top speed of vehicle-1 over different gradients.

the top speed.

The output power required to maintain the top speed of the vehicle over different gradients has been studied using Eq. (3.6), and the result is shown in Figure 3.4. It can be concluded from the figure that a vehicle with a power output of 700 W and a total weight of 130 kg can maintain a speed of 30 km/h for gradients up to 3 %.

Due to low energy density magnets based motor as powertrain, the vehicle-2 and vehicle-3 will be heavier than vehicle-1. The effect of an increase in mass on the accelerating time of vehicle-1 is shown in Figure 3.5. It is found that the acceleration time will increase by 4 s for a 20 kg increase of total vehicle mass. Based on the presented analysis, the values listed in Table 3.3 are selected as the specification for motors of vehicle-2 and vehicle-3.

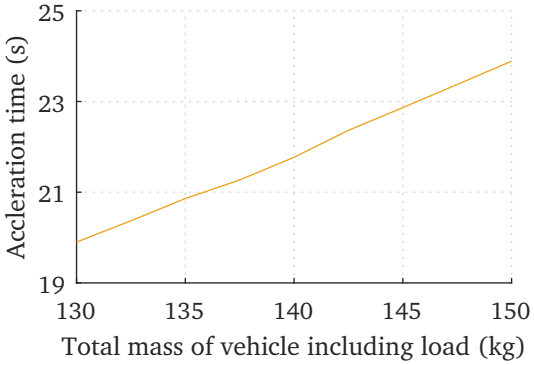

Figure 3.5: The time required for accelerating to the top speed of vehicle-1 vs. the total mass of the vehicle.

Parameter	Value
The rated power output	700 W
The rated speed	340 rpm
The rated torque	20 N m
Top speed of vehicle	30 km/h
Maximum mass of vehicle including driver	130 kg to 150 kg
Time to reach top speed	20 s to 24 s

Table 3.3: The powertrain specification of vehicle-2 and vehicle-3.

3.5 Conclusions

This chapter discussed a method to calculate the output power of an electric powertrain that satisfies the performance criteria such as the acceleration time and the maximum gradient on which the vehicle can maintain the top speed. Further, a simplified form is proposed for the equation of motion of a vehicle in Eq. (3.9) and Eq. (3.10), which are easier to solve numerically . The power rating of motors for vehicle-2 and vehicle-3 has been calculated using the equations and the geometrical dimensions of vehicle-1. The effect of increased mass of prototype motors on the performance of vehicle-2 and vehicle-3 has been studied, and it is found that acceleration time will increase from 20 s to 24 s when the total mass of the vehicle is increased by 20 kg. The next chapter will discuss the design of motors capable of meeting the performance requirement of two-wheeler identified in this chapter.

Chapter 4

Design of segmented armature torus PMBLDC motors

4.1 Introduction

Many approaches exist to synthesize an optimized design of AFM [69]–[74]. In [69]–[72], the authors used the sizing equations of AFM in the design optimisation. Though, the optimisation converges faster when using a model based on sizing equations, assumptions made while developing these equations make the resulting design less accurate [75]. Therefore, the optimised design will have to be analysed using an electromagnetic FE model for obtaining the accurate performance estimation [76]. In [73], the authors presented optimisation based on a magnetic circuit model. In [74], the authors used Taguchi method to optimise the design of an AFM, and an FE model of the motor is used to carry out design experiments required for the optimisation method.

The design tool developed in this work uses an FE model of the machine instead of lumped parameter or analytical model. When developing a design program for a new machine topology, using FE models helps to avoid the time required for the development of lumped parameter or analytical models. Though, the FE models provide accurate solutions, they require a longer time for solving each design iteration compared to lumped parameter or analytical

models.

This chapter discusses the design synthesis of a SAT PMBLDC motor using an FE model. A detailed description of the setting up of an FE based design-synthesis problem, starting from the definition of design variables, FE modelling of the machine, how the design synthesis is carried out, and to, how a design is finalised from a set of designs that satisfies the performance requirement, are included. Afterwards, the design-synthesis program presented is used to design the bonded RE magnet motor for vehicle-2 and the ferrite magnet motor for vehicle-3.

4.2 Finite element based design-synthesis program

The design-synthesis program presented here has two parts. The first part is an FE based design tool that will estimate the motor dimensions based on a given specification and constraints. The design tool will also calculate the performance of the designed motor. The second part is a search program that will use the design tool to identify the designs that meet the performance criteria specified by the designer. This section will explain the design variables of SAT PMBLDC motor, FE based design tool, and search program.

4.2.1 Design variables of SAT PMBLDC motor

The SAT motor topology used in this work has few changes from the topology proposed by Woolmer and McCulloch in their work [64], [67]. The motor presented by Woolmer and McCulloch has a variable stator tooth width and each stator slot has two coil sides. The stator of the SAT motor presented in this work has a constant tooth width and this helps to simplify their fabrication using steel laminations. Besides the ease of fabrication, designing an AFM with a constant tooth width could help to reduce the weight of the stator via optimal selection of the stator flux density. The main drawback of using a constant tooth width in an AFM is non-optimal utilisation of iron, which can be attributed to increase of flux in an AFM along the radial direction. Further, the motor developed in this study will use a single-layer winding because it is more suitable for BLDC motor operation [77]. Finally, pole arc to pole pitch ratio of the rotor, K_{p} is selected as one as this would ease the process of gluing the magnetized pole pieces onto the rotor core. If K_{p} of less than one is used, it would necessitate either magnetising the assembly of rotor core attached

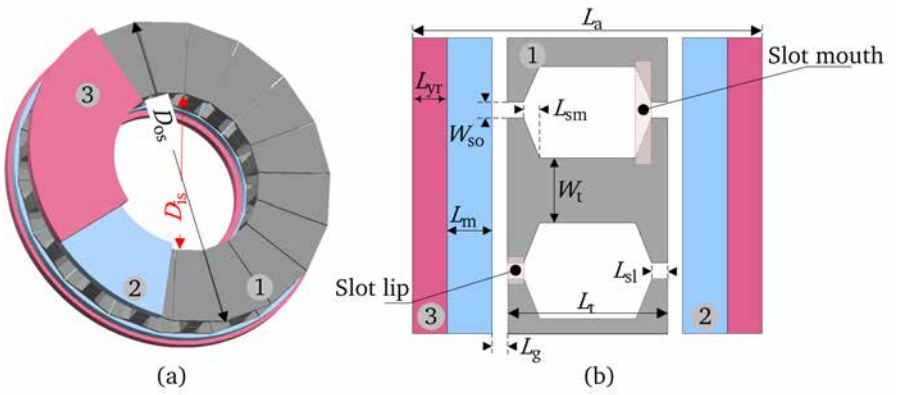

Figure 4.1: Variables defining the geometry of the SAT PMBLDC motor (1. segmented stator, 2. magnets and 3. rotor). (a) Cutaway model. (b) Sectional view of the inner periphery.

with non-magnetised pole pieces or building custom rigs to keep the magnets in their position during fabrication of the rotor assembly.

The set of dimensions that define the geometry of the SAT PMBLDC motor, excluding the winding is shown in Figure 4.1. The dimensions as seen from the inner periphery of the motor are indicated in Figure 4.1(b). The design variables of SAT PMBLDC motor can be grouped into three sets: specification, independent , and dependent variables as listed in Table 4.1. The independent variables are those design parameters that can be changed independently, without affecting the value of other independent variables. For example, the length of the airgap can be changed alone to generate different designs. The dependent variables are calculated by the design tool for given values of the specification and independent variables. It is important to note that some variables can be either independent or dependent . For example, if the axial length of the machine has to be specified in the design synthesis, then the outer diameter of the stator will be a dependent variable.

4.2.2 Finite element model based design tool

The FE based design tool creates either a partial or a full model of the machine based on the known variables of each stage. This model will be solved to find the unknown variables. The flowchart shown in Figure 4.2 will give an overview of different stages involved in the calculation of dependent variables and the motor performance.

Specification	Independent	Dependent
Rated voltage	Number of stator slots	Width of stator tooth
Rated power	Number of rotor poles	Depth of rotor yoke
Rated speed	Length of airgap	Diameter of a coil turn
	Outer diameter of stator	Number of turns per coil
	Gross slot fill factor	Axial length of tooth
	Width of slot opening	Axial length of motor
	Depth of slot lip	
	Depth of slot mouth	
	Depth of magnet	
	Magnet overhang	
	Diameter ratio of stator	
	Maximum current density	
	Ratio of pole arc to pole pitch	
	Maximum yoke flux density	
	Maximum tooth flux density	

Table 4.1: Classification of variables used to define the SAT motor geometry.

In the first stage, the rotor yoke depth is calculated iteratively using a stator-less three-dimensional (3D) static FE model of SAT PMBLDC motor. Iterations start with a minimum rotor yoke depth, and the depth will be increased in each iteration. Iteration stops when the maximum flux density inside the rotor yoke is below the value of flux density constraint. Similarly, the program calculates stator tooth width by gradually increasing tooth width of the FE model from a minimum value. Iteration stops when the maximum tooth flux density is below the value set by the constraint. For this stage, the axial length of the tooth is set as twice the sum of the slot lip depth and the slot mouth depth. The program records average airgap flux density at the end of this stage, B_{g0}, for future calculations.

The torque production in any motor with alternating phase currents is the result of the interaction of the airgap magnetic flux density distribution and the stator current MMF distribution along the stator airgap surface [78]. The stator current MMF distribution along the stator airgap surface is formed by ampere-conductors of stator slots. Each slot has to have sufficient ampere-conductors to generate the rated torque from zero speed to rated speed. As the ampere-conductors per slot is a function of the slot area and the current density, which is a design constant, an increase in ampere-conductors during

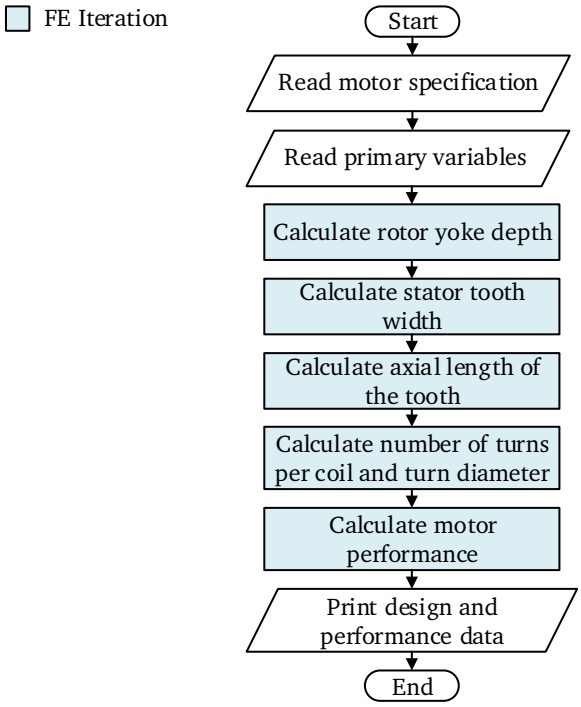

Figure 4.2: Flowchart of design tool showing different stages in the estimation of dependent variables and the motor performance.

iterations will enlarge the slot area. The maximum tooth flux density constraint determines the tooth width and hence, the slot width. Therefore, the slot area can be changed by varying the axial length of the tooth only. In design iterations, the axial length of the tooth can be calculated from the slot area based on the slot geometry shown in Figure 4.1(b). The design tool will calculate the slot area required to generate the rated torque for a given current density and the airgap flux density using the equation

$$\text{Slot area} = \frac{12T_{\mathrm{r}}}{K_{\mathrm{sff}} N_{\mathrm{s}} J B_{\mathrm{g}} \left(D_{\mathrm{os}}^2 - D_{\mathrm{is}}^2\right)} \tag{4.1}$$

where, T_{r} is the rated torque, K_{sff} is the gross slot fill factor, N_{s} is the number of stator slots, J is the current density, B_{g} is the average airgap flux density, D_{os} is the outer diameter of the stator, and D_{is} is the inner diameter of the stator. The equation (4.1) is obtained from the expression for the output power of PMBLDC motor, and the derivation is given in the Appendix A.1.

The flowchart of Figure 4.3 shows iterative steps implemented to calculate

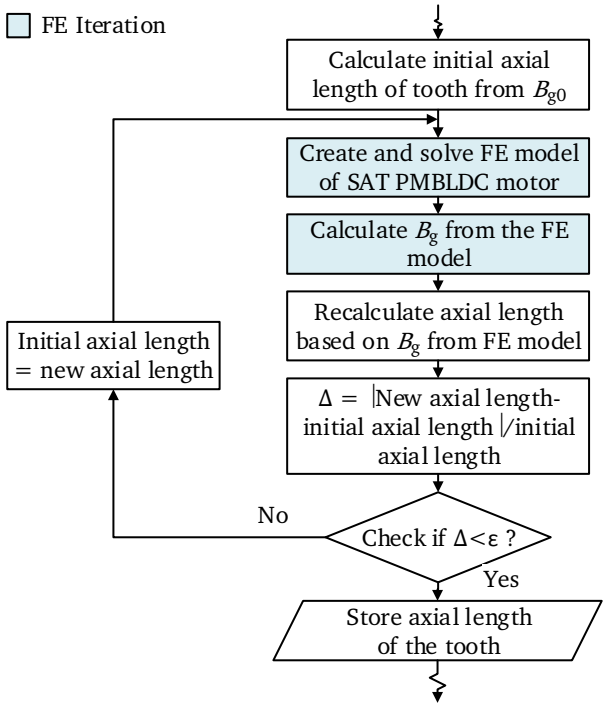

Figure 4.3: Flowchart for calculating the axial length of the stator tooth iteratively using FE models of a SAT PMBLDC motor.

the axial length of the tooth. The iteration starts with an initial value of the tooth length estimated from the airgap flux density B_{g0}, obtained from the previous stage. Once, the initial tooth length is known; the design tool creates an FE model of the machine. The FE model considers the armature reaction with the help of a single turn coil that carries a current equal to ampere-conductors per slot of the iteration. Here, ampere-conductors per slot of the iteration is the product of the slot fill factor, slot area of the iteration, and the current density. The FE model is solved to estimate the average airgap flux density, and this airgap flux density will be used to recalculate the tooth length. Iterations will continue until the change in the value of the slot length in the successive iterations is less than a predefined error ε.

In the next stage, the design tool will calculate the number of turns per coil and the diameter of a turn as shown in the flowchart of Figure 4.4. This stage starts by assuming the value of the line-to-line back EMF at rated speed as $0.95V_r$, where, V_r is the rated voltage of the vehicle battery. In the next step,

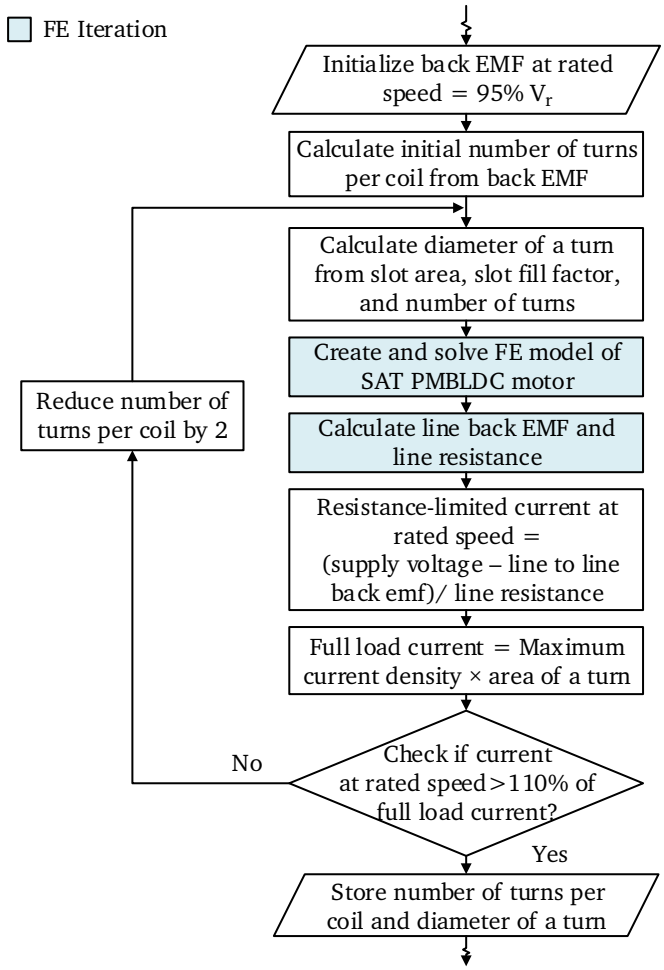

Figure 4.4: Flowchart for calculating the number of turns per coil and the diameter of a coil turn iteratively using FE models of a SAT PMBLDC motor.

the design tool calculates an initial number of turns per coil using the back EMF equation

$$E_{\mathrm{ph}} = \frac{N_{\mathrm{r}}}{60}\frac{N_{\mathrm{s}}}{3}\frac{\pi}{4}\left(D_{\mathrm{os}}^2 - D_{\mathrm{is}}^2\right) B_{\mathrm{g}} N_{\mathrm{c}} \tag{4.2}$$

where, N_{r} is the rated speed of motor and N_{c} is the number of turns per coil side. The diameter of a turn is calculated next from the slot area obtained earlier, the gross slot fill factor, and the number of turns. Using these initial data, the design tool creates an FE model of the SAT PMBLDC motor, and the model is solved to calculate the back EMF at rated speed and the phase re-

sistance. The subsequent steps calculate the resistance-limited phase current at the rated speed and the full-load phase current. The phase current should not be back EMF limited for speeds up to the rated speed to maintain a constant phase current at the rated torque using current control. Therefore, the resistance-limited phase current at rated speed should be higher than the full load current. If the difference between currents is less than 10% of the rated current, the coil turns are reduced to increase the current level.

In the final stage, the design tool will calculate the performance data such as input current, efficiency, and losses. using an FE model of the developed design. The design tool is implemented using Excel-VBA™and commercially available FE software MagNet™. Excel spreadsheet will store the values of the specification and independent variables, and the results of the design process, i.e., values of dependent variables, motor parameters, and performance data.

4.2.3 Search program

The search program finds designs that meet performance targets set by the designer. The objective function of the search program uses the design tool. The search program is implemented using integer constrained genetic algorithm available in MATLAB™. The integer constrained algorithm helps to define discrete data points for independent variables of the design program. Therefore, practical implementation requires minimal corrections on the synthesised design data. All intermediate points of the optimisation process are recorded, and the search program is stopped when there is no improvement in the value of the objective function.

4.3 Design of bonded RE magnet and ferrite magnet motors

This section discusses the design of in-wheel SAT PMBLDC motors for vehicle-2 and vehicle-3. Both vehicle-2 and vehicle-3 is using the body of vehicle-1 excluding the rear wheel and the controller. An axial length of 180 mm and an outer diameter of 330 mm define the maximum available space for the new motors, and these dimensions are shown in Figure 4.5. The powertrain specification identified in section 3.4 is listed in Table 4.2 including the battery specification, and the designs of both the bonded RE and the ferrite magnet

Figure 4.5: The maximum available space for motors in vehicle-2 and vehicle-3. (a) Axle length of vehicle-1. (b) Inner diameter of wheel of vehicle-1.

motors aim to meet these specifications.

Parameter	Value
The rated power output	700 W
The rated speed	340 rpm
The rated torque	20 N m
Top speed of vehicle	30 km/h
Maximum mass of vehicle including load	130 kg to 150 kg
Time to reach top speed	20 s to 24 s
Rated voltage of battery	48 V
Maximum battery current	25 A

Table 4.2: The performance and electrical specification of powertrains for vehicle-2 and vehicle-3.

The design program described in section 4.2 is used to design a bonded RE magnet motor for vehicle-2 and a ferrite magnet motor for vehicle-3. The number of independent variables that require optimisation has been reduced considerably by following the design guidelines of PMBLDC motor discussed by Hendershot and Miller [31], [55]. The SAT PMBLDC motors use a three-phase alternate tooth concentrated winding. Therefore, the number of stator slots will be an integral multiple of $2m$, where m is the number of phases. Further, the in-wheel direct drive powertrain is a low-speed application and hence, it is recommended to select a motor with a high number of poles [55]. A slot-pole combination that satisfies the relation, $P = N_s \pm 2$, will reduce

the cogging torque considerably [77]. Moreover, a N_s/P ratio close to 1 will minimise the tooth leakage flux and improve the winding factor of the concentrated winding [79]. These considerations resulted in slot-pole combinations of 12-10, 12-14, and 18-16. The higher slot-pole combinations are not considered to reduce the core loss and to simplify the fabrication. It is decided to select the 18 slot 16 pole configuration, because of the thinner rotor yoke compared to the other two slot-pole combinations. The airgap length of 0.4 mm is decided based on the manufacturing constraints. The selected topology allows winding of the individual tooth outside the motor, and this allows a higher fill factor than the 30 to 40% used in classical machines [64], [67]. The slot fill factor is defined with respect to the slot profile at the inner periphery of the SAT machine as shown in Figure 4.1(b). The winding layout of the alternate tooth wound machine is selected based on the work of Ishak et.al [79]. The selected winding arrangement is

A B' B' C A' A' B C' C'

where, A, B, and C are coils belong to phase-A, phase-B, and phase-C and A', B', and C' are coils of opposite polarity to the coils A, B, and C. The alternated tooth winding with respect to the stator slots is shown in Figure 4.6. The sec-

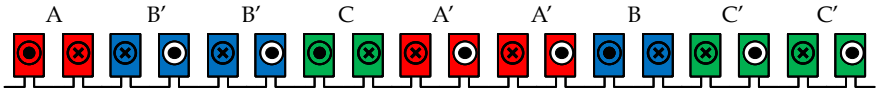

Figure 4.6: Alternate tooth concentrated winding of 18-slot 16-pole SAT PMBLDC motor.

tions around the slot opening are made sufficiently thick based on FE studies of the motor to avoid the saturation in these areas. A current density of less than 5 A/mm^2 is selected as the motor is not force-cooled.

The prototype machines will be using bonded rare earth magnets and ferrite magnets, and the properties of magnets are listed in Table 4.3. The bonded RE magnet grade used is superior to the ferrite magnet grade in both remnant flux density and maximum energy product. Both magnets have similar values of coercivity. The ease of assembly of magnets was given higher priority than the cost saving via magnet material reduction; hence a pole arc to pole pitch ratio of one is selected. Solid soft-iron is used to make the rotor yoke; therefore the maximum flux density inside the rotor yoke is set to 1.2 T to reduce the core loss [55]. The cold rolled silicon steel lamination of grade M400-50A

	Bonded RE	Ferrite
Name as per supplier catalogue	NDB-6	Y33BH
Measurement temperature (°C)	40	40
Remanent flux density (T)	0.6	0.4
Coercivity (kA/m)	330	302
BH_{max} (kJ/m^3)	48	33

Table 4.3: Properties of the bonded RE magnet and ferrite magnet used in the design of motors for vehicle-2 and vehicle-3.

Variable name	Value
Number of stator slots	18
Number of rotor poles	16
Length of airgap	0.4 mm
Gross slot fill factor	50%
Width of slot opening	1 mm
Depth of slot lip	2 mm
Depth of slot mouth	2 mm
Current density of coil	4.5 A/mm^2
Ratio of pole arc to pole pitch	1
Maximum flux density of rotor yoke	1.2 T
Maximum flux density of stator tooth	1.6 T

Table 4.4: Independent variables and their values of SAT PMBLDC motor, excluding optimisation variables.

is used to make the stator tooth, and a maximum flux density 1.6 T is possible in this material without considerable core loss.

Both the bonded RE magnet motor and the ferrite magnet motor use the same values for all non-optimised independent variables except for the outer diameter, and these values are listed in Table 4.4. The outer diameters of both machines used in the design synthesis are listed in Table 4.5. A larger value is selected for the outer diameter of the ferrite magnet motor to account for the lower value of remanent flux density.

The three remaining independent variables: depth of the magnet, magnet overhang, and diameter ratio of the stator are optimised to generate SAT PMBLDC motor designs. The discrete set of values for these parameters are shown in Table 4.6. The SAT PMBLDC motor topology has a lower core loss compared to topologies with stator yoke. Besides, the low flux density thresh-

Parameter	Value
Outer diameter of bonded RE magnet motor	225 mm
Outer diameter of ferrite magnet motor	260 mm

Table 4.5: The outer diameters of the bonded RE magnet motor and the ferrite magnet motor.

Variable name	Range
Depth of magnet	7 mm to 10 mm in steps of 0.5 mm
Magnet overhang	0 %, 5 % and 10 %
Diameter ratio of stator	45 % to 60 % in steps of 2.5 %

Table 4.6: independent variables used as optimisation variables in design-synthesis of SAT PMBLDC motors and their range.

old selected for the rotor yoke and the stator tooth will help to reduce the core loss. Therefore, the synthesis program is devised to identify the designs with low conduction losses, with the assumption that the core loss variation among these designs will be negligible.

The 3D FE model of SAT PMBLDC motor, excluding the elements of air volume, used in the design synthesis of the in-wheel motor is shown in Figure 4.7. Only a quarter of electromagnetic structure of SAT PMBLDC motor

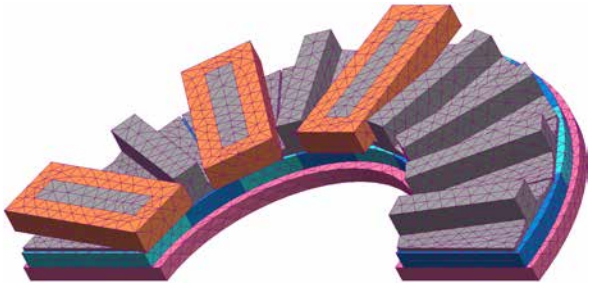

Figure 4.7: The FE model of SAT PMBLDC motor used in the design synthesis of in-wheel motor.

is modelled to reduce the number of elements of the FE model by utilising geometrical symmetries of the dual rotor topology and 18-slot 16-pole combination. Also, only one coil belong to each phase is modelled and the phase back EMF is calculated with the help of winding factor presented by Ishak et al. [79].

4.3.1 Results of design synthesis

Appendix B explains the implementation of the design synthesis program and lists codes used to implement it. The design synthesis uses a 3D FE model, and as explained in section 4.2.2, the design tool solves many FE models every time the search algorithm calls it. Therefore, it is not practical to assign a large value to the maximum number of generations, and wait until the genetic algorithm solver produces a unique solution. In this study, after a series of trial runs to establish convergence trend of design synthesis, it is decided to select a population size of fifty per generation and a maximum of fifteen generations. With these genetic algorithm solver settings, it takes 50 hours for completing the design synthesis. The optimisation convergence observed in the design synthesis of bonded RE magnet motor and ferrite magnet motor is shown in Figure 4.8. The figure shows the variations of the average conduction loss and

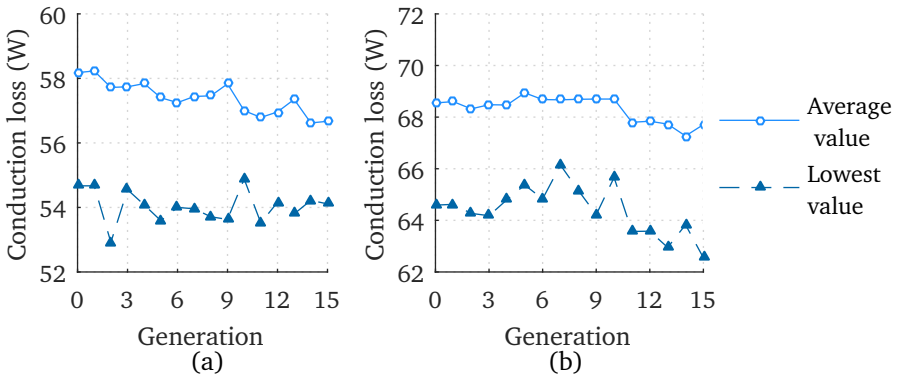

Figure 4.8: Results of integer constrained genetic algorithm based design synthesis of in-wheel motors. (a) Bonded RE magnet motor. (b) ferrite magnet motor.

the lowest conduction loss of populations of successive generations. In the design synthesis of both machines, the average loss of designs in each generation is moving towards the lowest loss, and there is no significant variation in the value of the lowest loss of population over fifteen generations. This implies that a unique solution is possible when a larger number of generations is selected for the genetic algorithm solver. Moreover, the conduction loss of the design from the unique solution will not be considerably lower than the lowest loss of generations shown in the Figures 4.8(a) and (b).

The design of bonded RE magnet motor

The design synthesis generated 801 designs, and a group of 15 designs with the lowest conductive loss and an axial length of less than 70 mm obtained from the synthesis is listed in Table 4.7. The notable points from the results of the design synthesis are

- Though magnet thickness is allowed to vary between 7 mm and 10 mm, most of the low-loss designs have a magnet thickness less than or equal to 8.5 mm.
- The majority of the low-loss designs has a diameter ratio less than or equal to 50 %. For the axial flux topology considered here, a lower diameter ratio for a given outer diameter result in less overhang section per turn and a shorter overhang winding results in lower conduction losses [80], [81].

Among all low-loss designs listed in Table 4.7, Design #277 is selected for further analysis because of the following reasons

- A lower number of turns per coil is preferred to reduce the phase self-inductance of the motor, and this will help to shorten the commutation time of BLDC motor [82], [83]. A lower value of the commutation time will decrease the duration of torque dip caused by the switching of current between two phases of the PMBLDC motor, and therefore, reduces the torque ripple of the motor.
- Though Design #277 and Design #597 have similar electrical performance, the former has a thinner rotor yoke when compared to the later resulting in a shorter total axial length of the motor.

The design of ferrite magnet motor

Similar to the design of the bonded RE magnet motor, the design synthesis of the ferrite magnet motor also generated 801 designs. From these designs, a group of 15 designs with the lowest conductive loss and an axial length of less than 70 mm is listed in Table 4.8. A final design selection criterion identical to the bonded RE magnet motor is followed in the case of the ferrite magnet motor also. Design #653 is selected for further analysis as it has the lowest number of turns and the shortest axial length of the motor among the low-loss designs considered.

Design #	Thickness of magnet	$\frac{\text{Total overhang}}{\text{Magnet length}}$	Stator diameter ratio	Rotor yoke length	Stator tooth width	Axial length of the tooth	Number of turns per coil	Conductive loss	Axial length of the motor
	mm	%	%	mm	mm		mm	W	mm
597	7	5	45	7	8.84	40.9	44	53.5	69.7
277	7	0	45	6	8.84	41.4	44	53.6	68.2
47	7.5	5	50	6	9.82	39.4	48	54.7	67.2
388	9	10	52.5	6	10.31	37.9	50	55.0	68.7
291	8.5	0	50	6	9.82	39.9	48	55.3	69.7
45	8	0	55	7	10.8	37.8	50	55.5	68.6
378	7	10	50	7	9.82	40.2	48	55.6	69.0
160	9	0	52.5	6	10.31	38.5	50	55.7	69.3
176	7.5	5	45	6	8.84	41.9	46	55.7	69.7
306	7	5	50	7	9.82	39.7	48	55.8	68.5
254	8.5	5	55	7	10.8	38.2	50	55.9	70.0
81	7.5	5	50	6	9.82	41.1	50	56.2	68.9
443	8.5	0	50	6	9.82	39.7	50	56.4	69.5
472	8	0	50	6	9.82	39.9	50	56.7	68.7
188	7.5	10	52.5	7	10.31	40.0	50	56.7	69.8

Table 4.7: Results from the design synthesis of the bonded RE magnet motor.

Design #	Thickness of magnet	$\frac{\text{Total overhang}}{\text{Magnet length}}$	Stator diameter ratio	Rotor yoke length	Stator tooth width	Axial length of the tooth	Number of turns per coil	Conductive loss	Axial length of the motor
	mm	%	%	mm	mm		mm	W	mm
795	8.5	10	45	6	10.2	36.5	46	62.6	66.3
648	7	10	45	6	10.2	37.1	46	63.6	63.9
653	7	5	45	5	10.2	37.6	46	63.9	62.4
162	9	5	50	6	11.3	35.7	48	64.2	66.5
112	8.5	5	52.5	6	11.9	34.7	50	64.3	64.5
36	8.5	5	50	5	11.3	35.6	48	64.6	63.4
218	9	10	52.5	6	11.9	34.8	50	65.1	65.6
301	8.5	5	45	6	10.2	37.2	48	65.3	67.0
131	7	0	45	6	10.2	38.0	48	65.5	64.8
452	9	0	47.5	5	10.8	37.3	48	65.6	66.1
767	8.5	10	47.5	6	10.8	36.6	48	65.7	66.4
29	7.5	0	47.5	5	10.8	37.4	48	65.7	63.2
15	7.5	0	52.5	6	11.9	35.7	50	65.8	63.5
103	8	10	50	6	11.3	35.8	50	66.0	64.6
129	7	0	47.5	5	10.8	37.6	48	66.0	62.4

Table 4.8: Results from the design synthesis of the ferrite magnet motor.

Trade-off of FE based design synthesis

The discrete set of values for the optimisation variables listed in Table 4.6 will result in 147 designs only (seven values for the depth of the magnet $\times$ three values for the magnet overhang $\times$ seven values for the diameter ratio of stator). However, the design program has generated 800 designs only to establish a trend of convergence. Among all the 800 designs, quite a few designs have the same set of values for the optimisation parameters, yet, these designs have a marginally different axial length of the tooth, in turn resulted in a different number of turns per coil. These variations can be explained with the help of the flowchart for calculating the axial length of the tooth, shown in Figure 4.3. This design step uses the airgap flux density, and the precision of airgap flux density of FE models generated in successive iteration depends on the mesh density of the airgap. The design-synthesis program uses a 3D FE model, and any quality improvement of mesh around the airgap region will exponentially increase the number of elements and the solution time. The FE model used in this study has a two decimal digit precision for the average airgap flux density measurement.

4.3.2 Comparison of bonded RE magnet and ferrite magnet motor designs

An overview of designs of the bonded RE magnet motor and the ferrite magnet motor is shown in Table 4.9. In the past, parameters such as torque density and power density have been used for comparing electrical machines with different materials and topologies, and more often, each author uses different definitions for these parameters [75], [76], [84]–[89]. For the two designs identified in this chapter, the mass of active materials and their percentage differences, using the bonded RE magnet motor as the reference, are listed in Table 4.10. From Table 4.10, it is clear that the ferrite magnet motor is heavier than the bonded RE magnet motor by 19.6 % for the same rated output power. Further, parameters such as torque per unit moment of inertia, power per unit volume, and power per unit mass of the two designs are calculated and listed in Table 4.11. These parameters are calculated from the mass of the active motor components, the total volume of the motor excluding the frame, and the rotor moment of inertia. The properties of magnets used in the designs are listed Table 4.3, and the remanent flux density of the ferrite

Parameters	Bonded RE magnet motor	Ferrite magnet motor
Outer diameter of stator (mm)	225	260
Number of poles	16	16
Number of slots	18	18
Length of airgap (mm)	0.4	0.4
Coil current density (A/mm^2)	4.5	4.5
Length of magnet (mm)	7	8.5
Magnet overhang ratio (%)	0	10
Diameter ratio of stator (%)	45	45
Length of rotor yoke (mm)	6	6
Width of stator tooth (mm)	8.8	10.2
Number of turns per coil	44	46
Axial length of tooth (mm)	41.4	36.6
Diameter of a coil turn (mm)	2.13	2.09
Axial length of motor (mm)	68.2	66.4
Phase resistance (mΩ)	104.9	130.8
Line back emf at rated speed (V)	43.8	45.3
Full load current (A)	16.0	15.5
Conductive loss (W)	53.6	62.5

Table 4.9: Summary of selected designs of the bonded RE magnet motor and the ferrite magnet motor.

magnet is 33.3 % less than that of the bonded RE magnet. However, the axial flux topology helped to bring performance indices of the ferrite magnet motor, such as torque per unit moment of inertia and power per unit mass, closer to that of the bonded RE motor with a 15 % increase in the outer diameter.

Material	Mass (kg)		
	Bonded RE motor	Ferrite magnet motor	Difference (%)
Magnet	2.44	2.93	19.7 ↑
Copper	2.05	2.39	16.7 ↑
Laminations M400-50A	3.85	4.77	24.0 ↑
Soft iron	3.33	3.87	16.2 ↑
Total	11.66	13.95	19.6 ↑

Table 4.10: Mass of active materials of the designed SAT PMBLDC traction motors.

Parameter	Bonded RE magnet motor	Ferrite magnet motor	Difference (%)
Volume of motor (m^3)	2.86×10^{-3}	3.59×10^{-3}	25.6 ↑
Moment of inertia of the rotor ($kg\,m^2$)	4.43×10^{-2}	4.68×10^{-2}	5.6 ↑
Torque per unit moment of inertia ($N\,m/(kg\,m^2)$)	451.47	427.35	-5.3 ↓
Power per unit volume (kW/m^3)	244.54	194.75	-20.3 ↓
Power per unit mass (W/kg)	60.00	50.16	-16.4 ↓

Table 4.11: Comparison of designs of the bonded magnet and the ferrite magnet SAT PMBLDC traction motors.

4.4 Conclusions

This chapter presented an FE based design-synthesis program for a SAT PM-BLDC motor. The program is used to design two direct drive in-wheel motors, a bonded RE magnet motor and a ferrite magnet motor. When comparing the magnets used in the motors, the ferrite magnet has a lower remanent flux density than the bonded RE magnet, and therefore, the weight of active materials of the ferrite magnet motor is heavier by 19.6 % than the bonded RE magnet motor for the same rated output. The design exercise achieved closer values of torque per unit moment of inertia and power per unit mass for both motors by choosing a 15 % larger outer diameter for the ferrite magnet motor. The next chapter will discuss the dynamic performance of the designed motors when they are connected to a three-phase inverter and a load, with the help of a

non-linear model of a PMBLDC motor.

Chapter 5

Non-linear dynamic model of PMBLDC drive based system

5.1 Introduction

In AFM, the flux in magnets and teeth travels parallel to the axis of rotation, while the flux in the stator yoke and the rotor yoke takes a circumferential path in a plane normal to the axis of rotation. In short, the main flux in AFM has a 3D path, unlike radial flux machines, where the main flux stays in a plane normal to the axis of rotation. Therefore, modelling and analysis of AFM necessitates using techniques such as magnetic equivalent circuit [90]–[94], analytical model [95], or 3D finite element method [96] that consider 3D flux path to obtain accurate results. The time required for solving a 3D model of the AFM makes simulating a system such as electric vehicles, which include a power electronic converter model and a load model along with an AFM, impractical. Therefore, simulating a system with AFM requires a model of the machine that has a solving time of similar order as that of models of other components without compromising the accuracy.

There are three models presently used for simulating the performance of a PMBLDC motor in a system such as an electric vehicle: linear phase variable model [97]–[107], non-linear phase variable model [108]–[113], and average value two axes model [114]–[116].

Linear phase variable model

The equivalent circuit representation of the linear phase variable model of PMBLDC motor is shown in Figure 5.1. In linear phase variable model, the

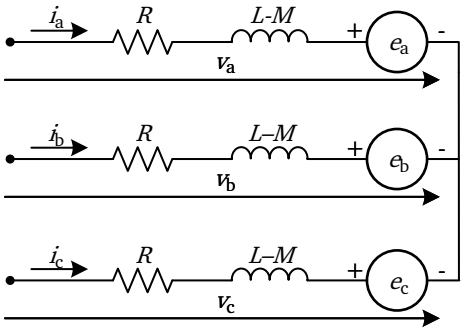

Figure 5.1: Equivalent circuit representation of the linear phase variable model of a PMBLDC motor.

motor is modelled with the help of two sets of formulas, named as voltage equation and torque equation. The voltage equation for each phase of the three-phase equivalent circuit is given by

$$\begin{aligned} v_{\mathrm{a}} &= i_{\mathrm{a}}R + (L-M)\frac{di_{\mathrm{a}}}{dt} + e_{\mathrm{a}} \\ v_{\mathrm{b}} &= i_{\mathrm{b}}R + (L-M)\frac{di_{\mathrm{b}}}{dt} + e_{\mathrm{b}} \\ v_{\mathrm{c}} &= i_{\mathrm{c}}R + (L-M)\frac{di_{\mathrm{c}}}{dt} + e_{\mathrm{c}} \end{aligned} \tag{5.1}$$

and the torque equation is

$$T_{\mathrm{em}} = \frac{e_{\mathrm{a}}i_{\mathrm{a}} + e_{\mathrm{b}}i_{\mathrm{b}} + e_{\mathrm{c}}i_{\mathrm{c}}}{\omega} \tag{5.2}$$

In Eq. (5.1) to Eq. (5.2), R is the phase resistance, L is the phase self-inductance, M is the mutual inductance between phases, e_{a}, e_{b}, and e_{c} are the instantaneous values of back EMF of phases, v_{a}, v_{b}, and v_{c} are the applied voltage across phases, i_{a}, i_{b}, and i_{c} are the instantaneous phase currents, T_{em} is the electro-magnetic torque generated, and ω is the angular velocity of rotor. The back EMF in the linear phase variable model follows the ideal waveform shown in Figure 2.14. The line-line back EMF E of Figure 2.14 can be written as [55]

$$E = k_{\mathrm{E}}\omega \tag{5.3}$$

where, k_{E} is a constant called the EMF constant. The peak value of phase back EMF will be half of line-line back EMF.

Non-linear phase variable model

The use of the linear phase variable model is limited to the cases where nonlinearities such as saturation of iron path, armature reaction, and cogging torque have negligible influence on the operation of a motor [107], [117], [118]. When the nonlinearities have considerable effect on the motor performance, it is necessary to use the non-linear phase variable model of the PMBLDC motor. The non-linear quantities are included either in the form of Fourier series [108] or a look-up table [109]–[113]. When a flux linkage look-up table is used, the phase voltage equation is

$$\begin{aligned} v &= iR + \frac{d}{dt}\left[\psi_{\mathrm{PM}}(\theta) + (L-M)i\right] \\ &= iR + \frac{d}{dt}[(L-M)i] + \omega\frac{d}{d\theta}\left[\psi_{\mathrm{PM}}(\theta)\right] \end{aligned} \tag{5.4}$$

where, $\psi_{\mathrm{PM}}(\theta)$ is the flux linkage of a phase produced by the magnet as a function of rotor position θ and i is the phase current. Since, the reluctance seen by the phase winding of a surface magnet machine does not vary with the rotor position, the inductances will be a constant if the effect of saturation on the inductances is neglected. Therefore, the the voltage equation (5.4) can be written as

$$\begin{aligned} v &= iR + (L-M)\frac{di}{dt} + \omega\frac{d}{d\theta}\left[\psi_{\mathrm{PM}}(\theta)\right] \\ &= iR + (L-M)\frac{di}{dt} + e \end{aligned} \tag{5.5}$$

where, e is the instantaneous phase back EMF. The voltage equation (5.5) does not consider armature reaction. The expression for the back EMF can be modified to account the effect of armature reaction as

$$\begin{aligned} e &= \omega\frac{d}{d\theta}\psi(\theta, i) \\ &= \omega\psi'(\theta, i) \end{aligned} \tag{5.6}$$

where, $\psi(\theta, i)$ is a look-up table of flux linkage variation of a phase with rotor position for different values of phase current and $\psi'(\theta, i)$ is the derivative of

the flux linkage look-up table. The torque equation (5.2), can be expressed in terms of the flux linkage derivative using Eq. (5.6) as

$$T_{\mathrm{em}} = \psi'_{\mathrm{a}}(\theta, i_{\mathrm{a}})i_a + \psi'_{\mathrm{b}}(\theta, i_{\mathrm{b}})i_b + \psi'_{\mathrm{c}}(\theta, i_{\mathrm{c}})i_c + T_{\mathrm{cg}}(\theta) \tag{5.7}$$

where, $T_{\mathrm{cg}}(\theta)$ is the cogging torque as a function of the rotor position.

The average value model

The average value models of the PMBLDC motor include a model by Han et al. that is derived from the phase-variable model [114], a model by Tabarraee et al. that considers nonlinearities due to flux harmonics [115], and a model by Jagiela et al. that uses FE derived look-up tables similar to the non-linear phase variable model's approach to include nonlinearities [116]. The average value model is not discussed further as it is beyond the scope of the work.

While developing all three models of PMBLDC motor, the authors assumed that the value of core loss is negligible. In the last decade, there is an increased interest in fractional-slot winding machines because of the benefits such as high power density, high efficiency, low cogging torque, and fault tolerance [77], [119]–[122]. Fractional slot machines have considerable rotor losses due to the rich presence of sub- and super-space harmonic components of armature flux that are not in synchronism with the rotor [122]–[131]. The measurement of these rotor losses is difficult, and therefore, it is useful to develop a model to predict them [132], [133]. Because of higher value of core loss in fractional-slot machines compared to integral slot machines, the lack of core loss calculation in PMBLDC motor models could introduce considerable error in the performance simulation of fractional-slot PM machines.

In this chapter, a core loss model of a PMBLDC motor is developed and incorporated into the non-linear phase variable model of the PMBLDC motor. Afterwards, the non-linear phase variable model with core loss calculation is used to evaluate the dynamic performance of both the bonded and the ferrite magnet motor designs.

5.2 The core losses in SAT PMBLDC motors

The time variation of flux density in components such as stator core, magnets, magnet retaining ring, and rotor yoke generate core losses in permanent mag-

net machines. Core losses can be classified as hysteresis loss, eddy current loss, and excess loss [134]. This study considers only the hysteresis and the eddy current losses. The SAT PMBLDC motor is a stator-yokeless topology, and both bonded and ferrite magnets are non-conducting magnets. Therefore, the flux density variation generates losses only in the segmented stator tooth and the solid rotor yoke of a SAT PMBLDC motor. From FE analysis of SAT PMBLDC motor, it is found that there is a considerable variation in the maximum value of flux densities in the tooth-tip and the remaining part of a stator tooth. The part of the tooth other than tooth-tip will be addressed as tooth henceforth. The tooth-tip and the tooth are considered as two different components for loss modelling. In a PMBLDC motor, both armature and permanent magnet produces flux. If effects of the current building up and the pulse width modulation (PWM) switching of the stator current are neglected, the relative motion between fluxes and the components is the cause of the flux density variation in the components. The tree diagram of Figure 5.2 will give an overview of

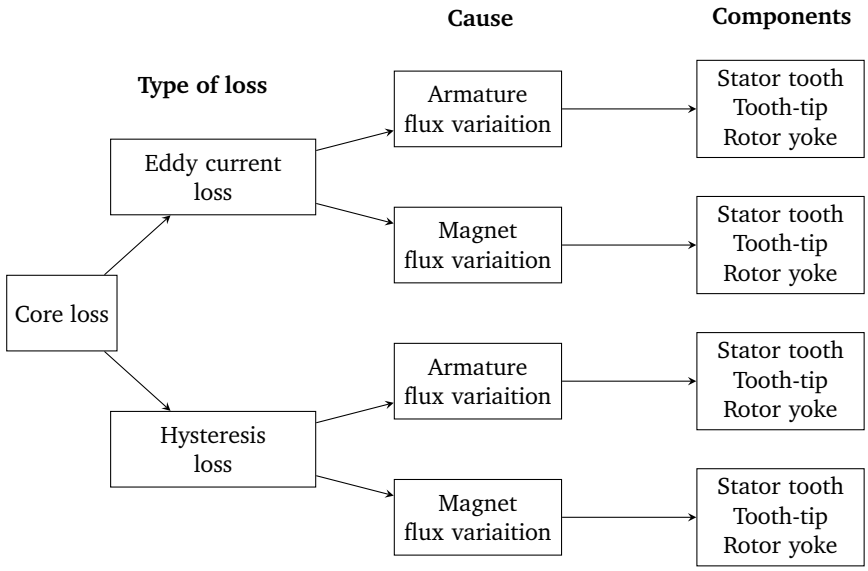

Figure 5.2: Different types of core loss, causes of core losses, and components of SAT PMBLDC motor generating core losses.

the different types of core loss, causes of core loss, and components of SAT PMBLDC motor that generate core losses. The following part of this section will discuss and propose a model to calculate core losses in the stator tooth, the tooth-tip, and the rotor yoke of SAT PMBLDC motor.

5.2.1 FE model for extracting parameters of core loss model

The design program explained in Chapter 4 uses an FE model based on a quarter model of 18-slot 16-pole SAT PMBLDC motor. In the FE model of the design program, shown in Figure 4.7, ampere-turns are applied in such a way that the electromagnetic condition is same as the full model only in a section of model along three tooth pitch. However, an FE model for extracting parameters of core loss model has to have magnetic flux and ampere-turns distributed correctly in the electromagnetic structure to accurately estimate the core loss. An iterative study of FE models of 18-slot 16-pole SAT PMBLDC motor concluded that it is necessary to model a minimum one half of the machine, as shown in Figure 5.3, to accurately represent the stator excitation. The flux

Figure 5.3: The half symmetry FE model of 18-slot 16-pole SAT PMBLDC motor used for extracting parameters of core loss model

density distribution on tooth faces of a 18-slot 16-pole SAT PMBLDC motor, when phase-A and phase-B carries a current of 15 A and −15 A respectively is shown in Figure 5.4. The flux density distribution shown in Figure 5.4, is obtained by setting the magnet-flux to zero in the FE model. It is clear from Figure 5.4 that the FE model cannot be reduced any further, for example to a 9-slot 8-pole section, because there is no electromagnetic periodicity exists in the flux density distribution generated by the phase currents of the alternate tooth wound 18-slot 16-pole SAT PMBLDC machine about a plane that passes through the slot openings.

5.2.2 Core losses in stator tooth-tip

When a permanent magnet machine is loaded, the armature flux will distort the tooth flux density distribution generated by the permanent magnets. The unexcited and the excited flux density distributions on a pair of tooth faces of

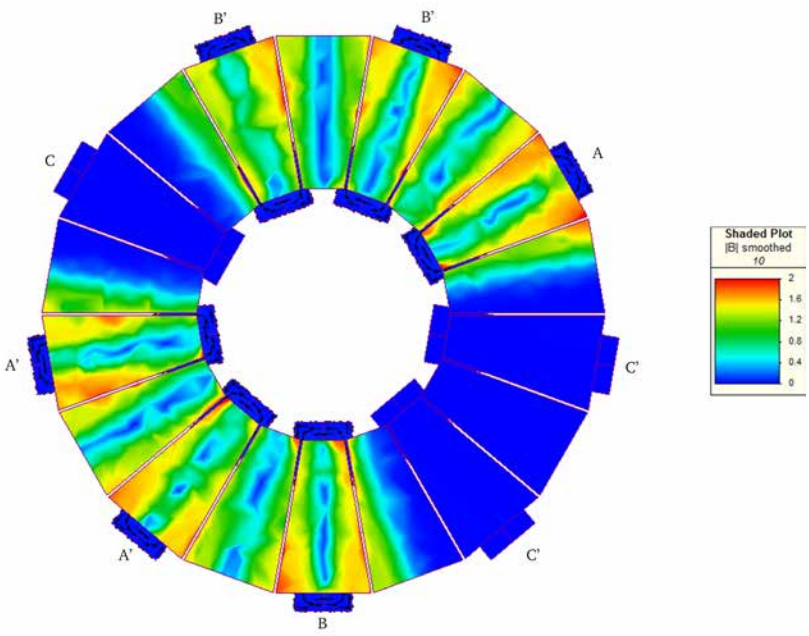

Figure 5.4: The flux density distribution on tooth faces of 18-slot 16-pole SAT PMBLDC motor when phase-A current is 15 A, phase-B current is −15 A, and the magnet-flux is zero.

the bonded RE SAT PMBLDC motor is shown in Figure 5.5. From Figure 5.5, it

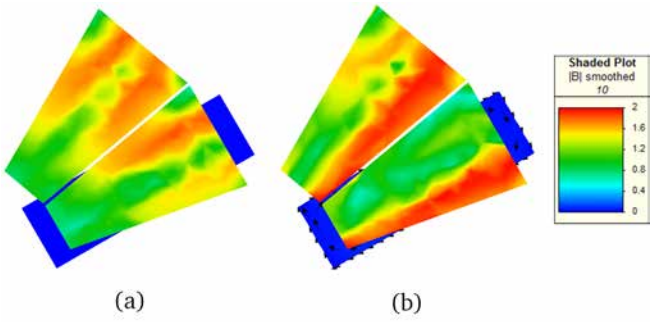

Figure 5.5: Flux density distribution on stator tooth faces of the bonded RE magnet SAT PMBLDC motor. (a) No-load. (b) when the armature carries a current of 15 A.

is clear that the armature current not only distorts the no-load field distribution of tooth-tip but also increases its maximum flux density. The variation of the peak value of the tooth-tip flux density with armature current for bonded RE magnet motor design is shown in Figure 5.6.

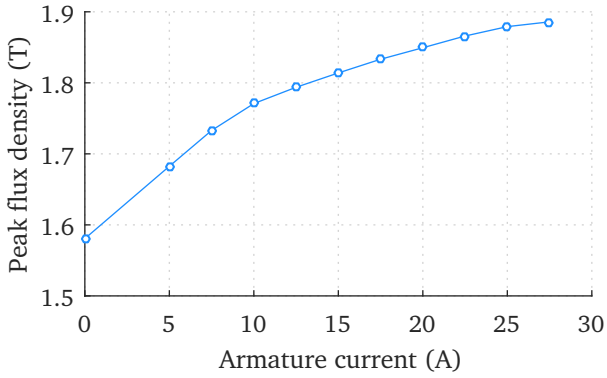

Figure 5.6: The variation of the peak value of the tooth-tip flux density with armature current for bonded RE magnet motor design.

The flux density variation inside two stator tooth-tips, one with coil and one without coil, is shown in Figure 5.7. The flux density variations are captured from a series of static FE simulations. In each simulation step, the rotor is rotated by an angle and a pair of phases are excited with a constant current to produce a positive motoring torque. The tooth-tip flux densities inside the tooth tip volume are sampled at three points of a plane located at the midpoint of the tooth-tip thickness. The captured flux density variations can be simplified as shown in Figure 5.8 to fit the core loss model for electrical machines with non-sinusoidal excitation, proposed by Slemon and Liu [135]. The simplified flux density waveform accounts the peak flux density and the rotor displacement over which the flux density variation occurs. The simplified flux density waveform changes the polarity over angle α_{tt}, the mean pole transition angle in electrical radians. The tooth-tip core loss per unit mass for the flux density waveform shown in Figure 5.8 is given by [135]

$$p_{\mathrm{tt}} = K_{\mathrm{h}} f^{\alpha} B_{\mathrm{ttm}}^{\beta} + \frac{4}{\pi} K_{\mathrm{e}} \frac{f^2 B_{\mathrm{ttm}}^2}{\alpha_{\mathrm{tt}}} \tag{5.8}$$

where K_{h}, α, β, and K_{e} are the constants obtained from the curve fitting of core loss data measured for a toroidal stack of steel laminations with sinusoidal excitation, f is the frequency of flux density variation, and B_{ttm} is the peak value of flux density at the tooth-tip.

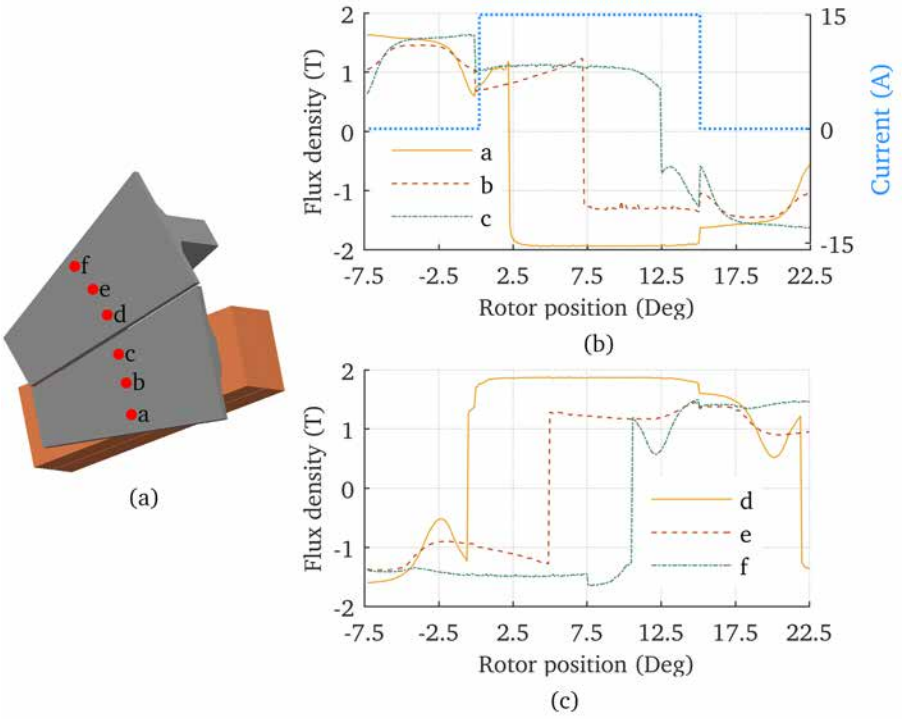

Figure 5.7: The flux density variation with rotor position for six points in a plane located at the middle of a tooth-tip of the bonded RE magnet SAT PMBLDC motor, when armature carries a current of 15 A. (a) Position of flux density sampling points in the stator. (b) Flux density variation in a tooth with current carrying coil. (c) Flux density variation in a tooth without coil.

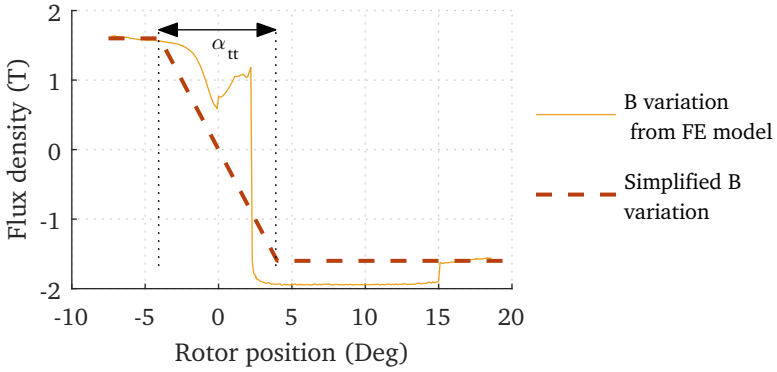

Figure 5.8: Tooth-tip flux density variation from the FE model and the simplified tooth-tip flux density variation of the SAT PMBLDC motor.

5.2.3 Core losses in stator tooth

The tooth core loss of a SAT PMBLDC motor is estimated by following a similar approach to the tooth-tip core loss. The flux density variation with rotor position for a tooth with coil and a tooth without coil of the bonded rare earth magnet SAT PMBLDC motor, when armature carries a current of 15 A, is shown in Figure 5.9. The flux density variations are captured at the geometrical centre of the tooth because the tooth has a uniform flux density across its cross section. The armature current affects only a peak during one cycle of tooth flux density variation and the effect on the affected peak is less pronounced as shown in Figure 5.9. Therefore, the tooth flux density variation with the armature current is not considered. The tooth core loss can be calculated using the model of Slemon and Liu [135] with the help of the simplified flux density variation shown in Figure 5.9. The tooth core loss per unit mass is given by [135]

$$p_{\mathrm{t}} = K_{\mathrm{h}} f^{\alpha} B_{\mathrm{tm}}^{\beta} + \frac{4}{\pi} K_{\mathrm{e}} \frac{f^2 B_{\mathrm{tm}}^2}{\alpha_{\mathrm{t}}} \tag{5.9}$$

where, B_{tm} is the peak value of the tooth flux density, and α_{t} is $2\pi/3$, the phase current conduction angle in electrical radians.

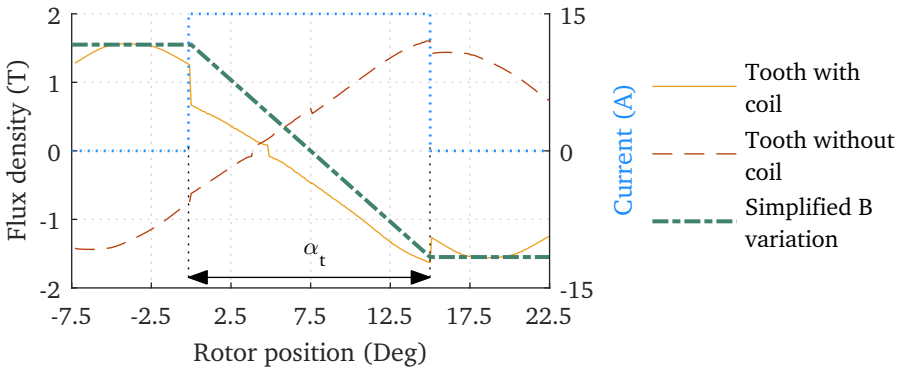

Figure 5.9: The flux density variation with rotor position for a tooth with a coil and a tooth without coil of the bonded RE magnet SAT PMBLDC motor, when the armature carries a current of 15 A.

5.2.4 Core losses in solid rotor yoke

The rotor yoke flux can vary with time because of the following reasons

1. The change in the reluctance seen by the rotor magnets as they move past slot openings and

2. The presence of armature flux, and the speed difference between the armature flux and the rotor.

The segmented tooth of the SAT topology allows fabrication of the motor with a narrow slot opening, and the designed motors have a 1 mm slot opening. The narrow slot opening creates only a minor flux density variation under no-load in the rotor yoke as shown in Figure 5.10. Therefore, the core loss generated in the rotor yoke due to slot opening is neglected because the reluctance seen by magnets remains nearly constant as the rotor rotates.

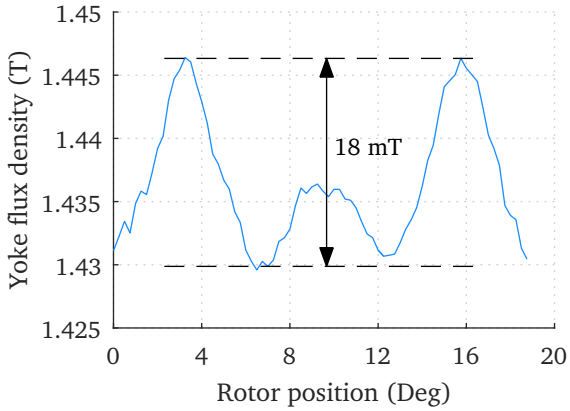

Figure 5.10: The rotor yoke flux density variation of the bonded RE SAT PMBLDC motor with rotor position under no-load.

The armature flux will generate both hysteresis and eddy current loss in the solid rotor yoke of a PMBLDC motor. The rotor yoke flux density of the bonded RE magnet SAT PMBLDC motor at no-load and when the armature carries a current of 20 A is shown in Figure 5.11. Comparing no-load and load flux density distributions in the rotor yoke, it is clear that the armature flux enhances some of the no-load peaks and diminishes the others. The sections of the rotor yoke that experience the maximum flux density will have a power loss corresponding to a minor hysteresis loop formed about the operating point defined by the no-load flux density 1.35 T. Even though, the area of the minor loop will increase with armature current, Bottauscio et al. in their work shown that the hysteresis loss from minor hysteresis loops will be a small fraction of the total rotor losses [123], and hence, the rotor yoke hysteresis loss is not

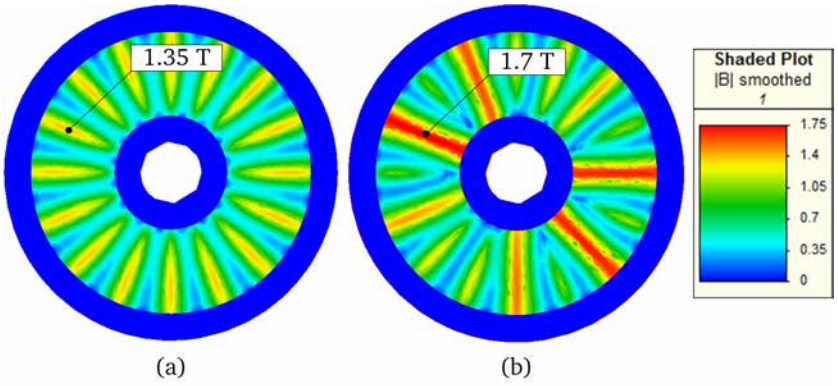

Figure 5.11: The rotor yoke flux density of the bonded RE magnet SAT PMBLDC motor. (a) No-load. (b) When armature carries a current of 20 A.

calculated in this work.

Eddy current losses in rotor yoke

The eddy current loss generated in a solid conducting rotor yoke of a permanent magnet motor by armature harmonic fluxes can be calculated using either an FE model [125], [133], [136], [137] or an analytical model [94], [124], [126], [138]–[144]. The studies comparing models to estimate eddy current loss in machine components found that the results obtained from the analytical model are within the acceptable limits of results of the FE model [132], [145]–[148]. However, Wang and Kemper in their comparison study of analytical and FE modelling of eddy current loss found that the analytical method underestimated values [149]. The axial flux topology of machines in this work necessitate 3D-FE modelling, and a 3D FE model of a SAT PMBLDC motor will take considerably longer simulation time because of the small element size required for the accurate simulation of eddy current distribution in a solid conducting yoke [128], [149]. Therefore, this work uses an analytical approach using a three-layer model proposed by Lawrenson et al. and Oberretl [150], [151].

The airgap flux density variation of the SAT PMBLDC motor and its normalised harmonics are shown in Figure 5.12. The airgap flux density variation of Figure 5.12 is generated from the FE model shown in Figure 5.3 by setting the magnet-flux to zero and the armature current to 15 A. The flux density distribution of Figure 5.12 is rich in harmonics because of the fractional-slot

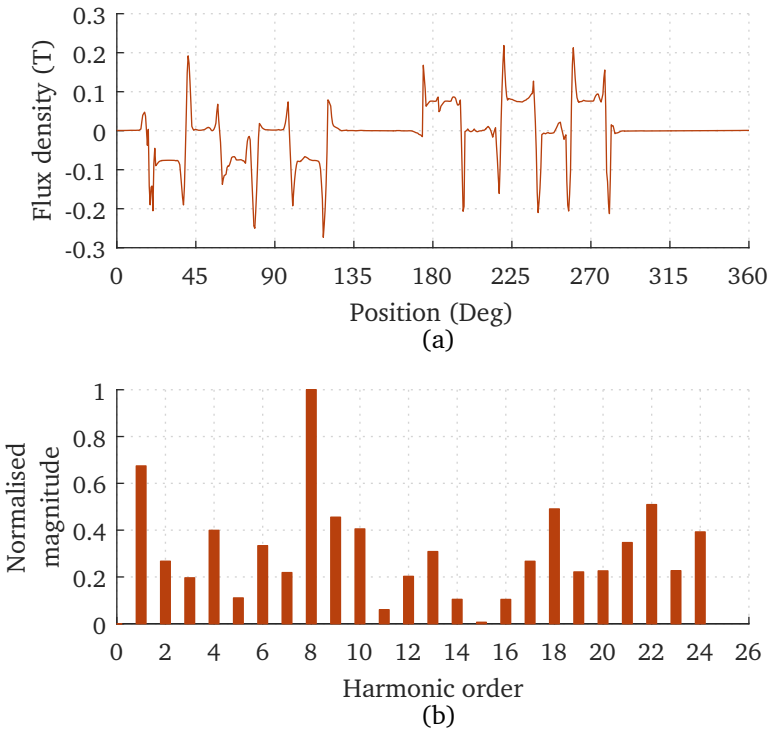

Figure 5.12: The airgap flux density harmonics of the bonded RE magnet SAT PMBLDC motor, when armature carries a current of 15 A, and the magnet-flux is set to zero. (a) The flux density variation over a 360° contour obtained from the FE model. The contour is a circle with radius equal to the mean stator radius and located at the middle of the airgap. (b) The normalised magnitude of airgap flux density harmonics.

concentrated winding employed in the design. Though, the three phase windings of PMBLDC motors are spatially separated from each other by 120° electrical; only two phases conducts at the same time and they each carry the same current but in opposite direction. As a result, rotating armature flux is not formed in PMBLDC motors, and the armature flux is either stationary or pulsating depending upon whether the winding carries a constant current or a varying current. Consequently, the velocity of the stationary armature flux density wave of a PMBLDC motor with respect to its rotor is the rotational speed of the machine.

In a PMBLDC motor, when a phase commutates and another phase starts conducting, the armature flux moves by 60° electrical. The movement of armature flux when the armature current transfer from one phase to another would generate eddy current in the rotor yoke, and the eddy current loss dur-

ing this transfer is not considered in this work.

The linear velocity of the armature flux density wave of a PMBLDC motor with respect to its rotor is given by

$$v = 2\pi n R_{\mathrm{Ymean}} \tag{5.10}$$

where, n is the rotational speed of the machine in revolutions per second, and R_{Ymean} is the mean radius of the rotor yoke. The wave length, λ_i of the ith harmonic of flux density wave is given by

$$\lambda_i = \frac{2\pi R_{\mathrm{Ymean}}}{i} \tag{5.11}$$

The angular frequency of the ith harmonic of flux density wave is given by

$$\omega_i = \frac{2\pi v}{\lambda_i} \tag{5.12}$$

Substituting Eq. (5.10) and Eq. (5.11) to Eq. (5.12)

$$\omega_i = 2\pi \times 2\pi n R_{\mathrm{Ymean}} \times \frac{i}{2\pi R_{\mathrm{Ymean}}} = 2\pi n i \tag{5.13}$$

The skin depth of ith harmonic of flux density wave is given by

$$\delta_i = \sqrt{\frac{2\rho_{\mathrm{Fe}}}{\mu_{\mathrm{Fe}}\omega_i}} \tag{5.14}$$

where, ρ_{Fe} is the resistivity, and μ_{Fe} is the average permeability of the rotor yoke material, which is normally made of solid soft iron in PMBLDC motors. Substituting Eq. (5.13) to Eq. (5.14)

$$\delta_i = \sqrt{\frac{\rho_{\mathrm{Fe}}}{i\pi\mu_{\mathrm{Fe}} n}} \tag{5.15}$$

The eddy current loss generated in a rotor yoke due to i^{th} harmonic of flux density wave can be calculated as [139], [142], [147]

$$P_{\mathrm{Lrye}i} = \frac{|B_i|^2 v^2 \delta_i}{4\rho_{\mathrm{Fe}}} \times A_{\mathrm{ry}} \tag{5.16}$$

where, $|B_i|$ is the magnitude of ith harmonic of the armature flux density wave and A_{ry} area of the rotor yoke face. Substituting Eq. (5.10) and Eq. (5.15) to

Eq. (5.16)

$$P_{\mathrm{Lrye}i} = \frac{|B_i|^2}{4\rho_{\mathrm{Fe}}} \times A_{\mathrm{ry}} \times (2\pi n R_{\mathrm{Ymean}})^2 \times \sqrt{\frac{\rho_{\mathrm{Fe}}}{i\pi\mu_{\mathrm{Fe}} n}}$$
$$= |B_i|^2 R_{\mathrm{Ymean}}^2 A_{\mathrm{ry}} \sqrt{\frac{\pi^3}{i\rho_{\mathrm{Fe}}\mu_{\mathrm{Fe}}}} \times n^{1.5} \tag{5.17}$$

The total eddy current loss generated due to armature flux density wave corresponding to a motor speed of n is given by

$$P_{\mathrm{Lrye}} = n^{1.5} \times R_{\mathrm{Ymean}}^2 A_{\mathrm{ry}} \sqrt{\frac{\pi^3}{\rho_{\mathrm{Fe}}\mu_{\mathrm{Fe}}}} \sum_{i=1}^{\infty} \frac{|B_i|^2}{\sqrt{i}} \tag{5.18}$$

The second term of Eq. (5.18) is independent of rotational speed of the PMBLDC motor and can be expressed as a function of source current, i_{s}

$$f_{\text{yoke eddy loss}}\{i_{\mathrm{s}}\} = R_{\mathrm{Ymean}}^2 A_{\mathrm{ry}} \sqrt{\frac{\pi^3}{\rho_{\mathrm{Fe}}\mu_{\mathrm{Fe}}}} \sum_{i=1}^{\infty} \frac{|B_i|^2}{\sqrt{i}} \tag{5.19}$$

Therefore, Eq. (5.18) can be written as

$$P_{\mathrm{Lrye}} = n^{1.5} \times f_{\text{yoke eddy loss}}\{i_{\mathrm{s}}\} \tag{5.20}$$

Rotor yoke eddy current loss in a PMBLDC motor with more than one rotor yoke can be calculated as

$$P_{\mathrm{Lrye}} = n_{\mathrm{y}} n^{1.5} \times f_{\text{yoke eddy loss}}\{i_{\mathrm{s}}\} \tag{5.21}$$

where, n_{y} is the number of rotor yokes in the motor. The equation (5.21) can be expressed in terms of the operating frequency of the motor similar to equations for core losses in the stator tooth-tip Eq. (5.8) and the stator tooth Eq. (5.9) as

$$P_{\mathrm{Lrye}} = n_{\mathrm{y}} \left(\frac{f}{p}\right)^{1.5} \times f_{\text{yoke eddy loss}}\{i_{\mathrm{s}}\} \tag{5.22}$$

where, p is the number of pole pairs of PMBLDC motor.

5.3 Dynamic model of PMBLDC motor drives

A block diagram of the proposed non-linear dynamic model of a PMBLDC motor drive is shown in Figure 5.13. The model consists of a DC voltage source model, a converter model, a three-phase PMBLDC motor model, and a load model. In addition, the model has a controller block, which generates the gate signal for the converter based on inputs such as the rotor position, the rotational speed of the rotor, and the source current. The model is implemented in Matlab-Simulink™. This section discusses the implementation of individual units of the dynamic model of a PMBLDC motor drive.

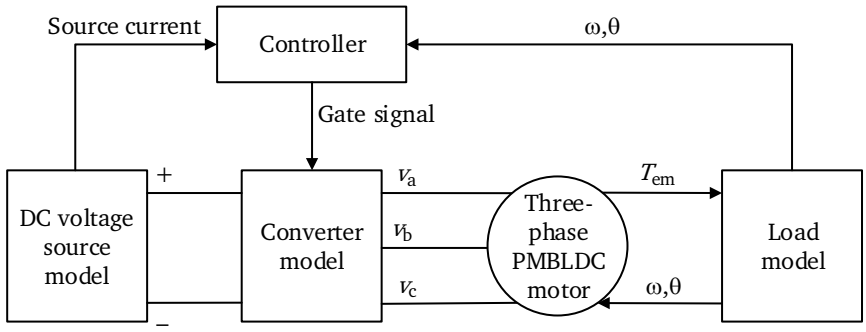

Figure 5.13: The block diagram of the non-linear dynamic model of SAT PMBLDC motor.

5.3.1 Three-phase PMBLDC motor model

The three-phase PMBLDC motor model consists of a block to solve the voltage equation (5.5) for all three phases, a block to solve the torque equation (5.7), and a block to calculate the core loss. The model presented in this work builds on the past works in the area of non-linear phase variable modelling of PMBLDC motors [109]–[113] by adding core loss calculations.

Voltage equation

The voltage equation for all three phases of a PMBLDC motor is solved to calculate phase currents using the model shown in Figure 5.14. A 2D look-up table of the flux-linkage-derivative, ψ', is used to account the effect of non-ideal back EMF waveform and the armature reaction. The look-up table of ψ'

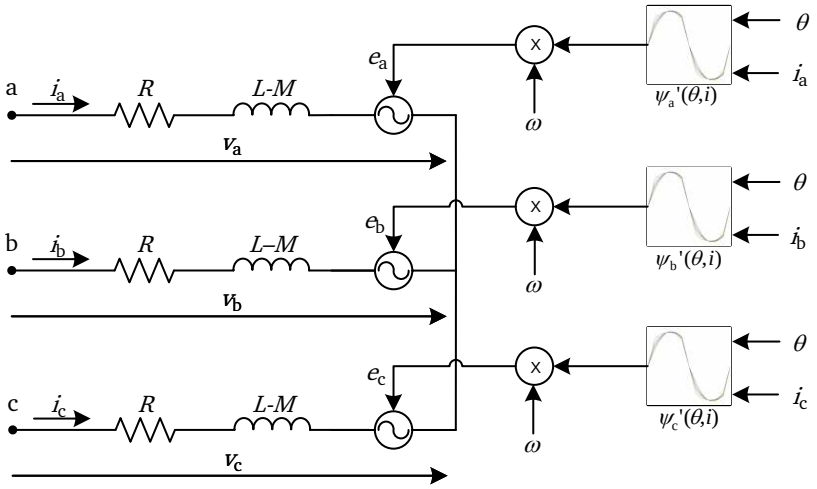

Figure 5.14: The model for solving the voltage equation of a three-phase PMBLDC motor.

is obtained by solving a static FE model of the PMBLDC motor for different armature currents and rotor positions.

Torque equation

The torque equation of a PMBLDC motor is solved using the model shown in Figure 5.15. Similar to the model of voltage equation, model for torque equation also uses the look-up table of flux-linkage-derivatives. The torque model also uses a look-up table of cogging torque vs. rotor position to simulate the effect of cogging torque on the net torque of the motor.

Core loss model

The core loss model incorporates hysteresis and eddy current loss generated in the stator core and eddy current loss generated in the rotor yoke into the non-linear phase variable model of PMBLDC motor. If M_{stt} is the mass of all tooth-tips and M_{st} is the mass of all tooth, the total core losses generated in

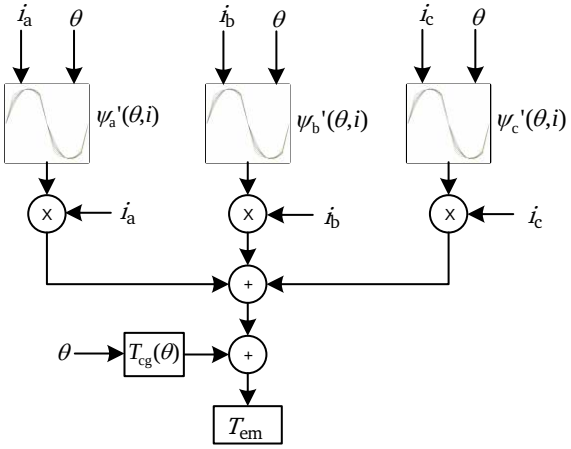

Figure 5.15: The model for solving the torque equation of a three-phase PMBLDC motor.

the stator core can be calculated from Eq. (5.8) and Eq. (5.9) as

$$\begin{aligned} P_{\mathrm{cs}} &= p_{\mathrm{tt}} M_{\mathrm{stt}} + p_{\mathrm{t}} M_{\mathrm{st}} \\ &= \left(K_{\mathrm{h}} f^{\alpha} B_{\mathrm{ttm}}^{\beta} + \frac{4}{\pi} K_{\mathrm{e}} \frac{f^2 B_{\mathrm{ttm}}^2}{\alpha_{\mathrm{tt}}} \right) M_{\mathrm{stt}} + \left(K_{\mathrm{h}} f^{\alpha} B_{\mathrm{tm}}^{\beta} + \frac{4}{\pi} K_{\mathrm{e}} \frac{f^2 B_{\mathrm{tm}}^2}{\alpha_{\mathrm{t}}} \right) M_{\mathrm{st}} \\ &= K_{\mathrm{h}} f^{\alpha} \left(M_{\mathrm{stt}} B_{\mathrm{ttm}}^{\beta} + M_{\mathrm{st}} B_{\mathrm{tm}}^{\beta} \right) \\ &\quad + \frac{4}{\pi} K_{\mathrm{e}} f^2 \left(\frac{M_{\mathrm{stt}} B_{\mathrm{ttm}}^2}{\alpha_{\mathrm{tt}}} + \frac{M_{\mathrm{st}} B_{\mathrm{tm}}^2}{\alpha_{\mathrm{t}}} \right) \end{aligned} \tag{5.23}$$

Total core loss can be obtained by adding Eq. (5.22) and Eq. (5.23),

$$\begin{aligned} P_{\mathrm{c}} = n_{\mathrm{y}} \left(\frac{f}{p} \right)^{1.5} &\times f_{\text{yoke eddy loss}}\{i_{\mathrm{s}}\} + K_{\mathrm{h}} f^{\alpha} \left(M_{\mathrm{stt}} B_{\mathrm{ttm}}^{\beta} + M_{\mathrm{st}} B_{\mathrm{tm}}^{\beta} \right) \\ &+ \frac{4}{\pi} K_{\mathrm{e}} f^2 \left(\frac{M_{\mathrm{stt}} B_{\mathrm{ttm}}^2}{\alpha_{\mathrm{tt}}} + \frac{M_{\mathrm{st}} B_{\mathrm{tm}}^2}{\alpha_{\mathrm{t}}} \right) \end{aligned} \tag{5.24}$$

The core loss equation (5.24) of a PMBLDC motor is solved using the model shown in Figure 5.16. The core loss model uses two look-up tables, one for peak tooth-tip flux density and another one for rotor yoke eddy current loss function. The look-up table of peak tooth-tip flux density vs. armature current can be generated from the same set of FE models used to calculate the variation of flux linkage with rotor position and armature current. The look-up table of the rotor yoke eddy current loss function is obtained by solving FE

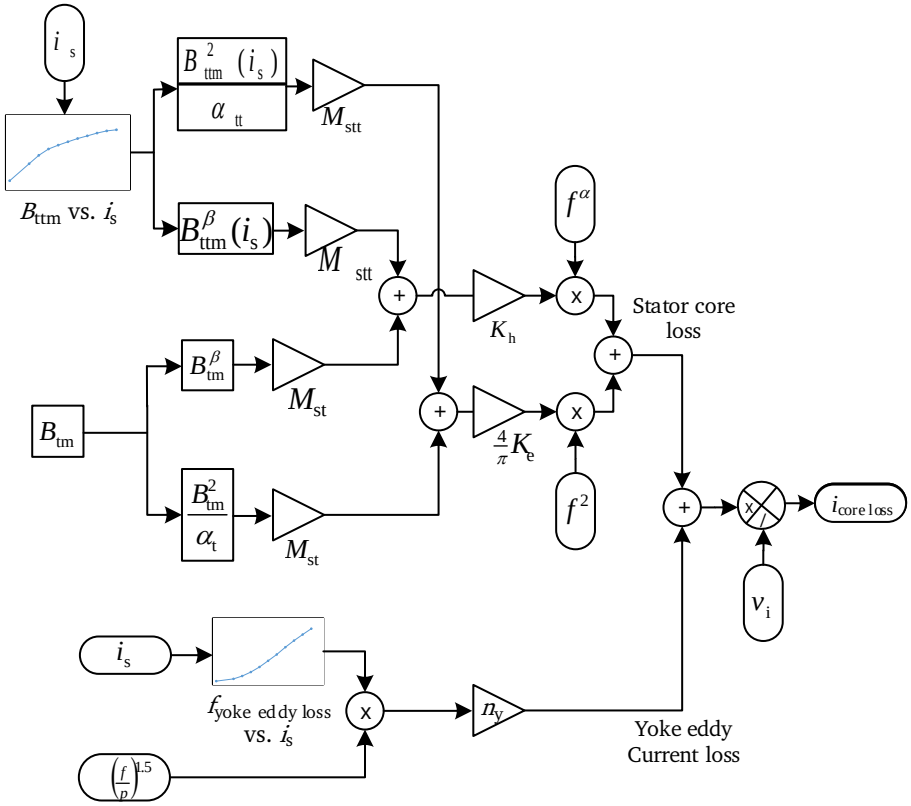

Figure 5.16: The core loss model of a PMBLDC motor.

models of a PMBLDC motor without magnet-flux for a set of armature current values. Though, removing magnet-flux will enhance the magnitude of stator flux density harmonics by lowering the saturation level of the flux path, the approach will help to capture low amplitude sub-harmonic components, which can penetrate deep into the yoke and induce most of the losses [126], [129], [133], [141], [142], [152]. The core loss model calculates the core loss component of the current, and in a Simulink model, this current will be drawn from the voltage source via a block named controlled current source, connected across the voltage source.

5.3.2 Power electronic converter model

Unlike an induction motor or DC motor, a PMBLDC motor will not run if connected directly to a power supply without a converter and a controller [31]. A

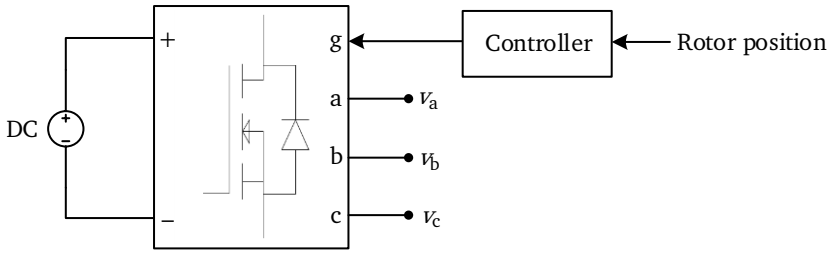

Figure 5.17: The model of a basic controller and converter combination required to drive a three-phase PMBLDC motor.

block diagram of a basic controller and a converter of a three-phase PMBLDC motor is shown in Figure 5.17. The controller will generate the gate pulses for the six-pulse converter based on the rotor position so that a positive shaft torque is produced.

5.3.3 Load model

The electromagnetic torque developed in the motor has to work against the load, inertia of rotating components, and moving friction. The equation governing the load behaviour can be written as

$$T_{\mathrm{em}} = T_{\mathrm{L}} + j\frac{d\omega}{dt} + b\omega \tag{5.25}$$

where, T_{L} is the load torque, j is the moment of inertia of rotating parts of the motor and the load, and b is the constant of moving friction. The model used to solve Eq. (5.25) is shown in Figure 5.18.

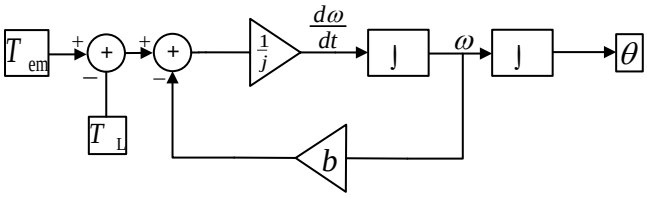

Figure 5.18: The constant torque load model.

5.4 Calculation of dynamic performance of the designed motors

The synthesis program used to design the bonded RE and the ferrite magnet SAT PMBLDC motors uses static FE models. The operation of PMBLDC motors includes states such as zero current duration for each one of the three phases for a third of the operating time and rapid building up of currents. Therefore, before fabrication of the motor prototypes, it is important to simulate the operation of each designed motor driving a load when fed by a PMBLDC drive, and confirm that the motor meets the target specification listed in Table 4.2. The dynamic model of PMBLDC motor presented in Section 5.3 will be used to simulate the performance curves of the designed motors. The dynamic model incorporates a number of parameters derived from FE models, either in the form of constants or look-up tables. This section will explain how the look-up tables of the dynamic model are obtained from static FE models of the SAT PMBLDC motor designs. Afterwards, how the phase self-inductance and other parameters used in the dynamic simulation are calculated is also presented. At the end, the results of dynamic simulation of both the bonded RE motor and the ferrite magnet motor are discussed.

5.4.1 Modelling the effect of armature reaction on back EMF

The back EMF waveform of a PMBLDC motor that includes the effect of the armature reaction can be modelled accurately using a look-up table of flux-linkage-derivative generated from a pair of FE models of the motor for different values of the rotor position and the armature current. The static FE model of SAT PMBLDC motor, simplified using the geometrical symmetry, used to calculate the flux-linkage-derivative is shown in Figure 5.19. In a three-phase PMBLDC motor, simulating the effect of armature reaction on the back EMF of a phase requires two stages because the armature-current-return-path of the phase under consideration switches from a preceding phase to an oncoming phase midway through the conduction. Therefore, estimating the effect of armature reaction on the back EMF of phase-a E_{a}, requires two stages as the armature-current-return-path switches from the phase-c to phase-b as shown in Figure 5.20. The armature current will switch from phase-c to phase-b when the flux linkage of phase-a, ψ_{a} is zero. In the first stage, phases a and c will be excited with different values of armature current for positions between 30°

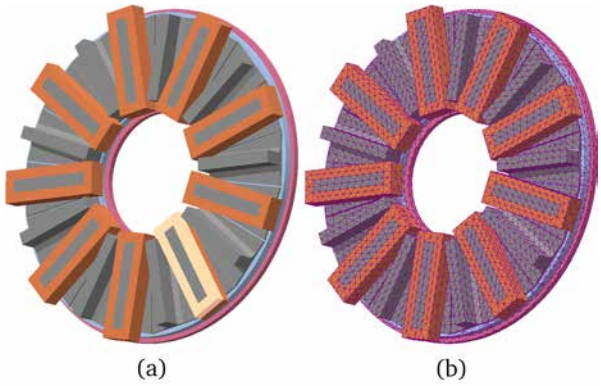

Figure 5.19: The static FE model of SAT PMBLDC motor used to calculate the flux-linkage-derivative as a function of rotor position and armature current. (a) SAT PMBLDC motor geometry utilizing half symmetry and the highlighted coil is a search coil to estimate the flux linkage of a phase. (b) Meshed model.

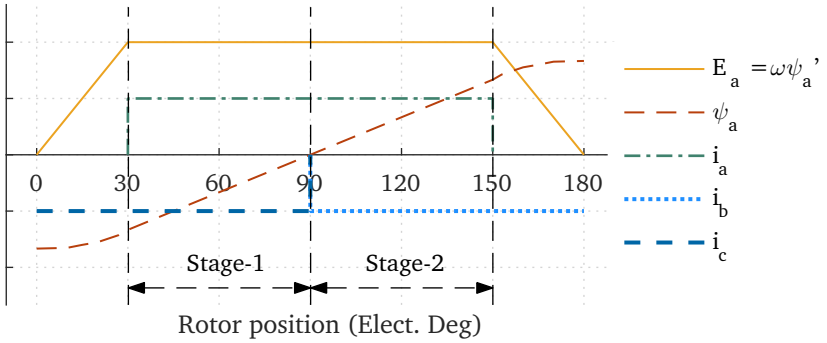

Figure 5.20: The two stages required for simulating the effect of armature reaction on back EMF is shown using ideal back EMF, flux linkage, and phase current waveforms of a PMBLDC motor.

electrical to 90° electrical. In the second stage, phases a and b will be excited with the same set of values of armature current used in the first stage for positions between 90° electrical to 150° electrical. The results of FE simulations of the two stages are combined to generate the overall flux linkage waveform for 120° electrical.

The results obtained from FE simulations in the form of flux linkage of a phase as a function of the armature current and the rotor position for the bonded RE magnet and the ferrite magnet designs are shown in Figure 5.21. From Figure 5.21, it is clear that the effect of saturation of the flux path is more pronounced in the bonded RE magnet motor. The flux-linkage-derivative

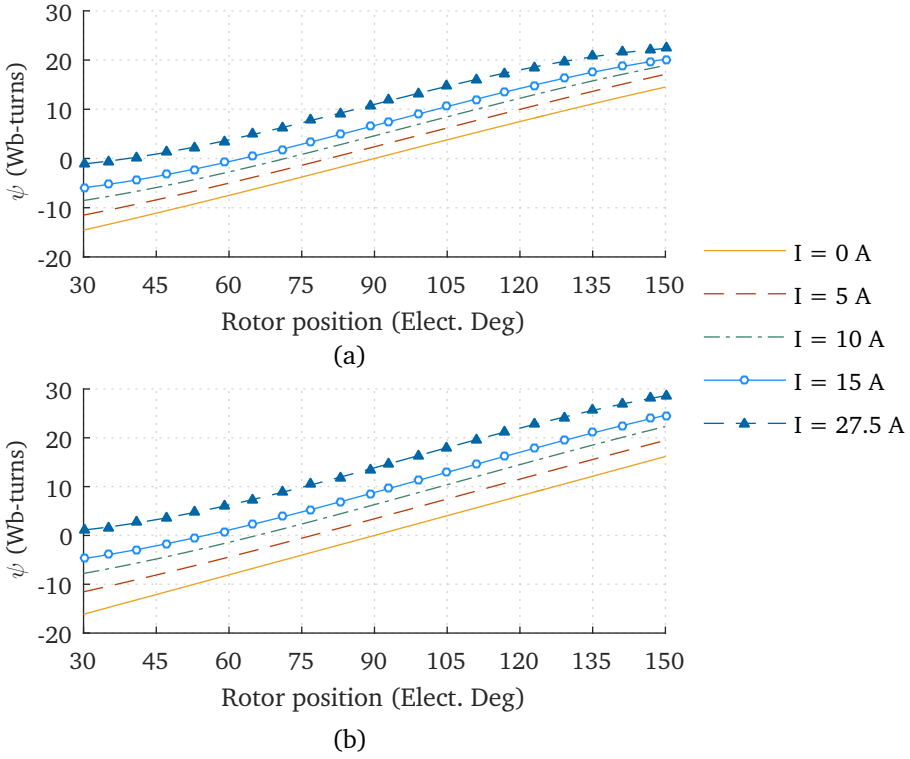

Figure 5.21: Variation of the flux linkage of a phase with rotor position for different armature currents. (a) The bonded RE magnet motor. (b) The ferrite magnet motor.

is obtained from the flux linkage data using the equation

$$\psi' = \frac{\Delta\psi}{\Delta\theta} \tag{5.26}$$

where, θ is rotor position in radians. The flux-linkage-derivative of a phase as a function of the armature current and the rotor position for the bonded RE magnet and the ferrite magnet designs are shown in Figure 5.22. When a coil axis aligns with an inter-polar axis of the rotor, the magnitude of flux produced by the magnet passing through the tooth that has the coil wound around will be minimum. The magnet flux linking with a coil will stay minimum when it aligns with the inter-polar axis irrespective of the magnitude of the armature current, and this leads to a convergence of curves around the rotor positions 90° electrical and 270° electrical as shown in Figure 5.22. In the dynamic model, the back EMF accounting the effect of armature reaction is calculated

from the flux-linkage-derivative look-up table using Eq. (5.6).

5.4.2 Cogging torque in 18-slot 16-pole SAT PMBLDC motor

Besides, the flux linkage derivative, cogging torque is another parameter that require a look-up table. The fractional-slot per pole configuration and a narrow slot opening, which is possible because of fabrication involving assembly of segmented stator structure, lead to a very low value of cogging torque for the 18-slot 16-pole SAT PMBLDC motors. Capturing low values of torque ripple using FE model of machines with the dimensions considered in this study can lead to a large number of small elements. Therefore, a machine with smaller dimensions nevertheless has the same tooth profile and slot opening of the designed motors is analysed using FE model. The machine has an axial length

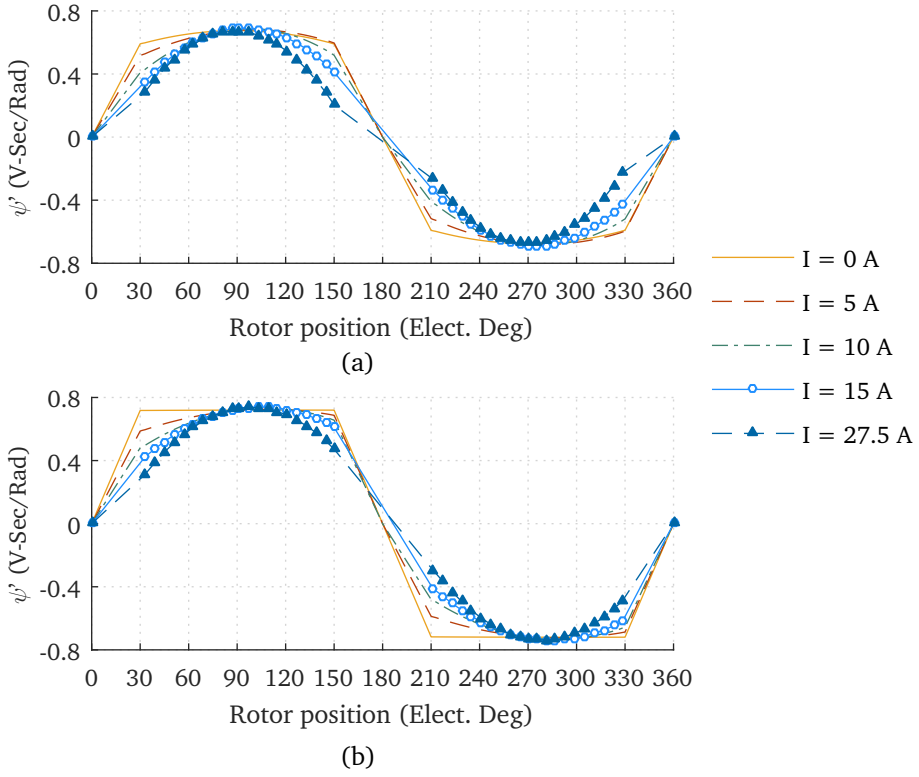

Figure 5.22: Variation of the flux-linkage-derivative of a phase with rotor position for different armature currents. (a) The bonded RE magnet motor. (b) The ferrite magnet motor.

of 25 mm and a diameter of 100 mm. The variation of cogging torque of the reduced size machine is shown in Figure 5.23. The peak to peak value of the cogging torque of the reduced size machine is found to be 16 mN m. Therefore, the effect of cogging torque on the net torque of the designed motor is neglected based on the analysis carried out on a reduced size machine.

5.4.3 Core loss modelling

Two look-up tables are required in the core loss model to capture the variations of the peak tooth-tip flux density with armature current and the rotor yoke eddy current loss function with armature current.

The variation of the peak tooth-tip flux density of the bonded RE magnet motor and the ferrite magnet motor for different armature current, shown in Figure 5.24, will be used in the stator core loss model to calculate tooth-tip losses. The peak tooth-tip flux density variation and the maximum tooth flux density listed in Table 5.2 are obtained from the FE models used to calculate the flux-linkage-derivative look-up table.

The variation of the rotor yoke eddy current loss function with armature current is estimated using the FE model shown in Figure 5.3. The magnet-flux of the FE model is set to zero and the model is solved for different values of armature current to capture the airgap flux density variation over a 360°. The magnitudes of the flux density harmonics are obtained using fast Fourier transform of the airgap flux density variation. Subsequently, Eq. (5.19) is used to calculate the rotor yoke eddy current loss function from the magnitudes of the flux density harmonics. The variation of the yoke eddy current loss

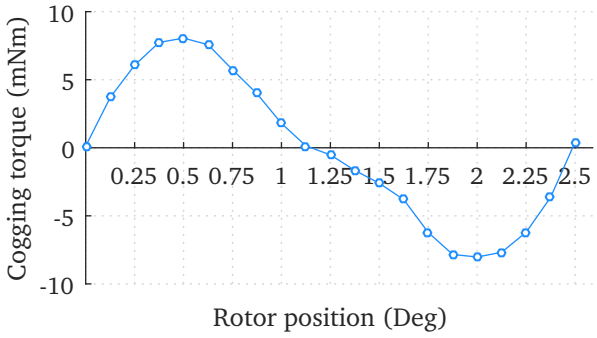

Figure 5.23: The cogging torque variation of a reduced size machine with same configuration of the designed SAT PMBLDC motor.

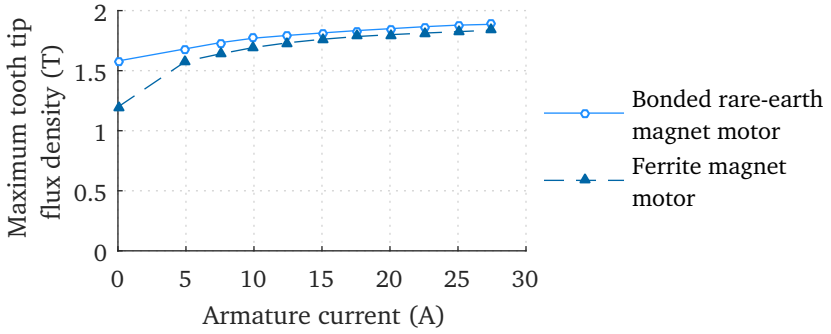

Figure 5.24: The variation of the peak tooth-tip flux density of the bonded RE magnet motor and the ferrite magnet motor for different armature current.

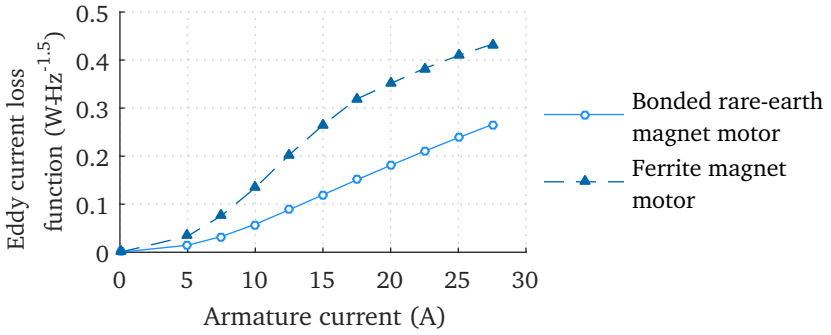

Figure 5.25: The values of yoke eddy current loss function of the bonded RE magnet motor and the ferrite magnet motor for different armature current.

function of the bonded RE magnet motor and the ferrite magnet motor for different armature current, shown in Figure 5.25, will be used in the rotor core loss model.

5.4.4 Calculation of phase self-inductance

Only alternate teeth carry a coil in the designs of SAT PMBLDC machine presented in this study. Though, the two consecutive coils carrying armature current will use the middle unwound tooth as a return path, there will be only a negligible flux-coupling between the coils [79]. Therefore, the mutual inductance between the phases will be zero for all practical purposes.

The values of phase self-inductance of the designed machines were estimated using the FE model shown in Figure 5.3. The magnet-flux of the FE

model is set to zero and the FE model is solved to find the flux linkage of a phase at 50 % of peak value of full load phase current. The phase self-inductance is calculated by dividing the flux linkage of the phase with the phase current. The phase resistance is also calculated from the same FE model using the values of ohmic loss generated in the coils belong to a phase. The phase resistance and the phase self-inductance of the bonded RE motor and the ferrite magnet motor are listed in Table 5.2.

5.4.5 Constants of dynamic model

The constants of the dynamic model and their values used in the simulation of the bonded RE motor and the ferrite magnet motor are listed in Table 5.1 and Table 5.2. Table 5.1 lists model parameters that have the same value for both the motors, and Table 5.2 lists model parameters that have different values for the two motors. Among parameters listed in Table 5.1 and Table 5.2, mean

Parameter	Value
Number of pole pairs	8
Mean pole transition angle	8.0°
Loss constants of M400-50A	
K_{h}	1.0976×10^{-2}
K_{e}	7.9211×10^{-5}
α	1.2337
β	1.7753

Table 5.1: The dynamic model parameters with same value for both the bonded RE magnet and ferrite magnet motors.

pole transition angle is measured from the FE models used to generate the flux-linkage-derivative look-up table and the loss constants are obtained from the curve fitting of core loss data measured for a toroidal stack of steel laminations with sinusoidal excitation. Further, Solidworks™, a 3D CAD software, is used to find the mass of tooth-tips, mass of tooth, and inertia of rotating parts.

Parameters	Bonded RE magnet motor	Ferrite magnet motor
Phase resistance (mΩ)	104.86	130.83
Phase self-inductance (mH)	4.05	4.44
Maximum tooth flux density (T)	1.60	1.25
Mass of tooth-tips (kg)	1.35	1.82
Mass of tooth (kg)	2.49	2.95
Inertia of rotating parts (kg m^2)	4.43×10^{-2}	4.68×10^{-2}

Table 5.2: The dynamic model parameters of the bonded RE magnet and the ferrite magnet motors.

5.4.6 Results of dynamic simulation of bonded RE magnet and ferrite magnet SAT PMBLDC motor designs

The performance of the SAT PMBLDC motors is simulated using the dynamic model by connecting it to a variable DC source model and a variable load torque model. The performance parameters are captured for different values of the input voltage starting from 12 V to 48 V when a rated torque of 20 N m is applied as a load. After simulating the performance of the motors corresponds to 48 V at 20 N m, the load torque will be reduced to zero in steps, and the performance will be recorded in each step. The predicted performance curves of the bonded RE magnet motor and the ferrite magnet motor, obtained from the dynamic simulation, are shown in Figure 5.26. Main observations from the performance curves are

- The maximum output power is considerably less than the target value of 700 W. The reduced output power will result in an increased acceleration time, and from the plot of output power vs. time to reach the top speed, shown in Figure 3.3, it can be concluded that acceleration time of both designs will be more than 25 s. Moreover, it is clear from Figure 3.4 that the motors cannot propel the vehicle at the top speed over a gradient of 3 %.

- The efficiency drops considerably at low speeds, especially when the speed drops below 50 % of the top speed.

- The bonded RE motors have marginally better torque when operating beyond the constant torque region.

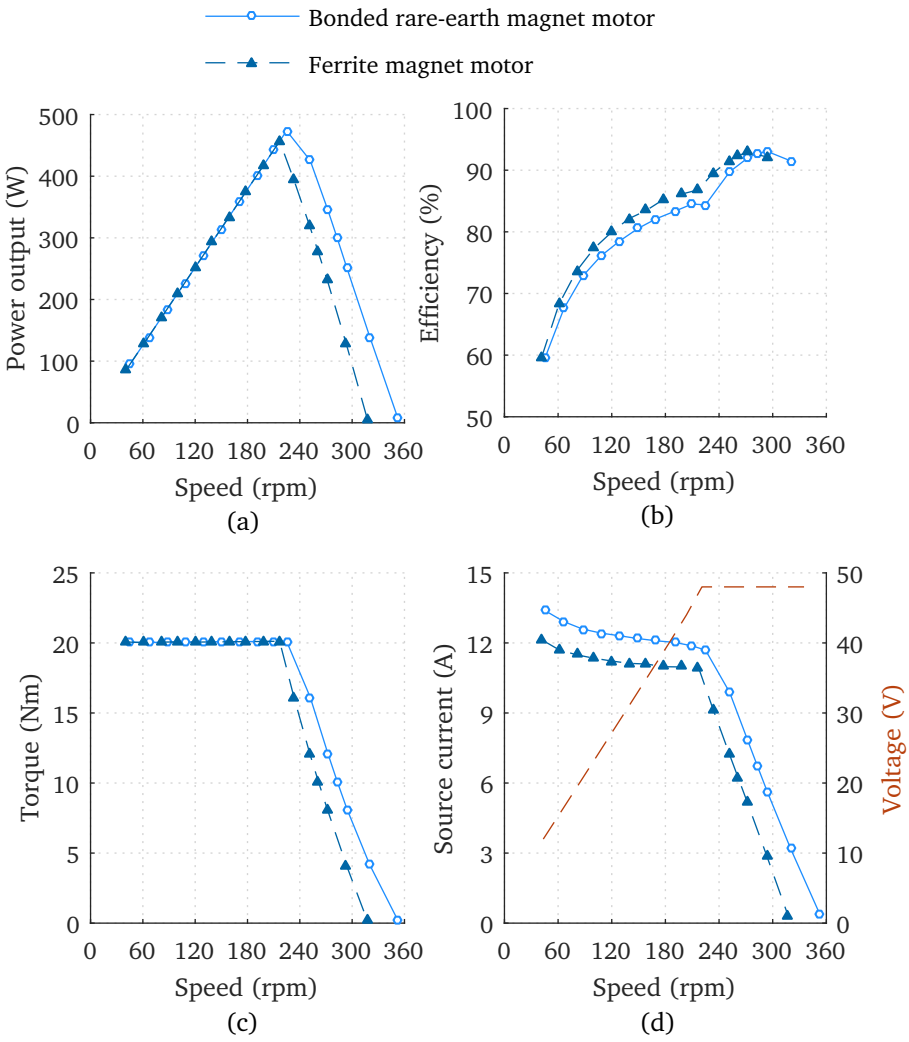

Figure 5.26: The performance characteristics of the bonded RE magnet motor and the ferrite magnet motor simulated using the dynamic model of a PMBLDC motor. (a) Power output vs. speed. (b) Efficiency vs. speed. (c) Torque vs. speed. (d) Source current and source voltage vs. speed.

- From the design summary presented in Table 4.9, the rated source currents of the bonded RE magnet motor and the ferrite magnet motor obtained from the design program are 16 A and 15.5 A respectively. However, the source current of the bonded RE magnet motor and the ferrite magnet motor obtained from the dynamic model, shown in Fig-

ure 5.26(d), are 11.7 A (26.9 %↓) and 11 A (29 %↓) respectively when the rated source voltage is applied.

The drop in the maximum power output of the motor compared to the designed value of 700 W can be explained with the help of waveforms acquired from the dynamic modelling of the bonded RE magnet motor, and these waveforms are shown in Figure 5.27. The Figure 5.27(a) corresponds to a source voltage of 24 V and a motor speed of 108 rpm, and Figure 5.27(b) corresponds to a source voltage of 48 V and a motor speed of 225 rpm. When the motor speed is 225 rpm, the rise time of current is less than half of the rise time at 108 rpm. As the rise time decreases, the voltage drop across the phase inductance, the value of inductance times di/dt, increases and at 225 rpm, the peak value inductive voltage drop is nearly equal to the peak value of the back EMF. The inductive voltage drop limits the armature current because there is less differential voltage available between the source and the back EMF. Further, the rated source voltage will be equal to the sum of the back EMF, the inductive voltage drop, and the resistive drop at a speed less than the designed speed of 340 rpm. The FE based design program of Chapter 4 has not considered the inductive voltage drop and this assumption was the reason for the difference between the designed output power and the output power obtained from the dynamic model.

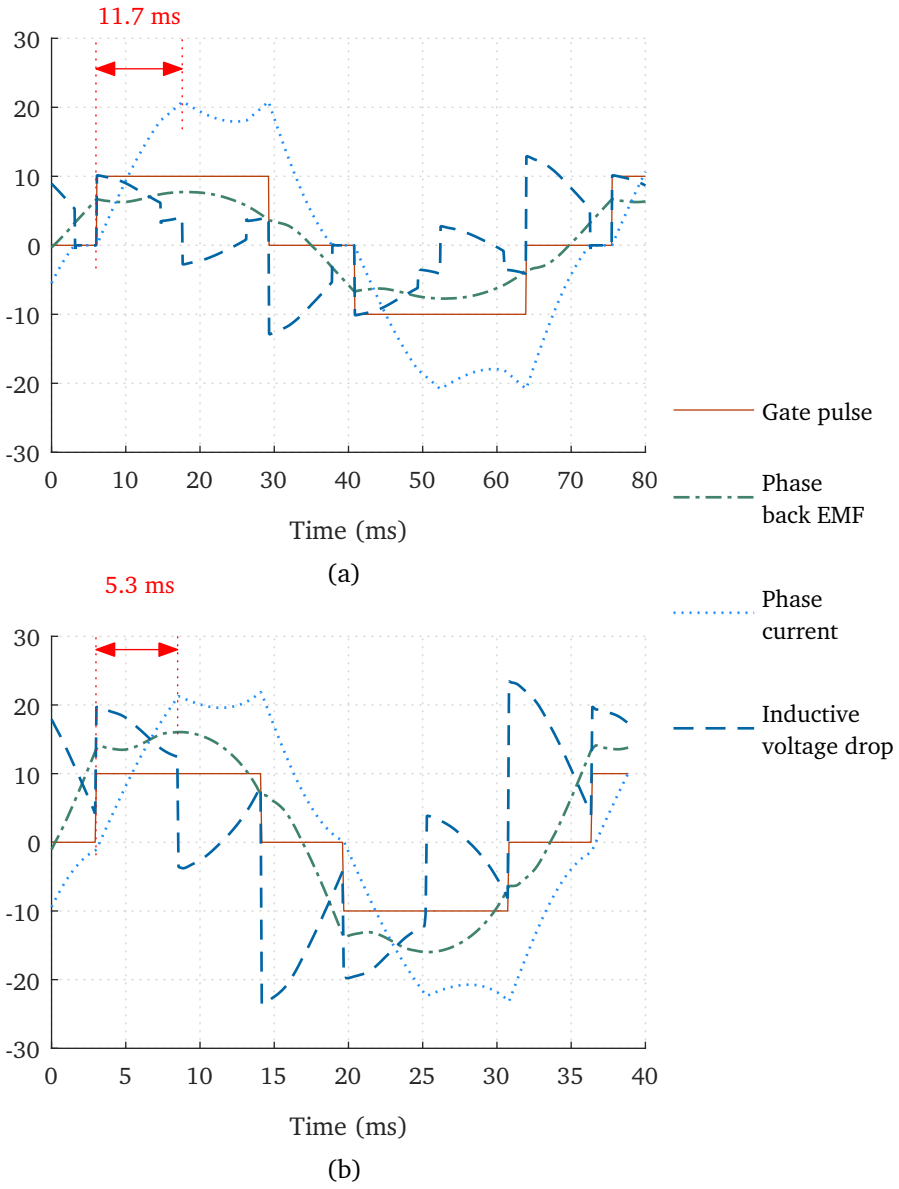

Figure 5.27: Waveforms of the gate pulse, the back EMF, the current, and inductive voltage drop of phase-a for different source voltages, obtained from the dynamic modelling of the bonded RE magnet motor with a load torque of 20 N m. (a) source voltage = 24 V, motor speed = 108 rpm. (b) source voltage = 48 V, motor speed = 225 rpm.

5.5 Revision of design-synthesis program of SAT PMBLDC motors

The dynamic modelling of the designed bonded RE magnet and ferrite magnet motors found that they will not generate the maximum power required to meet the specification of the two-wheeler powertrain listed in Table 4.2. This section discusses a revision of the design program carried out to include self-inductance of phases of the motor while calculating the values of dependent design variables. Besides, the section covers design generation of bonded RE magnet and ferrite magnet SAT PMBLDC motors using the revised program, comparison of the selected motor designs, and evaluation of the motor designs using the dynamic model of SAT PMBLDC motor.

5.5.1 Revised design-synthesis program

The dynamic analysis of the identified designs showed that the phase self-inductance has a significant role in deciding the rated current and the maximum power. Therefore, the design program has been revised to include the inductive voltage drop. During operation, a current loop of a PMBLDC motor consists of a voltage source, resistance and self-inductance of the conducting phases, and the back EMF of the conducting phases. Therefore, the voltage equation can be written as

$$V_{\mathrm{r}} = 2iR + 2L\frac{di}{dt} + E \tag{5.27}$$

Let's assume that in a PMBLDC motor, the full load phase current I_{fl} will reach its final value in ΔT seconds, and the rise time ΔT can be calculated as

$$\Delta T = \frac{\theta_{\mathrm{rise}}}{\omega_{\mathrm{r}}} \tag{5.28}$$

where, θ_{rise} is the angle of movement of the rotor in radians corresponds to a rise time ΔT at the rated angular velocity ω_{r}. The voltage equation (5.27) can be modified to include I_{fl} and θ_{rise} as

$$V_{\mathrm{r}} = 2I_{\mathrm{fl}}R + 2LI_{\mathrm{fl}}\frac{\omega_{\mathrm{r}}}{\theta_{\mathrm{rise}}} + K_{\mathrm{E}}\omega_{\mathrm{r}} \tag{5.29}$$

A rise time equal to 25 % of the phase conduction time in an half cycle is targeted for the revised designs. In the revised designed program, the number of turns per coil and the diameter of a turn is found by incorporating Eq. (5.29) to the flowchart of Figure 4.4, and the modified flowchart is shown in Figure 5.28. The phase self-inductance in the design program is calculated as explained in section 5.4.4, however, the current used in the simulation is full load current of the iteration.

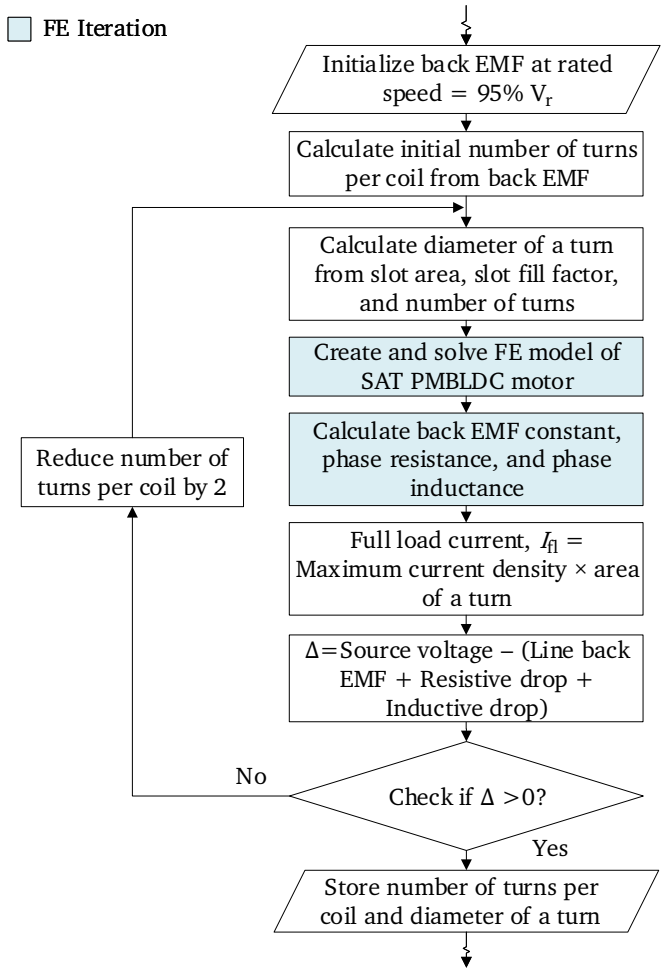

Figure 5.28: The revised flowchart that incorporate inductive voltage drop in the calculation of number of turns per coil and diameter of a coil turn of SAT PMBLDC motor.

5.5.2 Revised designs of bonded RE and ferrite magnet motors

The dynamic analysis of the SAT PMBLDC motors found that the inductance of the machine limits the maximum output power. Therefore, the design revision aimed to identify low loss designs with a lower value of the phase self-inductance. The phase self-inductance is proportional to the square of number turns per phase, and a reduction in the number of turns without changing other dimensions of the machine will not only reduce the inductance but also reduce the phase linkage and the back EMF generated. However, an increase in the magnet-flux that links with the coils of the phase winding would help to maintain a flux linkage sufficient to produce the required torque from a lower number of turns.

The most efficient way to increase the magnet-flux in an axial flux machine is to increase the outer diameter as this result in more magnet area as well as coil area. A different approach will be increasing the magnet thickness, which can lead to an increased reluctance of the flux path, and a longer axial length of the machine. Therefore, the outer diameter of both the bonded RE magnet motor and the ferrite magnet motor are increased, and their values are listed in Table 5.3. A smaller radius is chosen for the bonded RE magnet motor not

Parameter	Value
Outer diameter of bonded RE magnet motor	260 mm
Outer diameter of ferrite magnet motor	275 mm

Table 5.3: The revised outer diameters of the bonded RE magnet motor and the ferrite magnet motor.

only because of the higher energy density of the magnet but also owing to the fact that it will be fabricated first, and a more space between the machine and the wheel will give higher flexibility in the design of the connector that joins them. The values of the remaining variables are kept same as in the previous design synthesis.

The design synthesis using revised design program is set up to run for ten generations, and the optimisation convergence of the design synthesis of the bonded RE magnet motor and the ferrite magnet motor is shown in Figure 5.29. The design synthesis using revised design program generated 551 designs of the bonded RE magnet motor and the ferrite magnet motor. From

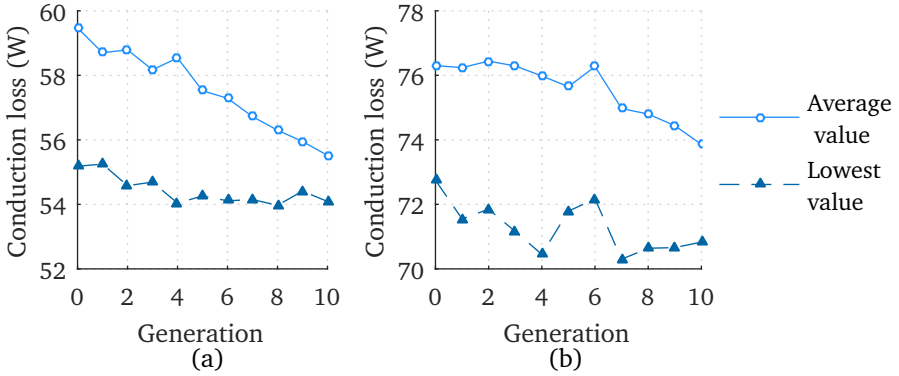

Figure 5.29: Results of revised design synthesis of in-wheel motors using integer constrained genetic algorithm. (a) Bonded RE magnet motor. (b) ferriterrite magnet motor.

these designs, a group of 15 designs with the lowest conductive loss is listed in Table 5.4 and Table 5.5 for the bonded RE magnet motor and the ferrite magnet motor respectively.

Design #410 is selected for the bonded RE magnet motor, and design #539 is chosen for the ferrite magnet motor, as they are the lowest loss design. A lower inductance design is not selected from the result of revised design synthesis as in section 4.3.1 because the effect of inductance is already accounted in the design program. The comparative study presented in the following part of this section will use four designs, and therefore, they are named for clarity. The initial and the revised design of the bonded RE magnet motor are named BRE-V1 and BRE-V2 respectively. The initial and the revised design of the ferrite magnet motor are named Fe-V1 and Fe-V2 respectively.

Design #	Thickness of magnet	$\frac{\text{Total overhang}}{\text{Magnet length}}$	Stator diameter ratio	Rotor yoke length	Stator tooth width	Axial length of the tooth	Number of turns per coil	Conductive loss	Axial length of the motor
	mm	%	%	mm	mm		mm	W	mm
410	7	0	45	8	10.2	32.8	28	54.0	63.6
492	7	10	45	8	10.2	33.0	28	54.6	63.8
230	7.5	10	45	8	10.2	32.7	22	54.0	64.5
158	7	5	45	8	10.2	33.1	22	55.2	63.9
311	8	5	47.5	8	10.8	31.9	22	55.5	64.7
88	9.5	10	52.5	7	11.9	30.6	24	56.1	64.4
4	7.5	5	47.5	8	10.8	32.7	26	56.3	64.5
194	7.5	0	52.5	8	11.9	31.5	30	56.5	63.3
63	7.5	0	50	7	11.3	32.4	24	56.8	62.2
256	7	5	57.5	8	13.0	30.4	32	56.9	61.2
313	7	10	52.5	8	11.9	31.0	24	56.9	61.8
303	7.5	5	52.5	7	11.9	31.1	24	57.0	60.9
279	7.5	0	47.5	8	10.8	32.9	24	57.1	64.7
124	8	5	50	7	11.3	32.2	24	57.2	63.0
153	7.5	10	55	8	12.5	31.2	26	57.3	63.0

Table 5.4: Results from the design synthesis of the bonded RE magnet motor using the revised design program.

Design #	Thickness of magnet	$\frac{\text{Total overhang}}{\text{Magnet length}}$	Stator diameter ratio	Rotor yoke length	Stator tooth width	Axial length of the tooth	Number of turns per coil	Conductive loss	Axial length of the motor
	mm	%	%	mm	mm		mm	W	mm
539	7.5	10	45	6	10.8	37.6	30	70.8	65.4
35	8	10	50	6	12.0	36.0	28	73.2	64.8
268	7	5	50	6	12.0	36.3	28	73.4	63.1
287	8	10	45	6	10.8	38.0	26	71.8	66.8
243	8.5	5	45	6	10.8	37.7	26	71.9	67.5
385	7	0	45	6	10.8	38.0	26	72.0	64.8
154	7.5	5	45	6	10.8	38.2	26	72.0	66.0
96	8.5	10	45	6	10.8	37.2	26	72.2	67.0
221	8	0	45	6	10.8	38.1	26	72.7	66.9
2	8	5	45	6	10.8	38.2	26	72.8	67.0
390	7.5	10	47.5	6	11.4	37.1	26	73.3	64.9
215	8	10	47.5	6	11.4	37.2	26	73.5	66.0
408	9	10	45	6	10.8	38.5	24	73.3	69.3
253	7	5	52.5	6	12.6	35.9	28	73.5	62.7
400	7	0	52.5	6	12.6	36.0	28	73.7	62.8

Table 5.5: Results from the design synthesis of the ferrite magnet motor using the revised design program.

5.5.3 Comparison of revised designs of bonded RE and ferrite magnet motors

An overview of the revised designs of the bonded RE magnet motor and the ferrite magnet motor is shown in Table 5.6. For the revised designs, the mass

Parameters	BRE-V2	Fe-V2
Outer diameter of stator (mm)	260	275
Number of poles-slots	16 - 18	16 - 18
Length of airgap (mm)	0.4	0.4
Coil current density (A/mm^2)	4.5	4.5
Length of magnet (mm)	7	7.5
Magnet overhang ratio (%)	0	10
Diameter ratio of stator (%)	45	45
Length of rotor yoke (mm)	8	6
Width of stator tooth (mm)	10.2	10.8
Number of turns per coil	28	30
Axial length of tooth (mm)	32.8	37.6
Diameter of a coil turn (mm)	2.5	2.7
Axial length of motor (mm)	63.6	65.4
Phase resistance (mΩ)	56.0	54.7
Line back emf at rated speed (V)	37.4	33.4
Full load current (A)	22.0	25.4
Conductive loss (W)	54.0	70.8

Table 5.6: Summary of the revised designs of SAT PMBLDC traction motors.

of active materials and their percentage differences using the bonded RE magnet motor as a baseline is listed in Table 5.7. The revised ferrite magnet design is heavier than the revised bonded RE magnet motor by 10.5 %, and this difference was 19.6 % for the initial designs. Further, parameters such as torque per unit moment of inertia, power per unit volume, and power per unit mass of the revised designs are calculated and listed in Table 5.8. Amongst the two revised designs, the rotor yoke of the bonded RE magnet is thicker, and it is heavier than the rotor yoke of the ferrite magnet motor by 8.6 %. In addition, the rotor moment of inertia of the revised ferrite magnet motor is lower by 26.1 %, and this can have an effect on the vehicle performance similar to using a lightweight wheel. It must be noted that the performance indices listed in Table 5.8 were not considered either in the design optimisation or while

selecting the designs.

	Mass (kg)		
Material	BRE-V2	Fe-V2	Difference (%)
Magnet	3.26	3.67	12.7 ↑
Copper	2.09	2.78	32.9 ↑
Laminations M400-50A	4.28	5.33	24.4 ↑
Soft iron	5.92	5.41	−8.6 ↓
Total	15.56	17.19	10.5 ↑

Table 5.7: Mass of active materials of the revised designs of SAT PMBLDC traction motors.

Parameter	BRE-V2	Fe-V2	Difference (%)
Volume of motor (m^3)	3.56×10^{-3}	4.32×10^{-3}	21.3 ↑
Moment of inertia of the rotor ($kg\,m^2$)	9.12×10^{-2}	6.73×10^{-2}	-26.1 ↓
Torque per unit moment of inertia ($N\,m/(kg\,m^2)$)	219.4	297.0	35.4 ↑
Power per unit volume (kW/m^3)	196.35	161.9	-17.5 ↓
Power per unit mass (W/kg)	45.0	40.7	-9.5 ↓

Table 5.8: Comparison of the revised designs of SAT PMBLDC traction motors.

5.5.4 Performance of revised designs of bonded RE magnet and ferrite magnet motors

The performance of the designs BRE-V2 and Fe-V2 when driven by a BLDC motor controller are simulated using the dynamic model. The dynamic model parameters are estimated from FE simulations. The flux linkage variation of the designs BRE-V2 and Fe-V2 with rotor position is shown in Figure 5.30. The variation of the flux-linkage-derivative of the designs BRE-V2 and Fe-V2 with rotor position calculated from the flux linkage data is shown in Figure 5.31. The tooth-tip flux density variation with armature current is shown in Figure 5.32, and the variation of eddy current loss function with armature current is shown in Figure 5.33 are used to model the core loss.

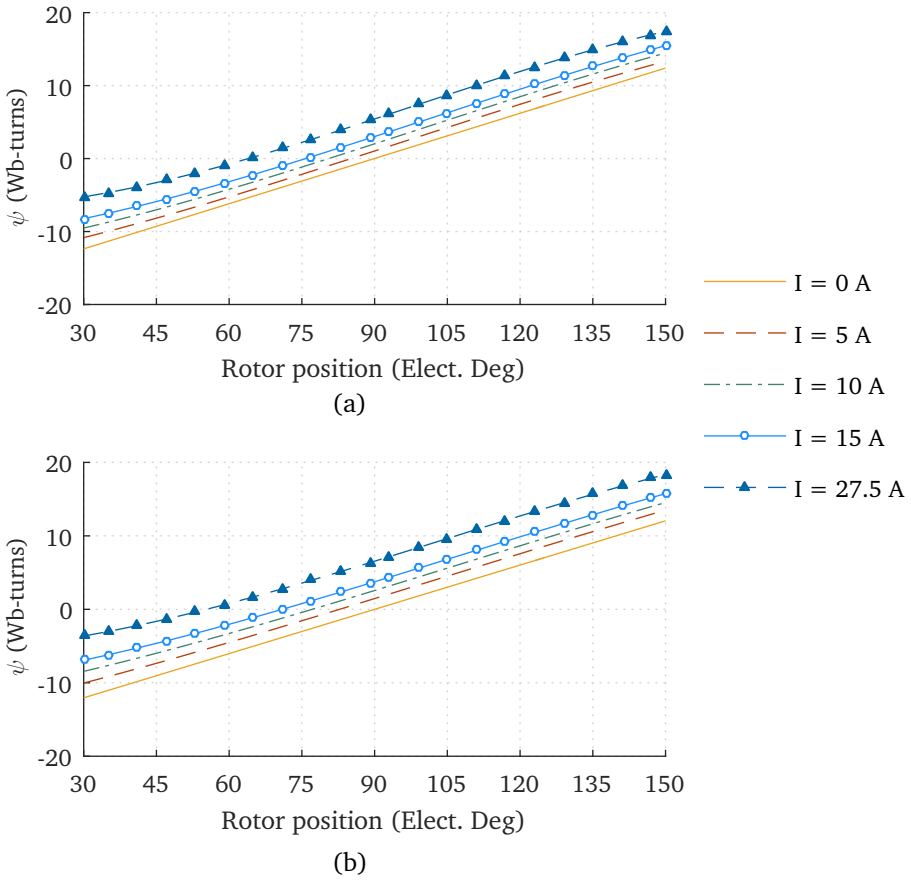

Figure 5.30: Variation of the flux linkage of a phase with rotor position for different armature currents. (a) Design BRE-V2. (b) Design FE-V2.

The number of pole pairs, mean pole transition angle, and loss constants of lamination material are not affected by the design revision. Therefore, the values listed in Table 5.1 can be used in dynamic modelling of the revised designs. The values of phase resistance, phase self-inductance, maximum tooth flux density, mass of tooth-tips, mass of tooth, and inertia of rotating parts of revised designs are listed in Table 5.9.

Similar to initial designs, the performance parameters of the revised designs are captured for different values of the input voltage starting from 12 V to 48 V when a rated torque of 20 N m is applied as a load. After simulating the performance of the motors corresponds to 48 V at 20 N m, the load torque

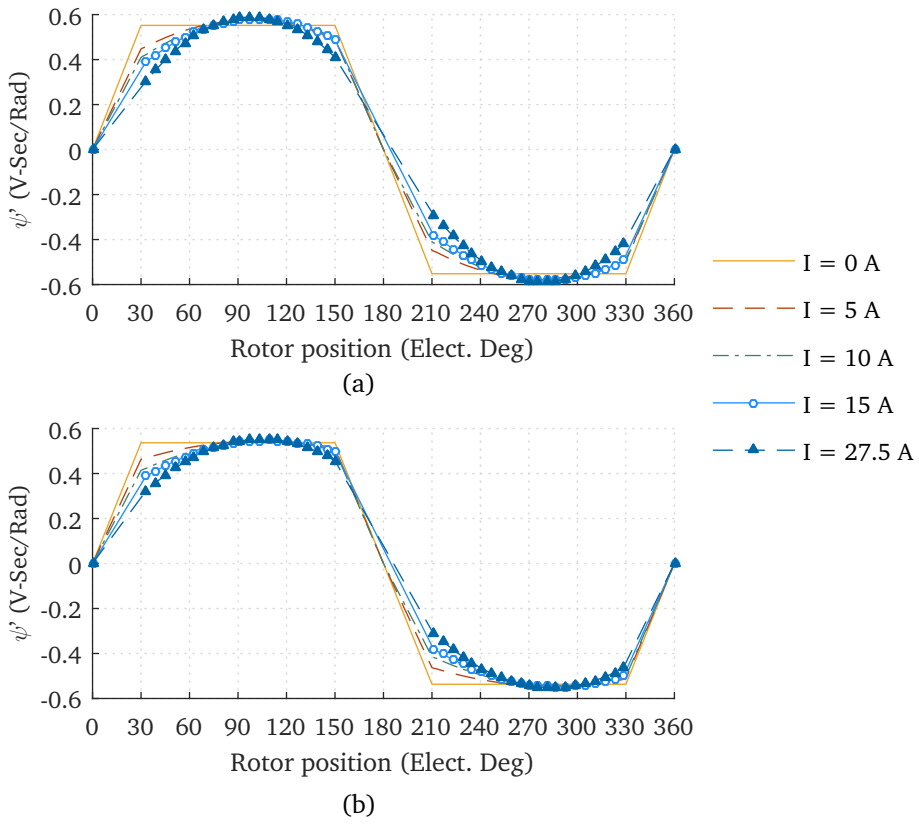

Figure 5.31: Variation of the flux-linkage-derivative of a phase with rotor position for different armature currents. (a) Design BRE-V2. (b) Design FE-V2.

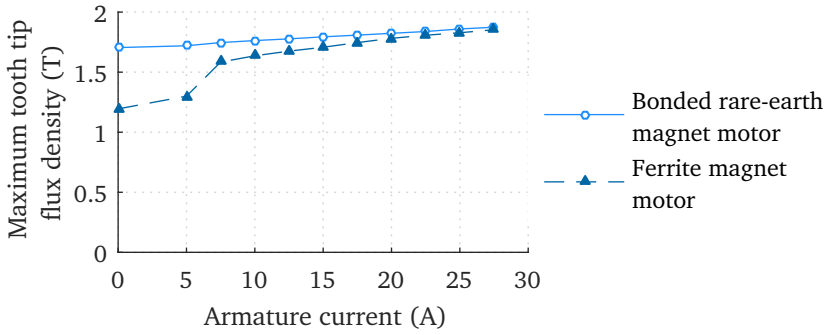

Figure 5.32: The peak tooth-tip flux density variations of revised designs.

will be reduced to zero in steps, and the performance will be recorded in each step. The performance curves of designs BRE-V2 and Fe-V2 obtained from the

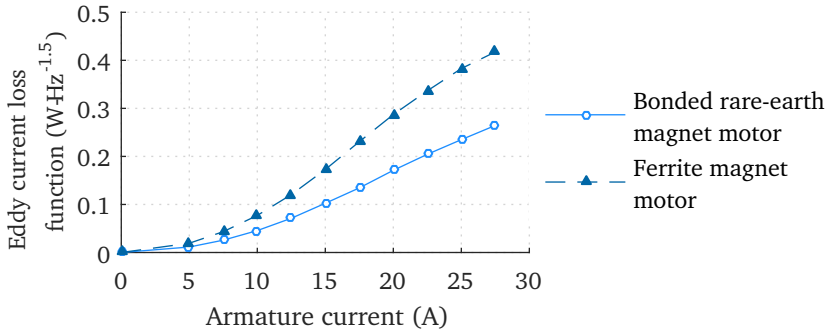

Figure 5.33: Variations of yoke eddy current loss function of revised designs.

Parameters	Bonded RE magnet motor	Ferrite magnet motor
Phase resistance (mΩ)	56	54.7
Phase self-inductance (mH)	4.3	5.6
Maximum tooth flux density (T)	1.6	1.3
Mass of tooth-tips (kg)	1.8	2.0
Mass of tooth (kg)	2.5	3.3
Inertia of rotating parts (kg m^2)	9.12×10^{-2}	6.73×10^{-2}

Table 5.9: The dynamic model parameters of revised designs of SAT PMBLDC motors.

dynamic simulation is plotted along with performance curves of designs BRE-V1 and Fe-V1 in Figure 5.34. The main observations from the performance curves are

- The maximum power of both BRE-V2 and Fe-V2 are close to 650 W, which is sufficient for an under 20 s acceleration time to the top speed and maintain the top speed for gradients up to 3 %.
- The efficiency of both BRE-V2 and Fe-V2 at low speeds are considerably improved compared to BRE-V1 and Fe-V1.
- Though the torque at the top speed for BRE-V2 and Fe-V2 is only 60 % of the peak torque, it is not expected to have a considerable effect on the acceleration time because the peak torque is available until the vehicle reaches 90 % of the top speed.
- The average source current of both BRE-V2 and Fe-V2 are considerably lower than the prediction of the design program. The accuracy of the

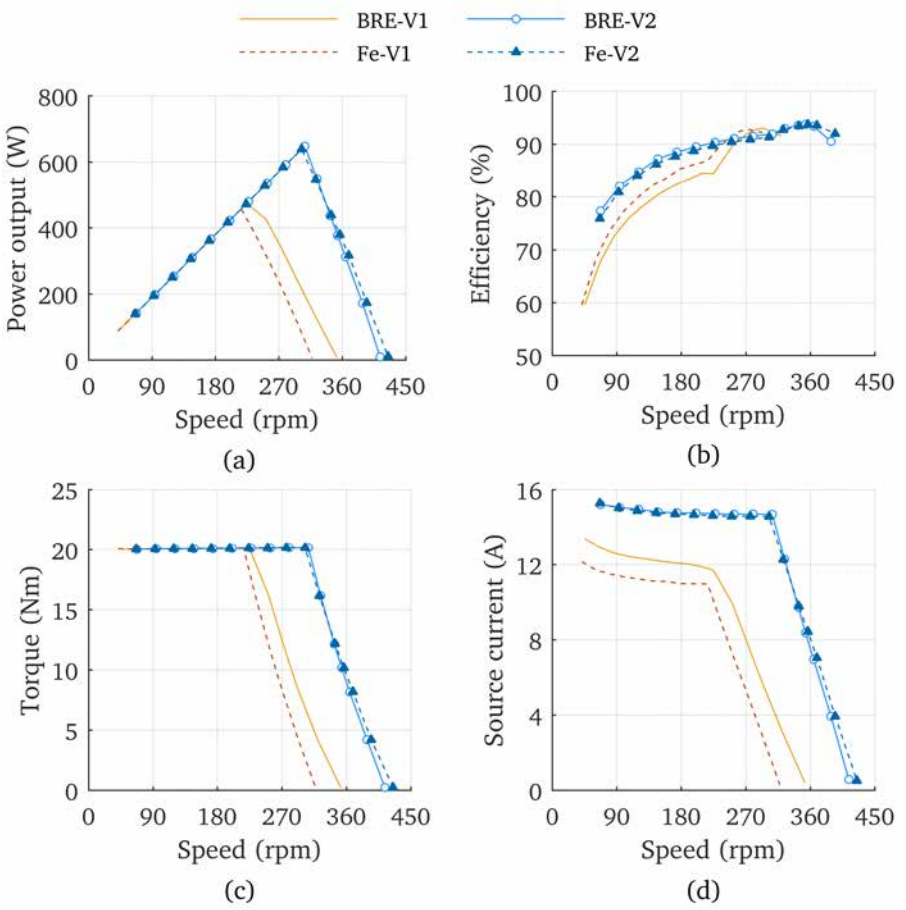

Figure 5.34: The performance characteristics of SAT PMBLDC motor designs BRE-V1, Fe-V1, BRE-V2, and Fe-V2 simulated using the dynamic model of a PMBLDC motor. (a) Power output vs. speed. (b) Efficiency vs. speed. (c) Torque vs. speed. (d) Source current and source voltage vs. speed.

current calculation is limited by the ideal current and back EMF waveform shapes used in conjunction with static FE model to reduce the computation time. The predicted current is the product of the area of the cross-section of a turn and the maximum current density, and the back EMF constant is corrected for an armature reaction that corresponds to the peak current. However, it is clear from the back EMF waveform of dynamic simulation, shown in Figure 5.27, and the flux-linkage-derivative, shown in Figure 5.31, that the effect of the armature reaction is not uniform during the entire conduction period. To summarise, the use of

ideal current and back EMF waveform in the design program results in an underestimation of the back EMF constant, and this causes an overestimation of the source current corresponds to the rated power and the rated torque.

5.6 Performance variation of ferrite magnet PMBLDC motor with temperature

Different aspects of magnet in operation such as reversible and irreversible demagnetization as a result of armature reaction and temperature induced operating point shift on the performance of PM machine have been researched extensively for RE magnets [153]–[156]. In most of these situations, ferrite magnets behave different from RE magnets, because the coercivity of ferrite magnets increase with temperature; in other words, ferrite magnets have a positive temperature coefficient and RE magnets have a negative temperature coefficient for coercivity. The remanence of both magnets decrease with temperature. Moreover, the knee point in demagnetization characteristics appears at low temperature for ferrite magnets and at higher temperature for RE magnets. In applications such as direct drive hub motors, heat from magnets are dissipated rapidly to the surrounding because of their positioning in outer casing and therefore, the possibility of high temperature demagnetization when using RE magnets are less. In contrast, for ferrite magnets used in a similar motor configuration, the inrush current at start can be seen as critical aspect from the magnet perspective, especially at low ambient temperatures, where the risk of demagnetisation is the highest.

Though the design of ferrite magnet machines is discussed extensively in literature [157]–[164]; the performance variation of ferrite magnet PMBLDC motors with temperature has not been examined in detail. Also, there is a lack of systematic approach presented for identifying the leeway for armature reaction with respect to irreversible demagnetization. The work presented in [165] discusses the effect of temperature on torque profile of a ferrite PMBLDC motor with the help of FE electro-magnetic and thermal model. In [164], the authors described a possible demagnetization due to load line intersecting beyond the knee point of a ferrite magnet at low temperature. In [166], the authors used the flux density distribution in magnets to estimate the level of demagnetization in a PM synchronous generator and also calculated the per-

formance variation with temperature. In [157], the authors used *B-H* curve of ferrite magnet corresponding to the lowest operating temperature to ensure that the field weakening operation is not causing any irreversible demagnetization in a PM synchronous motor. However, authors did not evaluate the performance variation with temperature. In [167], the authors used manufacturer supplied temperature coefficient of B_r and H_c of ferrite magnet to evaluate the performance of a line-start PM machine for different operating temperatures.

This section discusses the use of laboratory measured *B-H* characteristics of a ferrite magnet to evaluate the margin of safety to irreversible demagnetization in a SAT PMBLDC motor. In addition, *B-H* characteristics of the ferrite magnet for different temperatures have been used to study the performance variation of SAT PMBLDC motor design Fe-V2 with temperature.

5.6.1 Measured BH characteristics of ferrite magnet

The specification of the bonded RE magnet and the ferrite magnet from the product data sheet is shown in Table 5.10, and the measured second quadrant *B-H* characteristics of these magnets for temperatures starting from $-20\,^{\circ}\mathrm{C}$ to $100\,^{\circ}\mathrm{C}$ is shown in Figure 5.35. Only two curves are shown in Figure 5.35 for the bonded RE magnet, for temperatures $-20\,^{\circ}\mathrm{C}$ and $100\,^{\circ}\mathrm{C}$, because it has a low temperature coefficient and curves are closely spaced. However, the ferrite magnet experiences significant variations in both remanence and coercivity over the temperature range considered, and moreover knee-points are appearing in the second quadrants for temperatures below $70\,^{\circ}\mathrm{C}$.

With regard to a PM machine design, the critical value of demagnetizing field that the magnet can be exposed to without any permanent loss in remanence can be found from the ratio of a change in flux density B to a change in magnetization H of *B-H* curve. The ratio $\frac{\Delta B}{\Delta H}$ of *B-H* curve of the ferrite magnet material is plotted against the magnetizing field for different temperatures in Figure 5.36. It is clear from the figure that, $\frac{\Delta B}{\Delta H}$ remains constant until $250\,\mathrm{kA\,m^{-1}}$ and its values at lower temperatures are changing initially. Therefore, it can be concluded that, the ferrite magnet used in this study can safely withstand a demagnetizing field or an armature reaction field up to $250\,\mathrm{kA\,m^{-1}}$.

Grade	BH_{max} ($kJ\,m^{-3}$)	B_r (T)	H_c ($kA\,m^{-1}$)	Reversible temperature coefficient	
				$\%B_r$ ($\%\,°C^{-1}$)	$\%H_c$ ($\%\,°C^{-1}$)
NDB6	48.0 ± 8.0	0.52 ± 0.06	329.5 ± 25.5	-0.13	-0.4
Y33BH	33.25 ± 1.75	0.42 ± 0.1	247.5 ± 12.5	-0.2	$+0.3$

Table 5.10: Properties of the bonded RE magnet (grade:NDB6) and the ferrite magnet (grade:Y33BH) used in the designs of SAT PMBLDC motor as per magnet data sheets.

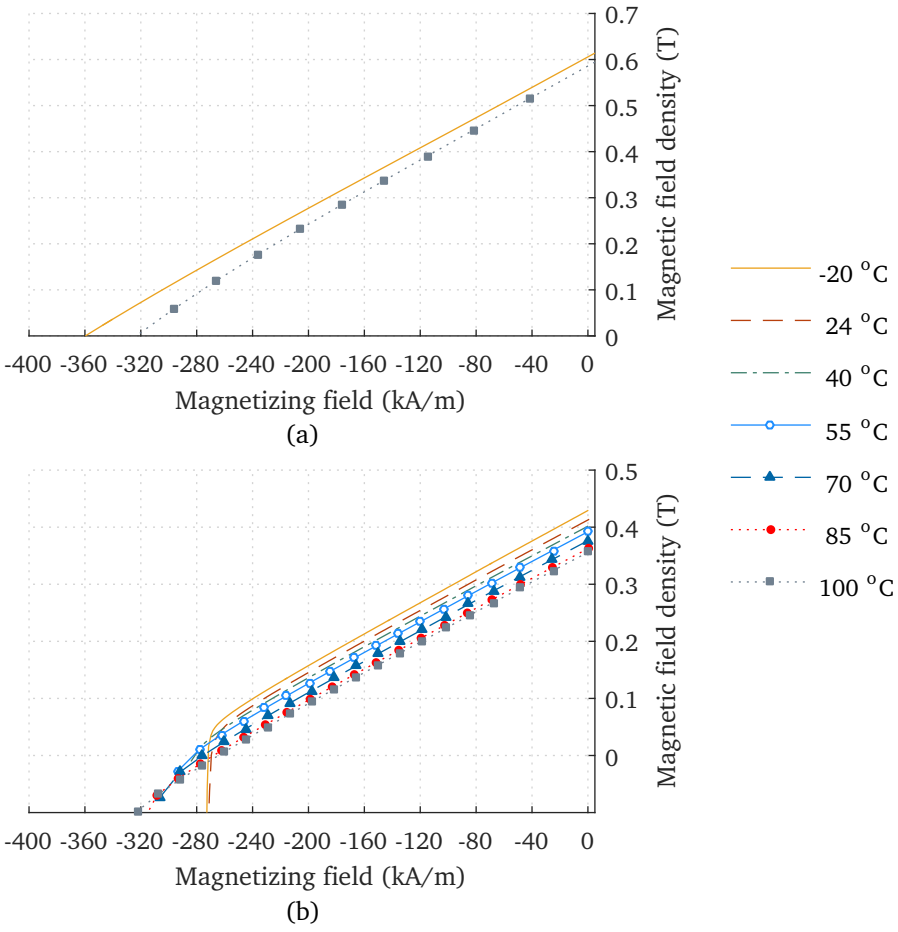

Figure 5.35: Measured demagnetization characteristics of magnets used in the design of SAT PMBLDC motors for different temperatures. (a) Bonded RE magnet. (b) ferriterrite magnet.

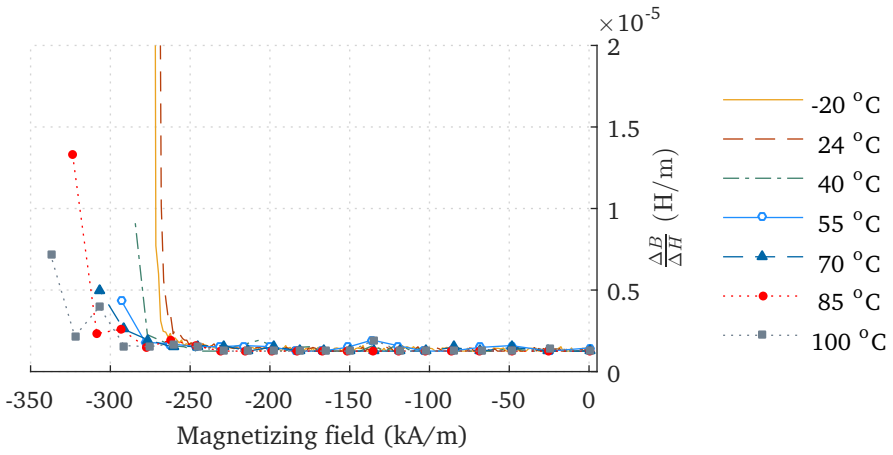

Figure 5.36: Differential permeability variation with magnetizing field of the ferrite magnet.

5.6.2 Estimation of demagnetization level of ferrite magnet in operating conditions

Ferrite magnets are more susceptible to demagnetization at lower temperatures and for this reason, the BH curve of ferrite magnet at $-20\,°C$ is used for demagnetization study. The 3D FE static analysis of design Fe-V2 is carried out for two values of peak armature currents 20 A and 200 A, corresponding to the full load and ten times the full load respectively. In [154], the authors proved that both anti-parallel and perpendicular field components to the direction of magnetization are necessary to accurately estimate the level of demagnetization. Therefore, $|H|$ and not $|B|$ field distribution is used in this study. Further, in [168], [169], the authors concluded that the edges and area of permanent magnet exposed to airgap are more susceptible to demagnetization than the inner volume. The demagnetizing field acting on the entire magnet disc is shown in the part (a) of Figure 5.37 and 5.38 and the field on a single pole is shown in the part (b) of the same figures. At ten times the rated current, 48 % of magnet volume is experiencing a demagnetizing field value more than $250\,kA\,m^{-1}$ and hence nearly half of the magnet disc will be demagnetized. It is clear from figures that at rated current only a small volume of magnet located in inter polar region will experience $|H|$ field approaching the critical value of $250\,kA\,m^{-1}$ for the presented design.

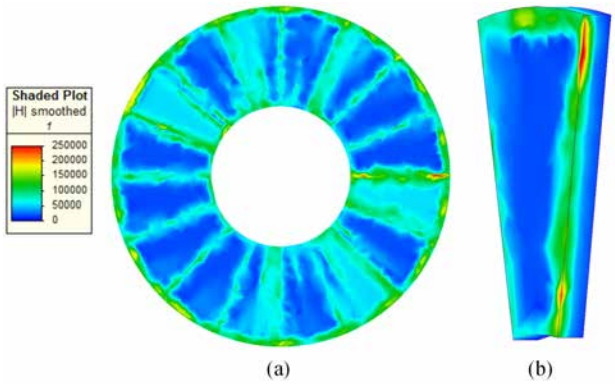

Figure 5.37: Demagnetizing field distribution for an armature current of 20 A in (a) 16-pole disc and (b) a pole.

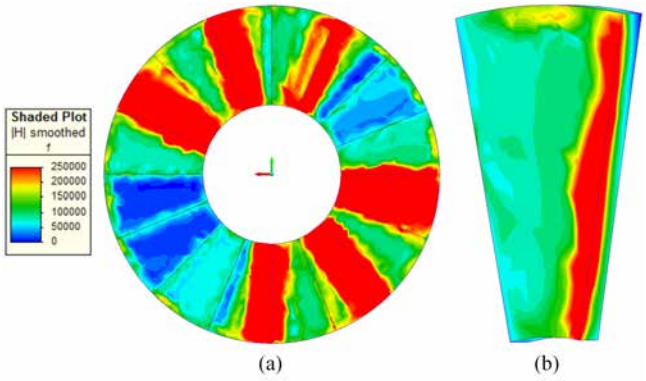

Figure 5.38: Demagnetizing field distribution for an armature current of 200 A in (a) 16-pole disc and (b) a pole.

5.6.3 Effect of temperature on performance of ferrite magnet motor

Besides the shift in knee point, the remanence also varies with temperature for the ferrite magnet as shown in Figure 5.35(b). The B_r diminishes by more than 10 % when temperature rises from $-20\,^{\circ}\mathrm{C}$ (the lowest ambient temperature considered) to a steady state magnet temperature under load (assumed to be between 55 to 70 °C), and this variation will have an impact on the motor performance.

As the rotor rotates, flux linkage variations will induce an EMF in the winding and the instantaneous EMF induced per phase is given by Eq. (5.6). The line-line EMF can be calculated from the instantaneous EMF induced per phase

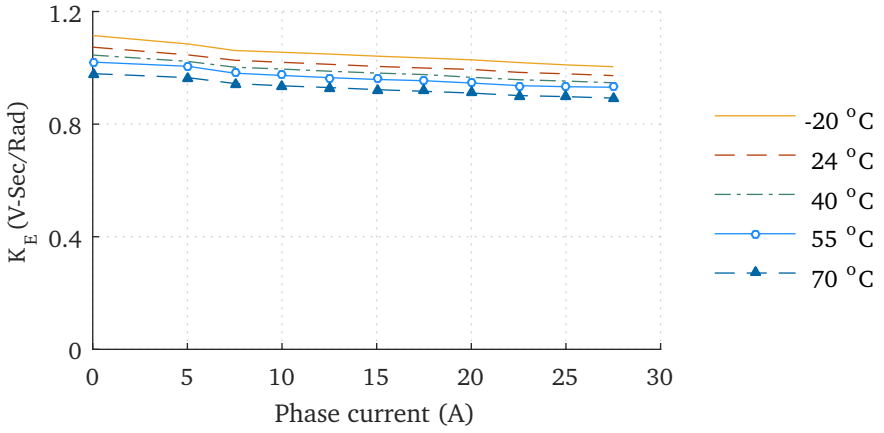

Figure 5.39: The variation of the EMF constant of design Fe-V2 with armature current for different magnet temperatures.

over 120° electrical as

$$\begin{aligned} E &= 2 \times mean(e) \\ &= 2 \times mean(\omega\psi'(\theta, i)) \\ &= 2 \times mean(\psi'(\theta, i)) \times \omega \end{aligned} \tag{5.30}$$

The EMF constant can be derived from the flux linkage variation by comparing Eq. (5.3) and Eq. (5.30) as

$$K_{\mathrm{E}} = 2 \times mean(\psi') \tag{5.31}$$

The variation of EMF constant of design Fe-V2 with armature current for different temperature, plotted in Figure 5.39, shows the effect of temperature on K.

The torque vs. speed characteristics of design Fe-V2 obtained from the simulation of dynamic model are shown in Figure 5.40(a). From Figure 5.40(a), it is clear that the motor operation beyond the base speed varies considerably with the magnet temperature and the maximum motor speed for a given load torque decreases with colder magnets. However, the presented design will meet the torque requirement for accelerating the vehicle to the top speed and maintaining the top speed up to a gradient of 3 % throughout the range of temperature considered in this study. The average value of the source current of the machine plotted against speed of the motor is shown in Figure 5.40(b).

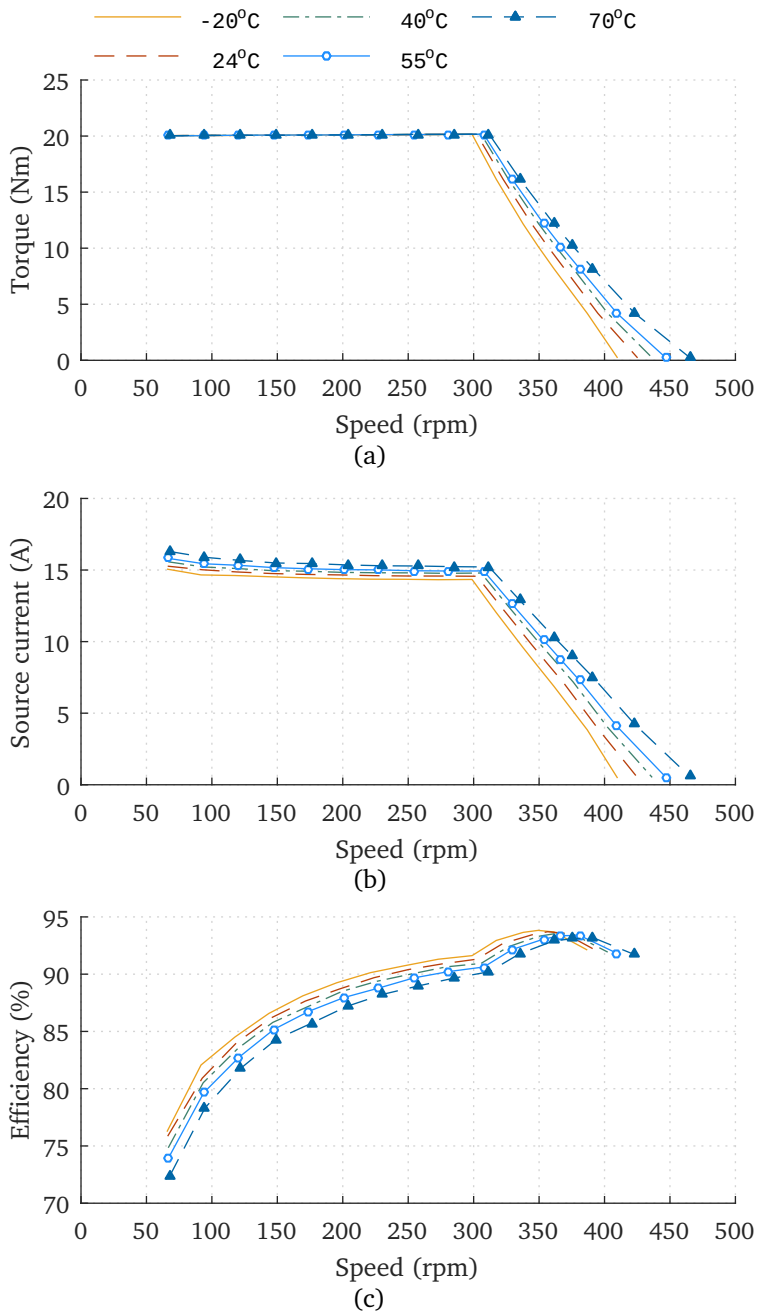

Figure 5.40: The temperature variation of performance characteristics of ferrite magnet SAT PMBLDC motor design Fe-V2 simulated using the dynamic model. (a) Torque vs. speed. (b) Source current vs. speed. (c) Efficiency vs. speed.

The weakened magnet field due to drop in remanence at higher temperature implies a reduced back EMF, which results in higher current throughout the speed range considered. The increased current at higher temperature gives rise to higher copper losses and reduced efficiency as shown in Figure 5.40(c). This trend reverses beyond the base speed as the torque increases with temperature for a given speed. This results in higher output power and hence, an improved efficiency in spite of drawing more current.

The impact of temperature dependence of ferrite magnet motor on system performance requires accurate modelling of power converters and controllers. The SAT PMBLDC motor discussed is designed for a low cost powertrain of electric two-wheelers and in such applications closed loop controls are not usually implemented because of the cost constraints. Nevertheless, the presented study with consideration of the motor alone can give controller designers a better outlook into the performance variation with temperature beyond the base speed, which will be helpful in designing a control strategy for mitigating perceived speed changes to the user.

5.7 Conclusions

This chapter presented a dynamic model of a PMBLDC motor that considers nonlinearities such as core losses and back EMF waveforms influenced by armature reaction. The model is computationally less demanding to the extent that it can be incorporated into a large-scale model of an electric drive system such as an electric vehicle.

The dynamic model is used to evaluate the performance of the bonded RE magnet motor and the ferrite magnet motor designed in Chapter 4 and found that the inductive voltage drop limits the maximum output power of both machines. The design program has been revised based on the finding from dynamic modelling of the designs to include the inductive voltage drop in design iterations. The performance evaluation of the designs generated using the revised design program found that both designs meet the powertrain specification for an electric two-wheeler identified in Chapter 3.

Knee points can appear in the second quadrant of demagnetisation characteristics of ferrite magnets. A method has been proposed to assess the extent of demagnetisation in magnets of a PMBLDC motor with the help of the ratio $\frac{\Delta B}{\Delta H}$. The method helps the designer to ensure that the designed ferrite

magnet motor is capable of working throughout the operating temperature, without any irreversible demagnetisation of magnets.

Ferrite magnets have a considerably higher temperature coefficient of remanence compared to RE magnets. The temperature dependent characteristics of ferrites have to be considered when designing ferrite magnet machines for applications such as electric powertrain where they are exposed to ambient temperature changes. The performance variation of the designed ferrite magnet motor has been simulated for temperatures starting from $-20\,^{\circ}\mathrm{C}$ to $70\,^{\circ}\mathrm{C}$, and it is found that the presented design will meet the torque requirement for accelerating the vehicle to the top speed and maintaining the top speed up to a gradient of 3 % over the entire temperature range.

The next chapter will discuss the fabrication of two prototype SAT PMBLDC motors, the first one with field poles made of a bonded RE magnet and the second one with field poles made of a ferrite magnet.

Chapter 6

Fabrication of prototype in-wheel motors

6.1 Introduction

The SAT topology of axial flux PMBLDC motor offers several performance advantages; however, the dual airgap assembly could cause constructional difficulties, especially when used as a direct drive in-wheel motor, such as maintaining the proper airgap dimensions and integrating the machine into the limited space available inside the wheel. Though many published works discuss the SAT topology [64]–[67], [170], [171], the discussion on fabrication was limited to making of the stator tooth. The complications while assembling the dual airgap axial flux machine and their solutions were not covered extensively in the literature. This chapter covers fabrication materials, the mechanical assembly adopted for the first prototype, construction of the first prototype, revisions in mechanical assembly of the second prototype based on learnings from the fabrication of the first prototype, and the building of the second prototype.

6.2 Mechanical assembly of SAT PMBLDC in-wheel motor

The mechanical assembly of the SAT PMBLDC in-wheel motor has been designed with following objectives

1. Limit variations in electromagnetic dimensions to a minimum in all conditions of the motor, i.e., running and stationary,
2. Safe operation of the direct drive in-wheel motor, and
3. Easier assembly, dismantling and reassembly of the motor.

Maintaining quality control over fabrication of components of the machine can limit the variation of most electromagnetic dimensions. However, the axial airgap could change while assembling the motor or over a period of running because of the mechanical weakening of either the bearing or the stator structure, as they have to withstand magnetic forces between magnet and stator tooth. The presence of uneven airgap either in static or dynamic condition can cause excessive force on the rotor and the stator, and could lead to noise and vibration [172], [173]. The SAT motor will be an unsprung mass added to the rear axle and therefore, all disturbances and shocks caused by vehicle movement will appear in the machine without any damping. Therefore, the mechanical structure should have enough strength to withstand any deformation caused by forces that can appear when the vehicle moves. The magnetic forces complicate the assembly of magnetized permanent magnet motor. Moreover, SAT motors require accurate alignment of north-south poles on each side of the stator. Therefore, the motor components should have profiles and guides to minimise the chances of incorrect assembly.

The mechanical design of radial flux PMBLDC in-wheel motor from vehicle-1 is used as a guideline for the component design of SAT PMBLDC motor because the detailed mechanical design study required for a traction motor is beyond the scope of this work. The following part of this section will describe each component of the SAT PMBLDC motor and how they are assembled.

6.2.1 The stator assembly of SAT PMBLDC in-wheel motor

The stator consists of a shaft, a pair of hubs, tooth holders, eighteen segmented stator tooth, and nine coils. An assembled view and an exploded view of the

stator is shown in Figure 6.1. The list of materials of the stator components is given in Table 6.1. The assembly of stator will start by fitting both hubs on

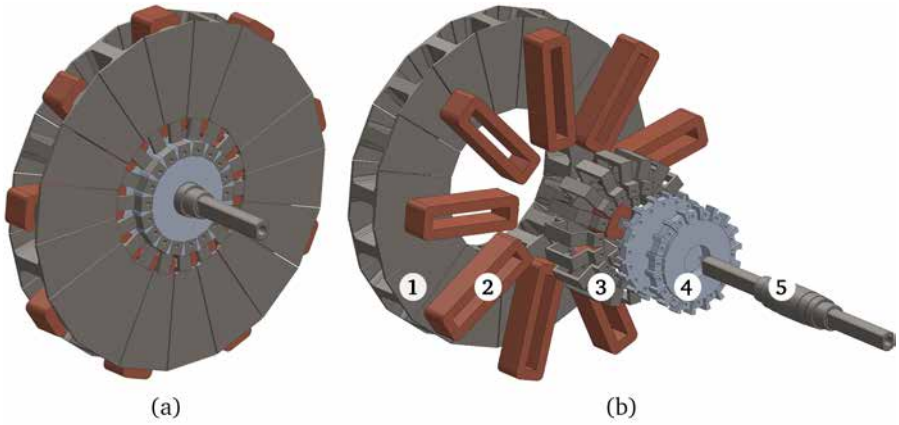

Figure 6.1: The stator assembly of SAT PMBLDC in-wheel motor. (a) Complete stator assembly. (b) Exploded view (1. Segmented stator tooth, 2. coils, 3. tooth holder, 4. spider, and 5. shaft).

Component	Material
Stator tooth	Non-oriented fully processed silicon steel (Grade: M400-50A)
Stator coil	Copper
Tooth holder	Stainless steel (Grade:303)
Spider	Aluminium (Grade:6061-T6)
Shaft	Steel (Grade:ISO 683/II Type 3)

Table 6.1: The materials used in the fabrication of the stator components of SAT PMBLDC motor prototype.

the shaft via thermal shrinking. The positioning of the hubs on the shaft will decide the axial airgap distance, and stepped profiles shown in Figure 6.2 are provided on the shaft to ease the assembly. The hubs are made in two pieces using aluminium to save the weight.

The stator tooth will be made using wire electrical discharge machining (EDM) of pre-bonded lamination materials. Finished stator tooth will be bonded to a stainless steel tooth holder using adhesives as shown in Figure 6.3(a). Afterwards, the coil will be wound around nine teeth as shown in Figure 6.3(b). The stator assembly will be completed by placing the segmented tooth and holder assembly into the slots provided on hubs, and kept in place with the

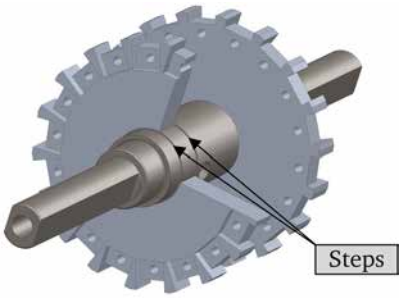

Figure 6.2: Assembly of the shaft and the spider of SAT PMBLDC motor. The steps are provided to maintain the airgap distance as well as to ease the assembly.

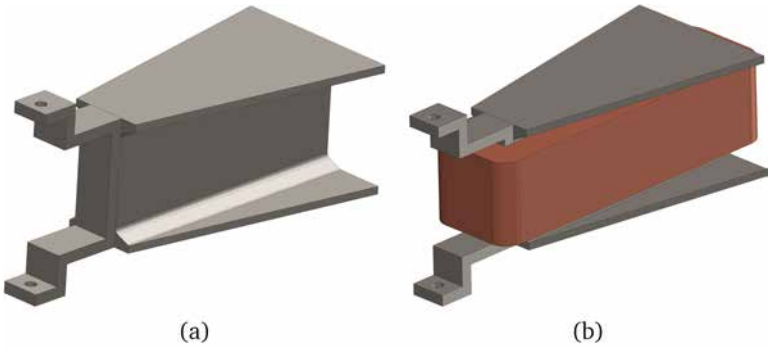

Figure 6.3: The stator tooth assembly of SAT PMBLDC motor. (a) A stator tooth with a tooth holder. (b) An assembly of a wound stator tooth.

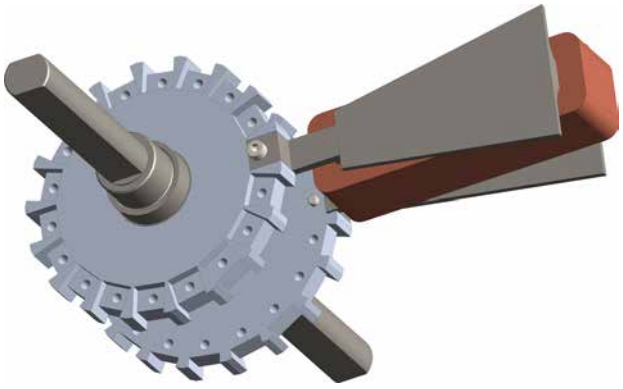

Figure 6.4: Assembly of the segmented stator tooth to spider of a SAT PMBLDC motor.

help of a pair hex bolts as shown in Figure 6.4. The proposed stator assembly is selected after considering many variations because the configuration does

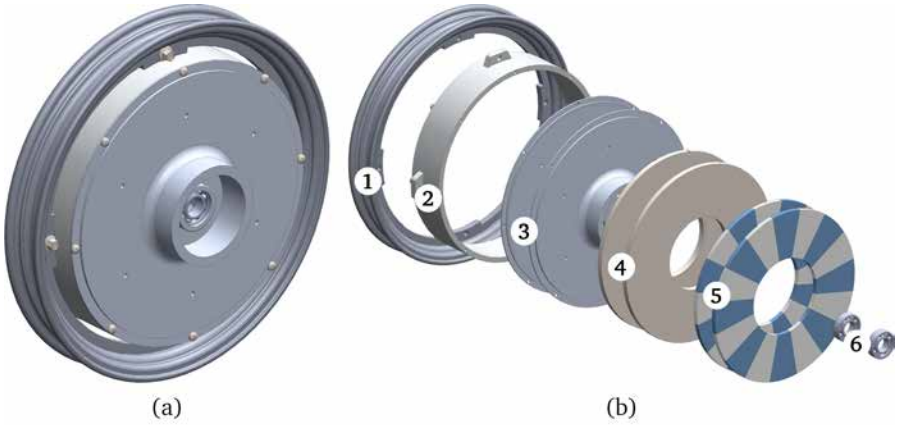

Figure 6.5: The rotor assembly of SAT PMBLDC in-wheel motor. (a) Complete rotor assembly. (b) Exploded view (1. Wheel rim, 2. spacer, 3. end covers, 4. rotor yokes, 5. rotor poles, and 6. bearings.).

Component	Material
Rotor poles	Bonded RE magnet (Grade:NDB-6)
Rotor yoke	Soft iron (Grade:16MnCr5)
End covers	Aluminium (Grade:6061-T6)
Spacer	Aluminium (Grade:6061-T6)
Wheel rim	Aluminium casting

Table 6.2: The materials used in the fabrication of the rotor components of bonded magnet SAT PMBLDC motor prototype.

not require modification of electromagnetic structure, and the resultant motor assembly is very compact along the axial length. Further, the assembly makes it easier to access and replace the individual coil in case of a winding fault.

6.2.2 The rotor assembly of SAT PMBLDC in-wheel motor

The rotor of SAT PMBLDC in-wheel motor consists of sixteen poles on each side of the rotor, a pair of yokes, a couple of end covers, a spacer, a wheel rim, and a pair of bearings. The complete assembly of the rotor and its exploded view is shown in Figure 6.5. The list of materials of the rotor components is given in Table 6.2.

A critical aspect of the rotor assembly is ensuring the north-south orientation of rotor poles facing each other. The magnet is glued to the rotor yoke

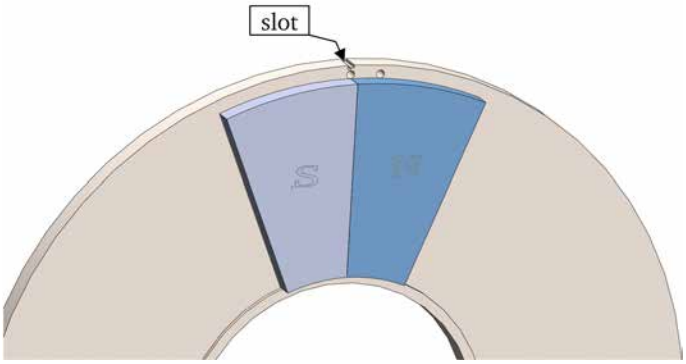

Figure 6.6: The rotor pole and yoke assembly: the first north pole is glued by aligning its straight edge with long edge of the asymmetric slot on the yoke and the face towards the second hole.

using the slot and holes provided on the yoke as a guide, as shown in Figure 6.6, to ensure that an identical set of yoke and pole assembly could be created. The completed assemblies of rotor poles and yoke will be screwed to end covers using holes provided along line-1 of Figure 6.7. The threaded holes on the yoke will be made in such a way that the asymmetric slot on the yoke, shown in Figure 6.6, will be radially aligned with hole-1 of the yoke shown in Figure 6.7. Afterwards, end cover assemblies will be screwed to the spacer along line-2 as shown in Figure 6.7. Hole-1 for spacer and hole-1 for yoke are radially aligned, and this ensures that the rotor poles on the left side of the spacer will be a mirror image of the rotor poles on the right side of the spacer, resulting in the required north-south orientation of poles facing each other. Each end cover will be press fitted with a single row deep groove ball bearing at the centre.

6.2.3 Whole assembly of in-wheel motor

The mechanical assembly of the motor starts with the mounting of the wheel rim on the spacer. The spacer will be then screwed to one of the end covers fitted with rotor poles and yoke. Afterwards, the stator will be placed inside the spacer. In the last phase of the assembly, the second end cover with rotor poles and yoke will be screwed onto the spacer as shown in Figure 6.7. A sectional view of the whole assembly and an exploded view of sub-assemblies of SAT PMBLDC motor is shown in Figure 6.8. The fabrication drawings of all components of the bonded RE magnet SAT PMBLDC motor are listed in

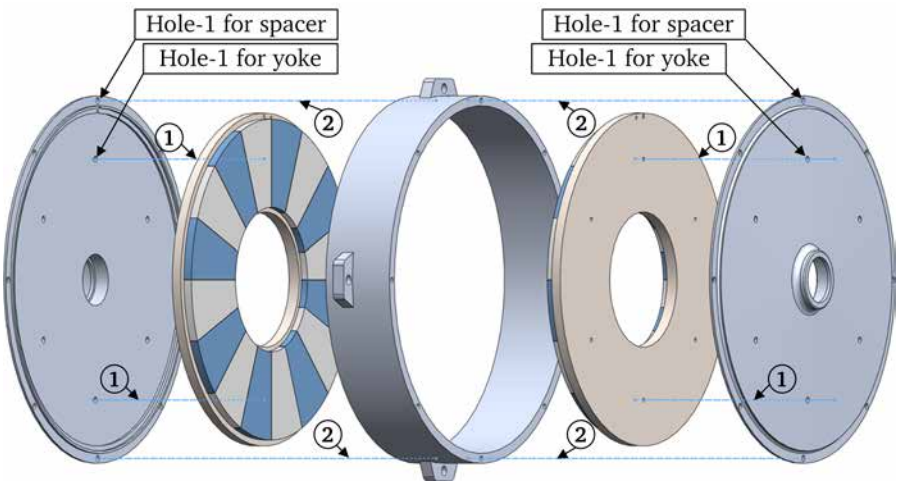

Figure 6.7: The exploded view of the rotor assembly of SAT PMBLDC motor. The rotor yoke and poles assembly will be screwed to the end cover along line-1, and the end covers will be screwed to the spacer along line-2.

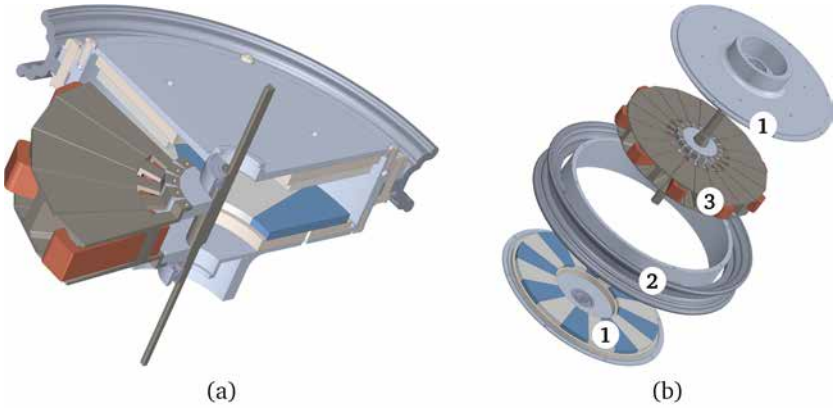

Figure 6.8: Mechanical assembly of SAT PMBLDC in-wheel motor. (a) Section view. (b) Exploded view of sub-assemblies (1. End cover and rotor poles, 2. wheel rim and spacer, and 3. stator).

Appendix E.

The stator tooth will experience the maximum force during the assembly when the stator is placed inside the rim connected with only one rotor because there is no counteracting force from the open side where the other rotor will be placed. The electromagnetic FE analysis is used to find the force on the tooth when there is only one rotor as shown in Figure 6.9(a), and the force

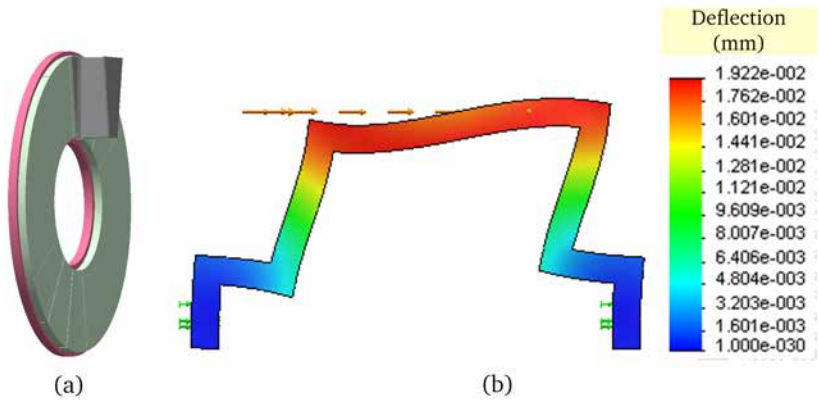

Figure 6.9: Estimating deflection of tooth holder of SAT PMBLDC motor. (a) Electromagnetic FE Model for calculating unbalanced force with rotor kept only one side. (b) Deflection in mm obtained from the structural analysis for a force twice the magnitude of the unbalanced force.

is found to be 94 N. Subsequently, a structural analysis is carried out with a force twice the estimated value, and the result is shown in Figure 6.9(b). The maximum deflections are around 20 μm at the inner diameter and 45 μm at the outer diameter of the stator; however, the axial airgap length is 400 μm.

6.3 Construction of bonded RE magnet motor

The bonded RE magnet machine was constructed first because the successful demonstration of the ferrite magnet machine was an important project deliverable. The approach will help to use the learnings from the fabrication of the first prototype to improve the mechanical design of the second prototype. This section will discuss the fabrication of the bonded magnet motor based on the mechanical design presented in Section 6.2.

The wire EDM of pre-bonded laminations was the preferred fabrication technique for the segmented stator tooth; however, budgetary constraints forced to go for wire EDM of riveted laminations. Two non-magnetic screws connect the tooth holder to the stacked tooth because the rivet joints prevented using adhesives. The fabricated tooth and tooth holder assembly, as well as wound coil, is shown in Figure 6.10, and the completed shaft is given in Figure 6.11. The hub of the machine is made of aluminium using CNC machining. The stator without coils are assembled to see the variations from the specified tol-

Figure 6.10: The segmented stator tooth with and without coil.

Figure 6.11: The finished shaft of the bonded magnet SAT PMBLDC motor.

erances, and the assembly is shown in Figure 6.12. The deviation of the axial length was less than 200 μm. However, there was considerable variation in slot openings, which can also be seen from Figure 6.12. The condition of stator was judged robust; therefore, the coil winding and the assembly of the stator are completed.

In the next stage, assembling bonded RE magnet poles on two rotor yokes is completed, and one of the two finished assemblies is shown in Figure 6.13. The yokes with rotor poles are screwed to the end covers, and later a bear-

Figure 6.12: The stator assembly of the bonded RE magnet SAT PMBLDC motor without winding.

Figure 6.13: The finished assembly of the bonded RE magnet poles and rotor yoke.

ing was installed to complete the end cover assembly. Subsequently, one of the end cover assemblies is attached to the spacer with wheel rim, and the finished stator assembly is inserted inside the spacer. The bonded RE magnet motor assembly right after the stator is inserted into the spacer is shown in Figure 6.14. In the final stage, the second end cover assembly was attached to

the spacer to complete the motor assembly.

In the completed RE magnet motor assembly, the rotor was not moving, and the examination of the structure found that the stator was not rigid enough to withstand the magnetic forces. The weak link was identified as the joint between the segmented tooth and the tooth holder. The rotor was moving freely without any rubbing after the following modifications

1. The stator is strengthened by filling resin in all tooth openings. The disadvantage of the solution is that the gluing will join all stator teeth, and they cannot be taken out in the event of a winding fault.

2. The airgap is enlarged by placing washers between the spacer and both end covers.

The strengthening of the stator is done by axially aligning all teeth and filling resin as shown in Figure 6.15. The completed assembly of the bonded RE

Figure 6.14: The bonded RE magnet SAT PMBLDC motor motor assembly right after the stator is inserted into the spacer with an end cover assembly.

Figure 6.15: Applying resin to the aligned stator of the bonded RE magnet motor.

magnet SAT PMBLDC motor is shown in Figure 6.16. The motor was rotated by increasing the speed slowly, and it is concluded that the motor assembly is not safe either to take any load or to rotate at speeds higher than 10 rpm.

The major observations and learnings from the fabrication of the bonded RE magnet motor are

- Though tooth holder shape of the bonded magnet motor helped to implement the electromagnetic design with no changes, it was very tedious to manage and place terminal leads of coils and hall sensors in between two hubs.

Figure 6.16: The fabricated prototype of bonded RE magnet SAT PMBLDC motor.

- The outer diameter of the end cover was made larger than that of the spacer to ease the assembly and dismantling with the help of wedges; however, the use of wedges was causing damages to the edges of the end plate.
- The threads created on aluminium hubs and spacers were susceptible to damages.

6.4 Revised of mechanical assembly of SAT PMBLDC motor

The mechanical assembly of SAT PMBLDC motor proposed in Section 6.2 has been revised to overcome the limitations identified after fabricating the bonded RE magnet motor. This section discusses changes made to the stator tooth, the tooth holder, the hub and the end cover.

The existing and the modified assemblies for attaching the segmented tooth to the shaft via a hub are shown in Figure 6.17. Further, an exploded view of the revised design is shown in Figure 6.18. The revised design offers benefits such as increased resistance to stator flexing and easier handling of lead wires.

Further, the hub is made of steel and therefore, threads for the screws will be considerably more durable than the threads made on an aluminium hub. The revised assembly requires modification of the electromagnetic design, especially the stator tooth. The hole for the tooth holder is created in such a way that the area available for the flux to flow will remain same throughout the tooth. The stator coils are not occupying the space around the tooth holder resulted in a lower gross fill factor for the revised design. The fabrication drawings of all components of the ferrite magnet SAT PMBLDC motor are listed in Appendix E.

The assembly process starts by fitting the hub on the shaft via thermal shrinking. The tooth holders will be screwed to the hub, and laminated teeth with and without coils will be inserted into the holders. A washer and a bolt will keep the tooth in position. The rotor assembly is similar to the earlier structure except for the increase in the thickness of end plates and the addition of threaded holes in between the holes for screws that connects the end plate assembly to the spacer as shown in Figure 6.19. Screws inserted in threaded holes will substitute the wedges while assembling or dismantling of the prototype. An exploded view of the revised assembly of SAT PMBLDC motor is shown in Figure 6.20. The electromagnetic FE analysis is used to find the force on the tooth when there is only one rotor and the force is found to be 70 N. Subsequently, a structural analysis is carried out with a force twice the estimated value, and the result is shown in Figure 6.21. The maximum deflection is around 100 μm at the outer diameter of the stator; however, the axial airgap length is 400 μm.

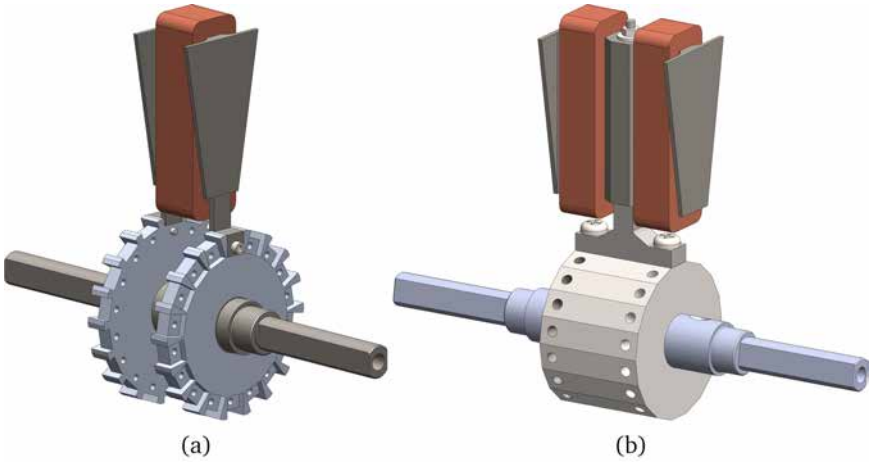

Figure 6.17: The assembly of a segmented stator tooth and hub. (a) The bonded RE magnet SAT PMBLDC motor. (b) The ferrite magnet SAT PMBLDC motor.

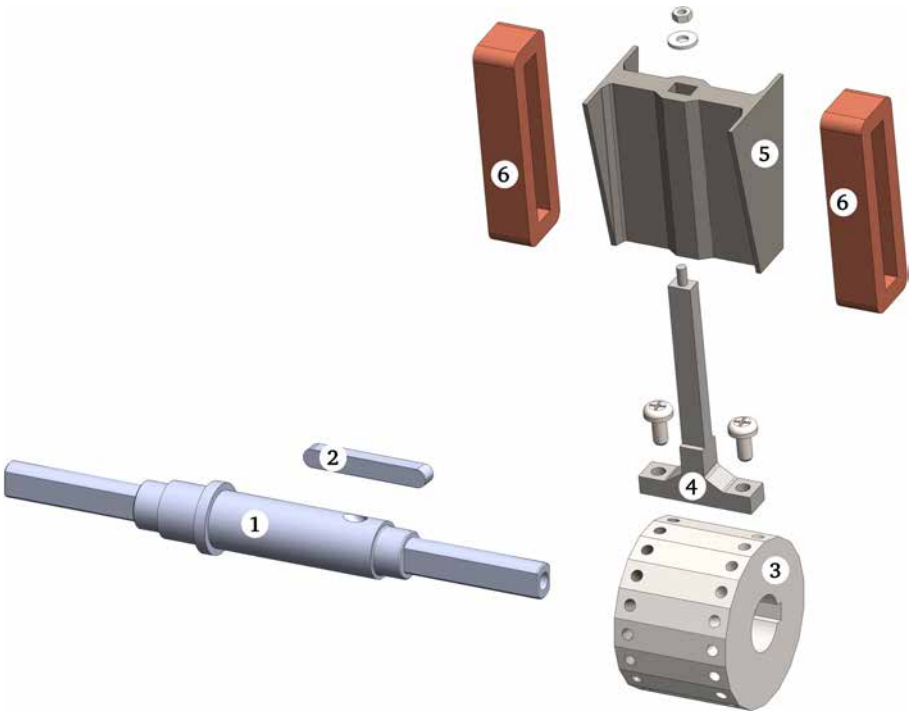

Figure 6.18: The exploded view of the revised design of assembly for mounting segmented stator tooth (1. Shaft, 2. shaft key, 3. hub, 4. tooth holder, 5. segmented stator tooth, and 6. coils).

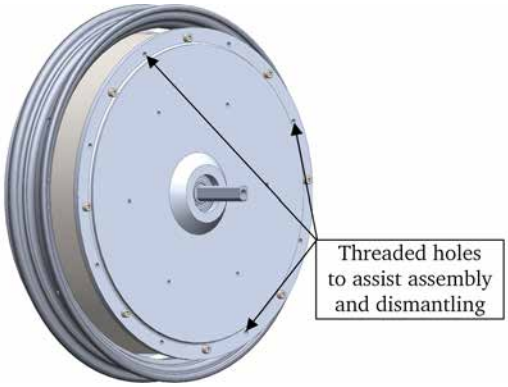

Figure 6.19: Threaded holes to ease the assembling and the dismantling of the SAT PMBLDC motor.

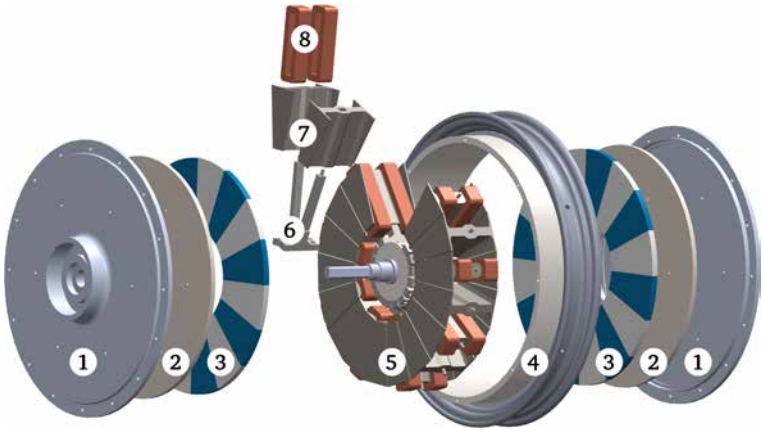

Figure 6.20: The exploded view of the revised assembly of SAT PMBLDC motor(1. End cover, 2. rotor yoke, 3. magnet poles, 4. wheel rim with spacer, 5. stator, 6. tooth holder, 7. segmented tooth, and 8. coils).

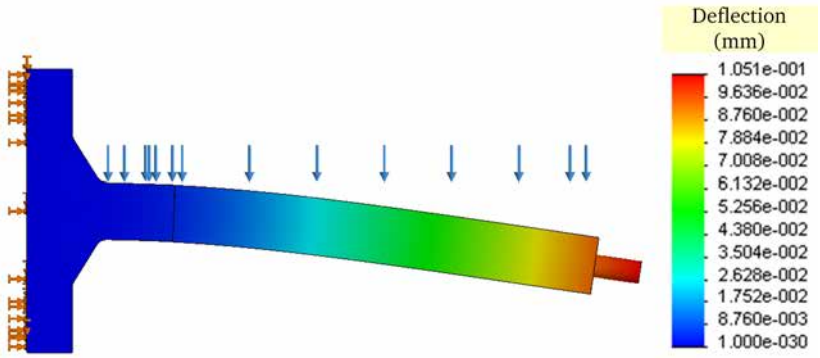

Figure 6.21: Estimated deflection of the revised tooth holder corresponds to twice the magnitude of unbalanced force expected during the assembly.

6.5 Construction of ferrite magnet motor

The stator tooth of the ferrite magnet SAT PMBLDC motor is made using laser cut laminations. The laminations are stacked and glued in a mould, and the completed tooth is shown in Figure 6.22. The stator tooth is wound with 30 turns of stranded copper wire as shown in Figure 6.23. The shaft, the hub, and a tooth holder of the ferrite magnet SAT PMBLDC motor is shown in Figure 6.24. The stator assembly starts with heating of the hub and allowing it to shrink onto the shaft, once the hub is in position tooth holders and teeth are attached. An image of the partially completed stator is shown in Figure 6.25, and the completed stator is shown in Figure 6.26. The slots for hall sensors are cut on the completed stator, and an image captured while machining the stator for creating the hall sensor slots is shown in Figure Figure 6.27. The hall sensors mounted on the stator surface is shown in Figure 6.28.

The ferrite magnet poles are glued to the rotor yoke surface to create the rotor pole and yoke assembly, and the completed assembly is shown in Figure 6.29. The sintered ferrite magnet poles had considerable variations in their thickness, and this resulted in an uneven surface variation of the rotor disc assembly as shown in Figure 6.30. Both airgaps of the ferrite magnet SAT PMBLDC motor has been increased to 2 mm, to accommodate uneven surface variations of finished rotors. The end cover and the spacer with the wheel are attached to the rotor disk in successive steps as shown in Figure 6.31 and Figure 6.32. Afterwards, the stator is inserted into the spacer as shown in Figure 6.33, and the completely assembled motor is shown in Figure 6.34. The dimensions of the fabricated shaft were marginally smaller than the dimensions specified in the part drawing, and this was causing the stator to move towards rotor poles. The stator is kept in position by drilling a threaded hole through the hub to the shaft and screwing the hub and the shaft together.

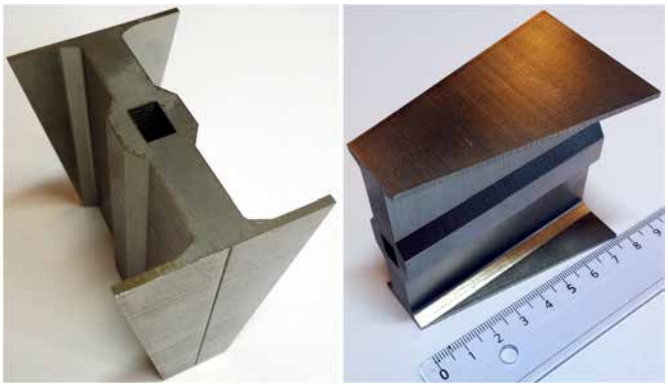

Figure 6.22: The stator tooth of the ferrite magnet SAT PMBLDC motor.

Figure 6.23: The stator tooth of the ferrite magnet SAT PMBLDC motor wound with 30 turns of stranded coper wire.

Figure 6.24: The shaft, the hub, and a tooth holder of the ferrite magnet SAT PMBLDC motor.

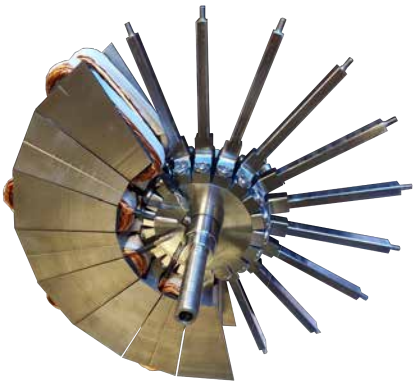

Figure 6.25: Assembling the stator of the ferrite magnet SAT PMBLDC motor.

Figure 6.26: The completed stator assembly of the ferrite magnet motor.

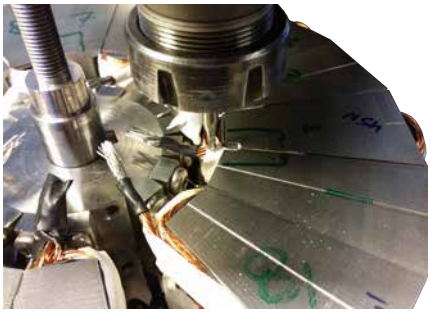

Figure 6.27: Creating slots for hall sensors on the completed stator assembly of the ferrite magnet SAT PMBLDC motor.

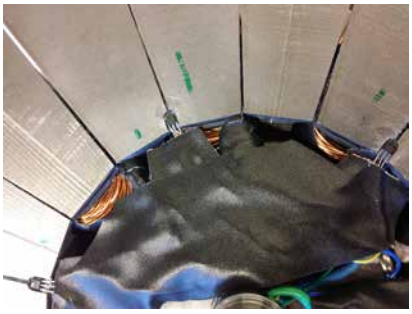

Figure 6.28: Hall sensors on the stator surface of the ferrite magnet SAT PMBLDC motor for rotor position sensing.

Figure 6.29: The ferrite magnet poles and rotor yoke assembly of the SAT PMBLDC motor.

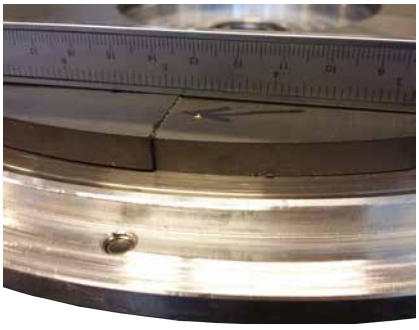

Figure 6.30: Uneven surface variation of ferrite magnet rotor caused by the manufacturing variations in the thickness of the sintered ferrite magnet.

Figure 6.31: The end cover of the ferrite magnet SAT PMBLDC motor with the rotor attached.

Figure 6.32: The rotor wheel and spacer assembly of the ferrite magnet SAT PMBLDC motor with attached end cover.

Figure 6.33: The ferrite magnet SAT PMBLDC motor assembly right after the stator is inserted into the spacer with an end cover assembly.

Figure 6.34: The fabricated prototype of ferrite magnet SAT PMBLDC in-wheel motor.

6.6 Installation of SAT PMBLDC motor in electric two-wheeler

The ferrite magnet SAT PMBLDC motor prototype has been assembled on the frame of vehicle-1 and the completed vehicle is shown in Figure 6.35. The battery of the vehicle is placed under the seat, and the battery specification is listed in Table 6.3. A commercially available PMBLDC controller drives the motor, and the controller is located between foot pegs.

Figure 6.35: The ferrite magnet SAT PMBLDC motor installed in a two wheeler.

Specification	Value
Battery type	Li-Mn
Rated voltage	48.75 V
Capacity	10 A h
Energy	480 W h

Table 6.3: The specification of battery of the electric two wheeler.

6.7 Conclusions

This chapter discussed the fabrication of SAT PMBLDC motor prototypes. Two different assembly designs of SAT PMBLDC motor are presented and studied using 3D models. The first assembly is implemented in the fabrication of

bonded RE magnet motor, and the prototype has issues such as stator flexing and difficulty to manage the lead wires of the coils and the sensors. The second assembly of SAT PMBLDC motor addresses limitations of the first prototype, and it is used in the fabrication of the ferrite magnet SAT PMBLDC motor. The operation of the first prototype is found to be restricted by its weak structure, and therefore, only the second prototype is installed in the electric two-wheeler. The next chapter will discuss the testing of the prototypes and vehicles to evaluate their performance.

Chapter 7

Experimental results

7.1 Introduction

One of the objectives of this research is to explore the use of ferrite magnets as a substitute for RE magnets in low-speed high-torque machines. A ferrite magnet SAT PMBLDC motor, which will be used as a direct drive powertrain in a moped, is designed and fabricated as a part of this investigation. Extensive testing of the ferrite magnet motor is carried out to compare its performance with the other motors that are part of the study, and to evaluate the reliability of the ferrite magnet in a real world application.

As the work aimed to fabricate an in-wheel motor for an electric moped, it is important to carry out tests that will help

- To understand the interior thermal conditions of the in-wheel motor,
- To evaluate the performance of the motor against a controlled load, and
- To assess the performance of the motor as a powertrain of the vehicle.

The main tests that were carried out on the motors are

1. Thermal performance test,
2. Back EMF test,
3. Performance evaluation under a constant load torque for different rotational speeds, and
4. Driving cycle test, after connecting each motor to the moped.

Practical difficulties limited evaluating all four motors using all four tests, and Table 7.1 lists the type of test conducted on each motor. The bonded RE magnet motor has been tested for back EMF only because of issues with the structural integrity of the prototype. The thermal test was not conducted on the ferrite magnet motor because of the lack of space inside the shaft for thermocouple lead wires. Yamaha EC-03, which is named as vehicle-4, has a powertrain consists of a single airgap axial flux motor with stator integrated into the vehicle body, therefore, only driving cycle test was conducted.

Motors tested	Type of tests			
	Thermal	Back EMF	Test bench performance	Driving cycle
Sintered RE magnet radial flux motor of vehicle-1	✓	✓	✓	✓
Bonded RE magnet SAT PMBLDC motor of vehicle-2	×	✓	×	×
Ferrite magnet SAT PMBLDC motor of vehicle-3	×	✓	✓	✓
Axial flux motor of vehicle-4	×	×	×	✓

Table 7.1: Lists of tests performed on the group of motors used in the study

This chapter discusses different tests carried out on motors and a comparative study of test results of the motors.

7.2 Experimental setup for testing of in-wheel motors using a stationary load

In hub motors, the stator is attached to a non-rotating shaft via spider and the wheel, which houses one or more rotor core and magnets, is connected to the shaft with the help of a set of end plates and bearings. Testing of a hub motor on a stationary test bench requires a different arrangement compared to an internal rotor motor because the external casing transfers the generated torque, not the shaft. The test bench used to carry out thermal, back EMF,

and performance tests on hub motors in this study is shown in Figure 7.1. The test bench consists of a four-quadrant drive, speed reduction gears to match the speed of the drive to the speed of the hub motor, and a sensor to measure torque and speed. A self-centring three-jaw chuck connects the casing of the hub motor and the shaft of the test bench. The shaft of the hub motor is held stationary by a mount that is bolted to the base plate.Another view of test bench taken while testing the ferrite magnet SAT PMBLDC motor prototype is shown in Figure 7.2.

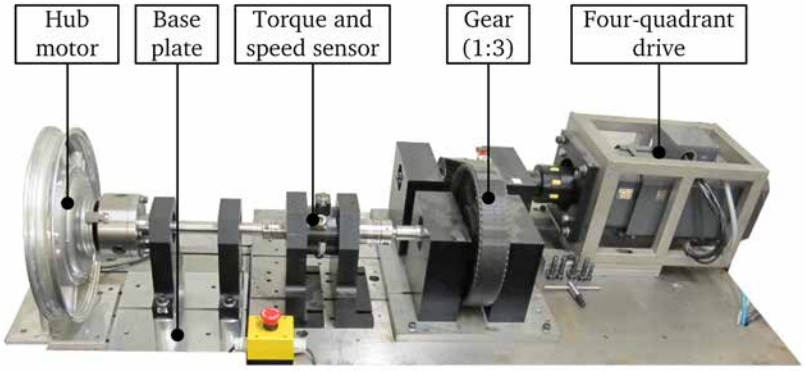

Figure 7.1: Test bench used to carry out thermal, back EMF, and performance test on hub motors.

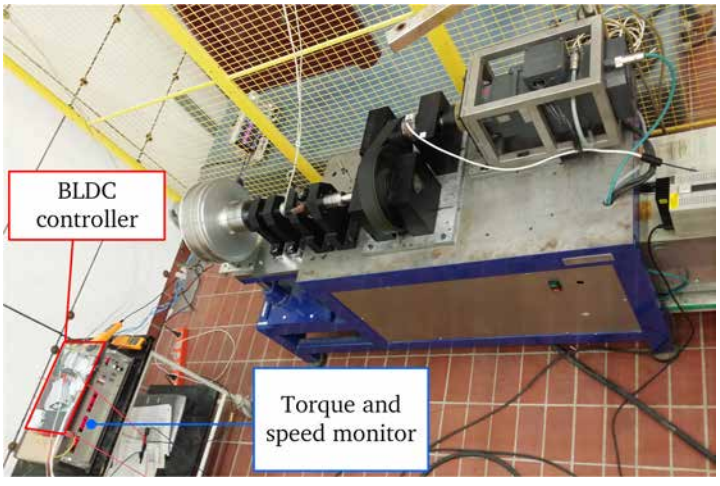

Figure 7.2: The performance test of ferrite magnet SAT PMBLDC motor prototype on the test bench.

The four-quadrant drive can act as a prime mover with an accurate speed control for carrying out the back EMF test or serve as a constant torque load that will feed the power back to the supply from the test bench when the hub motor drives it.

7.3 Thermal performance evaluation of in-wheel motors

In a surface magnet PMBLDC machine, most of the losses are produced in the stator. The heat generated from the losses has to have a good path to the outer casing, and any increase in resistance to the heat flow will increase the temperature of the winding and other components of the machine. In an internal rotor machine, the heat flows from the stator to the motor frame via conduction through the stator core, and relatively large surface area of the motor frame will ease the convective heat dissipation to the surrounding air.

In SAT PMBLDC motor, the stator is placed between two rotors, and only a path through the shaft and bearings is available for conductive heat transfer to the rotating casing. Therefore, in contrast to internal rotor machines, convective heat transfer between the stator and the rotor plays a major role in dissipating the losses of external rotor motors. Consequently, the rotor poles forms a part of the path that carries most of the heat from the stator of an external rotor surface permanent magnet machine. In a ferrite magnet machine, characteristics of the magnet are highly influenced by its operating temperature, and therefore, it is important to estimate the operating temperature of the rotor poles of the ferrite magnet SAT PMBLDC motor.

In this work, an FE thermal model is used to predict the temperature of components of the ferrite magnet SAT PMBLDC motor corresponding to the maximum output power. Initially, an FE thermal model of the radial flux external rotor PMBLDC motor from vehicle-1 is developed, and the thermal model is validated with the help of temperature data obtained from the machine. A similar approach to the radial flux motor is followed while developing an FE thermal model of SAT PMBLDC motor; however, the necessary corrections are made to account the change in topology of the machine. The entire thermal study was completed before fabricating the ferrite magnet motor prototype.

The sintered RE magnet motor from vehicle-1 has a continuous rating of 750 W, and a short-term peak rating of 1200 W. The exploded view of the

motor is shown in Figure 7.3. The stator, consist of a stator core and an arma-

Figure 7.3: Exploded view of the radial flux sintered RE magnet motor of vehicle-1 (1. End plate, 2. rim, 3. rotor core, 4. magnet, 5. winding, 6. stator core, 7. spider and 8. non rotating shaft).

ture winding, is attached to a non-rotating shaft via spider. The wheel houses the rotor core and magnets, and they are connected to the shaft via two end plates and a pair of bearings. An airgap of 0.5 mm separates the stator core and magnets.

The following part of the section will discuss FE thermal model of an external rotor radial flux PMBLDC motor, comparison of thermal model and test results, and FE thermal model of the ferrite magnet SAT PMBLDC motor.

7.3.1 Finite element thermal model of radial flux outer rotor PMBLDC motor

In thermal FE model, partial differential equations are solved numerically for a thermal network. The meshed FE model of the PMBLDC hub motor is shown in Figure 7.4. The model uses geometrical symmetries to reduce the simulation time. The commercial software package ThermNet™is used for solving the thermal model. Losses are modelled by applying the resistive loss density to the coil and the core loss density to the stator core. The resistive loss is calculated as

$$P_{\mathrm{r}} = mI_{\mathrm{ph}}R^2 \tag{7.1}$$

where, m is the number of conducting phases and I_{ph} is the RMS value of the phase current. The resistance varies with temperature and can be calculated

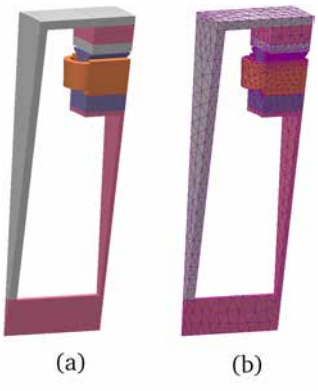

Figure 7.4: The FE thermal model of the radial flux PMBLDC hub motor simplified using the geometrical symmetry. (a) Simplified 3D geometry. (b) FE mesh.

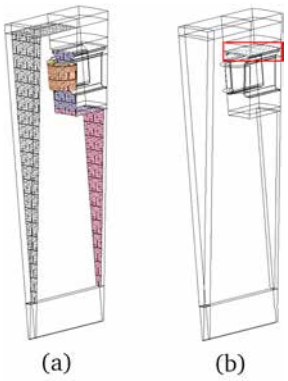

Figure 7.5: Internal convective heat transfer regions of the radial flux PMBLDC hub motor. (a) End space. (b) Airgap.

from a known resistance at another temperature as [55]

$$R_{T_2} = R_{T_1}\left(\frac{234.5 + T_2}{234.5 + T_1}\right) \tag{7.2}$$

where, R_{T_1} and R_{T_2} are resistances at temperatures T_1 and T_2 °C respectively. The sintered RE magnet motor considered here has coils with a turn diameter of 0.5 mm. Therefore, the ac effects such as skin, proximity and circulating current are not considered. The core losses are estimated individually for stator teeth and yoke as the field variations in them are different [174]. The loss per unit mass due to hysteresis p_{h}, eddy current in stator yoke p_{ey}, and eddy current in stator tooth p_{et} are calculated as [174]

$$p_{\mathrm{h}} = K_{\mathrm{h}} f^{\alpha} B_{\mathrm{m}}^{\beta} \tag{7.3}$$

$$p_{\mathrm{ey}} = K_{\mathrm{e}} \frac{8}{\pi} \frac{f^2 B_{\mathrm{m}}^2}{\beta_{\mathrm{m}}} \tag{7.4}$$

$$p_{\mathrm{et}} = K_{\mathrm{e}} \frac{4}{\pi} \frac{f^2 B_{\mathrm{m}}^2}{\alpha_{\mathrm{ta}}} \left(2 - \frac{\pi - \beta_{\mathrm{m}}}{\alpha_{\mathrm{ta}}}\right) \tag{7.5}$$

where f is the frequency of flux variation, B_{m} is the peak flux density, and α_{ta} and β_{m} are the tooth arc and the pole arc respectively in electrical radians. Internal convective transfer of heat through the airgap and the end space, shown in Figure 7.5, are modelled using experimentally derived empirical equations

with geometrical dimension and thermal properties of cooling media as parameters [175]. Vertical plate and horizontal cylinder analogies are used to model the convective heat dissipation from the motor casing. The bearing is modelled using an equivalent thermal gap, described by Staton et al. [176].

Thermal testing of radial flux hub motor

The test bench described in Section 7.2 is used for the thermal testing of the hub motor. Thermocouples are mounted in the slot, on the winding overhang, and on the stator core surface of the hub motor to capture the winding and core temperature. The temperature of the external casing was monitored using a thermal camera. The machine is run as a generator using the four-quadrant drive and is loaded using a resistor bank. The temperatures are recorded for every one second, and experiment is stopped when the temperature variation of winding over ten minutes was less than 0.5 °C.

FE thermal model validation of radial flux motor with test data

The thermal test has been conducted for three load steps, and a comparison of temperatures of winding and core obtained from the test and the steady-state analysis of FE thermal model is shown in Figure 7.6. The experimental and

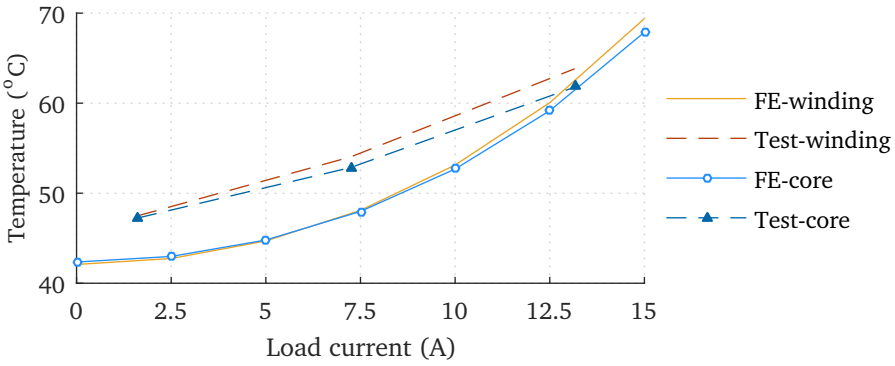

Figure 7.6: The steady-state temperature variation of winding and stator core of the sintered RE magnet radial flux hub motor for different load current.

the simulated temperatures differ more under lighter load condition than at higher load, and the difference could be because of under-estimation of constant losses such as core, windage, and friction losses. As the load increases,

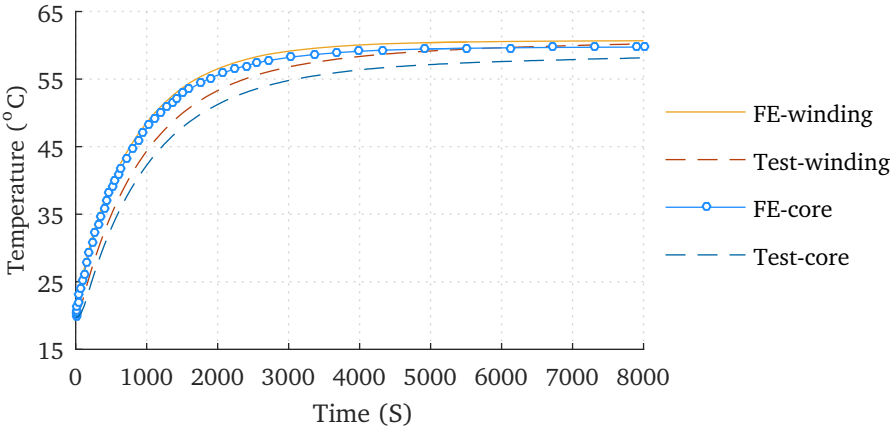

Figure 7.7: The temperature variation of winding and stator core with time for a winding current of 13 A.

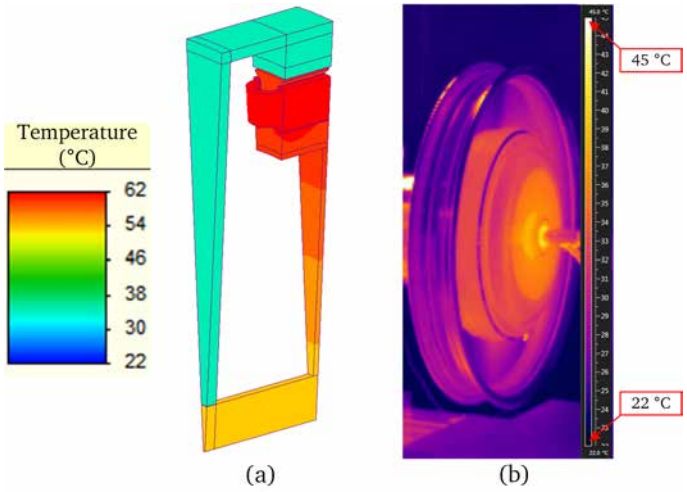

Figure 7.8: The surface temperature variation of the radial flux in-wheel motor corresponding to a winding current of 13 A. (a) FE thermal model. (b) Thermal image from a thermal camera.

the ratio of winding losses to constant losses increases, and hence, the FE prediction is much closer to the test data. Overall, the prediction of steady-state FE model is within 10 °C of experimental data.

The time variation of winding and stator core temperature, when the winding carries 13 A is plotted in Figure 7.7. The mass of the wheel rim and the spoke is not considered in the thermal model, resulting in a lower thermal ca-

pacity for the FE model, and this is reflected in the lower settling time for FE model results. Under higher load condition FE models shows pessimistic results, and therefore, magnets in a PMBLDC motor analysed based on the model presented could operate at a lower temperature than the estimated value.

A comparison between the outer casing temperature distribution from the FE thermal model and the thermal image from the test, corresponding to a winding current of 13 A, is shown in Figure 7.8. The thermal image shows a radially varying temperature distribution on the outer surface, and the maximum temperature occurs close to the centre, mainly in the bearing. The accuracy of the thermal camera used to capture external casing temperature, according to its specification sheet, is within $\pm 2\,^{\circ}$C. Figure 7.8 highlights the limitation of FE thermal model, as the FE result shows no considerable deviation in the surface temperature of the motor. The external surface involves a large area, and there are many changes in the geometry as the radius increases. The FE thermal model calculates heat dissipation using vertical plate and horizontal cylinder analogies, and the analogies are not capable of capturing air velocity gradients around the complex shape. Therefore, a detailed study using a computational fluid dynamic model is required to improve the prediction accuracy of the surface temperature distribution of an in-wheel motor.

7.3.2 FE thermal model of the ferrite magnet SAT PMBLDC motor

The steady-state and transient FE thermal analysis of the radial flux sintered RE magnet motor estimated the temperature of the winding and the stator core within 10 °C of test data. A similar approach to the radial flux hub motor was followed in the thermal modelling of the ferrite magnet SAT PMBLDC motor, and the aim of the thermal modelling was to find the temperature of the magnet when the machine produces the maximum power at an ambient temperature of 20 °C.

The FE thermal model of the ferrite magnet SAT PMBLDC motor, simplified using the geometrical symmetries, is shown in Figure 7.9. The core and winding loss densities corresponding to the maximum output power, obtained from the dynamic simulation of the ferrite magnet motor, is applied to the thermal model. Two internal convective heat transfer link has been modelled; the first one is between the stator tooth faces and the rotor poles and the second one between the inner periphery of the wheel and the stator surfaces exposed

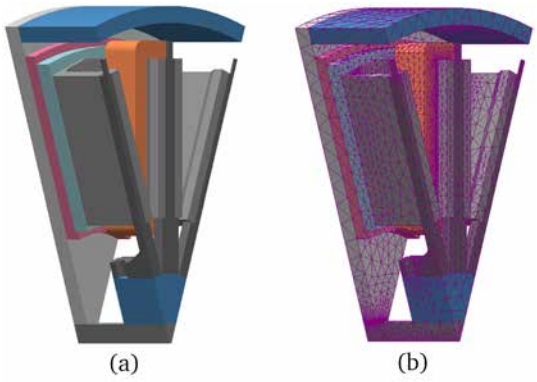

Figure 7.9: The FE thermal model of the ferrite magnet SAT PMBLDC motor simplified using the geometrical symmetry. (a) Simplified 3D geometry. (b) FE mesh.

to the inner air volume. The simulated temperature distribution of the ferrite magnet SAT PMBLDC motor when it delivers maximum output power is shown in Figure 7.10 , and from the distribution, it is found that the temper-

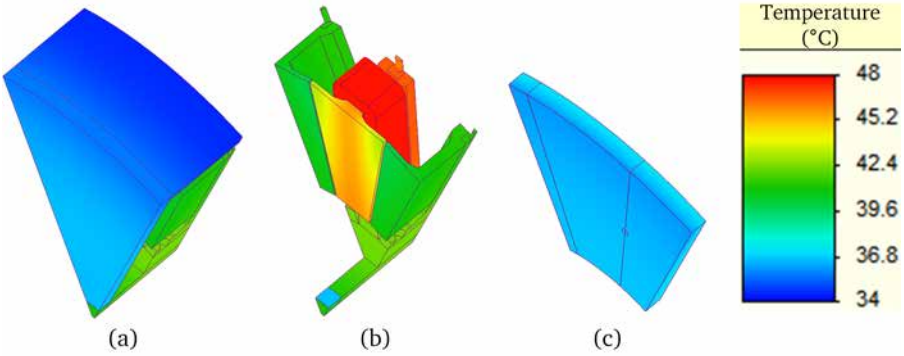

Figure 7.10: The temperature distribution of the ferrite magnet SAT PMBLDC motor at maximum output power obtained from the FE thermal simulation. (a) Outer casing. (b) Stator. (c) Magnet.

ature rise of the magnet from the ambient temperature is 17 °C. From the performance variation of the ferrite magnet motor presented in Section 5.6.3, it is concluded that the higher magnet temperature will reduce the low-speed efficiencies. However, the change in efficiency will be less than 2 % for a magnet temperature rise of 20 °C.

7.4 Performance evaluation of in-wheel motors using a stationary load

The back EMF and the stationary performance tests are carried out on the test bench. The back EMF test is performed on all machines excluding the single-stator single-rotor axial flux motor from vehicle-4. The performance test is carried out on the sintered RE magnet radial flux motor from vehicle-1 and the ferrite magnet SAT motor from vehicle-3 only.

7.4.1 Back EMF testing of motors

The back EMF test is conducted by rotating each machine at a constant speed using the four-quadrant drive. Both the sintered RE magnet motor and the ferrite magnet motor are tested at 340 rpm. However, the bonded magnet motor is rotated at 10 rpm and the line-to-line back EMF waveform is scaled to 340 rpm. The back EMF waveforms of all three motors are shown in Figure 7.11. The main observations from the back EMF test are following

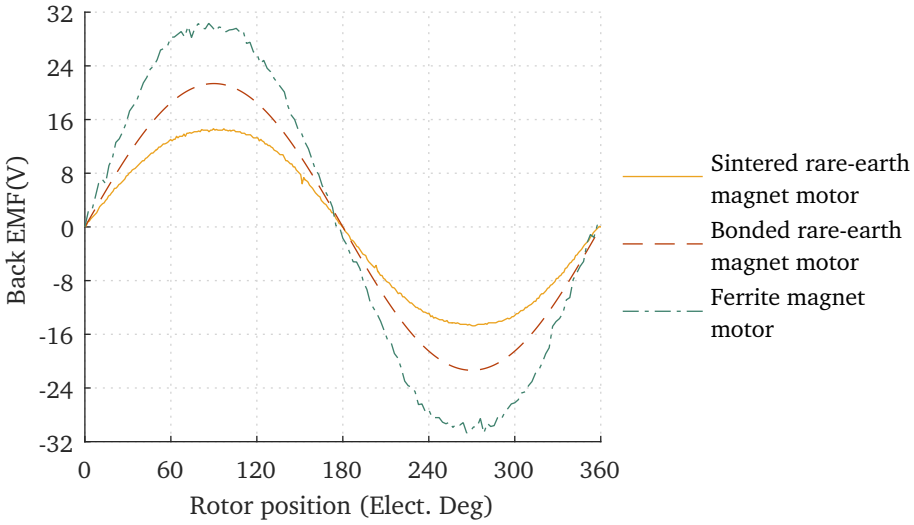

Figure 7.11: Line-to-line back EMF waveforms obtained from back EMF tests.

- The peak-to-peak line-to-line voltage of the bonded RE magnet motor and the ferrite magnet motor are 42.7 V and 61 V respectively. The airgap of the bonded RE magnet machine has been enlarged to compensate for

the stator flexing, and this affected the peak-to-peak value and the shape of its back EMF waveform.

- The peak-to-peak line-to-line voltage of the sintered RE magnet motor is considerably lower as it is designed for short-term peak power of 1.2 kW when connected to a 48 V battery. The higher output power of the machine is achieved by pushing more current into the machine, and lower back EMF will facilitate this.

7.4.2 Performance testing of motors

The performance test is used to evaluate the efficiency of sintered RE magnet motor from vehicle-1 and the ferrite magnet motor prototype, for speeds up to the maximum speed of the vehicle. A 1.2 kW PMBLDC motor controller is used to drive all PMBLDC motors tested using the test bench, and it has a loss of 30 W at the maximum rating. The input power of the PMBLDC motor drive is measured as the product of the voltage and the average current at the input terminals of the controller. The output torque is measured using a torque transducer, which has a maximum torque rating of 50 N m, and the output power is calculated as the product of the torque and the angular velocity of the motor. The torque transducer will also measure the rotational speed of the motor.

The efficiency map of the sintered RE magnet motor and the ferrite magnet SAT motor is shown in Figure 7.12. The measured values of input and output quantities are listed in Appendix C. The maximum efficiency, $\eta_{\max}$, of the sintered RE magnet motor and the ferrite magnet motor are 91.3 % and 96.6 % respectively. The efficiency of both motors have similar variation under 200 rpm, however, beyond 200 rpm the ferrite magnet motor has around 5 % higher efficiencies.

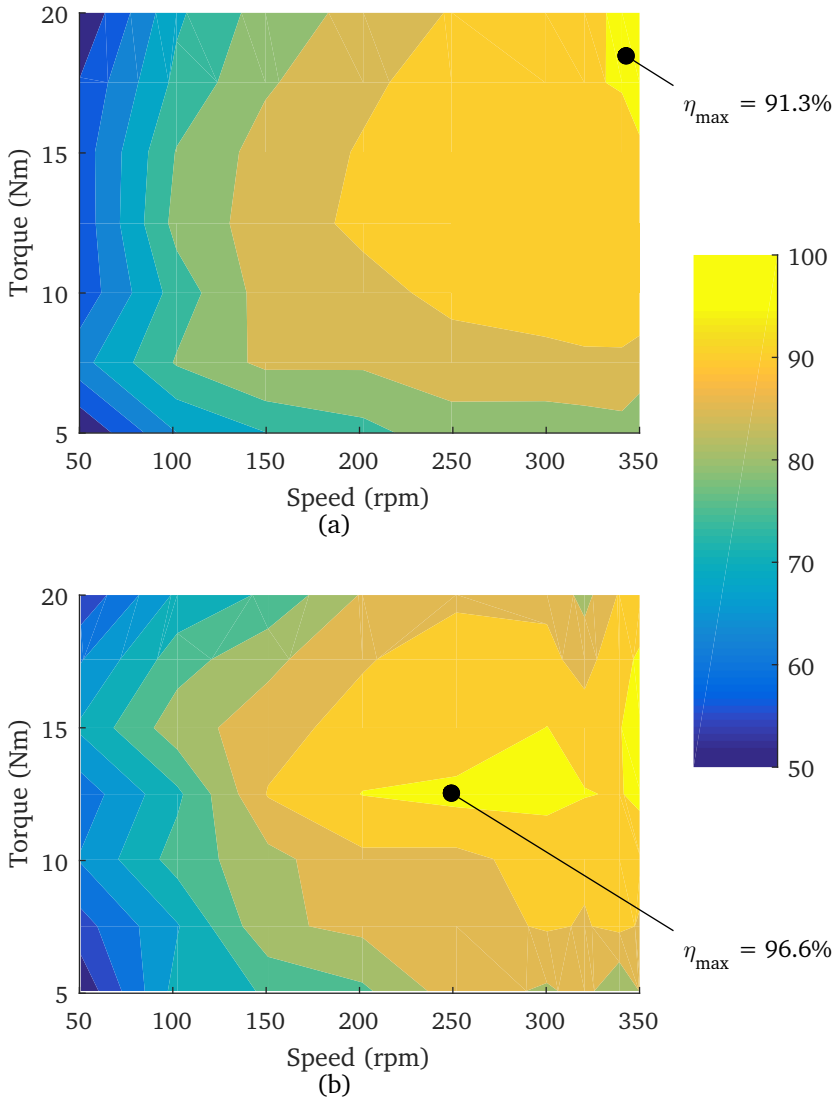

Figure 7.12: Efficiency map obtained from test bench evaluation of motors. (a) Sintered RE magnet PMBLDC hub motor of vehicle-1. (b) ferrite magnet SAT PMBLDC hub motor prototype made for vehicle-3.

7.5 Evaluation of energy consumption of electric two-wheelers

The performance of the ferrite magnet SAT PMBLDC motor as a direct drive powertrain of vehicle-3 is tested by driving the two-wheeler according to the driving cycle stated in ISO 13064-1:2012. The objective of the test was to determine the amount of energy drawn from the battery when the vehicle is driven as per the basic urban driving cycle. This section describes the testing procedure, test setup, and a comparative study of results from the driving cycle test of vehicle-1, vehicle-3, and vehicle-4.

All three vehicles have been driven according to the test sequence described in Appendix D. Each vehicle is fully charged before the test. The testing path is a straight-line road, and the vehicle is driven in the opposite direction for every successive cycle to nullify the effect of wind force on measurements. The tests are conducted in daylight, and ambient temperature variation during the testing was between 5 °C and 10 °C.

The energy drawn from the battery is calculated by integrating the instantaneous power, which is the product of the battery voltage and the current drawn from the battery, over time. The battery voltage is measured across its terminals and current drawn from the battery is measured on the positive lead of the three-phase inverter using a 30 A current probe. The voltage and current signals are recorded using a custom-built data acquisition unit shown in Figure 7.13. The data acquisition unit is built around the PIC32 micro-

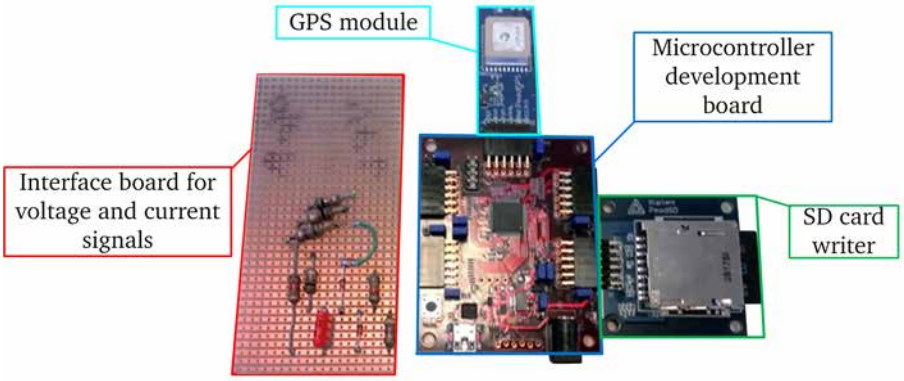

Figure 7.13: The data acquisition unit for recording battery voltage, battery current, and speed of the vehicle during driving cycle test.

controller based development board from Digilent™. The voltage and current signals are passed to the development board via an interface board so that they meet the voltage range of analogue inputs of the microcontroller, and the vehicle speed is captured using an attached GPS module. The controller will record the speed of the vehicle, the battery voltage, and the battery current in every second to an SD card via attached SD card writer. The development board was powered by a portable USB power source. The standard laboratory measurement devices are used to assess the accuracy and precision of the data acquisition unit.

Vehicle-1, vehicle-3, and vehicle-4 undergone the driving cycle test and instantaneous variations of the vehicle speed, the battery voltage, and battery current recorded using the data acquisition unit are shown in Figure 7.14. The highlights and observations from the driving cycle test of electric two-wheelers are following

- All vehicles have a 30 km/h speed limit. During testing, it was possible to maintain two steady-state speeds of 30 km/h and 20 km/h as required by the driving cycle.
- The both vehicle-1 and vehicle-4 have a 10 s acceleration time from 0 to 30 km/h. The ferrite magnet motor powered vehicle-3 has an acceleration time of 17 s, which is less than 20 to 25 s expected while identifying the rating of the powertrain. The reduced acceleration time of vehicle-3 can be attributed to the higher armature current than the rated value, nearly 30 A against the rated current of 16 A, which the controller is pushing to the machine during the initial acceleration.
- The higher current drawn by the ferrite magnet motor is causing higher oscillations in the battery voltage of vehicle-3 compared to vehicle-1 and vehicle-4.
- The energy consumed by vehicle-1, vehicle-3, and vehicle-4 to complete the eight driving cycles are 101.7 W h, 96.1 W h, and 107.0 W h respectively. The energy consumption of vehicle-1 is more than vehicle-3 and follows the similar trend exhibited by the efficiency of their traction motors, the sintered RE magnet motor and the ferrite magnet motor respectively, during their test bench performance evaluation.
- Though the ferrite magnet powertrain draws less energy to complete the test sequence, the acceleration time of vehicle-3 is 70 % more than

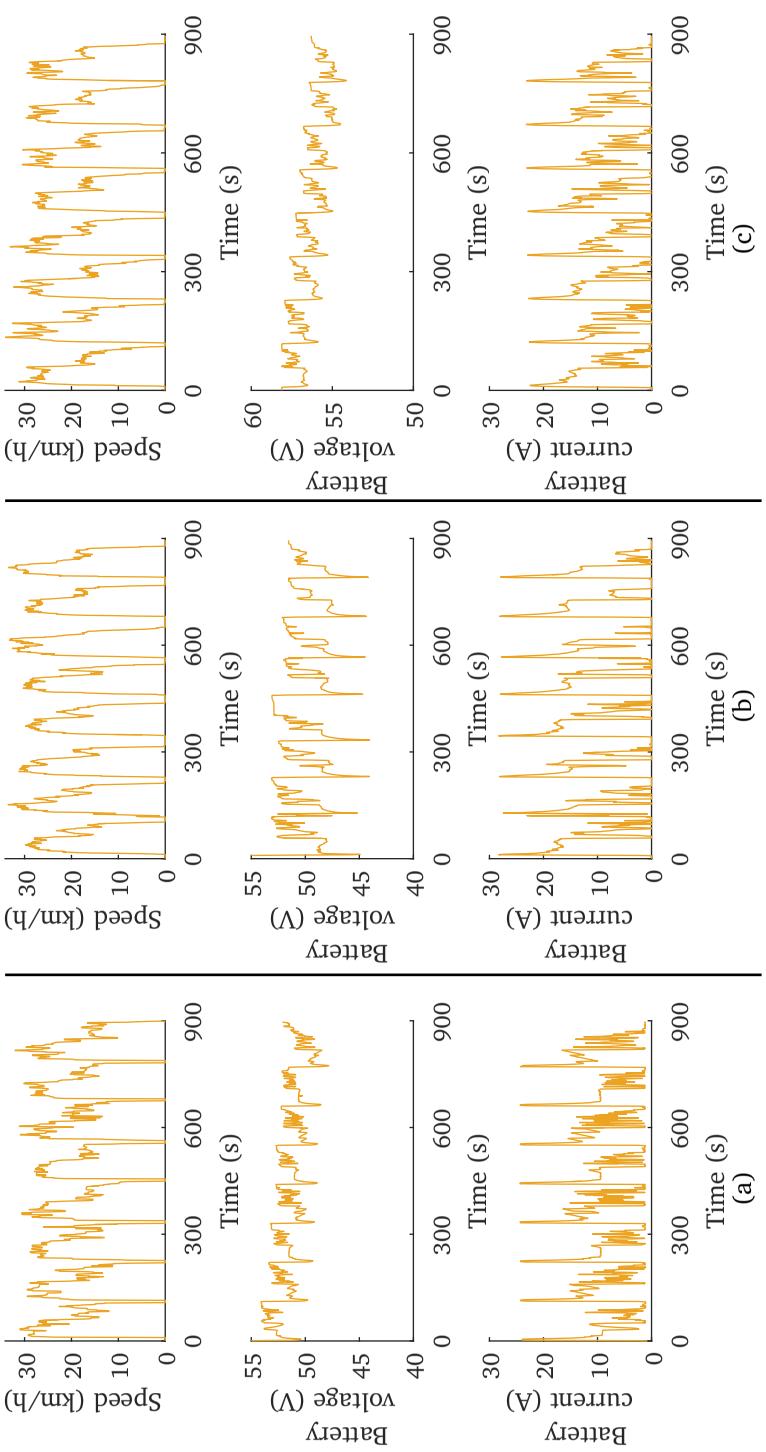

Figure 7.14: The time variation of speed of the vehicle, battery terminal voltage, and battery current obtained from driving cycle tests of electric two-wheelers. (a) vehicle-1 with sintered RE magnet radial flux PMBLDC motor. (b) vehicle-3 with ferrite magnet SAT PMBLDC motor. (c) vehicle-4 with single-airgap axial flux motor.

the other two vehicles. The low acceleration time of vehicle-3 can be attributed to the mass of its ferrite magnet powertrain, and the mass of ferrite magnet motor is heavier than the sintered RE motor by 30 kg. A structural optimisation of the ferrite magnet machine could reduce the mass because the mass of active material of the motor from Table 5.7 is 17.2 kg, and the mass of the completed motor is 37 kg.

7.6 Conclusions

This chapter discussed the testing of electric two-wheelers and the motors used in their powertrains. The motors are tested to measure thermal performance, back EMF, efficiency, and energy consumption. There were four vehicles and their motors, and the practical issues limited evaluating all four motors using all four tests.

The thermal testing of the sintered RE radial flux PMBLDC motor from vehicle-1 is used to validate its FE thermal model. Afterwards, a similar approach is used to develop an FE thermal model of the ferrite magnet SAT PMBLDC motor, and the model is used to predict the operating temperature of components of the motor. Thermal analysis of the ferrite magnet SAT PMBLDC motor concluded that a temperature rise corresponding to the rated torque condition will reduce low-speed efficiency by less than 2 %.

The test bench with a four-quadrant drive is used to measure the back EMF and the efficiency of the motors. It is found that for speeds higher than 200 rpm, the ferrite magnet motor has around 5 % higher efficiencies compared to the sintered RE magnet motor of vehicle-1. Further, the energy consumption of the ferrite magnet motor as an in-wheel powertrain of two-wheeler is evaluated using the basic urban driving cycle, and the result is compared to the results of two market sourced vehicles. It is found that the ferrite magnet powertrain consumes less energy to complete the test sequence, however, has 70 % more acceleration time.

The next chapter will compare the theoretical and the practical parts of the study and evaluate the different theoretical approaches followed in the design and the development of the SAT PMBLDC in-wheel motor using the experimentally measured data.

Chapter 8

Discussion on design, modelling, and experimental validation

8.1 Introduction

The development of a ferrite magnet motor powered electric two-wheeler started with estimating the specification of the powertrain. Subsequently, two SAT PMBLDC motors, one using a bonded RE magnet and the second one using a ferrite magnet, were designed with a rating that will meet the specification of the electric powertrain. The performance simulation of the two designed motors when connected to a PMBLDC drive and a constant torque load were carried out using non-linear dynamic models, and the designs were revised based on the results of dynamic modelling. Afterwards, prototypes of the machines were fabricated based on the revised designs. The ferrite magnet motor prototype is tested using a test bench with a four-quadrant drive and using as a powertrain of an electric two-wheeler.

This chapter discusses the evolution of the motor from the design to the prototype using indices such as mass, torque per unit moment of inertia, power per unit volume, and power per unit mass. Furthermore, the chapter presents an assessment of dynamic model using the test bench results of the ferrite magnet SAT PMBLDC motor as well as using the results from the drive cycle test of vehicle-3.

8.2 Evolution of SAT PMBLDC motor from design to prototype

The electromagnetic designs of the bonded RE magnet motor and the ferrite magnet motor had undergone many changes from the initial design to the prototype. The first set of designs selected for the both motors needed a revision because the first version of the design synthesis program did not consider the inductive voltage drop. The issues with fabrication and assembly of the bonded RE magnet machine forced to increase the airgap considerably. Even after enlarging the airgap and bonding the segmented teeth with resin, it is found that the bonded RE magnet prototype is not structurally sound enough for a normal operation. The experience from fabricating the bonded RE magnet machine compelled to identify an alternative assembly for the ferrite magnet prototype that will be more rigid, however, at the cost of changes to the electromagnetic structure and more weight to structural components. Besides the changes caused by an alternative assembly design, uneven thickness of ferrite magnet poles forced to increase the airgap of the ferrite magnet motor prototype to 2 mm from 0.4 mm.

The performance indicators of designs and prototypes are listed in Table 8.1 for the bonded RE magnet motor and in Table 8.2 for the ferrite magnet motor. The bonded RE magnet motor design, BRE-V2 was fabricated with no changes to the electromagnetic structure, and therefore, the weight of the active materials of the prototype is same as that of the design. However, in the case of the ferrite magnet motor, design Fe-V2 was modified to include a hole for the tooth holder, and this modification increased the mass of steel laminations, which is an active material of the machine. The ratio of the mass of structural components to the total mass is 34 % for the bonded RE magnet motor prototype and 43.6 % for the ferrite magnet motor prototype. The increased mass of structural components of the ferrite magnet motor can be attributed to the overall strengthening of the mechanical assembly compared to the bonded RE magnet motor.

The addition of structural components not only adds mass to the motor but also increases its volume. In ferrite magnet motor prototype, the increase in volume from the final design is considerably more than the bonded RE magnet motor prototype. The increase in the volume of a machine for a given rating reduces the power density of the machine as shown in Table 8.2 for the case

Parameter	Design BRE-V1	Design BRE-V2	Prototype
Mass of active materials (kg)	11.66	15.55	15.55
Mass of structural components (kg)	-	-	8.04
Volume of motor (m^3)	2.86×10^{-3}	3.56×10^{-3}	4.88×10^{-3}
Moment of inertia of the rotor ($kg\,m^2$)	4.43×10^{-2}	9.12×10^{-2}	18.24×10^{-2}
Torque per unit moment of inertia ($N\,m/(kg\,m^2)$)	451.47	219.41	109.64
Power per unit volume (kW/m^3)	244.54	196.35	143.38
Power per unit mass (W/kg)	60.00	45	29.66

Table 8.1: Comparison of designs and prototype of the bonded RE magnet SAT PMBLDC traction motors.

Parameter	Design Fe-V1	Design Fe-V2	Prototype
Mass of active materials (kg)	13.95	17.19	20.86
Mass of structural components (kg)	-	-	16.14
Volume of motor (m^3)	3.59×10^{-3}	4.32×10^{-3}	9.33×10^{-3}
Moment of inertia of the rotor ($kg\,m^2$)	4.68×10^{-2}	6.73×10^{-2}	17.80×10^{-2}
Torque per unit moment of inertia ($N\,m/(kg\,m^2)$)	427.35	297.02	112.37
Power per unit volume (kW/m^3)	194.75	161.90	72.33
Power per unit mass (W/kg)	50.16	40.71	18.92

Table 8.2: Comparison of designs and prototype of the ferrite magnet SAT PMBLDC traction motors.

of the ferrite magnet motor. Further, the addition of structural components reduces the value of indices such as torque per unit moment of inertia and power per unit mass. A design selection can be made based only on the indices calculated without taking into account of the structural mass, because the mass

of these components is an application dependent parameter, and a structural optimisation could reduce the mass of structural components.

8.3 Comparison of results of dynamic model and testing of ferrite magnet motor prototype

The dynamic model proposed in Chapter 5 is used to simulate the ferrite magnet motor prototype driving a constant torque load in a test bench as well as driving an electric two-wheeler. A comparative study of results of the simulation and the testing is presented to assess the accuracy of the model and to identify areas of improvements in the dynamic modelling of the PMBLDC motor.

8.3.1 Comparison of simulation and test data under constant torque load

The prototype is fabricated based on design Fe-V2; however, the electromagnetic design has been changed because of a slot created in the segmented tooth for the tooth holder. Further, the airgap length has been increased to accommodate uneven thickness of the magnet poles. The variation of flux-linkage-derivative of the prototype with rotor position for different values of phase current is calculated from a series static FE simulations, and the results are shown in Figure 8.1. The variation of flux-linkage-derivative with rotor position is used to estimate the line back EMF at 340 rpm, and the calculated line back EMF is plotted in Figure 8.2 along with the waveform obtained from the back EMF test of the ferrite magnet motor prototype. The deviation of the test back EMF waveform from the FE simulated back EMF waveform can be attributed to manufacturing variations from the dimensions of the assembly simulated in the FE software. The major variations observed in the prototype are in widths of slot openings, in dimensions of interpolar gaps, and in thickness of rotor poles.

For the prototype motor and design Fe-V2, the tooth-tip flux density variation with armature current is shown in Figure 8.3, and the change of rotor yoke eddy current loss function with armature current is shown in Figure 8.4. The prototype motor has a larger airgap; therefore, the tooth will saturate only at higher phase current. Further, the eddy current losses in the rotor yoke will

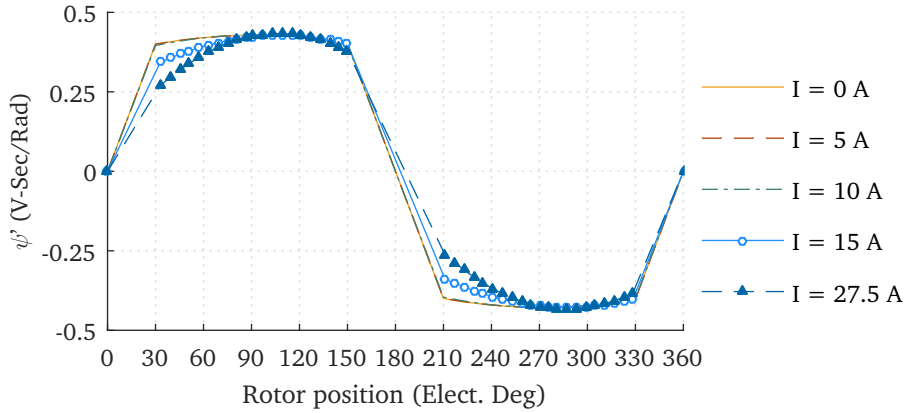

(a)

Figure 8.1: The variation of the flux-linkage-derivative with rotor position for different phase current obtained from a series of static FE simulations of the ferrite magnet SAT PMBLDC motor prototype.

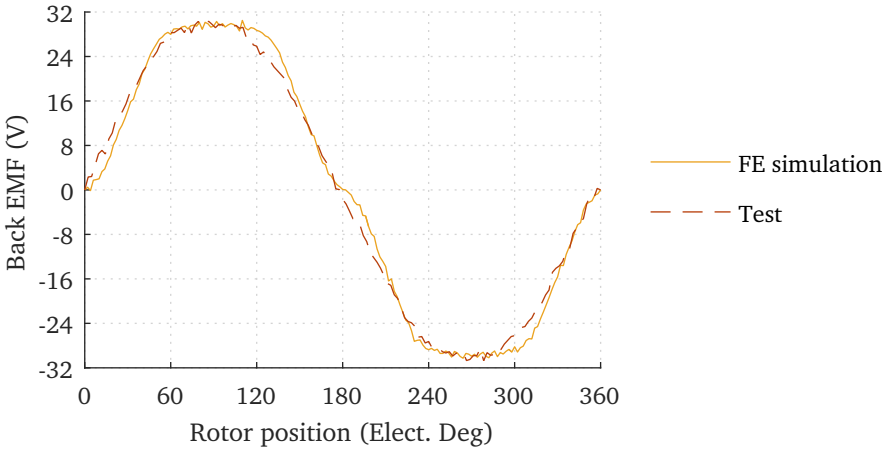

Figure 8.2: The test and the FE simulated line back EMF waveforms of the prototype ferrite magnet SAT PMBLDC motor.

be considerably lessened because the higher airgap will present an increased reluctance to the stator harmonic fluxes.

The number of pole pairs, mean pole transition angle, and loss constants of lamination material are not affected by the changes to the prototype from the design Fe-V2. Therefore, the values listed in Table 5.1 can be used in dynamic modelling of the prototype. The values of phase resistance, phase inductance, maximum tooth flux density, mass of tooth-tips, mass of tooth, and inertia of rotating parts of prototype design and the design Fe-V2 are listed in Table 8.3.

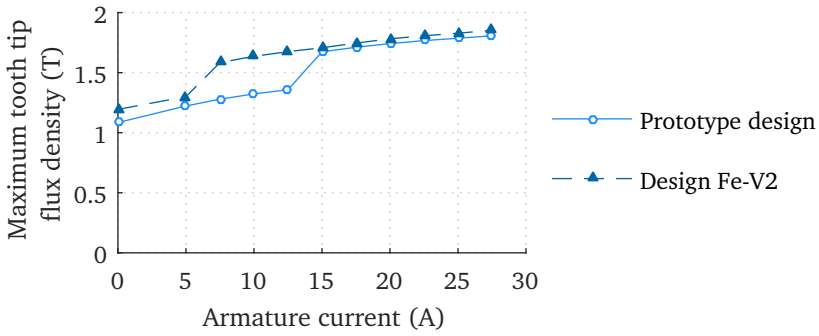

Figure 8.3: The variation of the peak tooth-tip flux densities of the ferrite magnet motor prototype model and design Fe-V2 for different armature current.

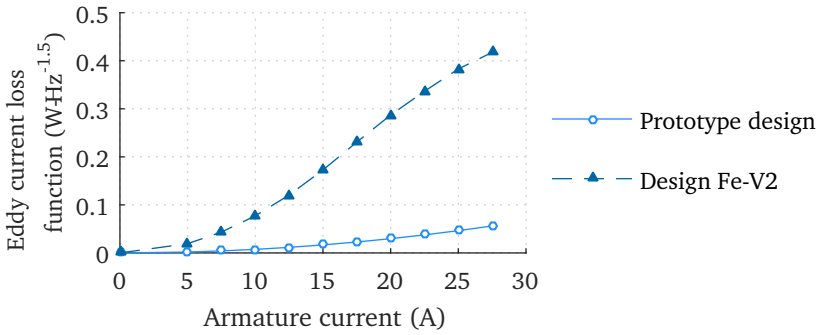

Figure 8.4: The values of yoke eddy current loss function of the ferrite magnet motor prototype model and design Fe-V2 for different armature current.

Parameters	Prototype	Fe-V2
Phase resistance (mΩ)	54.7	54.7
Phase self-inductance (mH)	1.8	5.6
Maximum tooth flux density (T)	0.9	1.3
Mass of tooth-tips (kg)	2.0	2.0
Mass of tooth (kg)	7.6	3.3
Inertia of rotating parts (kg m^2)	6.73×10^{-2}	6.73×10^{-2}

Table 8.3: The dynamic model parameters of prototype electromagnetic structure and design Fe-V2.

The phase current waveforms obtained from the dynamic modelling and the testing of the prototype motor are plotted in Figure 8.5. The waveform

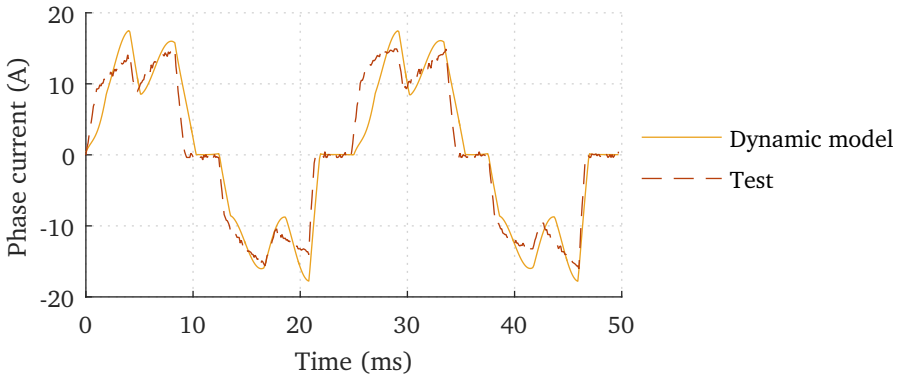

Figure 8.5: The test and simulated phase current waveforms of the prototype ferrite magnet SAT PMBLDC motor.

corresponds to a load torque of 10 N m at a speed of 300 rpm. The efficiency map obtained from the test and the simulation of the prototype ferrite magnet SAT PMBLDC motor is shown in Figure 8.6. The simulated current waveform closely follows that of the test. However, there is considerable variation in maximum efficiencies and distributions of efficiency bands of the dynamic model and the test data. The reasons for the difference between the simulated and the tested efficiency maps of the ferrite magnet prototype were explored, and they are

1. The simplified windage and friction loss model used in the dynamic model cannot expect to be accurate, especially when the motor is operating with an efficiency more than 90 %. The windage loss characterisation of the PMBLDC motor requires a detailed study using non-magnetic dummy rotors and computational fluid dynamic models [174], [177]–[179]. The lack of mechanical loss characterisation prevents the extraction of electromagnetic losses other than the conduction loss from the test data. The segregation of losses will help to improve the overall accuracy of the dynamic model by individually validating each loss model and thus improving the loss models used in the study. However, such characterisations are beyond the scope of the work.

2. The prototype motor uses a commercial controller, and the detailed operation and the component layout of the controller were not available. The dynamic model of the PMBLDC motor discussed in this work uses a basic six-pulse inverter. Using an in-house developed PMBLDC mo-

tor controller would help to model and validate the switching and conduction losses in the controller. The lack of an accurate model of the controller used is affecting the accuracy of the dynamic model of the PMBLDC motor.

3. The prototype motor has a considerable vibration between 310 rpm and 330 rpm only when connected to the test bench, and the readings of the torque and the speed from the sensors were oscillating substantially during this speed range.

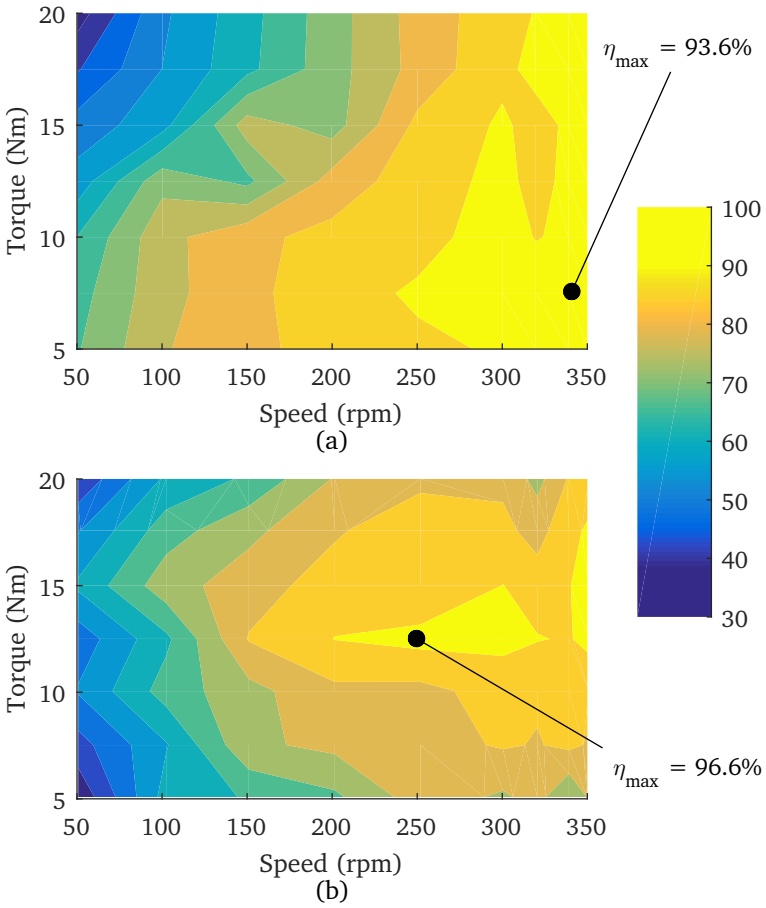

Figure 8.6: The efficiency map of the ferrite magnet SAT PMBLDC motor.(a) From the dynamic model. (b) From the testing.

8.3.2 Comparison of results of urban driving cycle simulation and testing of electric two-wheeler

A dynamic model of electric two-wheeler is developed around the nonlinear dynamic model of PMBLDC motor drive proposed in Chapter 5. A block diagram of the electric two-wheeler model is shown in Figure 8.7. The vehicle model consists of models of battery, converter, three-phase PMBLDC motor, controller, and two-wheeler load.

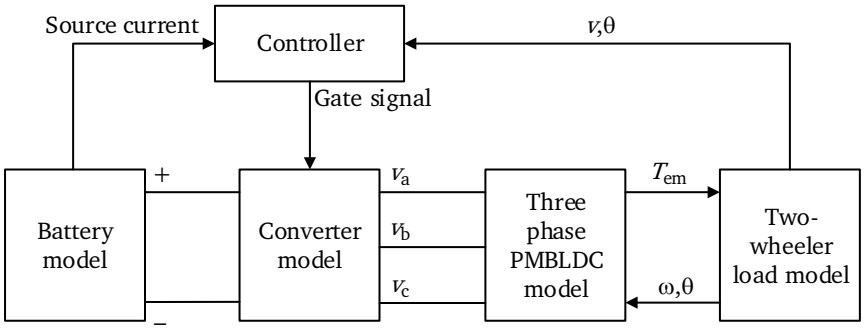

Figure 8.7: The block diagram of the dynamic model of an electric two-wheeler using PMBLDC motor drive as powertrain.

The battery model uses a Li-ion battery block provided in the Matlab-Simulink™ library and the model parameters are obtained from the battery specification of vehicle-3. The converter and the motor models are the same units explained in Chapter 5. The two-wheeler load model developed based on Eq. (3.8) is shown in Figure 8.8. A controller will regulate the speed of the vehicle so that it follows the urban driving cycle, and the model of the controller is shown in Figure 8.9. The controller model uses a look-up table of the urban driving cycle as velocity reference. A PID controller will minimise the error between the vehicle velocity and the reference velocity, and the PWM generator will use the output of the PID controller to create the gate pulses for the converter. Additionally, an AND gate connected to a block that detects over-current will turn off the gate pulses, if the source current exceeds the pre-defined current limit.

The results of the simulation and testing of vehicle-3 when it is driven according to the urban driving cycle is shown in Figure 8.10, and the main observations from the comparative study are following

- The simulated energy consumption of vehicle-3 for the complete driv-

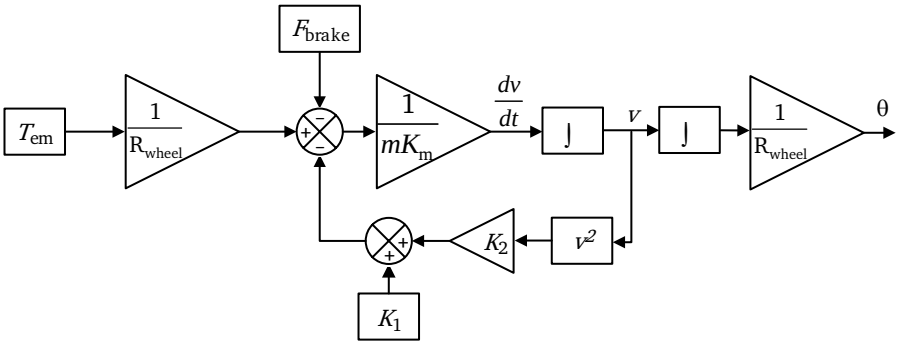

Figure 8.8: The two-wheeler load model.

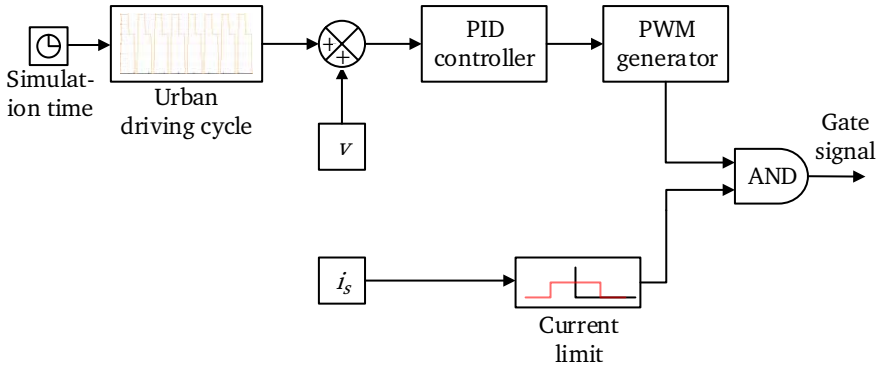

Figure 8.9: The controller model used to simulate the urban driving cycle of an electric two-wheeler.

ing cycle was 104 W h while the energy consumption of the vehicle from the testing was 96.1 W h. The vehicle model overestimates the energy consumption analogous to the test bench simulation, where the model overestimated the losses. Therefore, addressing the concerns presented in the discussion of dynamic model results will also improve the prediction accuracy of the vehicle model.

- The urban driving cycle pattern is more closely followed in the simulation compared to the testing. However, further tuning of the PID controller constants is required to reduce the settling time and the speed overshooting.

- The battery voltage drops more in the test during the initial acceleration of each drive cycle than the simulation. The profile of battery voltage

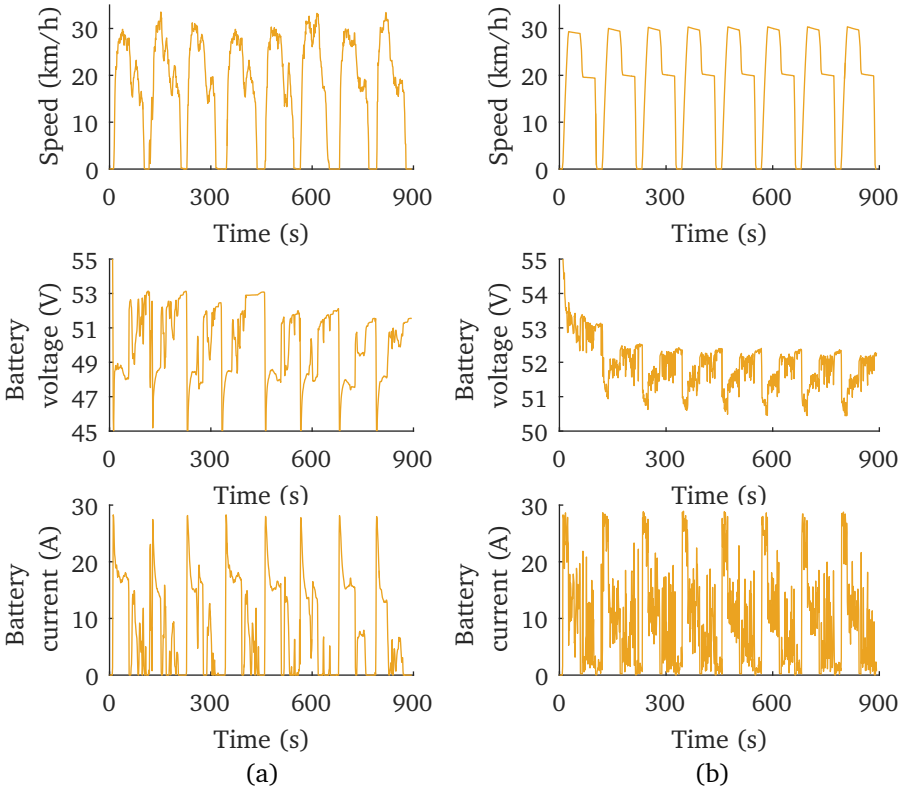

Figure 8.10: The time variation of speed of the vehicle, battery terminal voltage, and battery current of vehicle-3. (a) From the testing of vehicle-3. (b) From the simulation of non-linear dynamic model of the PMBLDC motor with two-wheeler load.

waveforms of test and simulations are identical, except during the first cycle.

- The time taken for simulating the urban driving cycle test was close to four days.

8.4 Conclusions

This chapter discussed changes in the electromagnetic design of the ferrite magnet SAT PMBLDC motor in different phases of the product development starting from the initial design to the final prototype. It is concluded that the structural components can add considerable mass to the motor depending on the application. In an application such as the direct drive in-wheel motor, a

structural optimisation is necessary to reduce the weight of structural components of the motor.

Further, the results of the dynamic modelling of PMBLDC motor is compared to the results of testing of the ferrite magnet motor prototype. The motor was operating with an efficiency of more than 90 %, and the accuracy with which all electromagnetic and mechanical losses are modelled is critical to estimate the system performance accurately at this level of efficiency. Further, the vehicle model also overestimates the energy consumption analogous to the test bench simulation. This work has attempted to incorporate the core loss calculation into the PMBLDC motor model and natural progress of the work will be including the improved models of mechanical losses such as aerodynamic loss and frictional loss.

The next chapter will conclude the work and present few future research directions on this subject.

Chapter 9

Conclusions and future work

9.1 Conclusions

The price fluctuations of RE metals and the uncertainty in their supply demanded an investigation of RE free high-efficiency machines. In this work, a direct drive powertrain for an electric two-wheeler for city commute was selected as the target application, because at present, the growth of such vehicles is hindered by its higher cost compared to ICE powered counterparts. Wider adoptions of LEV could ease the emission and congestion issues faced by cities.

A simplified expression for calculating the motive force of a moving vehicle has been proposed. The proposed modification makes it easier to incorporate the equations of motion of a vehicle into numerical solving techniques. A method was discussed to calculate the output power of an electric powertrain that satisfies the performance criteria such as the acceleration time and the maximum gradient on which the vehicle can maintain the top speed. The power rating of motors for vehicle-2 and vehicle-3 has been calculated using the equations presented and the geometrical dimensions of vehicle-1. The effect of increased mass of prototype motors on the performance of vehicle-2 and vehicle-3 has been studied, and it is found that acceleration time will increase from 20 s to 24 s when the total mass of vehicle is increased by 20 kg.

An FE based design-synthesis program for a SAT PMBLDC motor has been presented. The program is used to design two direct drive in-wheel motors, a bonded RE magnet motor and a ferrite magnet motor. The weight of active materials of the ferrite magnet motor is heavier by 10.5 % than the bonded RE magnet motor for the same rated output, because the ferrite magnet has a

lower remanent flux density than the bonded RE magnet.

A dynamic model of a PMBLDC motor that considers nonlinearities such as core losses and back EMF waveforms influenced by saturation and armature reaction has been proposed. The model is computationally less demanding to the extent that it can be incorporated into a large-scale model of an electric drive system such as an electric vehicle. The design-synthesis program has been revised based on the finding from dynamic modelling of the designs to include the inductive voltage drop in design iterations.

Knee points can appear in the second quadrant of demagnetisation characteristics of ferrite magnets. A method has been proposed to assess the extent of demagnetisation in magnets of a PMBLDC motor with the help of variation in slope of demagnetization curves. The method helps the designer to ensure that the designed ferrite magnet motor is capable of working throughout the operating temperature, without any irreversible demagnetisation of magnets.

Ferrite magnets have a considerably higher temperature coefficient of remanence compared to RE magnets. The temperature dependent characteristics of ferrites have to be considered when designing ferrite magnet machines for applications such as electric powertrain where they are exposed to ambient temperature changes. The performance variation of the designed ferrite magnet motor has been simulated for temperatures starting from $-20\,^{\circ}\mathrm{C}$ to $70\,^{\circ}\mathrm{C}$, and it is found that the presented design will meet the torque requirement for accelerating the vehicle to the top speed and maintaining the top speed up to a gradient of 3 % over the entire temperature range.

Two different assembly designs of SAT PMBLDC motor are presented and studied using 3D models. The first assembly is implemented in the fabrication of bonded RE magnet motor, and the prototype has issues such as stator flexing and difficulty to manage the lead wires of the coils and the sensors. The second assembly of SAT PMBLDC motor addresses limitations of the first prototype, and it is used in the fabrication of the ferrite magnet SAT PMBLDC motor. The operation of the first prototype is found to be restricted by its weak structure, and therefore, only the second prototype is installed in the electric two-wheeler.

The tests are carried out on the machines to measure thermal performance, back EMF, efficiency, and energy consumption. There were four vehicles and their motors, and practical issues limited evaluation of all four motors using all four tests.

The thermal testing of the sintered RE radial flux PMBLDC motor from

vehicle-1 is used to validate its FE thermal model. Afterwards, a similar approach is used to develop an FE thermal model of the ferrite magnet SAT PMBLDC motor, and the model is used to predict the operating temperature of components of the motor. Thermal analysis of the ferrite magnet SAT PMBLDC motor concluded that a temperature rise corresponding to the rated torque condition will reduce low-speed efficiency by less than 2 %.

The test bench with a four-quadrant drive is used to measure the back EMF and efficiency of the motors. It is found that for speeds higher than 200 rpm, the ferrite magnet motor has around 5 % higher efficiencies compared to the sintered RE magnet motor of vehicle-1. Further, the energy consumption of the ferrite magnet motor as in-wheel powertrain of two-wheeler is evaluated using the basic urban driving cycle, and the result is compared to the results of two market sourced vehicles. It is found that the ferrite magnet powertrain consumes less energy to complete the test sequence, however, has 70 % more acceleration time.

The evolution of the electromagnetic design of the two SAT PMBLDC motors in different phases of the product development starting from initial design to the final prototype has been analysed. It is concluded that the structural components can add considerable mass to the motor depending on the application. In an application such as the direct drive in-wheel motor, a structural optimisation is necessary to reduce the weight of structural components of the motor.

The results of the dynamic modelling of PMBLDC motor is compared to the results of testing of the ferrite magnet motor prototype. The motor was operating with an efficiency of more than 90 %, and the accuracy with which all electromagnetic and mechanical losses are modelled is critical to estimate the system performance accurately at this level of efficiency. Further, the vehicle model also overestimates the energy consumption analogous to the test bench simulation. This work has attempted to incorporate the core loss calculation into the PMBLDC motor model and natural progress of the work will be including the improved models of mechanical losses such as aerodynamic loss and frictional loss.

The direct-drive traction in-wheel motor presented in this work is a low-speed high-torque application of small size, and the wind turbines are an example of a large-size low-speed high-torque application. Even though there is a lack of optimisation in structural aspects of the designed ferrite magnet machine, the positive electromagnetic results provide a platform to expand the

use of ferrite magnets in higher rated applications than the traction motors covered in this work.

9.2 Future work

A structural study of the SAT PMBLDC in-wheel motor targeting to use economically viable lightweight materials and reducing the mass of structural parts could considerably lessen the mass of the prototype ferrite magnet machine. The reduced mass will benefit the acceleration time of the vehicle. The prototype motor has considerable vibration when operating between 310 rpm and 330 rpm only when connected to the test bench, and the proposed structural study can be extended to find a solution to the excessive vibration. Currently, the motor is operated only up to 350 rpm, and the structural analysis could explore the possibility to operate beyond 350 rpm.

The design-synthesis program selected designs with the lowest loss. Incorporating the multi-objective optimisation with target parameters such as torque per unit moment of inertia of rotor, power per unit volume, and power per unit mass along with efficiency, into the design-synthesis program will generate designs more adapted to performance, geometrical, and weight constraints of the powertrain.

The dynamic modelling of high-efficiency machines requires accurate models of mechanical losses along with models of electromagnetic losses. Developing accurate mechanical loss models such as aerodynamic loss caused by the internal and external structure of motor requires computational fluid dynamic study and extensive testing using dummy models of magnets inside the machine. The knowledge of aerodynamic loss not only improve the accuracy of models but also initiates works to reduce them for improving the efficiency of the motor. Another aspect of internal and external fluid flow analysis is the understanding of heat flow and loss dissipation of the machine. An improved thermal design of machines not only improves the efficiency and the service life but also helps the motors that use lower energy density magnets to operate at higher current density.

References

[1] P. C. Dent and M. H. Walmer, "4.6: supply chain sustainability - rare earth materials," in *2010 IEEE International Vacuum Electronics Conference (IVEC)*, IEEE, May 2010, pp. 57–58.

[2] C. Hurst, "China's rare earth elements industry: what can the west learn?," no. March, p. 43, 2010.

[3] K. Bourzac, "The rare-earth crisis," *Technology Review*, 2011.

[4] S. Eriksson and H. Bernhoff, "Rotor design for pm generators reflecting the unstable neodymium price," in *2012 XXth International Conference on Electrical Machines*, IEEE, Sep. 2012, pp. 1419–1423.

[5] M. Humphries, "Rare earth elements: the global supply chain," *Congressional Research Service*, 2012.

[6] J. Rowlatt, "Rare earths: neither rare, nor earths," *BBC news online*, Date accessed:2016-03-31.

[7] E. Commission, "Report on critical raw materials for the eu," *Retrieved April*, 2014.

[8] K. Strnat, "Modern permanent magnets for applications in electrotechnology," *Proceedings of the IEEE*, vol. 78, no. 6, pp. 923–946, Jun. 1990.

[9] J. Coey, "Permanent magnets: plugging the gap," *Scripta Materialia*, vol. 67, no. 6, pp. 524–529, Sep. 2012.

[10] "Nanopyme project website," *Http://nanopyme-project.eu/*, Date accessed : 2016-03-31.

[11] P. Chandrasekar, "360 degree perspective of the global electric vehicle market- 2010 edition," Frost & Sullivan, Tech. Rep., 2010.

[12] G. Giuliano and D. Narayan, "Another look at travel patterns and urban form: the us and great britain," *Urban Studies*, vol. 40, no. 11, pp. 2295–2312, Oct. 2003.

[13] B. Nykvist and M. Nilsson, "Rapidly falling costs of battery packs for electric vehicles," *Nature Climate Change*, vol. 5, no. 4, pp. 329–332, Mar. 2015.

[14] K. T. Ulrich, "Estimating the technology frontier for personal electric vehicles," *Transportation Research Part C- Emerging Technologies*, vol. 13, no. 5-6, pp. 448–462, Oct. 2005.

[15] C. C. Chan, "Engineering philosophy of electric vehicles," in *Electric Machines and Drives, 1999. International Conference IEMD '99*, 1999, pp. 255–257.

[16] M. Dijk, R. J. Orsato, and R. Kemp, "The emergence of an electric mobility trajectory," *Energy Policy*, vol. 52, pp. 135–145, Jan. 2013.

[17] B. M. Al-Alawi and T. H. Bradley, "Review of hybrid, plug-in hybrid, and electric vehicle market modeling studies," *Renewable and Sustainable Energy Reviews*, vol. 21, pp. 190–203, May 2013.

[18] F. E. Jamerson and E. Benjamin, "Worldwide electric powered two wheel market," in *26th Electric Vehicle Symposium 2012, EVS 2012*, 2012, pp. 220–2926.

[19] J. Larminie and J. Lowry, *Electric Vehicle Technology Explained*. Chichester, UK: John Wiley & Sons, Ltd, Aug. 2012, pp. 29–77.

[20] L. Ntziachristos, A. Mamakos, Z. Samaras, A. Xanthopoulos, and E. Iakovou, "Emission control options for power two wheelers in europe," *Atmospheric Environment*, vol. 40, no. 24, pp. 4547–4561, Aug. 2006.

[21] M. Kousoulidou, L. Ntziachristos, G. Mellios, and Z. Samaras, "Road-transport emission projections to 2020 in european urban environments," *Atmospheric Environment*, vol. 42, no. 32, pp. 7465–7475, Oct. 2008.

[22] P. Mock, S. A. Schmid, and H. E. Friedrich, *Market Prospects of Electric Passenger Vehicles*, 2010th ed. Amsterdam: Elsevier B.V, 2010, pp. 545–578.

[23] M. M. Thackeray, C. Wolverton, and E. D. Isaacs, "Electrical energy storage for transportation-approaching the limits of, and going beyond, lithium-ion batteries," *Energy & Environmental Science*, vol. 5, no. 7, pp. 7854–7863, 2012.

[24] B. G. Pollet, I. Staffell, and J. L. Shang, "Current status of hybrid, battery and fuel cell electric vehicles: from electrochemistry to market prospects," *Electrochimica Acta*, vol. 84, pp. 235–249, Dec. 2012.

[25] A. Poullikkas, "Sustainable options for electric vehicle technologies," *Renewable and Sustainable Energy Reviews*, vol. 41, pp. 1277–1287, Jan. 2015.

[26] R. Smokers, F. Fraga, and M. Verbeek, "Support for the revision of regulation (ec) no 443/2009 on co2 emissions from cars," Tech. Rep. 443, 2011, pp. 1–75.

[27] "Proposal for a regulation to define the modalities for reaching the 2020 target for reducing co2 emissions from new passenger cars," Tech. Rep., 2012.

[28] M. V. Prati, G. Zamboni, M. a. Costagliola, G. Meccariello, C. Carraro, and M. Capobianco, "Influence of driving cycles on euro 3 scooter emissions and fuel consumption," *Energy Conversion and Management*, vol. 52, no. 11, pp. 3327–3336, Oct. 2011.

[29] European Commission, "Roadmap to a single european transport area-towards a competitive and resource efficient transport system," *Office for Official Publications of the European*, pp. 1–31, 2011.

[30] J. de Santiago, H. Bernhoff, B. Ekergård, S. Eriksson, S. Ferhatovic, R. Waters, and M. Leijon, "Electrical motor drivelines in commercial all-electric vehicles: a review," *IEEE Transactions on Vehicular Technology*, vol. 61, no. 2, pp. 475–484, Feb. 2012.

[31] T. J. E. Miller, *Brushless permanent-magnet and reluctance motor drives*. Oxford University Press, 1989.

[32] T. G. Wilson and P. H. Trickey, "D-c machine with solid-state commutation," *Electrical Engineering*, vol. 81, no. 11, pp. 879–884, Nov. 1962.

[33] B. Chalmers, K. Pacey, and J. Gibson, "Brushless d.c. traction drive," *Proceedings of the Institution of Electrical Engineers*, vol. 122, no. 7, p. 733, 1975.

[34] Y. Takano, M. Takeno, N. Hoshi, A. Chiba, M. Takemoto, S. Ogasawara, and M. A. Rahman, "Design and analysis of a switched reluctance motor for next generation hybrid vehicle without pm materials," in *The 2010 International Power Electronics Conference - ECCE ASIA -*, IEEE, Jun. 2010, pp. 1801–1806.

[35] I. Boldea, L. N. Tutelea, L. Parsa, and D. Dorrell, "Automotive electric propulsion systems with reduced or no permanent magnets: an overview," *IEEE Transactions on Industrial Electronics*, vol. 61, no. 10, pp. 5696–5711, Oct. 2014.

[36] K. T. Chau, *Electric Vehicle Machines and Drives*. Singapore: John Wiley & Sons, Singapore Pte. Ltd, Jun. 2015.

[37] M. Zeraoulia, M. E. H. Benbouzid, and D. Diallo, "Electric motor drive selection issues for hev propulsion systems: a comparative study," *IEEE Transactions on Vehicular Technology*, vol. 55, no. 6, pp. 1756–1764, Nov. 2006.

[38] S. Yang, N. J. Baker, B. C. Mecrow, C. Hilton, G. Sooriyakumar, D. Kostic-Perovic, and A. Fraser, "Cost reduction of a permanent magnet in-wheel electric vehicle traction motor," in *2014 International Conference on Electrical Machines (ICEM)*, IEEE, Sep. 2014, pp. 443–449.

[39] J. Goss, M. Popescu, and D. Staton, "A comparison of an interior permanent magnet and copper rotor induction motor in a hybrid electric vehicle application," in *2013 International Electric Machines & Drives Conference*, IEEE, May 2013, pp. 220–225.

[40] M. Kimiabeigi, J. D. Widmer, R. Long, Y. Gao, J. Goss, R. Martin, T. Lisle, J. M. Soler Vizan, A. Michaelides, and B. Mecrow, "High-performance low-cost electric motor for electric vehicles using ferrite magnets," *IEEE Transactions on Industrial Electronics*, vol. 63, no. 1, pp. 113–122, Jan. 2016.

[41] D. G. Dorrell, M.-F. Hsieh, and A. M. Knight, "Alternative rotor designs for high performance brushless permanent magnet machines for hybrid electric vehicles," *IEEE Transactions on Magnetics*, vol. 48, no. 2, pp. 835–838, Feb. 2012.

[42] W. H. Kim, I. S. Jang, C. S. Jin, J. Lee, and S. G. Lee, "Design of novel overhang structure for separated pole-piece type ferrite magnet motor," *IEEE Transactions on Magnetics*, vol. 51, no. 3, pp. 1–4, Mar. 2015.

[43] M. M. Rahman, K.-T. Kim, and J. Hur, "Design and optimization of neodymium-free spoke-type motor with segmented wing-shaped pm," *IEEE Transactions on Magnetics*, vol. 50, no. 2, pp. 865–868, Feb. 2014.

[44] T. Takahashi, M. Takemoto, S. Ogasawara, W. Hino, and K. Takezaki, "Size and weight reduction of an in-wheel axial-gap motor using ferrite permanent magnets for electric city commuters," IEEE, 2015.

[45] K. Sone, M. Takemoto, S. Ogasawara, K. Takezaki, and H. Akiyama, "A ferrite pm in-wheel motor without rare earth materials for electric city commuters," *IEEE Transactions on Magnetics*, vol. 48, no. 11, pp. 2961–2964, Nov. 2012.

[46] K. Atallah and J. Wang, "A rotor with axially and circumferentially magnetized permanent magnets," *IEEE Transactions on Magnetics*, vol. 48, no. 11, pp. 3230–3233, Nov. 2012.

[47] J. A. Krizan and S. D. Sudhoff, "Theoretical performance boundaries for permanent magnet machines as a function of magnet type," in *2012 IEEE Power and Energy Society General Meeting*, IEEE, Jul. 2012, pp. 1–6.

[48] J. D. Widmer, R. Martin, and M. Kimiabeigi, "Electric vehicle traction motors without rare earth magnets," *Sustainable Materials and Technologies*, vol. 3, pp. 7–13, Apr. 2015.

[49] M. Hernandez, M. Messagie, O. Hegazy, L. Marengo, O. Winter, and J. Van Mierlo, "Environmental impact of traction electric motors for electric vehicles applications," *The International Journal of Life Cycle Assessment*, Oct. 2015.

[50] S. J. Galioto, P. B. Reddy, A. M. EL-Refaie, and J. P. Alexander, "Effect of magnet types on performance of high-speed spoke interior-permanent-magnet machines designed for traction applications," *IEEE Transactions on Industry Applications*, vol. 51, no. 3, pp. 2148–2160, May 2015.

[51] R. Wrobel and P. Mellor, "Design considerations of a direct drive brushless machine with concentrated windings," *IEEE Transactions on Energy Conversion*, vol. 23, no. 1, pp. 1–8, Mar. 2008.

[52] M. Bertoluzzo and G. Buja, "Propulsion systems for light electric vehicles," in *2010 IEEE International Symposium on Industrial Electronics*, IEEE, Jul. 2010, pp. 3650–3655.

[53] B. Gombert, R. Fischer, and W. Heinrich, “Wheel-hub motors: criteria of construction product management,” *ATZelektronik worldwide*, vol. 5, no. 1, pp. 4–10, 2010.

[54] R. Hosoya, H. Shimada, and S. Shimomura, “Design of a ferrite magnet vernier machine for an in-wheel machine,” in *2011 IEEE Energy Conversion Congress and Exposition*, IEEE, Sep. 2011, pp. 2790–2797.

[55] J. Hendershot and T. Miller, *Design of brushless permanent-magnet machines*. 2010.

[56] Z. Q. Zhu, J. X. Shen, and D. Howe, “Flux-weakening characteristics of non-sinusoidal back-emf pm machines in brushless dc and ac modes,” *Journal of Asian Electric Vehicles*, vol. 4, no. 2, pp. 919–925, 2006.

[57] D. G. Dorrell, M.-F. Hsieh, M. Popescu, L. Evans, D. A. Staton, and V. Grout, “A review of the design issues and techniques for radial-flux brushless surface and internal rare-earth permanent-magnet motors,” *IEEE Transactions on Industrial Electronics*, vol. 58, no. 9, pp. 3741–3757, Sep. 2011.

[58] A. Cavagnino, M. Lazzari, F. Profumo, and A. Tenconi, “A comparison between the axial flux and the radial flux structures for pm synchronous motors,” *IEEE Transactions on Industry Applications*, vol. 38, no. 6, pp. 1517–1524, Nov. 2002.

[59] J. F. Gieras, R.-J. Wang, and M. J. Kamper, *Axial Flux Permanent Magnet Brushless Machines*. Dordrecht: Kluwer Academic Publishers, 2005.

[60] K. Sitapati and R. Krishnan, “Performance comparisons of radial and axial field, permanent-magnet, brushless machines,” *IEEE Transactions on Industry Applications*, vol. 37, no. 5, pp. 1219–1226, 2001.

[61] M. Aydin, S. Huang, and T. Lipo, “Axial flux permanent magnet disc machines: a review,” *Proceedings of the 2004 SPEEDAM*, 2004.

[62] A. Di Gerlando, G. M. Foglia, R. Perini, and M. Ubaldini, “Permanent magnet synchronous machines with concentrated coil armature windings: analysis and test validation of single stator-double rotor, axial flux machines,” *Electrical Engineering*, vol. 90, no. 1, pp. 65–77, Dec. 2006.

[63] S. Kahourzade, A. Mahmoudi, H. W. Ping, and M. N. Uddin, "A comprehensive review of axial-flux permanent-magnet machines," *Canadian Journal of Electrical and Computer Engineering*, vol. 37, no. 1, pp. 19–33, 2014.

[64] T. Woolmer and M. McCulloch, "Analysis of the yokeless and segmented armature machine," in *2007 IEEE International Electric Machines & Drives Conference*, vol. 1, IEEE, May 2007, pp. 704–708.

[65] W. Fei, P. C. K. Luk, and K. Jinupun, "A new axial flux permanent magnet segmented-armature-torus machine for in-wheel direct drive applications," in *2008 IEEE Power Electronics Specialists Conference*, IEEE, Jun. 2008, pp. 2197–2202.

[66] F. Giulii Capponi, G. De Donato, and F. Caricchi, "Recent advances in axial-flux permanent-magnet machine technology," *IEEE Transactions on Industry Applications*, vol. 48, no. 6, pp. 2190–2205, Nov. 2012.

[67] T. J. Woolmer and M. McCulloch, "Axial flux permanent magnet machines: a new topology for high performance applications," in *IET Hybrid Vehicle Conference 2006*, vol. 2006, Coventry, UK: IEE, 2006, pp. 27–42.

[68] M. Ehsani, K. Rahman, and H. Toliyat, "Propulsion system design of electric and hybrid vehicles," *IEEE Transactions on Industrial Electronics*, vol. 44, no. 1, pp. 19–27, 1997.

[69] M. Aydin and T. Lipo, "Design and 3d electromagnetic field analysis of non-slotted and slotted torus type axial flux surface mounted permanent magnet disc machines," in *IEMDC 2001. IEEE International Electric Machines and Drives Conference (Cat. No.01EX485)*, IEEE, 2001, pp. 645–651.

[70] T. F. Chan and L. L. Lai, "An axial-flux permanent-magnet synchronous generator for a direct-coupled wind-turbine system," *IEEE Transactions on Energy Conversion*, vol. 22, no. 1, pp. 86–94, Mar. 2007.

[71] N. Rostami, M. R. Feyzi, J. Pyrhonen, A. Parviainen, and V. Behjat, "Genetic algorithm approach for improved design of a variable speed axial-flux permanent-magnet synchronous generator," *IEEE Transactions on Magnetics*, vol. 48, no. 12, pp. 4860–4865, Dec. 2012.

[72] A. Mahmoudi, S. Kahourzade, N. A. Rahim, and W. P. Hew, "Design, analysis, and prototyping of an axial-flux permanent magnet motor based on genetic algorithm and finite-element analysis," *IEEE Transactions on Magnetics*, vol. 49, no. 4, pp. 1479–1492, Apr. 2013.

[73] Y.-P. Yang, Y.-P. Luh, and C.-H. Cheung, "Design and control of axial-flux brushless dc wheel motors for electric vehicles-part i: multiobjective optimal design and analysis," *IEEE Transactions on Magnetics*, vol. 40, no. 4, pp. 1873–1882, Jul. 2004.

[74] F. Chuang, "Optimization for reduction of torque ripple in an axial flux permanent magnet machine," *IEEE Transactions on Magnetics*, vol. 45, no. 3, pp. 1760–1763, Mar. 2009.

[75] F. Leonardi and T. Lipo, "A general approach to sizing and power density equations for comparison of electrical machines," *IEEE Transactions on Industry Applications*, vol. 34, no. 1, pp. 92–97, 1998.

[76] M. N. Uddin, S. Kahourzade, A. Mahmoudi, H. W. Ping, and N. A. Rahim, "Design and prototyping of an optimised axial-flux permanent-magnet synchronous machine," *IET Electric Power Applications*, vol. 7, no. 5, pp. 338–349, May 2013.

[77] S. M. Jafari-Shiadeh and M. Ardebili, "Analysis and comparison of axial-flux permanent-magnet brushless-dc machines with fractional slot concentrated windings," in *4th Annual International Power Electronics, Drive Systems and Technologies Conference*, IEEE, Feb. 2013, pp. 72–77.

[78] T. M. Jahns, G. B. Kliman, and T. W. Neumann, "Interior permanent-magnet synchronous motors for adjustable-speed drives," *IEEE Transactions on Industry Applications*, vol. IA-22, no. 4, pp. 738–747, Jul. 1986.

[79] D. Ishak, Z. Zhu, and D. Howe, "Comparison of pm brushless motors, having either all teeth or alternate teeth wound," *IEEE Transactions on Energy Conversion*, vol. 21, no. 1, pp. 95–103, Mar. 2006.

[80] J. Cros and P. Viarouge, "Synthesis of high performance pm motors with concentrated windings," *IEEE Transactions on Energy Conversion*, vol. 17, no. 2, pp. 248–253, Jun. 2002.

[81] F. Magnussen and C. Sadarangani, "Winding factors and joule losses of permanent magnet machines with concentrated windings," in *IEEE International Electric Machines and Drives Conference, 2003. IEMDC'03.*, vol. 1, IEEE, 2003, pp. 333–339.

[82] R. Carlson, M. Lajoie-Mazenc, and J. Fagundes, "Analysis of torque ripple due to phase commutation in brushless dc machines," *IEEE Transactions on Industry Applications*, vol. 28, no. 3, pp. 632–638, 1992.

[83] Byoung-Hee Kang, Choel-Ju Kim, Hyung-Su Mok, and Gyu-Ha Choe, "Analysis of torque ripple in bldc motor with commutation time," in *ISIE 2001. 2001 IEEE International Symposium on Industrial Electronics Proceedings (Cat. No.01TH8570)*, vol. 2, IEEE, 2001, pp. 1044–1048.

[84] C. Chan, J. Jiang, G. Chen, and X. Wang, "A novel high power density permanent magnet variable-speed motor," *IEEE Transactions on Energy Conversion*, vol. 8, no. 2, pp. 297–303, Jun. 1993.

[85] S. Huang, F. Leonardi, and T. Lipo, "A general approach to sizing and power density equations for comparison of electrical machines," in *IAS '96. Conference Record of the 1996 IEEE Industry Applications Conference Thirty-First IAS Annual Meeting*, vol. 2, IEEE, 1996, pp. 836–842.

[86] F. Leonardi and T. Lipo, "A comparison of power density for axial flux machines based on general purpose sizing equations," *IEEE Transactions on Energy Conversion*, vol. 14, no. 2, pp. 185–192, Jun. 1999.

[87] K. Sitapati and R. Krishnan, "Performance comparisons of radial and axial field, permanent-magnet, brushless machines," *IEEE Transactions on Industry Applications*, vol. 37, no. 5, pp. 1219–1226, 2001.

[88] T. Miura, S. Chino, M. Takemoto, and S. Ogasawara, "A ferrite permanent magnet axial gap motor with segmented rotor structure for the next generation hybrid vehicle," in *The XIX International Conference on Electrical Machines - ICEM 2010*, IEEE, Sep. 2010, pp. 1–6.

[89] S. Kahourzade, A. Mahmoudi, A. Gandomkar, N. A. Rahim, H. W. Ping, and M. N. Uddin, "Design optimization and analysis of afpm synchronous machine incorporating power density, thermal analysis, and back-emf thd," en, *Progress In Electromagnetics Research*, vol. 136, pp. 327–367, 2013.

[90] Y. Kano, T. Kosaka, and N. Matsui, "A simple nonlinear magnetic analysis for axial-flux permanent-magnet machines," *IEEE Transactions on Industrial Electronics*, vol. 57, no. 6, pp. 2124–2133, Jun. 2010.

[91] G. De Donato, F. G. Capponi, and F. Caricchi, "No-load performance of axial flux permanent magnet machines mounting magnetic wedges," *IEEE Transactions on Industrial Electronics*, vol. 59, no. 10, pp. 3768–3779, Oct. 2012.

[92] R. Ni, G. Wang, X. Gui, and D. Xu, "Investigation of d and q -axis inductances influenced by slot-pole combinations based on axial flux permanent-magnet machines," *IEEE Transactions on Industrial Electronics*, vol. 61, no. 9, pp. 4539–4551, Sep. 2014.

[93] T. Zhou, Y. Huang, J. Dong, B. Guo, and L. Zhang, "Design and modeling of axial flux permanent magnet machine with yokeless and segment armature using magnetic equivalent circuit," in *2014 17th International Conference on Electrical Machines and Systems (ICEMS)*, IEEE, Oct. 2014, pp. 618–623.

[94] O. Maloberti, R. Figueredo, C. Marchand, Y. Choua, D. Condamin, L. Kobylanski, and E. Bomme, "3d-2d dynamic magnetic modeling of an axial flux permanent magnet motor with soft magnetic composites for hybrid electric vehicles," *IEEE Transactions on Magnetics*, vol. 50, no. 6, pp. 1–11, Jun. 2014.

[95] A. Parviainen, M. Niemela, and J. Pyrhonen, "Modeling of axial flux permanent-magnet machines," *IEEE Transactions on Industry Applications*, vol. 40, no. 5, pp. 1333–1340, Sep. 2004.

[96] B. Xia, J.-X. Shen, P. C.-K. Luk, and W. Fei, "Comparative study of air-cored axial-flux permanent-magnet machines with different stator winding configurations," *IEEE Transactions on Industrial Electronics*, vol. 62, no. 2, pp. 846–856, Feb. 2015.

[97] T. M. Jahns, "Torque production in permanent-magnet synchronous motor drives with rectangular current excitation," *IEEE Transactions on Industry Applications*, vol. IA-20, no. 4, pp. 803–813, Jul. 1984.

[98] P. Pillay and R. Krishnan, "Modeling, simulation, and analysis of permanent magnet motor drives. ii. the brushless dc motor drive," *IEEE Transactions on Industry Applications*, vol. 25, no. 2, pp. 274–279, 1989.

[99] P. Luk and C. Lee, “Efficient modelling for a brushless dc motor drive,” in *Proceedings of IECON’94 - 20th Annual Conference of IEEE Industrial Electronics*, vol. 1, IEEE, 1994, pp. 188–191.

[100] C. Chan, J. Jiang, W. Xia, and K. Chan, “Novel wide range speed control of permanent magnet brushless motor drives,” *IEEE Transactions on Power Electronics*, vol. 10, no. 5, pp. 539–546, 1995.

[101] S. Safi, “Analysis and simulation of the high-speed torque performance of brushless dc motor drives,” *IEE Proceedings - Electric Power Applications*, vol. 142, no. 3, p. 191, 1995.

[102] D.-K. Kim, K.-W. Lee, and B.-I. Kwon, “Commutation torque ripple reduction in a position sensorless brushless dc motor drive,” *IEEE Transactions on Power Electronics*, vol. 21, no. 6, pp. 1762–1768, Nov. 2006.

[103] T.-Y. Kim, B.-K. Lee, and C.-Y. Won, “Modeling and simulation of multiphase bldc motor drive systems for autonomous underwater vehicles,” in *2007 IEEE International Electric Machines & Drives Conference*, vol. 2, IEEE, May 2007, pp. 1366–1371.

[104] L. D. L. Deng, P. L. P. Liu, Q. F. Q. Fu, Q. Z. Q. Zheng, and H. L. H. Liu, “Study on commutation for permanent magnet brushless dc motor,” in *2008 World Automation Congress*, 2008, pp. 1–4.

[105] C.-T. Pan and E. Fang, “A phase-locked-loop-assisted internal model adjustable-speed controller for bldc motors,” *IEEE Transactions on Industrial Electronics*, vol. 55, no. 9, pp. 3415–3425, Sep. 2008.

[106] N. Samoylenko and J. Jatskevich, “Dynamic performance of brushless dc motors with unbalanced hall sensors,” *IEEE Transactions on Energy Conversion*, vol. 23, no. 3, pp. 752–763, Sep. 2008.

[107] M.-F. Tsai, T. P. Quy, B.-F. Wu, and C.-S. Tseng, “Model construction and verification of a bldc motor using matlab/simulink and fpga control,” in *2011 6th IEEE Conference on Industrial Electronics and Applications*, IEEE, Jun. 2011, pp. 1797–1802.

[108] Y. Jeon, H. Mok, G. Choe, D. Kim, and J. Ryu, “A new simulation model of bldc motor with real back emf waveform,” in *COMPEL 2000. 7th Workshop on Computers in Power Electronics. Proceedings*, IEEE, 2000, pp. 217–220.

[109] O. Mohammed, S. Liu, and Z. Liu, "A phase variable model of brushless dc motors based on finite element analysis and its coupling with external circuits," *IEEE Transactions on Magnetics*, vol. 41, no. 5, pp. 1576–1579, May 2005.

[110] J. Chen, Y. Guo, J. Zhu, and J. Jin, "Performance analysis of a surface mounted permanent magnet brushless dc motor using an improved phase variable model," in *2007 IEEE Industry Applications Annual Meeting*, IEEE, Sep. 2007, pp. 2169–2174.

[111] W. Hong, W. Lee, and B.-K. Lee, "Dynamic simulation of brushless dc motor drives considering phase commutation for automotive applications," in *2007 IEEE International Electric Machines & Drives Conference*, vol. 2, IEEE, May 2007, pp. 1377–1383.

[112] M. Fazil and K. R. Rajagopal, "Nonlinear dynamic modeling of a single-phase permanent-magnet brushless dc motor using 2-d static finite-element results," *IEEE Transactions on Magnetics*, vol. 47, no. 4, pp. 781–786, Apr. 2011.

[113] L. Queval and H. Ohsaki, "Nonlinear abc-model for electrical machines using n-d lookup tables," *IEEE Transactions on Energy Conversion*, vol. 30, no. 1, pp. 316–322, Mar. 2015.

[114] Q. Han, N. Samoylenko, and J. Jatskevich, "Average-value modeling of brushless dc motors with 120 deg voltage source inverter," *IEEE Transactions on Energy Conversion*, vol. 23, no. 2, pp. 423–432, Jun. 2008.

[115] K. Tabarraee, J. Iyer, and J. Jatskevich, "Average-value modeling of brushless dc motors with trapezoidal back-emf," in *2011 IEEE International Symposium on Industrial Electronics*, IEEE, Jun. 2011, pp. 531–537.

[116] M. Jagiela, T. Garbiec, J. Gwozdz, and J. Kolodziej, "Fast steady-state field-circuit model for smpm-bldc motors driven from 120 deg and 180 deg quasi-square wave inverters," *IEEE Transactions on Magnetics*, vol. PP, no. 99, pp. 1–1, 2015.

[117] P. Damodharan and K. Vasudevan, "Sensorless brushless dc motor drive based on the zero-crossing detection of back electromotive force (emf) from the line voltage difference," *IEEE Transactions on Energy Conversion*, vol. 25, no. 3, pp. 661–668, Sep. 2010.

[118] C. Xia, Y. Wang, and T. Shi, "Implementation of finite-state model predictive control for commutation torque ripple minimization of permanent magnet brushless dc motor," *IEEE Transactions on Industrial Electronics*, vol. 60, no. 3, pp. 896–905, Mar. 2013.

[119] Z. Zhu, "Fractional slot permanent magnet brushless machines and drives for electric and hybrid propulsion systems," en, *COMPEL - The international journal for computation and mathematics in electrical and electronic engineering*, vol. 30, no. 1, A. Masmoudi, Ed., pp. 9–31, Jan. 2011.

[120] G. De Donato, F. Giulii Capponi, A. Rivellini, and F. Caricchi, "Integer-slot vs fractional-slot concentrated-winding axial-flux permanent magnet machines: comparative design, fea and experimental tests," in *2011 IEEE Energy Conversion Congress and Exposition*, IEEE, Sep. 2011.

[121] G. De Donato, F. Giulii Capponi, G. A. Rivellini, and F. Caricchi, "Integral slot versus fractional slot concentrated-winding axial flux permanent magnet machines: comparative design, fea, and experimental tests," *IEEE Transactions on Industry Applications*, vol. 48, no. 5, pp. 1487–1495, Sep. 2012.

[122] A. EL-Refaie, "Fractional-slot concentrated-windings synchronous permanent magnet machines: opportunities and challenges," *IEEE Transactions on Industrial Electronics*, vol. 57, no. 1, pp. 107–121, Jan. 2010.

[123] O. Bottauscio, G. Pellegrino, P. Guglielmi, M. Chiampi, and A. Vagati, "Rotor loss estimation in permanent magnet machines with concentrated windings," *IEEE Transactions on Magnetics*, vol. 41, no. 10, pp. 3913–3915, Oct. 2005.

[124] D. Ishak, Z. Zhu, and D. Howe, "Eddy-current loss in the rotor magnets of permanent-magnet brushless machines having a fractional number of slots per pole," *IEEE Transactions on Magnetics*, vol. 41, no. 9, pp. 2462–2469, Sep. 2005.

[125] M. Nakano, H. Kometani, and M. Kawamura, "A study on eddy-current losses in rotors of surface permanent-magnet synchronous machines," *IEEE Transactions on Industry Applications*, vol. 42, no. 2, pp. 429–435, Mar. 2006.

[126] N. Bianchi and E. Fornasiero, “Impact of mmf space harmonic on rotor losses in fractional-slot permanent-magnet machines,” *IEEE Transactions on Energy Conversion*, vol. 24, no. 2, pp. 323–328, Jun. 2009.

[127] E. Fornasiero, N. Bianchi, and S. Bolognani, “Slot harmonic impact on rotor losses in fractional-slot permanent-magnet machines,” *IEEE Transactions on Industrial Electronics*, vol. 59, no. 6, pp. 2557–2564, Jun. 2012.

[128] J. Pyrhonen, H. Jussila, Y. Alexandrova, P. Rafajdus, and J. Nerg, “Harmonic loss calculation in rotor surface permanent magnets-new analytic approach,” *IEEE Transactions on Magnetics*, vol. 48, no. 8, pp. 2358–2366, Aug. 2012.

[129] L. Wu, R. Qu, and D. Li, “Reduction of rotor eddy-current losses for surface pm machines with fractional slot concentrated windings and retaining sleeve,” *IEEE Transactions on Magnetics*, vol. 50, no. 11, pp. 1–4, Nov. 2014.

[130] L. Chu, G.-l. Li, Z. Qian, and W.-x. Yin, “Analysis of eddy current loss on permanent magnets in pmsm with fractional slot,” in *2015 IEEE 10th Conference on Industrial Electronics and Applications (ICIEA)*, IEEE, Jun. 2015, pp. 1246–1250.

[131] A. Masmoudi and A. Masmoudi, “3-d analytical model with the end effect dedicated to the prediction of pm eddy-current loss in fspmms,” *IEEE Transactions on Magnetics*, vol. 51, no. 4, pp. 1–11, Apr. 2015.

[132] A. Cassat, C. Espanet, and N. Wavre, “Bldc motor stator and rotor iron losses and thermal behavior based on lumped schemes and 3-d fem analysis,” *IEEE Transactions on Industry Applications*, vol. 39, no. 5, pp. 1314–1322, Sep. 2003.

[133] N. Bianchi, D. Durello, and A. Fasolo, “Relationship between rotor losses and size of permanent-magnet machines,” *IEEE Transactions on Industry Applications*, vol. 49, no. 5, pp. 2015–2023, Sep. 2013.

[134] G. Bertotti, “General properties of power losses in soft ferromagnetic materials,” *IEEE Transactions on Magnetics*, vol. 24, no. 1, pp. 621–630, 1988.

[135] G. Slemon and X. Liu, “Core losses in permanent magnet motors,” *IEEE Transactions on Magnetics*, vol. 26, no. 5, pp. 1653–1655, 1990.

[136] G. Ugalde, Z. Zhu, J. Poza, and A. Gonzalez, "Analysis of rotor eddy current loss in fractional slot permanent magnet machine with solid rotor back-iron," in *The XIX International Conference on Electrical Machines - ICEM 2010*, IEEE, Sep. 2010, pp. 1–6.

[137] A. Cavagnino, M. Lazzari, A. Miotto, A. Tenconi, and S. Vaschetto, "Impact of the rotor back-iron resistivity on the rotor eddy-current losses in fractional-slot concentrated windings pm machines," in *2011 IEEE Energy Conversion Congress and Exposition*, IEEE, Sep. 2011, pp. 1604–1611.

[138] Z. Zhu, K. Ng, N. Schofield, and D. Howe, "Improved analytical modelling of rotor eddy current loss in brushless machines equipped with surface-mounted permanent magnets," *IEE Proceedings - Electric Power Applications*, vol. 151, no. 6, p. 641, 2004.

[139] H. Polinder, M. Hoeijmakers, and M. Scuotto, "Eddy-current losses in the solid back-iron of pm machines for different concentrated fractional pitch windings," in *2007 IEEE International Electric Machines & Drives Conference*, vol. 1, IEEE, May 2007, pp. 652–657.

[140] N. Bianchi, S. Bolognani, and E. Fomasiero, "A general approach to determine the rotor losses in three-phase fractional-slot pm machines," in *2007 IEEE International Electric Machines & Drives Conference*, vol. 1, IEEE, May 2007, pp. 634–641.

[141] L. Alberti, E. Fornasiero, and N. Bianchi, "Impact of the rotor yoke geometry on rotor losses in permanent-magnet machines," *IEEE Transactions on Industry Applications*, vol. 48, no. 1, pp. 98–105, Jan. 2012.

[142] R. Di Stefano and F. Marignetti, "Electromagnetic analysis of axial-flux permanent magnet synchronous machines with fractional windings with experimental validation," *IEEE Transactions on Industrial Electronics*, vol. 59, no. 6, pp. 2573–2582, Jun. 2012.

[143] J. Li, D.-W. Choi, D.-H. Son, and Y.-H. Cho, "Effects of mmf harmonics on rotor eddy-current losses for inner-rotor fractional slot axial flux permanent magnet synchronous machines," *IEEE Transactions on Magnetics*, vol. 48, no. 2, pp. 839–842, Feb. 2012.

[144] J. Wang, H. Lin, H. Li, S. Fang, Y. Huang, J. Dong, and H. Yang, "Linear representation of saturation characteristics associated with eddy currents in ferromagnetic materials," *IEEE Transactions on Magnetics*, vol. 50, no. 2, pp. 121–124, Feb. 2014.

[145] N. Schofield, "Parasitic rotor losses in a brushless permanent magnet traction machine," in *Eighth International Conference on Electrical Machines and Drives*, vol. 1997, IEE, 1997, pp. 200–204.

[146] H. Toda, Z. Xia, J. Wang, K. Atallah, and D. Howe, "Rotor eddy-current loss in permanent magnet brushless machines," *IEEE Transactions on Magnetics*, vol. 40, no. 4, pp. 2104–2106, Jul. 2004.

[147] A. Jassal, H. Polinder, D. Lahaye, and J. Ferreira, "Comparison of analytical and finite element calculation of eddy-current losses in pm machines," in *The XIX International Conference on Electrical Machines - ICEM 2010*, IEEE, Sep. 2010, pp. 1–7.

[148] D. Liu, A. Jassal, H. Polinder, and J. Ferreira, "Validation of eddy current loss models for permanent magnet machines with fractional-slot concentrated windings," in *2013 International Electric Machines & Drives Conference*, IEEE, May 2013, pp. 678–685.

[149] R.-J. Wang and M. Kamper, "Calculation of eddy current loss in axial field permanent-magnet machine with coreless stator," *IEEE Transactions on Energy Conversion*, vol. 19, no. 3, pp. 532–538, Sep. 2004.

[150] P. Lawrenson, P. Reece, and M. Ralph, "Tooth-ripple losses in solid poles," *Proceedings of the Institution of Electrical Engineers*, vol. 113, no. 4, p. 657, 1966.

[151] K. Oberretl, "Eddy current losses in solid pole shoes of synchronous machines at no-load and on load," *IEEE Transactions on Power Apparatus and Systems*, vol. PAS-91, no. 1, pp. 152–160, Jan. 1972.

[152] L. Alberti, E. Fornasiero, N. Bianchi, and S. Bolognani, "Rotor losses measurements in an axial flux permanent magnet machine," *IEEE Transactions on Energy Conversion*, vol. 26, no. 2, pp. 639–645, Jun. 2011.

[153] T. Sebastian, "Temperature effects on torque production and efficiency of pm motors using ndfeb magnets," *IEEE Transactions on Industry Applications*, vol. 31, no. 2, pp. 353–357, 1995.

[154] S. Ruoho and A. Arkkio, "Partial demagnetization of permanent magnets in electrical machines caused by an inclined field," *IEEE Transactions on Magnetics*, vol. 44, no. 7, pp. 1773–1778, Jul. 2008.

[155] S. Ruoho, J. Kolehmainen, J. Ikaheimo, and A. Arkkio, "Interdependence of demagnetization, loading, and temperature rise in a permanent-magnet synchronous motor," *IEEE Transactions on Magnetics*, vol. 46, no. 3, pp. 949–953, Mar. 2010.

[156] C. Kral, R. Sprangers, J. Waarma, A. Haumer, O. Winter, and E. Lomonova, "Modeling demagnetization effects in permanent magnet synchronous machines," in *The XIX International Conference on Electrical Machines - ICEM 2010*, IEEE, Sep. 2010, pp. 1–6.

[157] K. Sone, M. Takemoto, S. Ogasawara, K. Takezaki, and H. Akiyama, "A ferrite pm in-wheel motor without rare earth materials for electric city commuters," *IEEE Transactions on Magnetics*, vol. 48, no. 11, pp. 2961–2964, Nov. 2012.

[158] H.-s. Kim, Y.-M. You, and B.-i. Kwon, "Rotor shape optimization of interior permanent magnet bldc motor according to magnetization direction," *IEEE Transactions on Magnetics*, vol. 49, no. 5, pp. 2193–2196, May 2013.

[159] H.-W. Kim, K.-T. Kim, Y.-S. Jo, and J. Hur, "Optimization methods of torque density for developing the neodymium free spoke-type bldc motor," *IEEE Transactions on Magnetics*, vol. 49, no. 5, pp. 2173–2176, May 2013.

[160] M. M. Rahman, K. T. Kim, and J. Hur, "Design and optimization of neodymium-free spoke-type motor with segmented wing-shaped pm," *IEEE Transactions on Magnetics*, vol. 50, no. 2, pp. 865–868, Feb. 2014.

[161] S.-M. Jang, H.-J. Seo, Y.-S. Park, H.-I. Park, and J.-Y. Choi, "Design and electromagnetic field characteristic analysis of 1.5 kw small scale wind power generator for substitution of nd-fe-b to ferrite permanent magnet," *IEEE Transactions on Magnetics*, vol. 48, no. 11, pp. 2933–2936, Nov. 2012.

[162] M. R. Mohammad, K.-T. Kim, and J. Hur, "Design and analysis of a spoke type motor with segmented pushing permanent magnet for concentrating air-gap flux density," *IEEE Transactions on Magnetics*, vol. 49, no. 5, pp. 2397–2400, May 2013.

[163] P. Sekerak, V. Hrabovcova, J. Pyrhonen, L. Kalamen, P. Rafajdus, and M. Onufer, "Comparison of synchronous motors with different permanent magnet and winding types," *IEEE Transactions on Magnetics*, vol. 49, no. 3, pp. 1256–1263, Mar. 2013.

[164] D. G. Dorrell, M.-F. Hsieh, and A. M. Knight, "Alternative rotor designs for high performance brushless permanent magnet machines for hybrid electric vehicles," *IEEE Transactions on Magnetics*, vol. 48, no. 2, pp. 835–838, Feb. 2012.

[165] O. Craiu, N. Dan, and E. Badea, "Numerical analysis of permanent magnet dc motor performances," *IEEE Transactions on Magnetics*, vol. 31, no. 6, pp. 3500–3502, 1995.

[166] I. Petrov, M. Polikarpova, and J. Pyrhonen, "Rotor surface ferrite magnet synchronous machine for generator use in a hybrid application-electromagnetic and thermal analysis," in *IECON 2013 - 39th Annual Conference of the IEEE Industrial Electronics Society*, IEEE, Nov. 2013, pp. 3090–3095.

[167] C. Debruyne, M. Polikarpova, S. Derammelaere, P. Sergeant, J. Pyrhonen, J. J. M. Desmet, and L. Vandevelde, "Evaluation of the efficiency of line-start permanent-magnet machines as a function of the operating temperature," *IEEE Transactions on Industrial Electronics*, vol. 61, no. 8, pp. 4443–4454, Aug. 2014.

[168] K.-C. Kim, S.-B. Lim, D.-H. Koo, and J. Lee, "The shape design of permanent magnet for permanent magnet synchronous motor considering partial demagnetization," *IEEE Transactions on Magnetics*, vol. 42, no. 10, pp. 3485–3487, Oct. 2006.

[169] T. Higashi, T. Miyoshi, R. Kato, M. Kono, M. Inoue, T. Nagumo, T. Fukui, K. Ohsaki, and M. Iwasaki, "Development of rare earth-saving magnet using localized diffusion method," *SAE Int. J. Alt. Power*, vol. 2, no. 2, pp. 394–400, Apr. 2013.

[170] W. Fei and P. Luk, "Cogging torque reduction techniques for axial flux surface mounted permanent magnet segmented armature torus machines," in *2008 IEEE International Symposium on Industrial Electronics*, IEEE, Jun. 2008, pp. 485–490.

[171] M. Doppelbauer, "Numerical iron loss calculation of a new axial flux machine with segmented-armature-torus topology," in *7th IET International Conference on Power Electronics, Machines and Drives (PEMD 2014)*, Institution of Engineering and Technology, 2014, pp. 0377–0377.

[172] J. F. Gieras, R.-J. Wang, and M. J. Kamper, *Axial Flux Permanent Magnet Brushless Machines*. Dordrecht: Springer Netherlands, 2008.

[173] F. Sahin, "Design and development of a high speed axial flux permanent magnet machine," PhD thesis, University of eindhoven, 2001.

[174] Fang Deng, "An improved iron loss estimation for permanent magnet brushless machines," *IEEE Transactions on Energy Conversion*, vol. 14, no. 4, pp. 1391–1395, 1999.

[175] *Thermnet help*, 2014.

[176] D. Staton, A. Boglietti, and A. Cavagnino, "Solving the more difficult aspects of electric motor thermal analysis," in *IEMDC 2003 - IEEE International Electric Machines and Drives Conference*, vol. 2, 2003, pp. 747–755.

[177] Y. Huang, J. Dong, J. Zhu, and Y. Guo, "Core loss modeling for permanent magnet motor based on flux variation locus and finite-element method," *IEEE Transactions on Magnetics*, vol. 48, no. 2, pp. 1023–1026, Feb. 2012.

[178] R. Wrobel and G. Vainel, "Investigation of mechanical loss and heat transfer in an axial-flux pm machine," *Energy Conversion Congress and Exposition (ECCE), 2013 IEEE*, 2013.

[179] R. Wrobel, G. Vainel, C. Copeland, T. Duda, D. Staton, and P. H. Mellor, "Investigation of mechanical loss components and heat transfer in an axial-flux pm machine," *IEEE Transactions on Industry Applications*, vol. 51, no. 4, pp. 3000–3011, Jul. 2015.

Appendix A

Derivations of formulae

A.1 Expression for slot area

An expression for slot area can be obtained from the output power equation of three-phase PMBLDC motor as

$$\begin{aligned}
P_{\mathrm{r}} &= 2E_{\mathrm{ph}}I_{\mathrm{ph}} \\
&= 2\left(P\phi Z\frac{N_{\mathrm{r}}}{60}\frac{1}{A}\right)\left(\frac{\pi}{4}D_{\mathrm{ct}}^2JA\right) \\
&= 2\left[B_{\mathrm{g}}\frac{\pi}{4}\left(D_{\mathrm{os}}^2-D_{\mathrm{is}}^2\right)\frac{2N_{\mathrm{c}}N_{\mathrm{s}}}{2\times 3}\frac{N_{\mathrm{r}}}{60}\right]\left(\frac{\pi}{4}D_{\mathrm{ct}}^2J\right) \\
&= \left[\frac{N_{\mathrm{s}}}{3\times 4}B_{\mathrm{g}}J\left(D_{\mathrm{os}}^2-D_{\mathrm{is}}^2\right)\frac{2\pi N_{\mathrm{r}}}{60}\right]\left(N_{\mathrm{c}}\frac{\pi}{4}D_{\mathrm{ct}}^2\right) \\
&= \left[\frac{N_{\mathrm{s}}}{12}JB_{\mathrm{g}}\left(D_{\mathrm{os}}^2-D_{\mathrm{is}}^2\right)\omega_{\mathrm{r}}\right](K_{\mathrm{sff}}\times\text{Slot area})
\end{aligned}$$

$P_{\mathrm{r}}/\omega_{\mathrm{r}}=T_{\mathrm{r}}$, is the rated torque. Therefore, slot area is

$$\text{Slot area}=\frac{12T_{\mathrm{r}}}{K_{\mathrm{sff}}N_{\mathrm{s}}JB_{\mathrm{g}}\left(D_{\mathrm{os}}^2-D_{\mathrm{is}}^2\right)}$$

Appendix B

Implementation of design program

B.1 Overview of design program

The design program was implemented using three platforms as shown in Figure B.1. The search program uses genetic algorithm to find a least copper loss

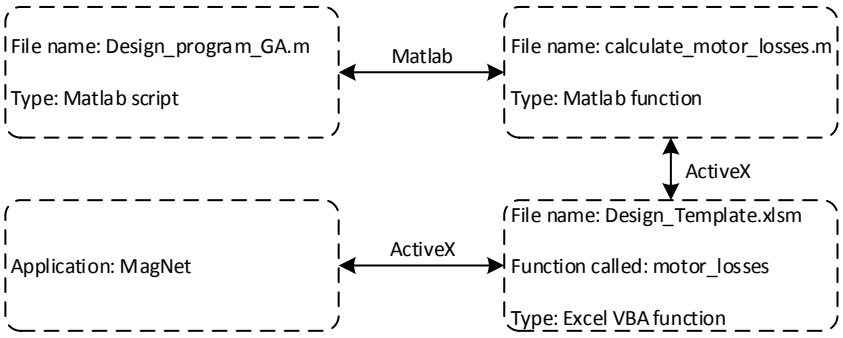

Figure B.1: An overview of implementation of design program

design and it is implemented in a Matlab script file named Design_program_GA.m. The objective function of the genetic algorithm is a custom Matlab function named calculate_motor_losses.m. The objective function uses ActiveX interface to call an Excel VBA function named motor_losses, which is written inside a module of an Excel file named Design_Template.xlsm. The Excel file

Design_Template.xlsm has a number of functions implemented to synthesis a design of SAT PMBLDC motor based on the values of design variables. The VBA functions uses an FE model. The Excel file Design_Template.xlsm uses ActiveX interface to call electromagnetic field simulation package named Mag-Net. The following sections lists the Matlab and Excel VBA code used in the design synthesis program.

B.2 Matlab implementation of design optimisation

File name: Design_program_GA.m

```
% Using the Mixed-Integer Genetic Algorithm
%-----------------------------------------
%Parameter names are explained in Design_Template.xlsm
clear; clc;

%Independant variable that will be optimised
%[Lm,h,lambda_d]
Lm =(5:0.2:10)';
h =(0:0.025:0.3)';
lamda_d=(0.4:0.02:0.8)';

%[Lm,beta,h,lambda_d]
lowerbound = [3,0,0.4];
upperbound = [10,0.5,0.8];
initial_value= [5,0.1,0.6];

motor_function=@(x)calculate_motor_losses(x(1),x(2),x(3));

opts = optimoptions(@fmincon,'Algorithm','interior-point');

problem = createOptimProblem('fmincon','x0',initial_value,...
    'objective',motor_function,'lb',lowerbound,'ub',upperbound,'options',opts)↩
        ;

gs = GlobalSearch('Display','iter', 'MaxTime',60*60*1, 'TolFun',0.1,...
    'TolX',0.1,'PlotFcns',{@gsplotfunccount,@gsplotbestf});

tic

[xmin,fmin,flag,outpt,allmins] = run(gs,problem);

end_time = toc;
```

B.3 Objective function of optimisation

File name: calculate_motor_losses.m

```
function losses  = calculate_motor_losses (Lm,h,lambda_d)
    % Only copper losses are being considered at present
    Dos = 225;
    P = 16;
    S = 18;
    Lg = 0.4;
    SFg = 0.5;
    Wso = 1;
    Lsl = 2;
    Lsm = 2;
    J = 4.5;
    beta = 1;

    ex = actxserver('Excel.Application');
    wb = ex.Workbooks.Open('D:\Design program\Design_Template.xlsm');
    losses = ex.Run('motor_losses',Dos, P, S, Lg, SFg, Wso, Lsl, Lsm, J, Lm, ↩
        beta, h, lambda_d);
    invoke(wb, 'SaveAs','D:\Design program\Design_Template.xlsm');
    wb.Saved = 1;
    invoke(wb, 'Close');
    ex.Quit;
    ex.delete;
```

B.4 Functions implemented in Excel VBA

The following sections of the VBA code refers to two sheets 'Design_Details' shown in Figure B.2 and 'Iterations' shown in Figure B.3.

```
Option Explicit

'OBJECTS TO ACCESS THE MagNet
    Dim mn, mndoc, mnview, mnc, mnmsh, mnuf As Object

'CONSTANTS
    Const Pi = 3.14159265358979


'DESIGN VARIABLES
'================
'Motor spec
    Dim Vr, Nr, Pr
'Iteration
    Dim iter As Integer
    Dim fsym As Integer
```

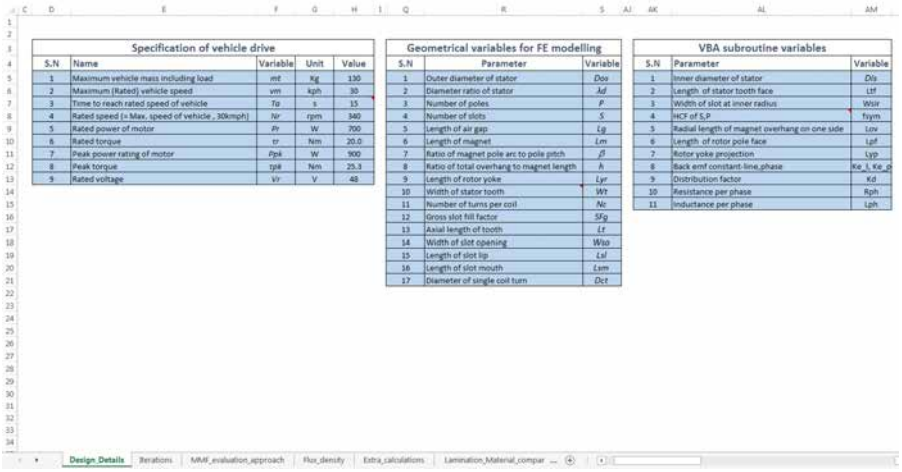

Specification of vehicle drive

S.N	Name	Variable	Unit	Value
1	Maximum vehicle mass including load	*mt*	Kg	130
2	Maximum (Rated) vehicle speed	*vm*	kph	30
3	Time to reach rated speed of vehicle	*To*	s	15
4	Rated speed (= Max. speed of vehicle , 30kmph)	*Nr*	rpm	340
5	Rated power of motor	*Pr*	W	700
6	Rated torque	*tr*	Nm	20.0
7	Peak power rating of motor	*Ppk*	W	900
8	Peak torque	*tpk*	Nm	25.3
9	Rated voltage	*Vr*	V	48

Geometrical variables for FE modelling

S.N	Parameter	Variable
1	Outer diameter of stator	*Dos*
2	Diameter ratio of stator	*λd*
3	Number of poles	*P*
4	Number of slots	*S*
5	Length of air gap	*Lg*
6	Length of magnet	*Lm*
7	Ratio of magnet pole arc to pole pitch	*β*
8	Ratio of total overhang to magnet length	*h*
9	Length of rotor yoke	*Lyr*
10	Width of stator tooth	*Wt*
11	Number of turns per coil	*Nc*
12	Gross slot fill factor	*SFg*
13	Axial length of tooth	*Lt*
14	Width of slot opening	*Wso*
15	Length of slot lip	*Lsl*
16	Length of slot mouth	*Lsm*
17	Diameter of single coil turn	*Dct*

VBA subroutine variables

S.N	Parameter	Variable
1	Inner diameter of stator	*Dis*
2	Length of stator tooth face	*Ltf*
3	Width of slot at inner radius	*Wsir*
4	HCF of S,P	*fsym*
5	Radial length of magnet overhang on one side	*Lov*
6	Length of rotor pole face	*Lpf*
7	Rotor yoke projection	*Lyp*
8	Back emf constant-line,phase	*Ke_l, Ke_p*
9	Distribution factor	*Kd*
10	Resistance per phase	*Rph*
11	Inductance per phase	*Lph*

Design_Details | Iterations | MMF_evaluation_approach | Flux_density | Extra_calculations | Lamination_Material_compar ...

Figure B.2: Sheet-1 of Excel file used in the design program

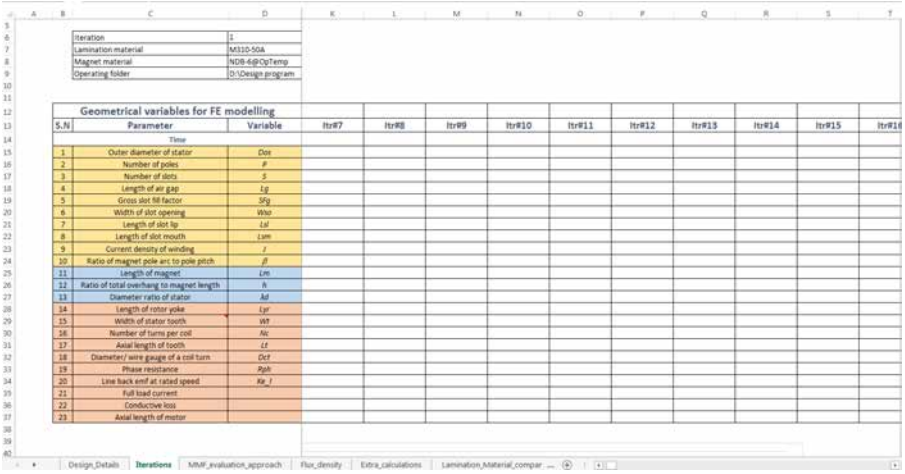

Iteration	1
Lamination material	M310-50A
Magnet material	NDB-6@OpTemp
Operating folder	D:\Design program

Geometrical variables for FE modelling

S.N	Parameter	Variable	Itr#7	Itr#8	Itr#9	Itr#10	Itr#11	Itr#12	Itr#13	Itr#14	Itr#15	Itr#16
	Time											
1	Outer diameter of stator	*Dos*										
2	Number of poles	*P*										
3	Number of slots	*S*										
4	Length of air gap	*Lg*										
5	Gross slot fill factor	*SFg*										
6	Width of slot opening	*Wso*										
7	Length of slot lip	*Lsl*										
8	Length of slot mouth	*Lsm*										
9	Current density of winding	*J*										
10	Ratio of magnet pole arc to pole pitch	*β*										
11	Length of magnet	*Lm*										
12	Ratio of total overhang to magnet length	*h*										
13	Diameter ratio of stator	*λd*										
14	Length of rotor yoke	*Lyr*										
15	Width of stator tooth	*Wt*										
16	Number of turns per coil	*Nc*										
17	Axial length of tooth	*Lt*										
18	Diameter/ wire gauge of a coil turn	*Dct*										
19	Phase resistance	*Rph*										
20	Line back emf at rated speed	*Ke_l*										
21	Full load current											
22	Conductive loss											
23	Axial length of motor											

Design_Details | Iterations | MMF_evaluation_approach | Flux_density | Extra_calculations | Lamination_Material_compar ...

Figure B.3: Sheet-2 of Excel file used in the design program

```
'STATOR
'base variables
    Dim S, Nc As Integer
    Dim Dos, lambda_d, Wt, SFg, Lt, Wso, Lsl, Lsm As Double
    Dim MatTooth, MatMagnet As String
    Dim WGi, J

'derived variables
    Dim Dis, Ltf, Wsir, Dct

'ROTOR
```

```
'base variables
    Dim P As Integer
    Dim Lg, Lm, beta, h, Lyr As Double
'derived variables
    Dim Lov, Lpf

'PROGRAM VARIABLES
'=================
    Dim Wr As Double     ' Angular velocity
    Dim WG As Variant    ' Wire diameters stored in gauge order
    Dim CompName, Path
    Dim i     'Loop variable
    Dim RotationAxis, Center
    Dim B_face       'Boundary face
    Dim max_B, av_Bg     'Maximum flux density of rotor yoke and avearage air ↩
        gap flux density
    Dim area_w, area_s   ' Winding and slot area
    Dim area_s_av, Lw      'Area and length of slot available for winding
    Dim del_rotor_pos    'Rotor position correction needed to capture flux ↩
        linkage corresponding to switching position
    Dim Lyp      'Rotor yoke projection
    Dim Ke_l, Ke_p, Kd
    Dim Rph
    Dim Pit, Iit, Ebit, Jit 'Iterative value of power, current, back emf and ↩
        current density
    Dim logfile, file_path As String
    Dim temp     'temperory variable
    Dim R_s, Theta_m, Z_s ' Sampling radius, maximum angle and sampling z co-↩
        ordinate
    Dim fl_sampling_point, sample_ang  'Flux linkage sampling point

Sub Start_MagNet_program()
    Set mn = CreateObject("MagNet.application")
    mn.Visible = False
    mn.setWindowRect (1.5 * 1920), 0, 960, 1080
End Sub

Sub Excel_config()
    Application.DisplayAlerts = False ' To prevent "Excel is waiting for ↩
        another application to complete an OLE action" pausing the iteration
    Application.ScreenUpdating = False
End Sub

Sub New_model()
    Set mndoc = mn.newdocument()
    Set mnview = mndoc.getView()
    Set mnc = mn.getConstants
    mndoc.setDefaultLengthUnit ("Millimeters")
    mndoc.setNumberOfMultiCoreSolveThreads (0)
    mn.setSelectionTolerance (1)
    mnview.setScaledToFit (True)
End Sub

Sub Read_motor_spec()
    Vr = Worksheets("Design_Details").Cells(13, 8).Value
```

```
    Nr = Worksheets("Design_Details").Cells(8, 8).Value
    Pr = Worksheets("Design_Details").Cells(9, 8).Value
End Sub

Sub Calculate_secondary_variables()
    Dis = Dos * lambda_d
    Wt = Pi * Dis / (2 * S)
    Lov = 0.25 * h * (Dos - Dis)
    Lpf = (0.5 * Dos + Lov) * Cos(beta * Pi / P) - (0.5 * Dis - Lov) * Cos(↩
        beta * -Pi / P)
    fsym = Excel.WorksheetFunction.Gcd(S, P)
    Wr = 2 * Pi * Nr / 60
    Cal_rotor_pos
End Sub

Sub Create_stator_teeth()
'Tooth tip
    mnview.getSlice.moveInALine 0.5 * Lt
    mnview.newLine 0.5 * Dis * Cos(-Pi / S + Wso / Dis), 0.5 * Dis * Sin(-Pi /↩
        S + Wso / Dis), 0.5 * Dis * Cos(Pi / S - Wso / Dis), 0.5 * Dis * Sin↩
        (Pi / S - Wso / Dis)
    mnview.newLine 0.5 * Dis * Cos(Pi / S - Wso / Dis), 0.5 * Dis * Sin(Pi / S↩
        - Wso / Dis), 0.5 * Dos * Cos(Pi / S - Wso / Dos), 0.5 * Dos * Sin(↩
        Pi / S - Wso / Dos)
    mnview.newLine 0.5 * Dos * Cos(Pi / S - Wso / Dos), 0.5 * Dos * Sin(Pi / S↩
        - Wso / Dos), 0.5 * Dos * Cos(-Pi / S + Wso / Dos), 0.5 * Dos * Sin↩
        (-Pi / S + Wso / Dos)
    mnview.newLine 0.5 * Dos * Cos(-Pi / S + Wso / Dos), 0.5 * Dos * Sin(-Pi /↩
        S + Wso / Dos), 0.5 * Dis * Cos(-Pi / S + Wso / Dis), 0.5 * Dis * ↩
        Sin(-Pi / S + Wso / Dis)

    ReDim CompName(0)
    CompName(0) = "ToothTip"
    mnview.SelectAll mnc.infoSetSelection, mnc.infoSliceSurface
    mnview.makeComponentInALine -Lsl, CompName, "Name=" & MatTooth, mnc.↩
        infoMakeComponentRemoveVertices
    Del_construction_line

'Tooth
    mnview.getSlice.moveToASurface "ToothTip,Face#6"
    mnview.newLine 0, 0, 0, 0.5 * Wt
    mnview.newLine 0, 0.5 * Wt, 0.5 * Lt - Lsl - Lsm, 0.5 * Wt
    mnview.newLine 0.5 * Lt - Lsl - Lsm, 0.5 * Wt, 0.5 * Lt - Lsl, 0.5 * Dis *↩
        Sin(Pi / S - Wso / Dis)
    mnview.newLine 0.5 * Lt - Lsl, 0.5 * Dis * Sin(Pi / S - Wso / Dis), 0.5 * ↩
        Lt - Lsl, 0
    mnview.SelectAll mnc.infoSetSelection, mnc.infoSliceLine
    mnview.mirrorSelectedEdges 0, 0, 1, 0, True

    Ltf = 0.5 * Dis * Cos(Pi / S - Wso / Dis) - 0.5 * Dos * Cos(Pi / S - Wso /↩
        Dos)
    ReDim CompName(0)
    CompName(0) = "Tooth"
    mnview.SelectAll mnc.infoSetSelection, mnc.infoSliceSurface
```

```
    mnview.makeComponentInALine Ltf, CompName, "Name=" & MatTooth, mnc.↩
        infoMakeComponentRemoveVertices
    Del_construction_line

'Union of Tooth tip and tooth in to single component
    ReDim CompName(1)
    CompName(0) = "ToothTip"
    CompName(1) = "Tooth"
    Path = mndoc.unionComponents(CompName, 1)
    mndoc.renameObject Path, "Tooth#1"
    mnview.selectObject "ToothTip", mnc.infoSetSelection
    mnview.selectObject "Tooth", mnc.infoAddToSelection
    mnview.deleteSelection
    mndoc.rotateComponent "Tooth#1", 0, 0, 0, 0, 0, 1, 180 / S, 1
    mndoc.setMaxElementSize "Tooth#1", Lt / 4

'Creating a number teeth for half section model using geometrical symmetry
    For i = 1 To ((S / fsym) - 1)
        mndoc.rotateComponent mndoc.copyComponent("Tooth#1", 1), 0, 0, 0, 0, ↩
            0, 1, i * (360 / S), 1
        mndoc.renameObject "Copy of Tooth#1 #" & i, "Tooth#" & (i + 1)
    Next
    i = 0

End Sub

Sub Create_winding()
    Dim theta, theta1   'Angles corresponding to width of slot bottom and half↩
         tooth width at inner radius
    Dim Wc              ' Coil width
    mnview.getSlice.moveToASurface "Tooth#1,Body#1,Face#5"

    theta1 = Excel.WorksheetFunction.Asin(Wt / Dis)
    theta = 2 * Pi / S - 2 * theta1
    Wsir = Dis * Sin(theta / 2)
    Wc = 0.8 * Wsir     'where 0.8 is a the ratio of width of coil side to ↩
        width slot at inner radius

    mnview.newLine -0.5 * Dis * Cos(Pi / S - Wso / Dis) + Wc, 0, -0.5 * Dis * ↩
        Cos(Pi / S - Wso / Dis) + Wc, 0.5 * Wt + Wc
    mnview.newLine -0.5 * Dis * Cos(Pi / S - Wso / Dis) + Wc, 0.5 * Wt + Wc, ↩
        -0.5 * Dos * Cos(Pi / S - Wso / Dos) - Wc, 0.5 * Wt + Wc
    mnview.newLine -0.5 * Dos * Cos(Pi / S - Wso / Dos) - Wc, 0.5 * Wt + Wc, ↩
        -0.5 * Dos * Cos(Pi / S - Wso / Dos) - Wc, 0
    mnview.newLine -0.5 * Dos * Cos(Pi / S - Wso / Dos) - Wc, 0, -0.5 * Dis * ↩
        Cos(Pi / S - Wso / Dis) + Wc, 0
    mnview.SelectAll mnc.infoSetSelection, mnc.infoSliceLine
    mnview.rotateSelectedEdges 0, 0, -180 / S, False

    ReDim CompName(0)
    CompName(0) = "Tooth#1,Body#1,Face#5"
    mnview.extractEdges CompName

    mnview.rotateToAxis mnc.infoPositiveZAxis
    ReDim CompName(0)
```

```
    CompName(0) = "Coil#1Side#1"
    mnview.SelectAt 0.5 * (Dis - Wc) * Cos(1.1 * Pi / S), 0.5 * (Dis - Wc) * ↩
        Sin(1.1 * Pi / S), mnc.infoSetSelection, mnc.infoSliceSurface
    mnview.makeComponentInALine -(0.5 * Lt - Lsl - Lsm), CompName, "Name=↩
        Copper: 5.77e7 Siemens/meter", mnc.infoMakeComponentRemoveVertices
    Del_construction_line

    mnview.selectObject "Coil#1Side#1", mnc.infoSetSelection
    mndoc.mirrorComponent mndoc.copyComponent("Coil#1Side#1", 1), 0, 0, 0, Sin↩
        (Pi / S), -Cos(Pi / S), 0, 1
    mndoc.renameObject "Copy of Coil#1Side#1 #1", "Coil#1Side#2"
    mndoc.rotateComponent "Coil#1Side#1", 0, 0, 0, 0, 0, 1, (360 / S), 1
    mndoc.rotateComponent "Coil#1Side#2", 0, 0, 0, 0, 0, 1, (360 / S), 1

'Making coil
    ReDim CompName(1)
    CompName(0) = "Coil#1Side#2,Face#3"
    CompName(1) = "Coil#1Side#1,Face#3"
    mndoc.makeSimpleCoil 1, CompName
    mndoc.setCoilNumberOfTurns "Coil#1", Nc / 2
    mndoc.setParameter "Coil#1", "StrandArea", 0.000001 * (Pi * Dct ^ 2) / 4, ↩
        mnc.infoNumberParameter

End Sub

Sub Create_rotor_poles()
    Dim flgP

    flgP = -1

    mnview.rotateToAxis mnc.infoPositiveZAxis
    mnview.getSlice.moveToAPlane 0, 0, 0, 0, 0, 1, 1, 0, 0
    mnview.getSlice.moveInALine Lg + 0.5 * Lt

'MAGNET IN CIRCULAR SEGMENT
    mnview.newarc 0, 0, (0.5 * Dis - Lov) * Cos(beta * -Pi / P), (0.5 * Dis - ↩
        Lov) * Sin(beta * -Pi / P), (0.5 * Dis - Lov) * Cos(beta * Pi / P), ↩
        (0.5 * Dis - Lov) * Sin(beta * Pi / P) 'inner face
    mnview.newLine (0.5 * Dis - Lov) * Cos(beta * Pi / P), (0.5 * Dis - Lov) *↩
         Sin(beta * Pi / P), (0.5 * Dos + Lov) * Cos(beta * Pi / P), (0.5 * ↩
        Dos + Lov) * Sin(beta * Pi / P)   'side face
    mnview.newarc 0, 0, (0.5 * Dos + Lov) * Cos(beta * -Pi / P), (0.5 * Dos + ↩
        Lov) * Sin(beta * -Pi / P), (0.5 * Dos + Lov) * Cos(beta * Pi / P), ↩
        (0.5 * Dos + Lov) * Sin(beta * Pi / P) 'outer face
    mnview.newLine (0.5 * Dos + Lov) * Cos(beta * -Pi / P), (0.5 * Dos + Lov) ↩
        * Sin(beta * -Pi / P), (0.5 * Dis - Lov) * Cos(beta * -Pi / P), (0.5 ↩
        * Dis - Lov) * Sin(beta * -Pi / P)   'side face

    mnview.SelectAll mnc.infoSetSelection, Array(mnc.infoSliceLine, mnc.↩
        infoSliceArc)
    mnview.rotateSelectedEdges 0, 0, 180 / P, False

    For i = 1 To (P / fsym)
        mnview.SelectAll mnc.infoSetSelection, mnc.infoSliceSurface
        ReDim CompName(0)
```

```
        CompName(0) = "Pole#" & i
        mnview.SelectAll mnc.infoSetSelection, mnc.infoSliceSurface
        mnview.makeComponentInALine Lm, CompName, "Name=" & MatMagnet & ";Type↩
            =Uniform;Direction=[0,0," & flgP & "]", mnc.↩
            infoMakeComponentRemoveVertices
        mndoc.setMaxElementSize "Pole#" & i, Lm

        flgP = flgP * -1
        mnview.SelectAll mnc.infoSetSelection, Array(mnc.infoSliceLine, mnc.↩
            infoSliceArc)
        mnview.rotateSelectedEdges 0, 0, 360 / P, False
    Next

    Del_construction_line
    i = 0
End Sub

Sub Create_rotor_yoke()
    'The rotor yoke projects 5%(Lyp) each on both sides

    Dim Rory, Riry

    Lyp = 0.05 * 0.5 * (Dos - Dis)
    Rory = 0.5 * Dos + Lov + Lyp     'Outer radius of rotor yoke
    Riry = (0.5 * Dis - Lov) * Cos(beta * -Pi / P) - Lyp     'Inner radius of ↩
        rotor yoke

    mnview.getSlice.moveToASurface "Pole#1,Face#2"

    mnview.newLine Riry, 0, Rory, 0
    mnview.newarc 0, 0, Rory, 0, Rory * Cos(2 * Pi / fsym), Rory * Sin(2 * Pi ↩
        / fsym)
    mnview.newLine Rory * Cos(2 * Pi / fsym), Rory * Sin(2 * Pi / fsym), Riry ↩
        * Cos(2 * Pi / fsym), Riry * Sin(2 * Pi / fsym)
    mnview.newarc 0, 0, Riry, 0, Riry * Cos(2 * Pi / fsym), Riry * Sin(2 * Pi ↩
        / fsym)

    ReDim CompName(0)
    CompName(0) = "Rotor_Yoke"
    mnview.SelectAt 0.5 * (Riry + Rory) * Cos(2 * Pi / fsym), 0.5 * (Riry + ↩
        Rory) * Sin(2 * Pi / fsym), mnc.infoSetSelection, mnc.↩
        infoSliceSurface
    mnview.makeComponentInALine Lyr, CompName, "Name=Remko: Soft pure iron", ↩
        mnc.infoMakeComponentRemoveVertices
    mndoc.setMaxElementSize "Rotor_Yoke", 2 * Lyr
    Del_construction_line

End Sub

Sub Create_air_vols()

    mnview.getSlice.moveToAPlane 0, 0, 0, 0, 0, 1, 1, 0, 0

'Ouline of air volume
    mnview.newLine 0.25 * Dis, 0, 0.5 * Dos + 0.25 * Dis, 0
```

```
    mnview.newarc 0, 0, 0.5 * Dos + 0.25 * Dis, 0, (0.5 * Dos + 0.25 * Dis) * ↩
        Cos(2 * Pi / fsym), (0.5 * Dos + 0.25 * Dis) * Sin(2 * Pi / fsym)
    mnview.newLine (0.5 * Dos + 0.25 * Dis) * Cos(2 * Pi / fsym), (0.5 * Dos +↩
        0.25 * Dis) * Sin(2 * Pi / fsym), 0.25 * Dis * Cos(2 * Pi / fsym), ↩
        0.25 * Dis * Sin(2 * Pi / fsym)
    mnview.newarc 0, 0, 0.25 * Dis, 0, 0.25 * Dis * Cos(2 * Pi / fsym), 0.25 *↩
        Dis * Sin(2 * Pi / fsym)

'Stator air volume
    ReDim CompName(0)
    CompName(0) = "S_Air"
    mnview.SelectAt 0.5 * Dos * Cos(Pi / fsym), 0.5 * Dos * Sin(Pi / fsym), ↩
        mnc.infoSetSelection, mnc.infoSliceSurface
    mnview.makeComponentInALine 0.5 * (Lt + Lg), CompName, "Name=AIR", mnc.↩
        infoMakeComponentRemoveVertices
    'mndoc.setMaxElementSize CompName(0), Lg
    If (360 / fsym) > 90 Then
        B_face = 5
    Else
        B_face = 4
    End If

    'Boundary conditions
    'Normal boundary condition at half sectional symmetry plane
    ReDim CompName(0)
    CompName(0) = "S_Air,Face#1"
    mndoc.createBoundaryCondition CompName, "BC#1"
    mndoc.setMagneticFieldNormal "BC#1"

    'Periodic
    ReDim CompName(1)
    CompName(0) = "S_Air,Face#" & B_face
    CompName(1) = "S_Air,Face#2"
    mndoc.createBoundaryCondition CompName, "BC#2"
    ReDim RotationAxis(2)
    RotationAxis(0) = 0
    RotationAxis(1) = 0
    RotationAxis(2) = 1
    ReDim Center(2)
    Center(0) = 0
    Center(1) = 0
    Center(2) = 0
    If (P / fsym) Mod 2 = 1 Then
        mndoc.setOddPeriodic "BC#2", Null, 360 / fsym, RotationAxis, Null, ↩
            Null, Center
    Else
        mndoc.setEvenPeriodic "BC#2", Null, 360 / fsym, RotationAxis, Null, ↩
            Null, Center
    End If

'Rotor air volume
    mnview.getSlice.moveToASurface "S_Air,Face#2"
    ReDim CompName(0)
    CompName(0) = "R_Air"
```

```
    mnview.SelectAt 0.5 * Dos * Cos(Pi / fsym), 0.5 * Dos * Sin(Pi / fsym), ↩
        mnc.infoSetSelection, mnc.infoSliceSurface
    mnview.makeComponentInALine (Lm + 3 * Lyr + 0.5 * Lg), CompName, "Name=AIR↩
        ", mnc.infoMakeComponentRemoveVertices
    'mndoc.setMaxElementSize CompName(0), Lg

    'Boundary conditions
    ReDim CompName(0)
    CompName(0) = "R_Air,Face#" & B_face
    mndoc.createBoundaryCondition CompName, "BC#3"
    ReDim RotationAxis(2)
    RotationAxis(0) = 0
    RotationAxis(1) = 0
    RotationAxis(2) = 1
    ReDim Center(2)
    Center(0) = 0
    Center(1) = 0
    Center(2) = 0
    If (P / fsym) Mod 2 = 1 Then
        mndoc.setOddPeriodic "BC#3", Null, 360 / fsym, RotationAxis, Null, ↩
            Null, Center
    Else
        mndoc.setEvenPeriodic "BC#3", Null, 360 / fsym, RotationAxis, Null, ↩
            Null, Center
    End If
    Del_construction_line
End Sub

Sub Create_motion_component()
    ReDim CompName(1)
    CompName(0) = "R_Air"
    CompName(1) = "Rotor_Yoke"
    mndoc.makeMotionComponent CompName

    For i = 1 To (P / fsym)
        ReDim CompName(0)
        CompName(0) = "Pole#" & i
        mndoc.addReferencePaths "Motion#1", CompName
    Next
    i = 0
End Sub

Sub Cal_rotor_pos()
'Rotor position correction needed to capture flux linkage corresponding to a ↩
    switching on position
    Dim ini_rotor_pos

    ini_rotor_pos = 360 + ((360 / (2 * P)) - (3 * (360 / (2 * S)))) * P / 2 '↩
        Initial rotor position w.r.t stator coil axis in electrical degree
    If ini_rotor_pos > 0 And ini_rotor_pos <= 29 Then
        del_rotor_pos = (29 - ini_rotor_pos) / (P / 2)
    ElseIf ini_rotor_pos > 29 And ini_rotor_pos <= 89 Then
        del_rotor_pos = (89 - ini_rotor_pos) / (P / 2)
    ElseIf ini_rotor_pos > 89 And ini_rotor_pos <= 209 Then
        del_rotor_pos = (209 - ini_rotor_pos) / (P / 2)
```

```
    ElseIf ini_rotor_pos > 209 And ini_rotor_pos <= 269 Then
        del_rotor_pos = (269 - ini_rotor_pos) / (P / 2)
    ElseIf ini_rotor_pos > 269 And ini_rotor_pos <= 360 Then
        del_rotor_pos = (389 - ini_rotor_pos) / (P / 2)
    End If

End Sub

Sub Par_rotor_position()
    Dim rotor_pos_val(0) As String
    ' 8 sampling points for flux linkage
    'rotor_pos_val(0) = "" & del_rotor_pos & "," & (del_rotor_pos + 1 * 2 / P)↩
         & "," & (del_rotor_pos + 11 * 2 / P) & "," & (del_rotor_pos + 21 * 2↩
         / P) & "," & (del_rotor_pos + 31 * 2 / P) & "," & (del_rotor_pos + ↩
        41 * 2 / P) & "," & (del_rotor_pos + 51 * 2 / P) & "," & (↩
        del_rotor_pos + 61 * 2 / P) & ""
    ' 6 sampling points for flux linkage
    rotor_pos_val(0) = "" & del_rotor_pos & "," & (del_rotor_pos + 1 * 2 / P) ↩
        & "," & (del_rotor_pos + 16 * 2 / P) & "," & (del_rotor_pos + 31 * 2 ↩
        / P) & "," & (del_rotor_pos + 46 * 2 / P) & "," & (del_rotor_pos + 61↩
         * 2 / P) & ""
    fl_sampling_point = 6
    sample_ang = (15 * 2 / P) * (Pi / 180) 'mech rad

    mndoc.setParameter "", "rotor_pos", rotor_pos_val(0), mnc.↩
        infoNumberParameter
    mndoc.setParameter "R_Air", "RotationAxis", "[0,0,1]", mnc.↩
        infoArrayParameter
    mndoc.setParameter "R_Air", "RotationAngle", "%rotor_pos%deg", mnc.↩
        infoNumberParameter
    mndoc.setParameter "Rotor_Yoke", "RotationAxis", "[0,0,1]", mnc.↩
        infoArrayParameter
    mndoc.setParameter "Rotor_Yoke", "RotationAngle", "%rotor_pos%deg", mnc.↩
        infoNumberParameter

    For i = 1 To (P / fsym)
        mndoc.setParameter "Pole#" & i, "RotationAxis", "[0, 0, 1]", mnc.↩
            infoArrayParameter
        mndoc.setParameter "Pole#" & i, "RotationAngle", "%rotor_pos%deg", mnc↩
            .infoNumberParameter
    Next
    i = 0

End Sub

Sub Eb_for_90eDeg_to_150eDeg()
'Subroutine for evalauting the flux linkage and back emf constant
'for (30 ele deg to 150 ele deg)
    Dim ini_rotor_pos, del_rotor_pos, tr_time_step, solvTimeStep
    Dim m_time(1)
    Dim m_speed(1)

    del_rotor_pos = (80 / (P / 2)) - ini_rotor_pos  'Motion component position↩
         at start corresponding to 80 ele deg
    If del_rotor_pos <= 0 Then
```

```
        del_rotor_pos = (360 / (P / 2)) + del_rotor_pos
    End If
    tr_time_step = 10 / (P / 2)

    mndoc.setMotionSourceType "Motion#1", mnc.infoVelocityDriven
    m_time(0) = 0
    m_speed(0) = 1000
    m_time(1) = 1000
    m_speed(1) = 1000
    mndoc.setMotionSpeedVsTime "Motion#1", m_time, m_speed

    ReDim solvTimeStep(10)
    solvTimeStep(0) = 0
    solvTimeStep(1) = del_rotor_pos + 0 * tr_time_step
    solvTimeStep(2) = del_rotor_pos + 0.8 * tr_time_step
    solvTimeStep(3) = del_rotor_pos + 0.9 * tr_time_step
    solvTimeStep(4) = del_rotor_pos + 1 * tr_time_step
    solvTimeStep(5) = del_rotor_pos + 2 * tr_time_step
    solvTimeStep(6) = del_rotor_pos + 3 * tr_time_step
    solvTimeStep(7) = del_rotor_pos + 4 * tr_time_step
    solvTimeStep(8) = del_rotor_pos + 5 * tr_time_step
    solvTimeStep(9) = del_rotor_pos + 6 * tr_time_step
    solvTimeStep(10) = del_rotor_pos + 7 * tr_time_step

    mndoc.setTimeStepMethod mnc.infoUserDefinedTimeStep
    mndoc.setUserDefinedTimeSteps solvTimeStep
    mndoc.solveTransient3dWithMotion

End Sub

Sub Calculate_motor_parameter()
    Dim fl1, fl2, ke_c
    Dim zero_coerc_prop
    Par_rotor_position
    mndoc.solveStatic3d
    mndoc.getSolution.getFluxLinkageThroughCoil 1, "Coil#1", fl1
    mndoc.getSolution.getFluxLinkageThroughCoil 2, "Coil#1", fl2
    ke_c = Abs((fl2 - fl1) / ((Pi / 180) * (2 / P)))

    For i = 3 To fl_sampling_point
        fl1 = fl2
        mndoc.getSolution.getFluxLinkageThroughCoil i, "Coil#1", fl2
        ke_c = ke_c + Abs((fl2 - fl1) / sample_ang)
    Next
    i = 0
    ke_c = 2 * ke_c / (fl_sampling_point - 1) ' 2 times the single section ↩
        average value

' Inductance calculation
    ReDim zero_coerc_prop(0, 2)
    zero_coerc_prop(0, 0) = 20
    zero_coerc_prop(0, 1) = 1.2
    zero_coerc_prop(0, 2) = 0
```

```
    mndoc.getModelMaterialDatabase.setMagneticPermeability MatMagnet, ↩
        zero_coerc_prop, mnc.infoLinearIsotropicReal
    mndoc.setParameter "Coil#1", "WaveFormType", "DC", mnc.infoStringParameter
    mndoc.setParameter "Coil#1", "Current", tempI, mnc.infoNumberParameter
    mndoc.setParameter "", "rotor_pos", "7.5", mnc.infoNumberParameter
    mndoc.solveStatic3d

    mndoc.getSolution.getFluxLinkageThroughCoil 1, "Coil#1", fl1
    Lph = 3 * 2 * fl1 / tempI

'Based on [Ishak2006a] Kd, distribution factor for alternate tooth wound ↩
     machine is 1 for S12P10 and S12P14 and 0.959795 for S18P16
    If (S = 18 And P = 16) Then
        Kd = 0.959795
    Else
        Kd = 1
    End If

    Ke_p = (S / (2 * 3)) * Kd * ke_c
    Ke_l = 2 * Ke_p
    Rph = (S / (2 * 3)) * (2 * mndoc.getSolution.getDCResistanceOfCoil(1, "↩
        Coil#1")) 'number of coils per phase  times 2X resistances of half ↩
        coil

End Sub

Sub Del_construction_line()
    mnview.SelectAll mnc.infoSetSelection, Array(mnc.infoSliceLine, mnc.↩
        infoSliceArc)
    mnview.deleteSelection
End Sub

Sub Create_rotor_air()
'Creating rotor air for rotor yoke thickness analysis
    mnview.getSlice.moveToAPlane 0, 0, -(Lg + Lm + Lyr + 10), 0, 0, 1, 1, 0, 0

'Ouline of air volume
    mnview.newLine 0.25 * Dis, 0, 0.5 * Dos + 0.25 * Dis, 0
    mnview.newarc 0, 0, 0.5 * Dos + 0.25 * Dis, 0, (0.5 * Dos + 0.25 * Dis) * ↩
        Cos(2 * Pi / fsym), (0.5 * Dos + 0.25 * Dis) * Sin(2 * Pi / fsym)
    mnview.newLine (0.5 * Dos + 0.25 * Dis) * Cos(2 * Pi / fsym), (0.5 * Dos +↩
         0.25 * Dis) * Sin(2 * Pi / fsym), 0.25 * Dis * Cos(2 * Pi / fsym), ↩
        0.25 * Dis * Sin(2 * Pi / fsym)
    mnview.newarc 0, 0, 0.25 * Dis, 0, 0.25 * Dis * Cos(2 * Pi / fsym), 0.25 *↩
         Dis * Sin(2 * Pi / fsym)

'Air volume
    ReDim CompName(0)
    CompName(0) = "Air_Vol"
    mnview.SelectAt 0.5 * Dos * Cos(Pi / fsym), 0.5 * Dos * Sin(Pi / fsym), ↩
        mnc.infoSetSelection, mnc.infoSliceSurface
    mnview.makeComponentInALine 2 * (Lg + Lm + Lyr + 10), CompName, "Name=AIR"↩
        , mnc.infoMakeComponentRemoveVertices

    If (360 / fsym) > 90 Then
```

```
        B_face = 5
    Else
        B_face = 4
    End If

'    'Periodic boundary conditions
    ReDim CompName(0)
    CompName(0) = "Air_Vol,Face#" & B_face
    mndoc.createBoundaryCondition CompName, "BC#1"
    ReDim RotationAxis(2)
    RotationAxis(0) = 0
    RotationAxis(1) = 0
    RotationAxis(2) = 1
    ReDim Center(2)
    Center(0) = 0
    Center(1) = 0
    Center(2) = 0
    If (P / fsym) Mod 2 = 1 Then
        mndoc.setOddPeriodic "BC#1", Null, 360 / fsym, RotationAxis, Null, ↩
            Null, Center
    Else
        mndoc.setEvenPeriodic "BC#1", Null, 360 / fsym, RotationAxis, Null, ↩
            Null, Center
    End If
End Sub

Sub Rotor_yoke_thickness()
    Application.StatusBar = " Rotor yoke thickness is being calculated"
    Lt = 0  'Defining tooth thickness equal to zeor to find thickness rotor ↩
        yoke with only airgap
    Lyr = 4 'Initial value of rotor yoke thickness

    Do
        New_model
        Create_rotor_poles
        For i = 1 To (P / fsym)
            ReDim CompName(0)
            CompName(0) = "Pole#" & i
            mndoc.shiftComponent mndoc.copyComponent(CompName, 1), 0, 0, -(Lm ↩
                + 2 * Lg), 1
        Next

        Create_rotor_yoke
        mndoc.shiftComponent mndoc.copyComponent("Rotor_Yoke", 1), 0, 0, -(Lyr↩
            + Lm + 2 * Lg + Lm), 1
        Create_rotor_air
        mndoc.solveStatic3d
        Set mnmsh = mndoc.getSolution.getMesh(1)
        Set mnuf = mndoc.getSolution.getsystemfield(mnmsh, "B")
        max_B = mnuf.getMax()
        Set mnmsh = Nothing
        Set mnuf = Nothing

        If (max_B < 1.4) Then
            av_Bg = Average_flux_density(0.25 * (Dos + Dis), 360 / fsym, 0)
```

```
        End If

        Lyr = Lyr + 1
        mn.closeDocument (False)
    Loop Until max_B < 1.4
    Application.StatusBar = " Rotor yoke thickness is calculated"
End Sub

Function Average_flux_density(R_s, Theta_m, Z_s)
        Dim B_sum, Fd, itr_B
        B_sum = 0
        Set mnmsh = mndoc.getSolution.getMesh(1)
        Set mnuf = mndoc.getSolution.getsystemfield(mnmsh, "B")
        'itr_B = Worksheets("Flux_density").Cells(1, 2).Value
        For i = 1 To Int(Theta_m)
            mnuf.getfieldatpoint R_s * Cos(i * Pi / 180), R_s * Sin(i * Pi / ↩
                180), Z_s, Fd
            B_sum = B_sum + Abs(Fd(2))
        Next
        Average_flux_density = B_sum / Int(Theta_m)
        Set mnmsh = Nothing
        Set mnuf = Nothing
End Function

Sub Calculate_coil_turn_and_area()
    Dim frEb, area_new, delta, loop_tr, tempI, finalI

    loop_tr = 0
    area_s = Pr / ((2 * S / 3) * av_Bg * (Pi * (Dos ^ 2 - Dis ^ 2) * 0.000001 ↩
        / 4) * J * SFg * Nr / 60)

'Loop to decide the copper area
    Do
        loop_tr = loop_tr + 1
        area_s_av = area_s - 2 * (Wso * Lsl + 0.5 * Lsm * (Wso + Wt))    '↩
            Available area for winding
        Lw = area_s_av / Wt
        Lt = Lw + 2 * (Lsm + Lsl)

        'Calculating the slot ampere-turns required to generate Pr. Slot ↩
            ampere-turns = Nc*area of a turn*J = coper area * J = SFg*slot ↩
            area*J
        New_model
        Create_stator_teeth
        Create_rotor_poles
        Create_rotor_yoke
        Create_air_vols
        'mn.Visible = True
        mndoc.solveStatic3d

        av_Bg = Average_flux_density(0.25 * (Dos + Dis), 360 / fsym, 0.5 * (Lt↩
            + Lg))
        mn.closeDocument (False)
        area_new = Pr / ((2 * S / 3) * av_Bg * (Pi * (Dos ^ 2 - Dis ^ 2) * ↩
            0.000001 / 4) * J * SFg * Nr / 60)
```

```
        delta = (area_new - area_s) * 100 / area_s

        Application.StatusBar = " loop: " & loop_tr

        If ((Abs(delta) < 2.5)) Then
            Exit Do
        End If
        area_s = area_new
    Loop Until (loop_tr = 20)

'Loop to decide Nc and Dct
    frEb = 95
    temp = (frEb / 100) * 0.5 * Vr / ((S / 3) * av_Bg * (Pi * (Dos ^ 2 - Dis ^↩
          2) * 0.000001 / 4) * Nr / 60) ' The number turns required to ↩
         generate a voltage of frEb% of Vr corresponding to the average air ↩
         gap flux density
    Nc = 2 * Int(temp / 2) ' Even number of turns are selceted to utilise half↩
          sectional symmetry

    loop_tr = 0
    Do
        loop_tr = loop_tr + 1
        Dct = Sqr(4 * SFg * area_new / (Pi * Nc))

        'Evaluating whether the resistnace of coil will allow to bulid up the ↩
             necessary current
        New_model
        Create_stator_teeth
        Create_rotor_poles
        Create_rotor_yoke
        Create_winding
        Create_air_vols
        tempI = J * Pi * Dct ^ 2 / 4
        Calculate_motor_parameter
        mn.closeDocument (False)

        delta = Vr - 2 * tempI * Rph - (2 * tempI * Lph * Wr / (0.25 * 2 * Pi ↩
             / 3)) - Ke_l * Wr 'it is assumed that rise time of current is 25%↩
              of duty cycle

        Worksheets("MMF_evaluation_approach").Cells(4 + 5, 2 + loop_tr).Value ↩
             = loop_tr
        Worksheets("MMF_evaluation_approach").Cells(6 + 4, 2 + loop_tr).Value ↩
             = Nc
        Worksheets("MMF_evaluation_approach").Cells(7 + 4, 2 + loop_tr).Value ↩
             = Dct
        Worksheets("MMF_evaluation_approach").Cells(8 + 4, 2 + loop_tr).Value ↩
             = "" & Rph & " and " & Lph
        Worksheets("MMF_evaluation_approach").Cells(9 + 4, 2 + loop_tr).Value ↩
             = Ke_l * Wr
        Worksheets("MMF_evaluation_approach").Cells(10 + 4, 2 + loop_tr).Value↩
              = tempI
        Worksheets("MMF_evaluation_approach").Cells(11 + 4, 2 + loop_tr).Value↩
              = finalI
```

```
        Worksheets("MMF_evaluation_approach").Cells(12 + 4, 2 + loop_tr).Value↩
             = delta
        Application.StatusBar = " Delta = " & delta

        If delta > 0 Then
            Exit Do
        Else
            Nc = Nc - 2
        End If
    Loop Until (loop_tr = 20)

End Sub

Function motor_losses(a1 As Double, a2 As Double, a3 As Double, a4 As Double, ↩
     a5 As Double, a6 As Double, a7 As Double, a8 As Double, a9 As Double, a10↩
      As Double, a11 As Double, a12 As Double, a13 As Double)
    Excel_config
    Dim t1, t2
    Dim dt As Long
    t1 = time
    Dos = a1
    P = a2
    S = a3
    Lg = a4
    SFg = a5
    Wso = a6
    Lsl = a7
    Lsm = a8
    J = a9
    Lm = Round(a10, 1)
    beta = a11
    h = Round(a12, 2)
    lambda_d = Round(a13, 4)

    Start_MagNet_program
    Read_motor_spec
    Calculate_secondary_variables

    iter = 4 + Worksheets("Iterations").Cells(6, 4).Value
    MatTooth = Worksheets("Iterations").Cells(7, 4).Value
    MatMagnet = Worksheets("Iterations").Cells(8, 4).Value

    Rotor_yoke_thickness
    Calculate_coil_turn_and_area

    Worksheets("Iterations").Cells(6, 4).Value = iter - 4 + 1
    Worksheets("Iterations").Cells(14, iter).Value = time - t1
    Worksheets("Iterations").Cells(15, iter).Value = Dos
    Worksheets("Iterations").Cells(16, iter).Value = P
    Worksheets("Iterations").Cells(17, iter).Value = S
    Worksheets("Iterations").Cells(18, iter).Value = Lg
    Worksheets("Iterations").Cells(19, iter).Value = SFg
    Worksheets("Iterations").Cells(20, iter).Value = Wso
    Worksheets("Iterations").Cells(21, iter).Value = Lsl
    Worksheets("Iterations").Cells(22, iter).Value = Lsm
```

```
    Worksheets("Iterations").Cells(23, iter).Value = J
    Worksheets("Iterations").Cells(24, iter).Value = beta
    Worksheets("Iterations").Cells(25, iter).Value = Lm
    Worksheets("Iterations").Cells(26, iter).Value = h
    Worksheets("Iterations").Cells(27, iter).Value = lambda_d
    Worksheets("Iterations").Cells(28, iter).Value = Lyr
    Worksheets("Iterations").Cells(29, iter).Value = Wt
    Worksheets("Iterations").Cells(30, iter).Value = Nc
    Worksheets("Iterations").Cells(31, iter).Value = Lt
    Worksheets("Iterations").Cells(32, iter).Value = Dct
    Worksheets("Iterations").Cells(33, iter).Value = Rph
    Worksheets("Iterations").Cells(34, iter).Value = Ke_l * Wr
    Worksheets("Iterations").Cells(35, iter).Value = J * Pi * Dct ^ 2 / 4
    Worksheets("Iterations").Cells(36, iter).Value = 2 * Rph * (J * Pi * Dct ^↩
        2 / 4) ^ 2
    Worksheets("Iterations").Cells(37, iter).Value = Lt + 2 * (Lg + Lm + Lyr)
    motor_losses = 2 * Rph * (J * Pi * Dct ^ 2 / 4) ^ 2

    mn.Close (False)
    Set mn = Nothing
End Function
```

Appendix C

Measurements from the test bench evaluation of motors

C.1 Sintered rare-earth magnet PMBLDC hub motor

Speed (rpm)	Measured Torque (N m)	Input voltage (V)	Input current (A)	Input power (W)	Output power (W)	Efficiency (%)
49	5.1	49.1	1.0	49.1	24.6	50.2
105	5.0	48.8	1.7	83.0	53.9	64.9
151	5.0	49.2	2.3	113.2	79.1	69.9
204	5.0	48.5	3.0	145.5	106.8	73.4
250	5.1	49.5	3.4	168.3	130.9	77.8
299	5.0	49.0	4.0	196.0	150.3	76.7
323	5.0	48.8	4.4	214.7	165.7	77.2
341	5.0	48.7	4.6	224.0	175.0	78.1
350	5.0	48.6	4.9	238.1	179.6	75.4

Table C.1: The performance measurement data of the sintered rare-earth magnet PMBLDC hub motor corresponding to a load torque of 5 N m.

Speed (rpm)	Measured Torque (N m)	Input voltage (V)	Input current (A)	Input power (W)	Output power (W)	Efficiency (%)
49	7.5	49.3	1.2	59.2	37.5	63.3
102	7.5	49.2	2.1	103.3	78.0	75.5
148	7.5	49.4	2.9	143.3	116.2	81.1
200	7.5	49.2	3.9	191.9	155.0	80.8
252	7.6	48.8	4.9	239.1	197.9	82.8
301	7.5	48.7	5.7	277.6	233.3	84.0
317	7.5	48.5	6.0	291.0	245.7	84.4
338	7.6	48.5	6.5	315.3	265.5	84.2
350	7.6	48.4	6.8	329.1	274.9	83.5

Table C.2: The performance measurement data of the sintered rare-earth magnet PM-BLDC hub motor corresponding to a load torque of 7.5 N m.

Speed (rpm)	Measured Torque (N m)	Input voltage (V)	Input current (A)	Input power (W)	Output power (W)	Efficiency (%)
48	10.0	49.0	1.8	86.2	48.8	56.5
100	10.1	49.5	2.9	143.6	103.7	72.2
153	10.0	48.8	4.0	195.2	160.2	82.1
201	10.0	49.5	5.0	247.5	206.3	83.3
248	10.0	48.5	6.2	300.7	259.7	86.4
299	10.1	49.5	7.3	361.4	313.1	86.7
322	10.1	49.1	7.9	387.9	337.2	86.9
339	10.0	49.3	8.2	404.3	355.0	87.8
350	10.0	48.8	8.6	419.7	366.5	87.3

Table C.3: The performance measurement data of the sintered rare-earth magnet PM-BLDC hub motor corresponding to a load torque of 10 N m.

Speed (rpm)	Measured Torque (N m)	Input voltage (V)	Input current (A)	Input power (W)	Output power (W)	Efficiency (%)
51	12.4	49.1	2.3	112.9	64.1	56.8
104	12.5	48.9	3.6	176.0	135.0	76.7
148	12.5	48.7	4.8	233.8	192.2	82.2
202	12.5	49.5	6.2	306.9	264.4	86.2
248	12.6	48.8	7.7	375.8	324.6	86.4
299	12.6	49.5	9.0	445.5	388.3	87.2
322	12.5	49.2	9.7	477.2	418.1	87.6
342	12.4	49.0	10.3	504.7	440.5	87.3
350	12.5	48.9	10.4	508.6	454.5	89.4

Table C.4: The performance measurement data of the sintered rare-earth magnet PM-BLDC hub motor corresponding to a load torque of 12.5 N m.

Speed (rpm)	Measured Torque (N m)	Input voltage (V)	Input current (A)	Input power (W)	Output power (W)	Efficiency (%)
52	15.3	48.6	2.9	140.9	80.6	57.2
101	15.0	49.0	4.3	210.7	158.7	75.3
148	15.0	48.9	5.8	283.6	232.5	82.0
203	15.0	49.1	7.6	373.2	318.9	85.5
250	15.0	48.6	9.3	452.0	392.7	86.9
300	15.0	49.2	10.8	531.4	471.2	88.7
320	15.0	49.0	11.5	563.5	502.7	89.2
341	15.0	49.3	12.2	601.5	535.6	89.1
350	15.0	49.1	12.5	613.8	549.8	89.6

Table C.5: The performance measurement data of the sintered rare-earth magnet PM-BLDC hub motor corresponding to a load torque of 15 N m.

Speed (rpm)	Measured Torque (N m)	Input voltage (V)	Input current (A)	Input power (W)	Output power (W)	Efficiency (%)
54	17.7	49.0	3.5	171.5	95.0	55.4
100	17.5	48.5	5.3	257.1	183.3	71.3
150	17.5	49.5	7.0	346.5	274.9	79.3
198	17.5	48.5	8.9	431.7	362.9	84.1
249	17.5	48.9	10.7	523.2	456.3	87.2
298	17.6	49.5	12.3	608.9	543.0	89.2
320	17.5	49.2	13.2	649.4	583.1	89.8
342	17.4	48.8	14.0	683.2	616.0	90.2
350	17.5	48.5	14.4	698.4	637.7	91.3

Table C.6: The performance measurement data of the sintered rare-earth magnet PM-BLDC hub motor corresponding to a load torque of 17.5 N m.

Speed (rpm)	Measured Torque (N m)	Input voltage (V)	Input current (A)	Input power (W)	Output power (W)	Efficiency (%)
49	20.0	49.5	4.1	203.0	101.6	50.1
102	20.1	49.4	6.3	309.2	213.6	69.1
149	20.0	49.3	8.2	404.3	312.1	77.2
206	20.0	48.5	10.8	523.8	427.1	81.5
248	20.0	48.6	12.4	602.6	514.2	85.3
300	20.0	49.3	14.2	700.1	625.2	89.3
319	20.1	49.1	15.2	746.3	668.1	89.5
341	20.0	49.1	16.1	790.5	714.2	90.3
350	20.0	48.9	16.5	806.9	733.0	90.9

Table C.7: The performance measurement data of the sintered rare-earth magnet PM-BLDC hub motor corresponding to a load torque of 20 N m.

C.2 Ferrite magnet SAT PMBLDC hub motor

Speed (rpm)	Measured Torque (N m)	Input voltage (V)	Input current (A)	Input power (W)	Output power (W)	Efficiency (%)
53	5.1	48.6	1.0	46.7	23.9	51.2
103	5.2	48.9	1.5	73.4	52.9	72.1
150	5.5	49.2	2.2	108.2	81.7	75.5
203	5.0	48.8	2.7	131.8	104.2	79.1
250	4.9	48.8	3.0	146.4	128.3	87.6
300	5.0	49.0	3.7	181.3	152.7	84.2
323	5.1	48.9	3.9	190.7	165.7	86.9
340	5.0	48.7	4.2	204.5	163.8	80.1
349	5.1	48.7	4.3	209.4	179.1	85.5

Table C.8: The performance measurement data of the ferrite magnet SAT PMBLDC motor corresponding to a load torque of 5 N m.

Speed (rpm)	Measured Torque (N m)	Input voltage (V)	Input current (A)	Input power (W)	Output power (W)	Efficiency (%)
50	7.3	48.6	1.3	63.2	36.7	58.0
103	7.5	48.6	2.2	106.9	74.4	69.6
152	7.6	48.7	2.8	136.4	114.6	84.0
199	7.6	49.0	3.6	176.4	152.1	86.2
253	7.5	48.8	4.5	219.6	193.4	88.1
300	7.6	49.4	5.2	256.9	232.5	90.5
322	7.5	49.2	5.5	270.6	242.8	89.7
339	7.6	48.9	5.9	288.5	262.7	91.1
349	7.6	48.7	6.2	301.9	270.4	89.6

Table C.9: The performance measurement data of the ferrite magnet SAT PMBLDC motor corresponding to a load torque of 7.5 N m.

Speed (rpm)	Measured Torque (N m)	Input voltage (V)	Input current (A)	Input power (W)	Output power (W)	Efficiency (%)
49	10.2	49.0	1.6	78.4	51.3	65.4
104	10.1	49.4	2.8	138.3	106.7	77.2
150	10.1	48.6	3.8	184.7	153.9	83.4
205	10.0	48.3	4.9	236.7	210.4	88.9
250	10.0	48.6	5.9	286.7	253.9	88.6
299	10.2	49.3	6.9	340.2	313.1	92.0
320	10.1	49.5	7.1	351.5	318.3	90.6
340	10.0	49.2	7.6	373.9	345.4	92.4
351	9.9	49.0	8.0	392.0	356.5	91.0

Table C.10: The performance measurement data of the ferrite magnet SAT PMBLDC motor corresponding to a load torque of 10 N m.

Speed (rpm)	Measured Torque (N m)	Input voltage (V)	Input current (A)	Input power (W)	Output power (W)	Efficiency (%)
50	12.6	49.0	2.1	102.9	63.9	62.1
104	12.4	49.1	3.6	176.8	130.7	73.9
155	12.5	49.4	4.0	197.6	178.5	90.4
201	12.6	48.6	5.6	272.2	258.9	95.1
254	12.4	49.4	6.8	335.9	324.5	96.6
299	12.4	48.7	8.0	389.6	375.7	96.4
319	12.8	49.5	8.5	420.8	400.9	95.3
340	12.5	49.1	9.2	451.7	427.3	94.6
352	12.5	49.0	9.5	465.5	449.7	96.6

Table C.11: The performance measurement data of the ferrite magnet SAT PMBLDC motor corresponding to a load torque of 12.5 N m.

Speed (rpm)	Measured Torque (N m)	Input voltage (V)	Input current (A)	Input power (W)	Output power (W)	Efficiency (%)
50	15.1	49.0	2.2	107.8	76.4	70.9
101	15.2	49.0	3.8	186.2	154.4	82.9
150	15.1	49.0	5.2	254.8	223.1	87.5
200	15.1	49.2	6.9	339.5	314.2	92.5
253	14.9	48.7	8.7	423.7	384.2	90.7
302	15.0	49.2	9.8	482.2	458.6	95.1
320	15.0	49.0	10.5	514.5	475.8	92.5
340	14.9	48.5	11.3	548.1	519.8	94.9
350	14.9	49.4	11.4	563.2	542.4	96.3

Table C.12: The performance measurement data of the ferrite magnet SAT PMBLDC motor corresponding to a load torque of 15 N m.

Speed (rpm)	Measured Torque (N m)	Input voltage (V)	Input current (A)	Input power (W)	Output power (W)	Efficiency (%)
51	17.6	49.0	2.9	142.1	91.9	64.6
100	17.4	49.2	4.6	226.3	175.9	77.7
149	17.8	49.3	6.5	320.5	268.4	83.7
203	17.6	49.0	8.5	416.5	372.0	89.3
250	17.5	49.1	9.9	486.1	455.5	93.7
301	17.5	48.5	12.1	586.9	535.9	91.3
320	18.0	49.1	12.4	608.8	536.2	88.1
341	17.3	48.8	13.3	649.0	607.1	93.5
352	17.6	48.5	13.8	669.3	641.4	95.8

Table C.13: The performance measurement data of the ferrite magnet SAT PMBLDC motor corresponding to a load torque of 17.5 N m.

Speed (rpm)	Measured Torque (N m)	Input voltage (V)	Input current (A)	Input power (W)	Output power (W)	Efficiency (%)
52	19.9	49.5	3.8	188.1	105.1	55.9
102	20.0	49.5	5.9	292.1	207.2	71.0
151	20.4	49.0	8.0	392.0	297.3	75.8
200	19.9	48.8	9.9	483.1	412.6	85.4
253	19.9	49.1	12.0	589.2	521.9	88.6
302	20.1	49.3	14.0	690.2	613.5	88.9
320	20.0	48.9	14.8	723.7	603.2	83.3
334	20.0	49.4	15.5	765.7	692.5	90.4
353	20.2	49.5	16.1	797.0	735.6	92.3

Table C.14: The performance measurement data of the ferrite magnet SAT PMBLDC motor corresponding to a load torque of 20 N m.

Appendix D

Basic urban driving cycle as per ISO 13064-1:2012

The basic urban driving cycle is listed in Table D.1. In this study vehicle are

Phase	Operation	Acceleration (km/h)	Speed (m/s^2)	Duration (s)	Cumulative time (s)
1	Idling	-	0	8	8
2	Acceleration	Full throttle	0 to max		-
3	Steady speed	Full throttle	max	57	-
4	Deceleration	−0.56	max to 20		65
5	Steady speed	-	20	36	101
6	Deceleration	−0.93	20 to 0	6	107
7	Idling	-	0	5	112

Table D.1: Basic urban drive cycle as per ISO 13064-1:2012

tested by driving them for eight cycles and Figure D.1 shows the composition of the test sequence.

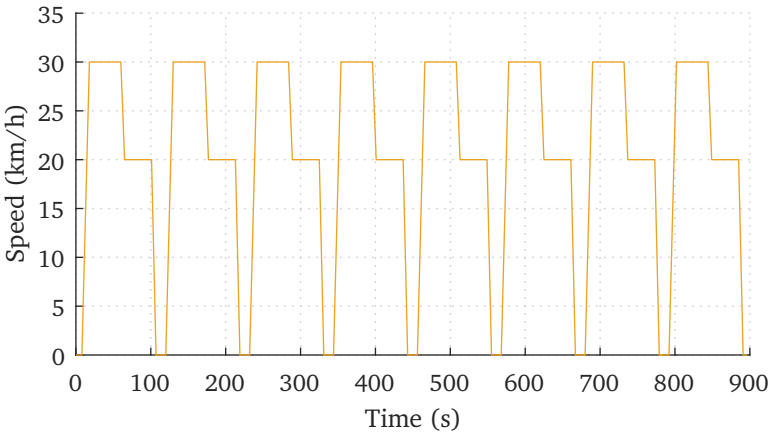

Figure D.1: The composition of test sequence based on the basic urban cycle as per ISO 13064-1:2012 undergone by electric two wheelers

Appendix E

Fabrication drawing of components of prototype motors

E.1 Rare-earth magnet SAT PMBLDC motor

list of drawings

1. Stator tooth
2. Winding diagram
3. Tooth holder
4. Stator hub
5. Shaft
6. Magnet poles
7. Rotor yoke
8. End cover without brake drum
9. End cover with brake drum
10. Spacer

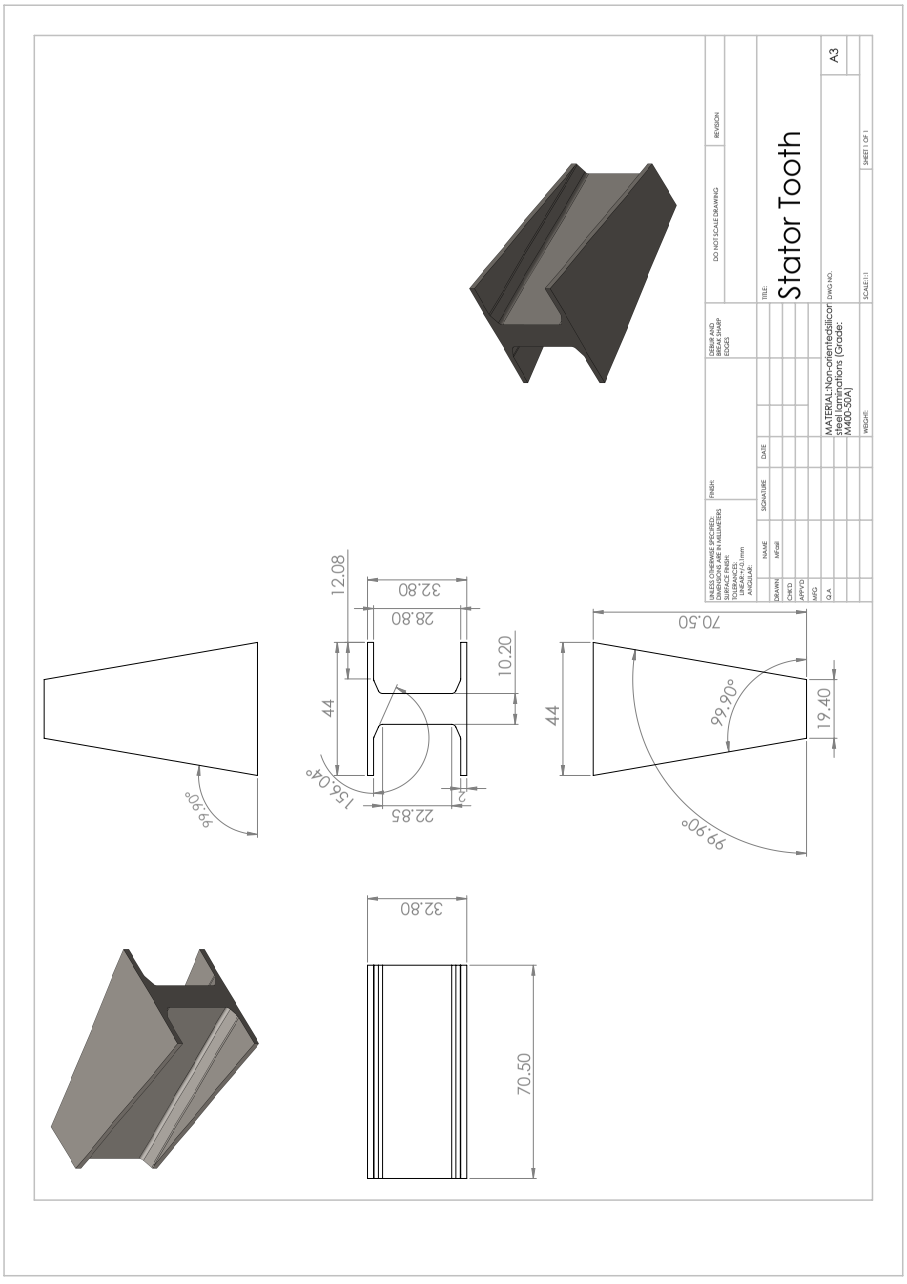
Stator Tooth
A3
MATERIAL:Non-orientedsilicon steel laminations (Grade: M400-50A)
DO NOT SCALE DRAWING
REVISION
DRAWN
CHK'D
APP'D
MFG
Q.A
NAME
SIGNATURE
DATE
FINISH:
SCALE:1:1
SHEET 1 OF 1
99.90°
12.08
32.80
28.80
10.20
44
156.04°
22.85
70.50
99.90°
44
19.40
99.90°
32.80
70.50

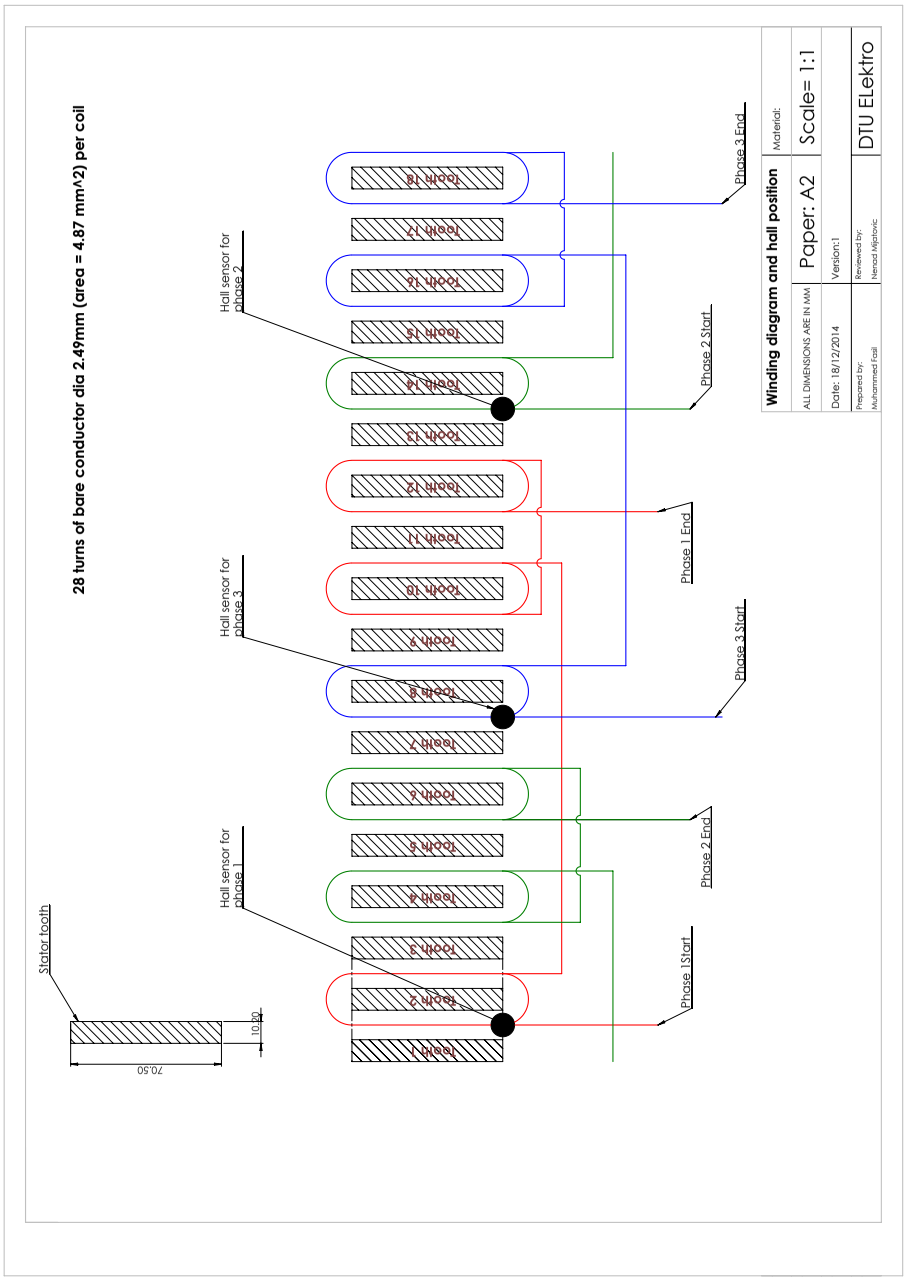
28 turns of bare conductor dia 2.49mm (area = 4.87 mm^2) per coil
Winding diagram and hall position
ALL DIMENSIONS ARE IN MM
Paper: A2
Scale= 1:1
Date: 18/12/2014
Version:1
Prepared by: Muhammed Fazil
Reviewed by: Nenad Mijatovic
DTU ELektro
Material:
Stator tooth
70.50
10.20
Hall sensor for phase 1
Hall sensor for phase 2
Hall sensor for phase 3
Phase 1Start
Phase 1 End
Phase 2 Start
Phase 2 End
Phase 3 Start
Phase 3 End
Tooth 1
Tooth 2
Tooth 3
Tooth 4
Tooth 5
Tooth 6
Tooth 7
Tooth 8
Tooth 9
Tooth 10
Tooth 11
Tooth 12
Tooth 13
Tooth 14
Tooth 15
Tooth 16
Tooth 17
Tooth 18

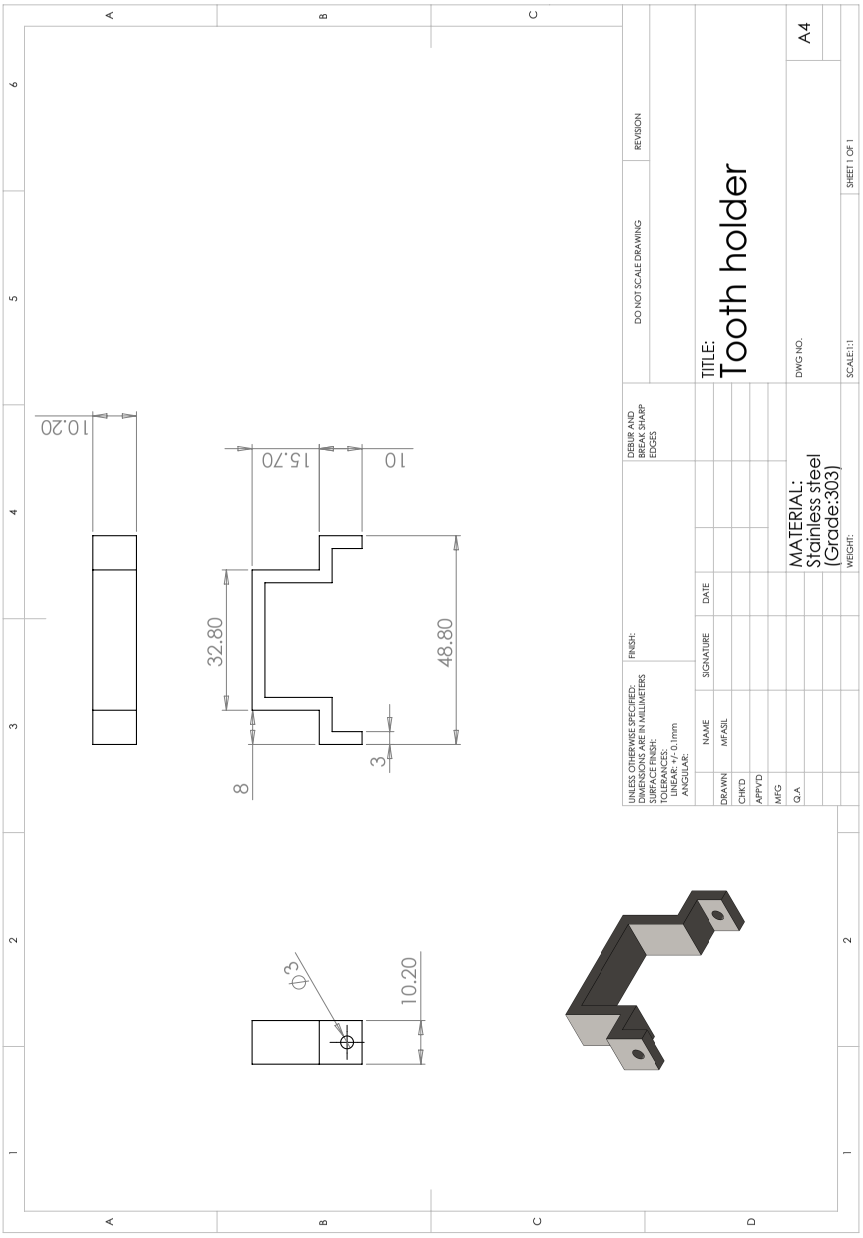
10.20
15.70
10
32.80
48.80
8
3
ϕ3
10.20
TITLE:
Tooth holder
MATERIAL:
Stainless steel
(Grade:303)
A4
DO NOT SCALE DRAWING
REVISION
DEBUR AND
BREAK SHARP
EDGES
FINISH:
UNLESS OTHERWISE SPECIFIED:
DIMENSIONS ARE IN MILLIMETERS
SURFACE FINISH:
TOLERANCES:
LINEAR: +/-0.1mm
ANGULAR:
NAME
SIGNATURE
DATE
DRAWN
MFASIL
CHK'D
APPV'D
MFG
Q.A
DWG NO.
WEIGHT:
SCALE:1:1
SHEET 1 OF 1

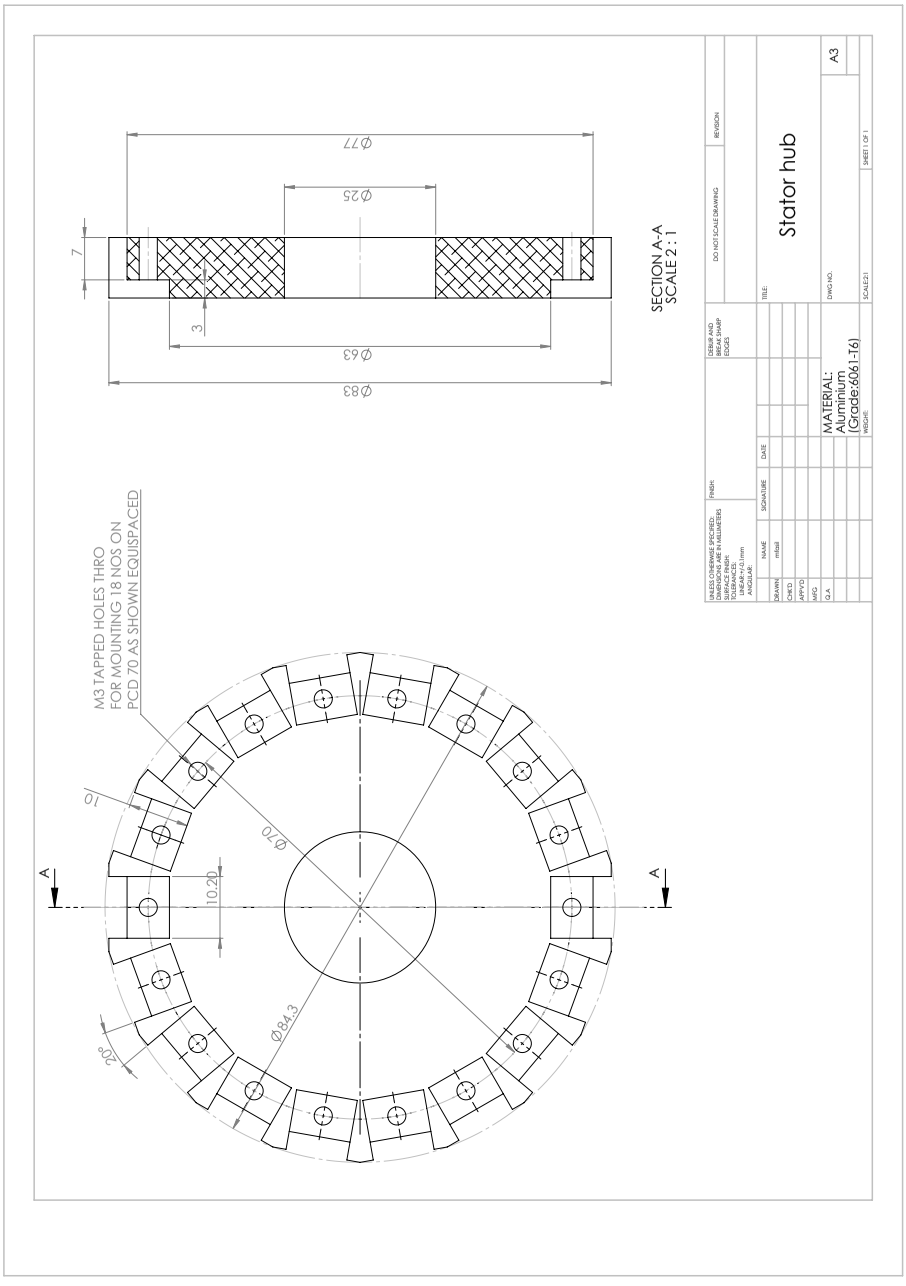
Ø77
Ø25
7
3
Ø63
Ø83
SECTION A-A
SCALE 2 : 1
M3 TAPPED HOLES THRO
FOR MOUNTING 18 NOS ON
PCD 70 AS SHOWN EQUISPACED
10
Ø70
10.20
20°
Ø84.3
A
A
Stator hub
MATERIAL:
Aluminium
(Grade:6061-T6)
A3

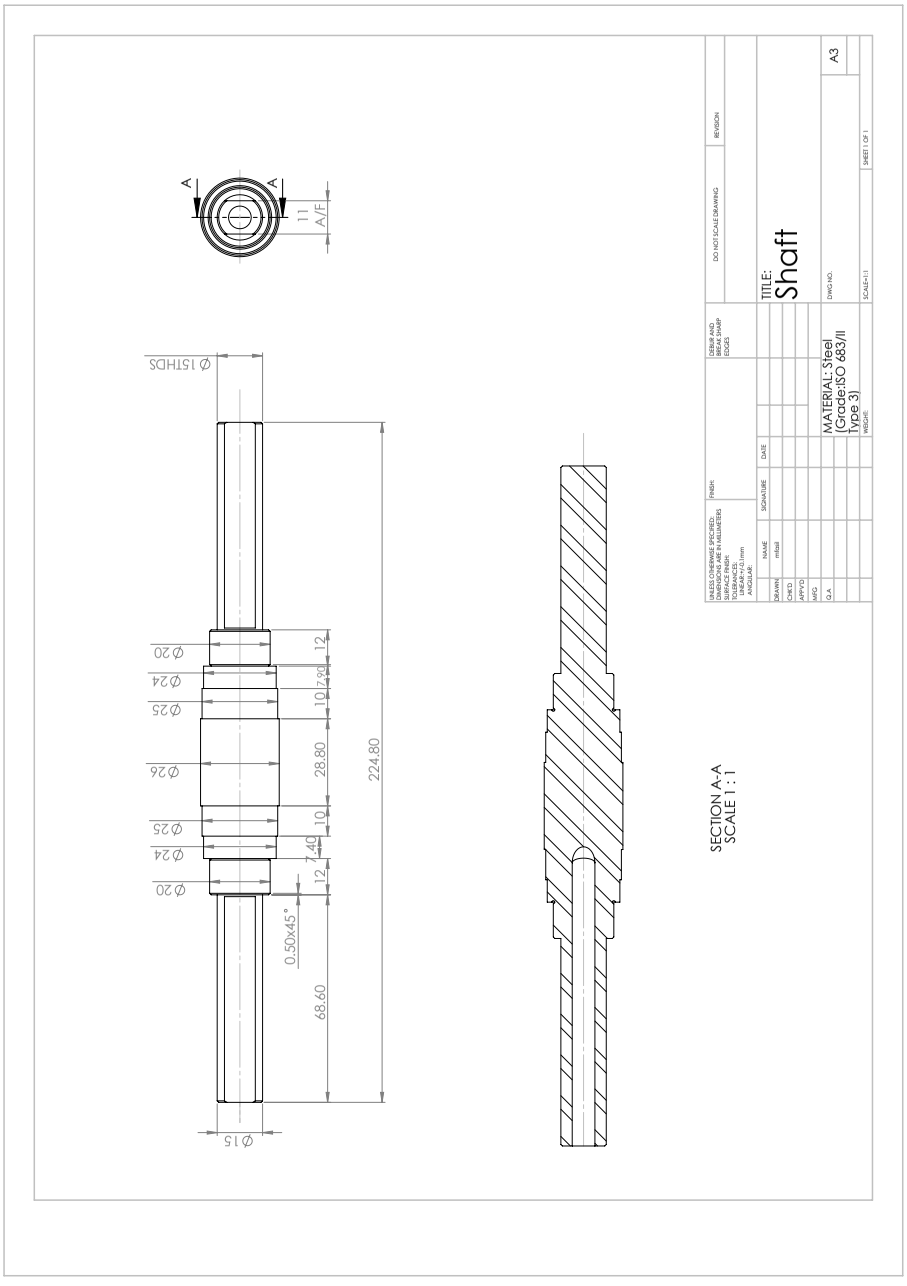
A
A
11
A/F
Ø 15THDS
Ø20
Ø24
Ø25
Ø26
Ø25
Ø24
Ø20
12
7.90
10
28.80
10
7.40
12
0.50x45°
68.60
224.80
Ø15
SECTION A-A
SCALE 1 : 1
UNLESS OTHERWISE SPECIFIED:
DIMENSIONS ARE IN MILLIMETERS
SURFACE FINISH:
TOLERANCES:
LINEAR +/-0.1mm
ANGULAR:
FINISH:
DEBUR AND
BREAK SHARP
EDGES
DO NOT SCALE DRAWING
REVISION
NAME
SIGNATURE
DATE
DRAWN
mtsai
CHK'D
APP'D
MFG
Q.A
MATERIAL: Steel
(Grade:ISO 683/II
Type 3)
WEIGHT:
TITLE:
Shaft
DWG NO.
A3
SCALE:1:1
SHEET 1 OF 1

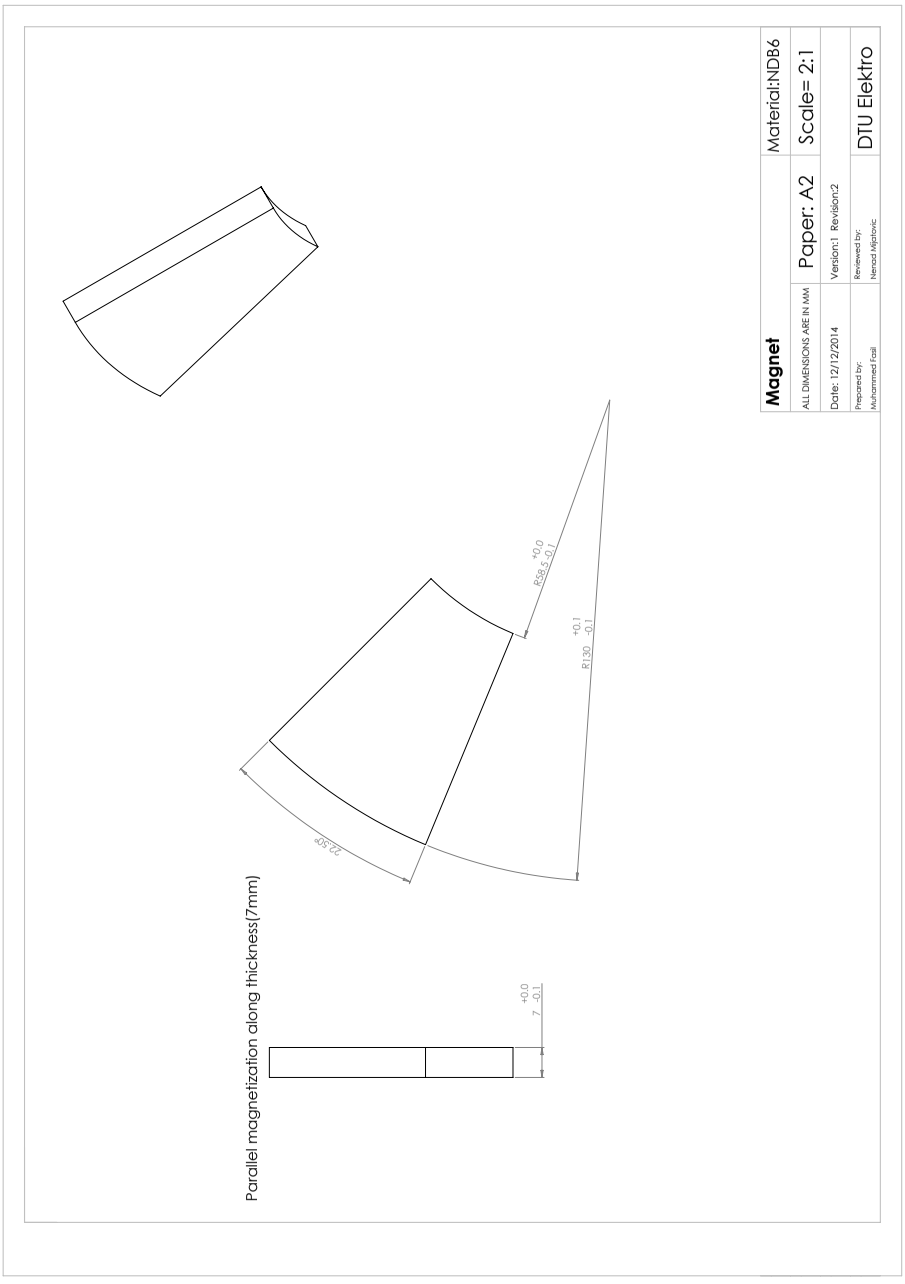
Magnet
Material:NDB6
ALL DIMENSIONS ARE IN MM
Paper: A2
Scale= 2:1
Date: 12/12/2014
Version:1 Revision:2
Prepared by:
Muhammed Fasil
Reviewed by:
Nenad Mijatovic
DTU Elektro
Parallel magnetization along thickness(7mm)
22.50°
R58.5 +0.0 -0.1
R130 +0.1 -0.1
7 +0.0 -0.1

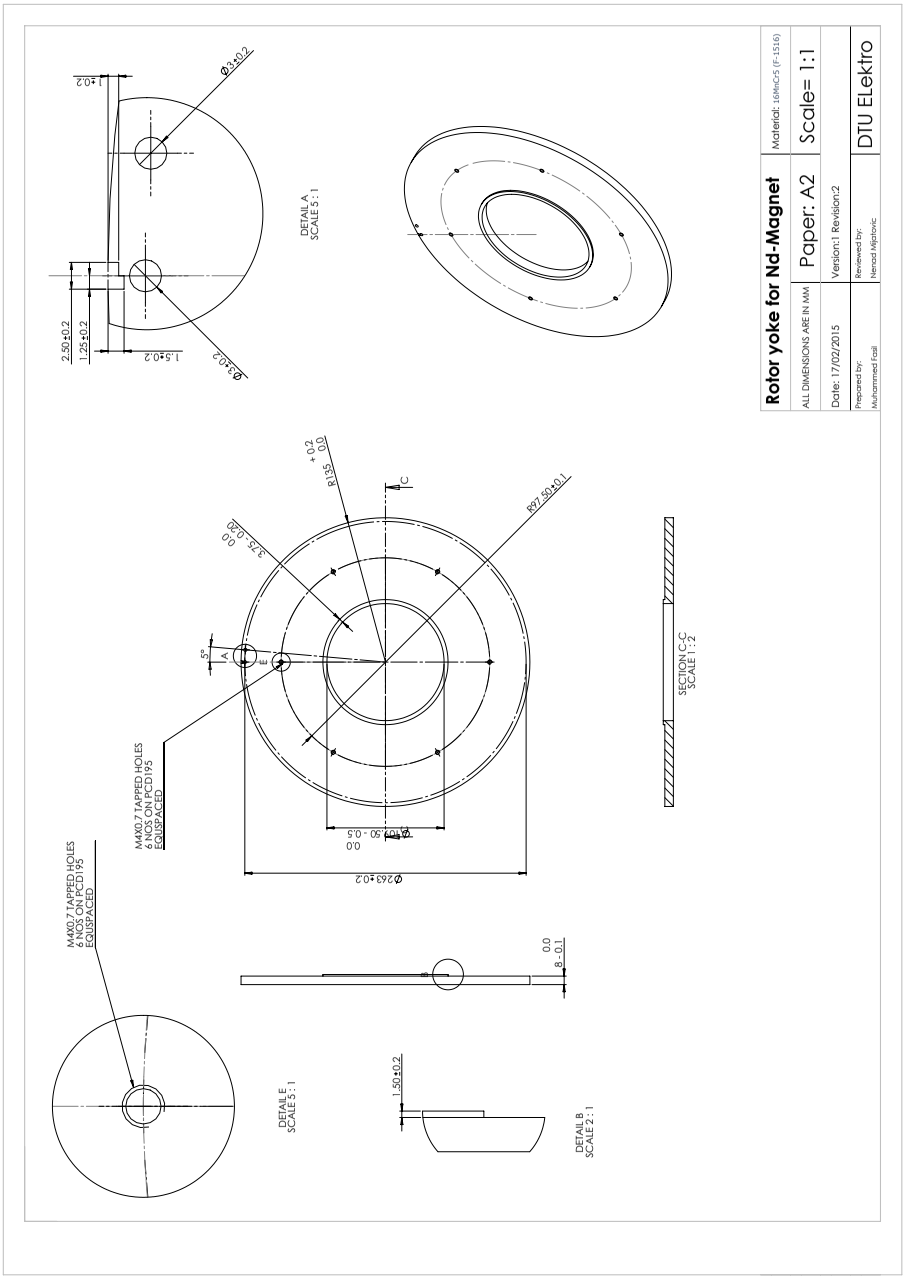
Rotor yoke for Nd-Magnet
Material: 16MnCr5 (F-15.16)
ALL DIMENSIONS ARE IN MM
Paper: A2
Scale= 1:1
Date: 17/02/2015
Version:1 Revision:2
Prepared by:
Mohammed Fasil
Reviewed by:
Nenad Mijatovic
DTU ELektro
DETAIL A
SCALE 5 : 1
DETAIL E
SCALE 5 : 1
DETAIL B
SCALE 2 : 1
SECTION C-C
SCALE 1 : 2
M4X0.7 TAPPED HOLES
6 NOS ON PCD195
EQUISPACED
M4X0.7 TAPPED HOLES
6 NOS ON PCD195
EQUISPACED

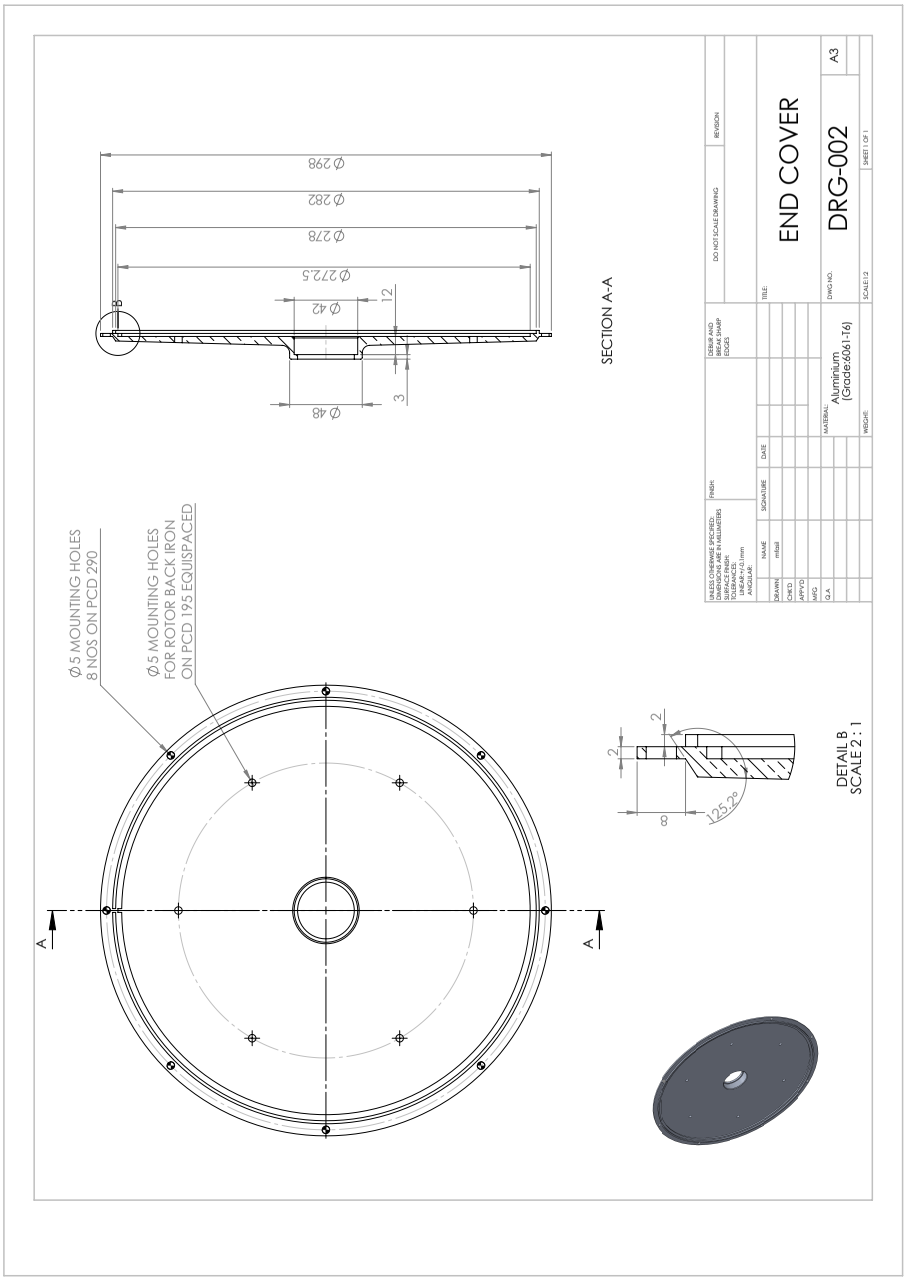
Ø 5 MOUNTING HOLES
8 NOS ON PCD 290
Ø 5 MOUNTING HOLES
FOR ROTOR BACK IRON
ON PCD 195 EQUISPACED
SECTION A-A
Ø 298
Ø 282
Ø 278
Ø 272.5
Ø 42
Ø 48
12
3
DETAIL B
SCALE 2 : 1
125.2°
END COVER
DRG-002
A3
Aluminium
(Grade:6061-T6)

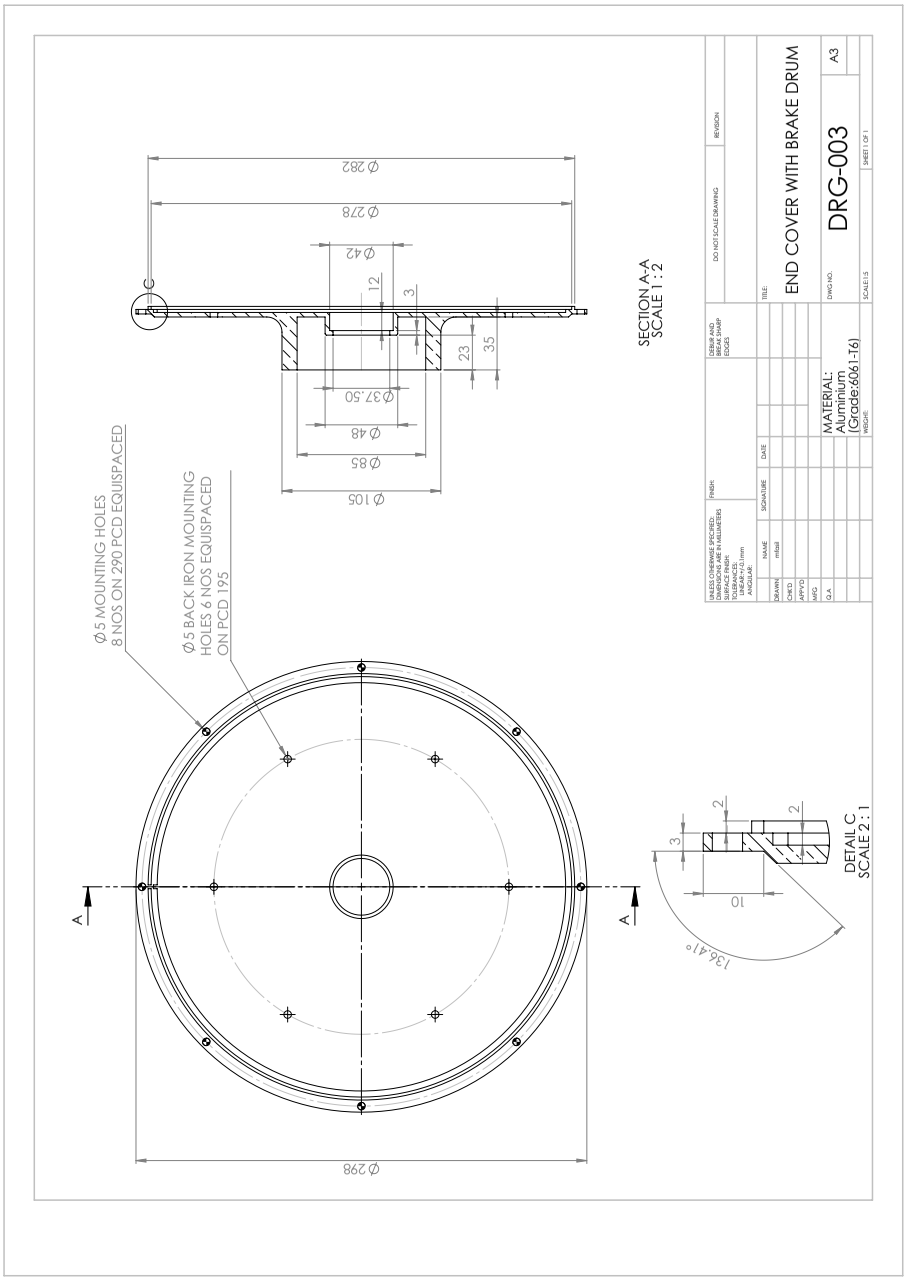
Ø 282
Ø 278
Ø 42
12
3
23
35
Ø 37.50
Ø 48
Ø 85
Ø 105
SECTION A-A
SCALE 1 : 2
Ø 5 MOUNTING HOLES
8 NOS ON 290 PCD EQUISPACED
Ø 5 BACK IRON MOUNTING
HOLES 6 NOS EQUISPACED
ON PCD 195
A
A
Ø 298
2
3
2
10
136.41°
DETAIL C
SCALE 2 : 1
UNLESS OTHERWISE SPECIFIED:
DIMENSIONS ARE IN MILLIMETERS
SURFACE FINISH:
TOLERANCES:
LINEAR +/-0.1mm
ANGULAR:
NAME
SIGNATURE
DATE
DRAWN
CHKD
APPVD
MFG
Q.A
FINISH:
DEBUR AND
BREAK SHARP
EDGES
MATERIAL:
Aluminium
(Grade:6061-T6)
WEIGHT:
DO NOT SCALE DRAWING
REVISION
TITLE:
END COVER WITH BRAKE DRUM
DWG NO.
DRG-003
A3
SCALE:1:5
SHEET 1 OF 1

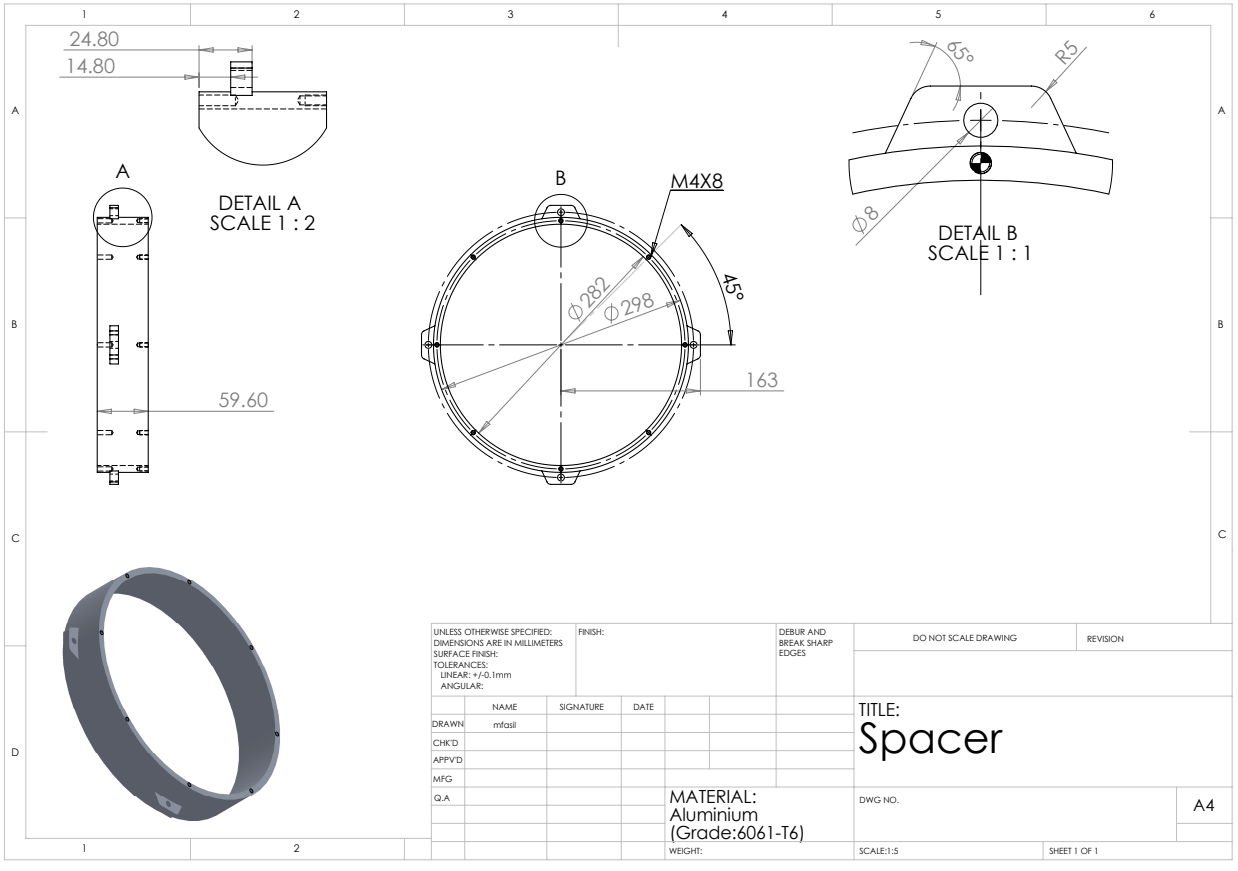
24.80
14.80
A
DETAIL A
SCALE 1 : 2
59.60
B
M4X8
45°
Ø282
Ø298
163
65°
R5
Ø8
DETAIL B
SCALE 1 : 1
UNLESS OTHERWISE SPECIFIED:
DIMENSIONS ARE IN MILLIMETERS
SURFACE FINISH:
TOLERANCES:
LINEAR: +/-0.1mm
ANGULAR:
FINISH:
DEBUR AND BREAK SHARP EDGES
DO NOT SCALE DRAWING
REVISION
NAME
SIGNATURE
DATE
DRAWN
mfasil
CHK'D
APPV'D
MFG
Q.A
TITLE:
Spacer
MATERIAL:
Aluminium
(Grade:6061-T6)
DWG NO.
A4
WEIGHT:
SCALE:1:5
SHEET 1 OF 1

E.2 Ferrite magnet magnet SAT PMBLDC motor

list of drawings

1. Stator tooth
2. Winding diagram
3. Tooth holder
4. Stator hub
5. Shaft
6. Magnet poles
7. Rotor yoke
8. End cover without brake drum
9. End cover with brake drum
10. Spacer

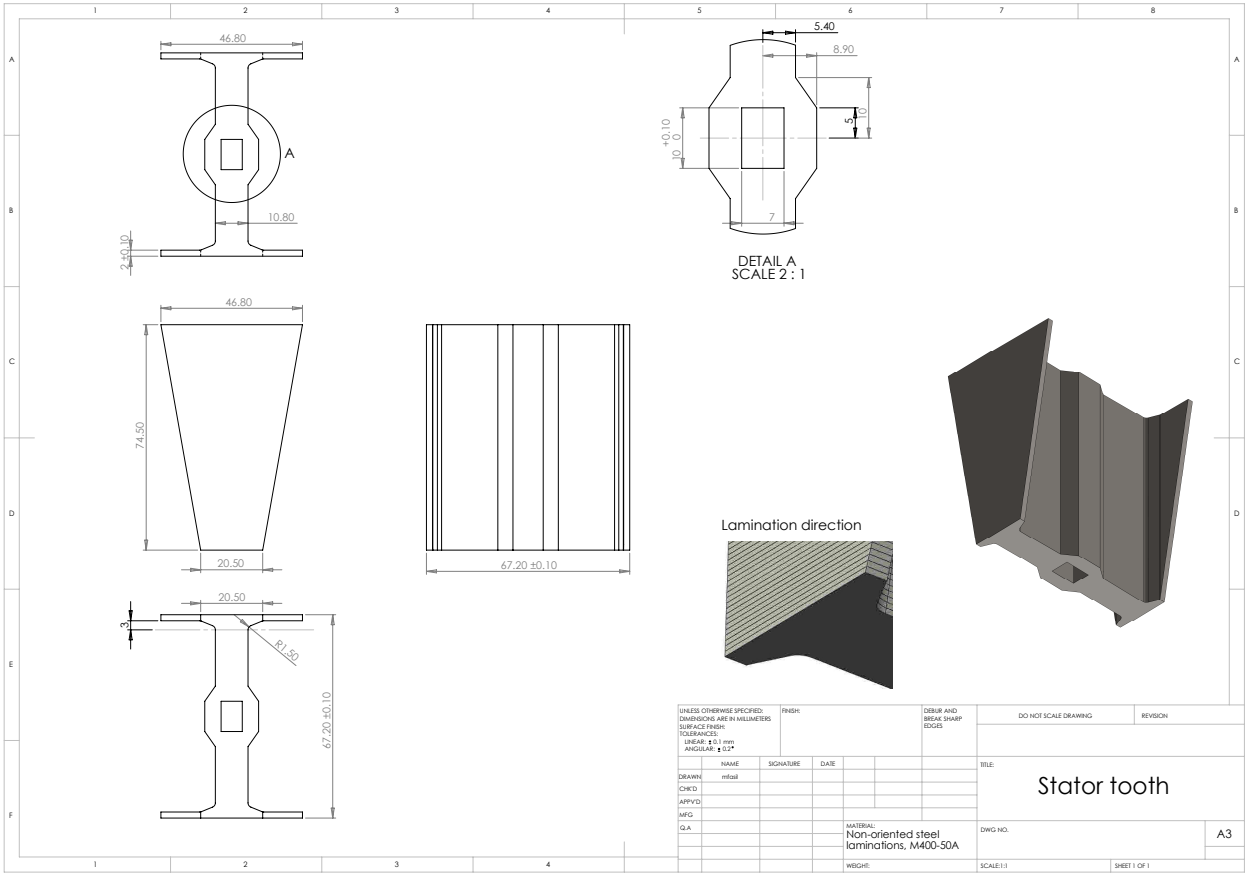
46.80
A
10.80
2 ±0.10
46.80
74.50
20.50
20.50
3
R1.50
67.20 ±0.10
67.20 ±0.10
5.40
8.90
5
10
+0.10
0
10
7
DETAIL A
SCALE 2 : 1
Lamination direction
UNLESS OTHERWISE SPECIFIED:
DIMENSIONS ARE IN MILLIMETERS
SURFACE FINISH:
TOLERANCES:
LINEAR: ± 0.1 mm
ANGULAR: ± 0.2°
FINISH:
DEBUR AND BREAK SHARP EDGES
DO NOT SCALE DRAWING
REVISION
NAME
SIGNATURE
DATE
DRAWN
mfasil
CHK'D
APPV'D
MFG
Q.A
TITLE:
Stator tooth
MATERIAL:
Non-oriented steel laminations, M400-50A
DWG NO.
A3
WEIGHT:
SCALE:1:1
SHEET 1 OF 1

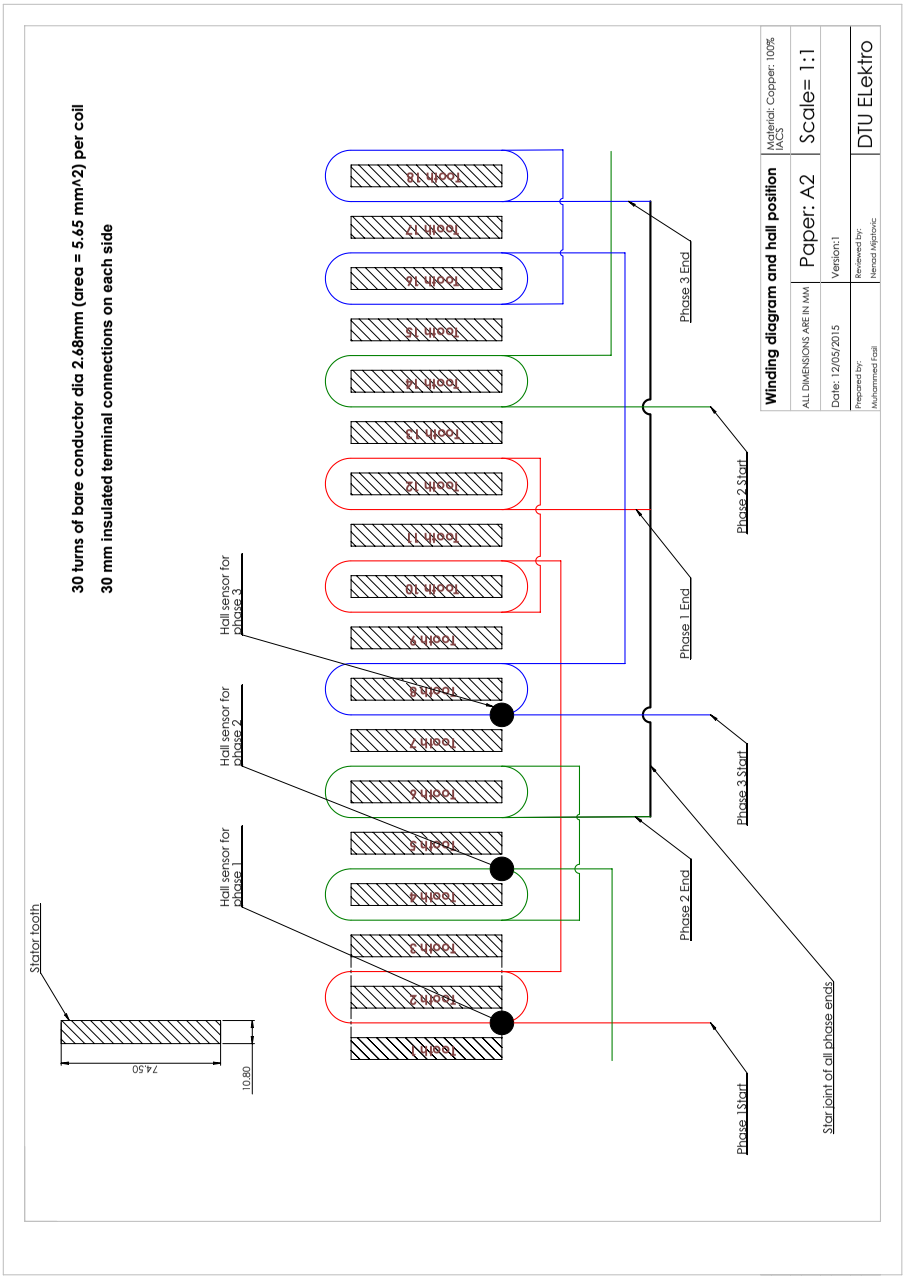
30 turns of bare conductor dia 2.68mm (area = 5.65 mm^2) per coil
30 mm insulated terminal connections on each side
Stator tooth
74.50
10.80
Hall sensor for phase 1
Hall sensor for phase 2
Hall sensor for phase 3
Tooth 1
Tooth 2
Tooth 3
Tooth 4
Tooth 5
Tooth 6
Tooth 7
Tooth 8
Tooth 9
Tooth 10
Tooth 11
Tooth 12
Tooth 13
Tooth 14
Tooth 15
Tooth 16
Tooth 17
Tooth 18
Phase 1Start
Phase 2 End
Phase 3 Start
Phase 1 End
Phase 2 Start
Phase 3 End
Star joint of all phase ends
Winding diagram and hall position
Material: Copper: 100% IACS
ALL DIMENSIONS ARE IN MM
Paper: A2
Scale= 1:1
Date: 12/05/2015
Version:1
Prepared by: Mohammed Fazil
Reviewed by: Nenad Mijatovic
DTU ELektro

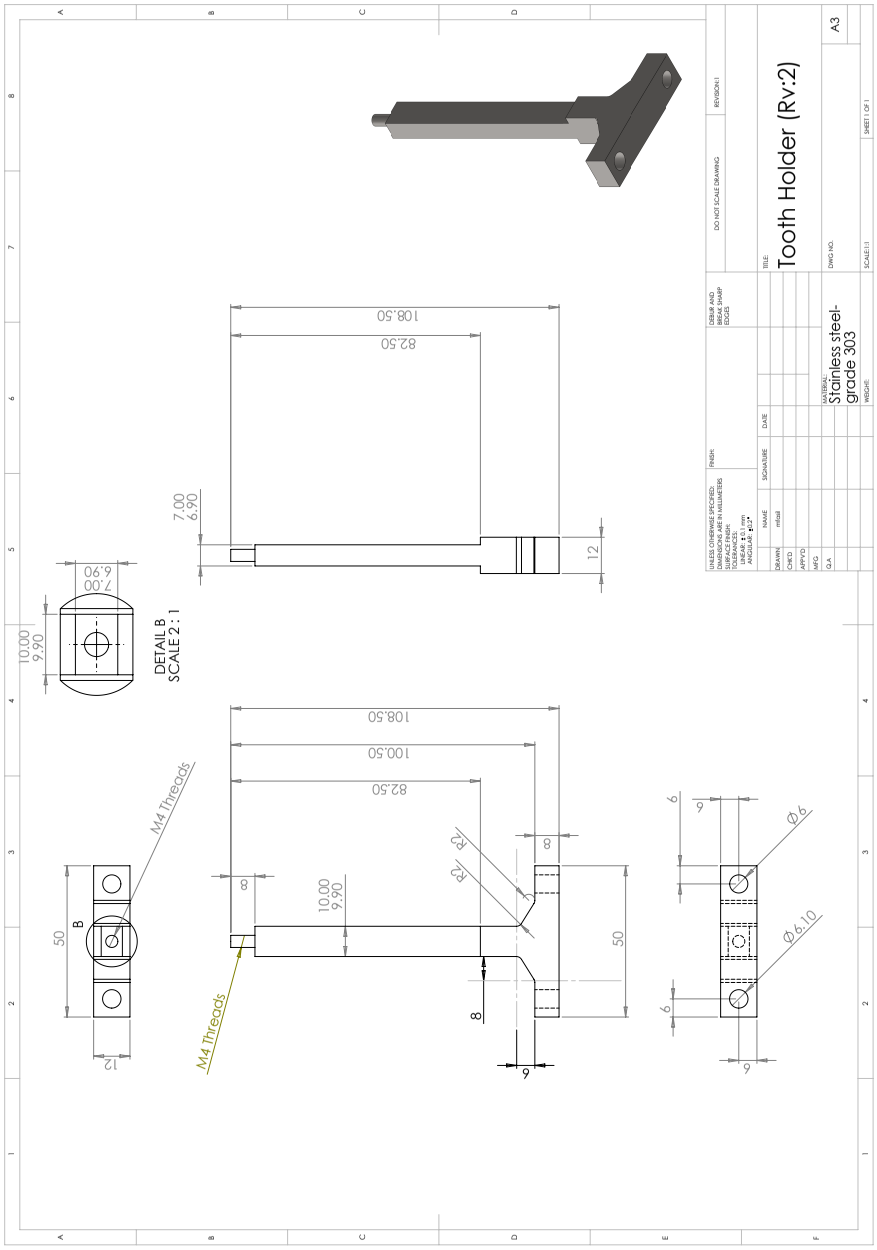
Tooth Holder (Rv:2)
Stainless steel-grade 303
A3
DO NOT SCALE DRAWING
DRAW AND BREAK SHARP EDGES
108.50
82.50
100.50
7.00
6.90
10.00
9.90
12
DETAIL B
SCALE 2 : 1
M4 Threads
M4 Threads
50
8
R2
Ø6
Ø6.10

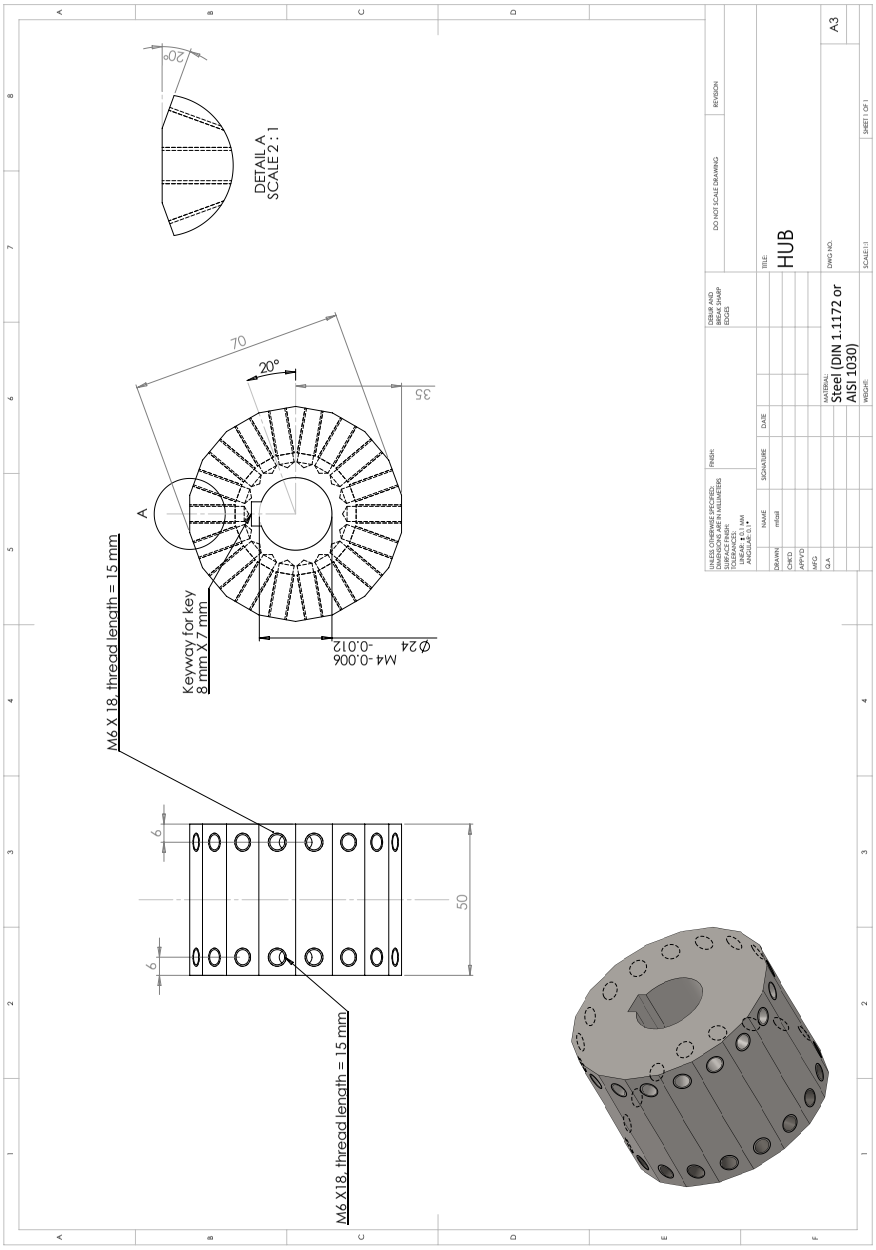
DETAIL A
SCALE 2 : 1
20°
70
20°
35
A
Keyway for key
8 mm X 7 mm
Ø24 -0.012
M4 -0.006
M6 X 18, thread length = 15 mm
M6 X18, thread length = 15 mm
6
6
50
HUB
Steel (DIN 1.1172 or AISI 1030)
A3

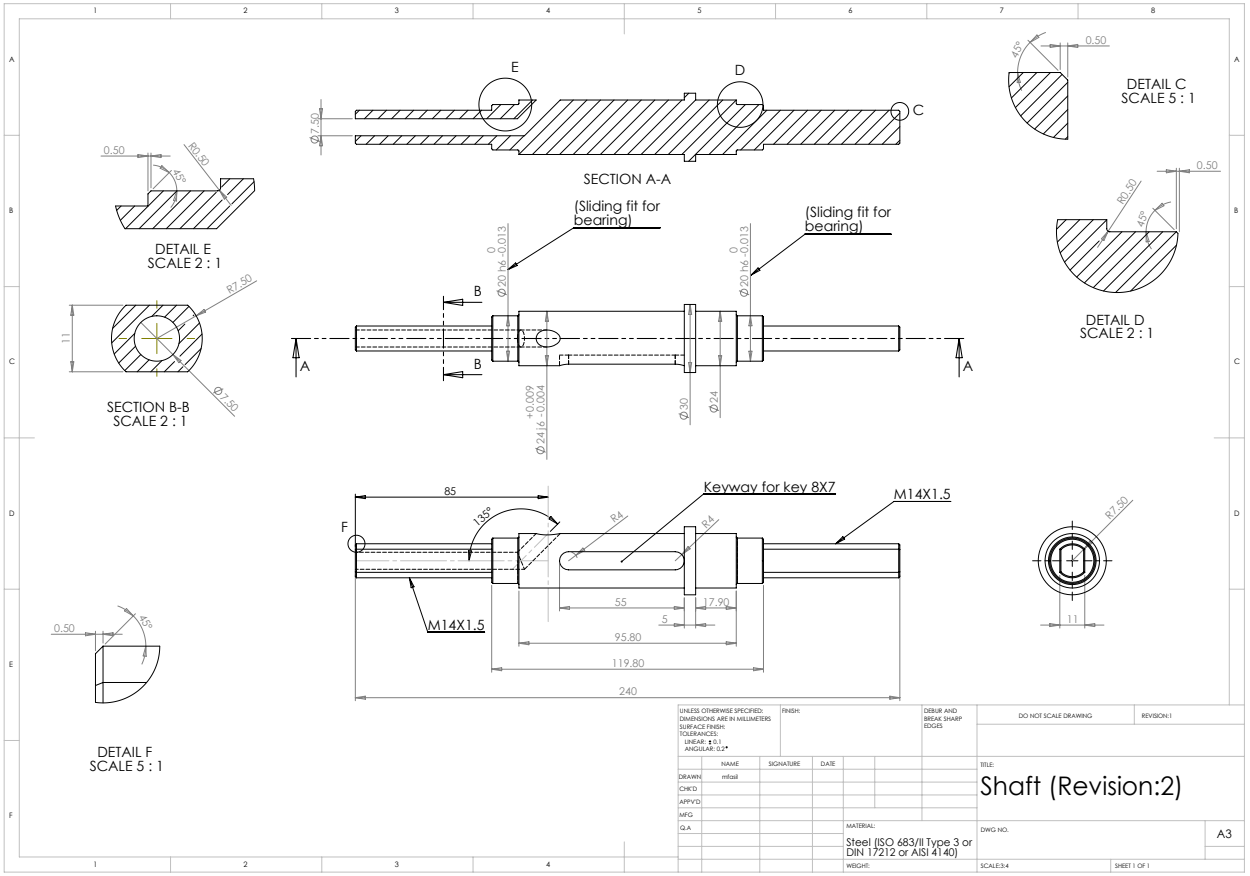
SECTION A-A
DETAIL C
SCALE 5 : 1
DETAIL E
SCALE 2 : 1
DETAIL D
SCALE 2 : 1
SECTION B-B
SCALE 2 : 1
DETAIL F
SCALE 5 : 1
(Sliding fit for bearing)
(Sliding fit for bearing)
Keyway for key 8X7
M14X1.5
M14X1.5
85
135°
55
17.90
5
95.80
119.80
240
Shaft (Revision:2)
Steel (ISO 683/II Type 3 or DIN 17212 or AISI 4140)
A3

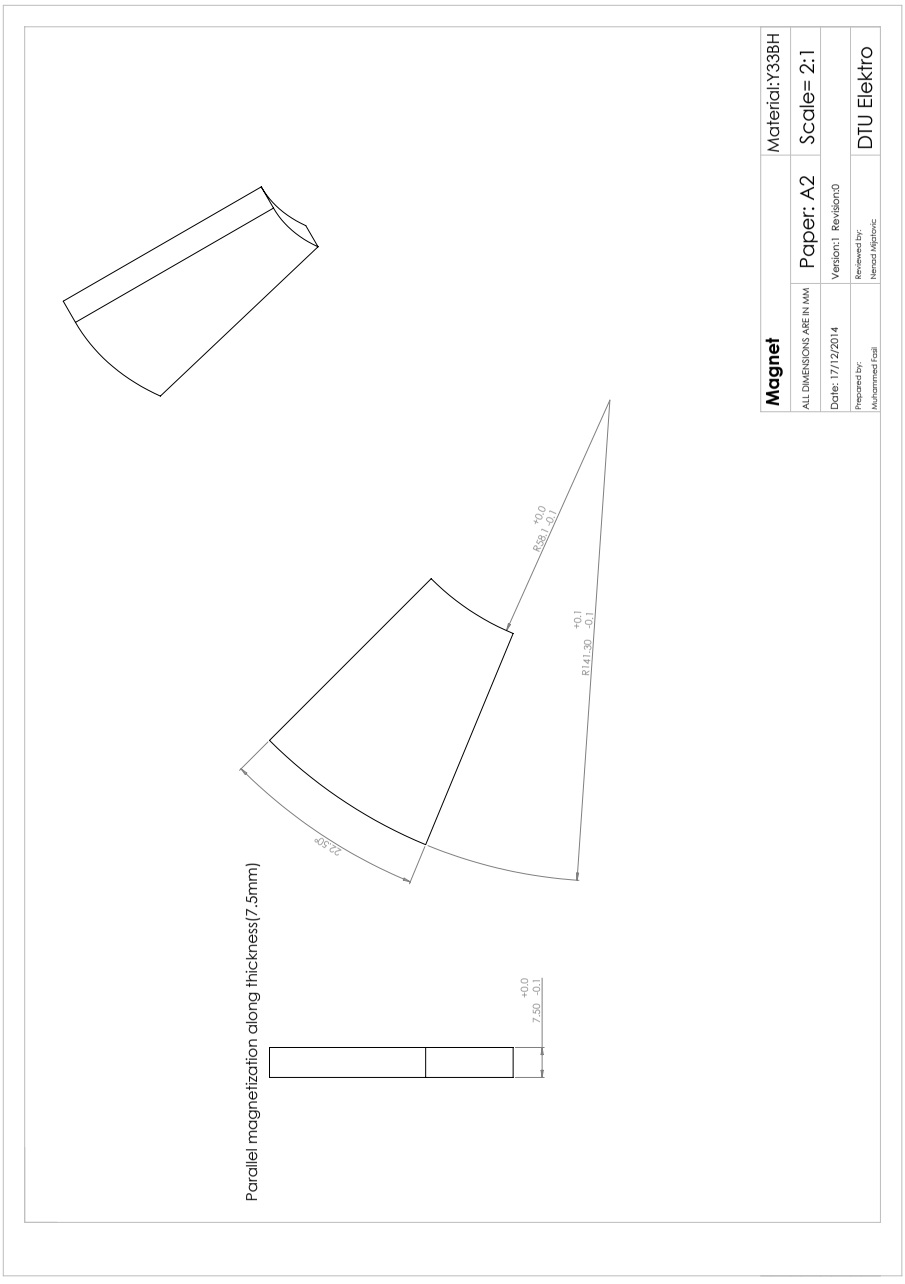
Magnet
Material:Y33BH
ALL DIMENSIONS ARE IN MM
Paper: A2
Scale= 2:1
Date: 17/12/2014
Version:1 Revision:0
Prepared by:
Mohammed Fail
Reviewed by:
Nenad Mijatovic
DTU Elektro
Parallel magnetization along thickness(7.5mm)
7.50 +0.0 -0.1
22.50°
R141.30 +0.1 -0.1
R98.1 +0.0 -0.1

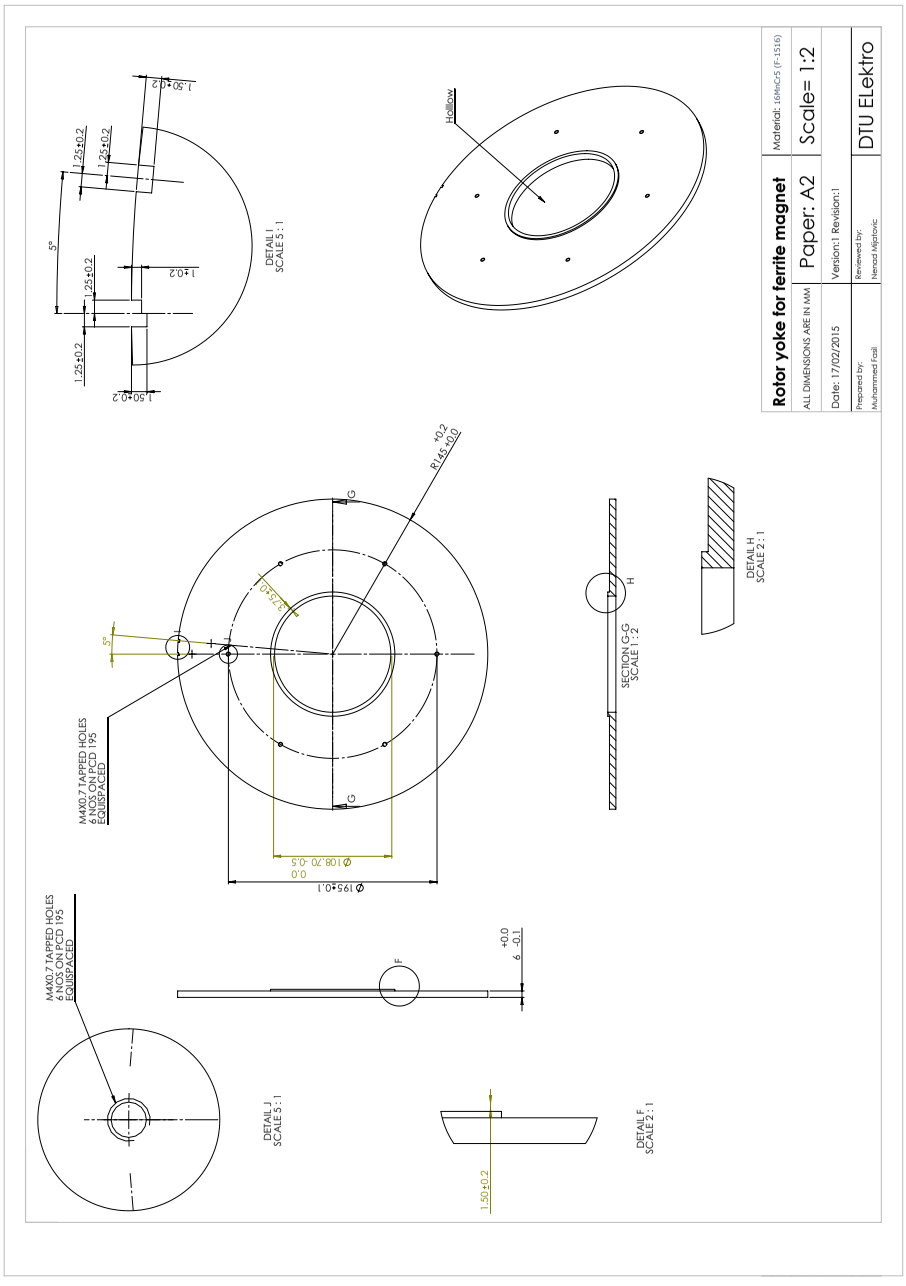
Rotor yoke for ferrite magnet
Material: 16MnCr5 (F-1516)
ALL DIMENSIONS ARE IN MM
Paper: A2
Scale= 1:2
Date: 17/02/2015
Version:1 Revision:1
Prepared by:
Muhammed Fasil
Reviewed by:
Nenad Mijatovic
DTU Elektro
Hollow
DETAIL I
SCALE 5 : 1
1.25±0.2
1.50±0.2
5°
MAX0.7 TAPPED HOLES
6 NOS ON PCD 195
EQUISPACED
Ø195±0.1
Ø108.70 -0.0 -0.5
R145±0.2 +0.2
SECTION G-G
SCALE 1 : 2
DETAIL H
SCALE 2 : 1
DETAIL J
SCALE 5 : 1
DETAIL F
SCALE 2 : 1
6 -0.1 +0.0
1.50±0.2

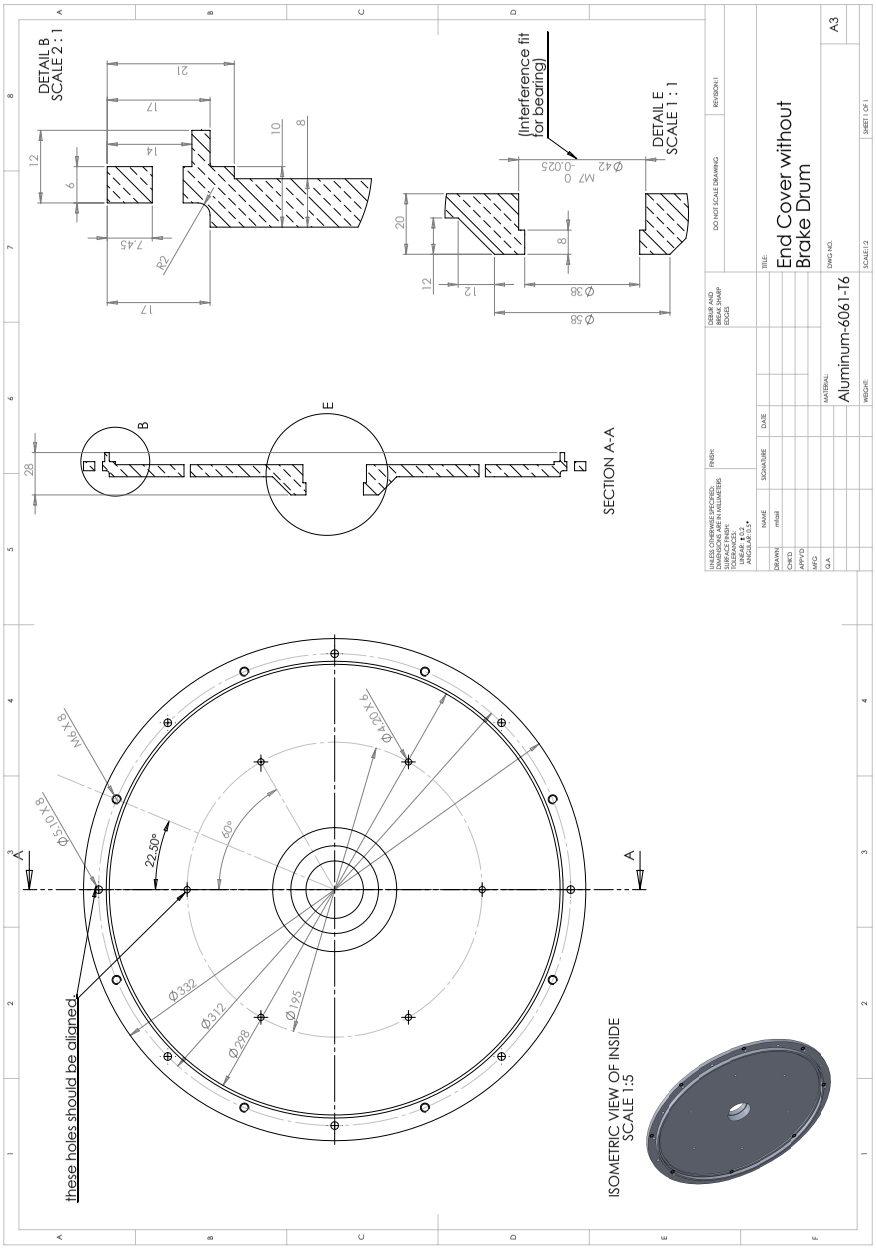
End Cover without
Brake Drum
Aluminum-6061-T6
A3
DETAIL B
SCALE 2 : 1
DETAIL E
SCALE 1 : 1
(Interference fit
for bearing)
SECTION A-A
ISOMETRIC VIEW OF INSIDE
SCALE 1:5
these holes should be aligned

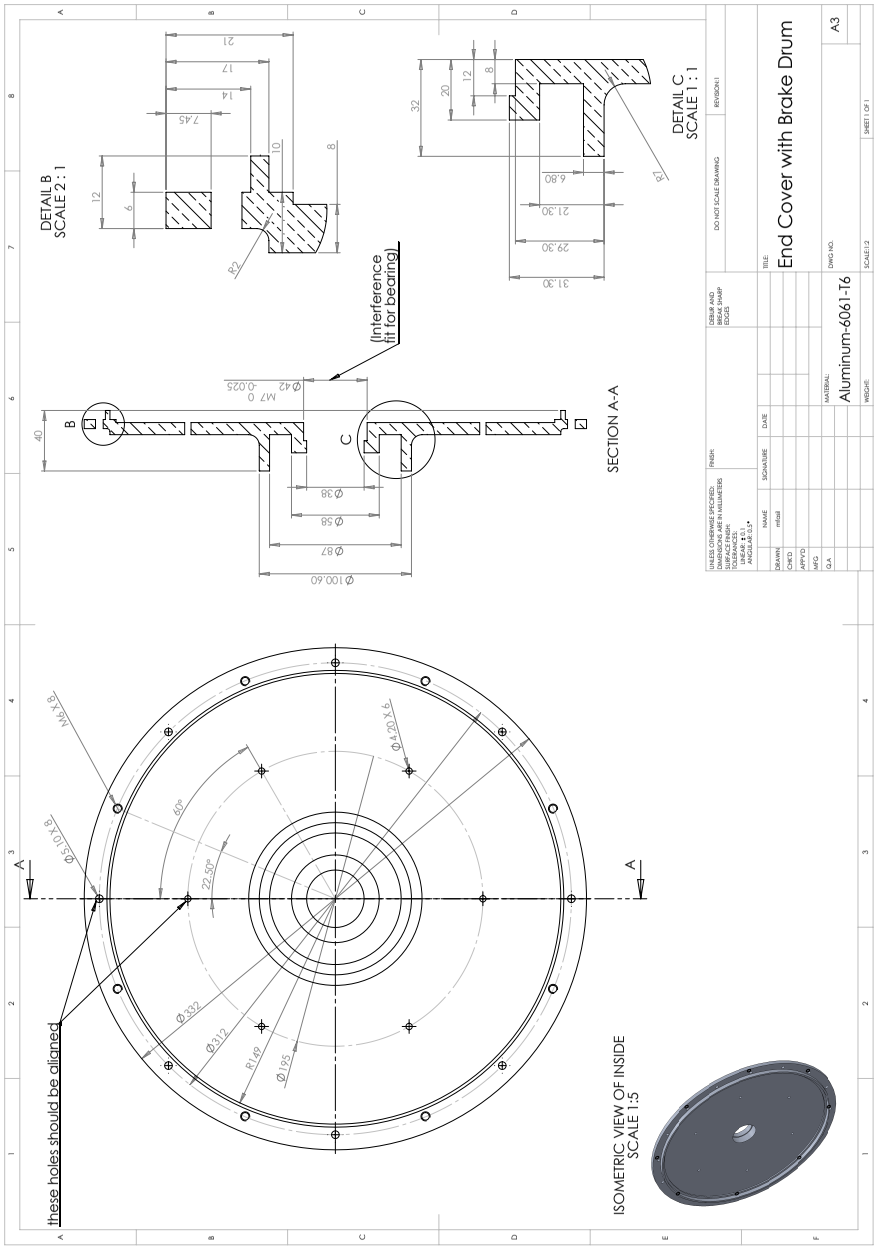
End Cover with Brake Drum
Aluminum-6061-T6
A3
DETAIL B
SCALE 2 : 1
DETAIL C
SCALE 1 : 1
SECTION A-A
(Interference fit for bearing)
these holes should be aligned
ISOMETRIC VIEW OF INSIDE
SCALE 1:5

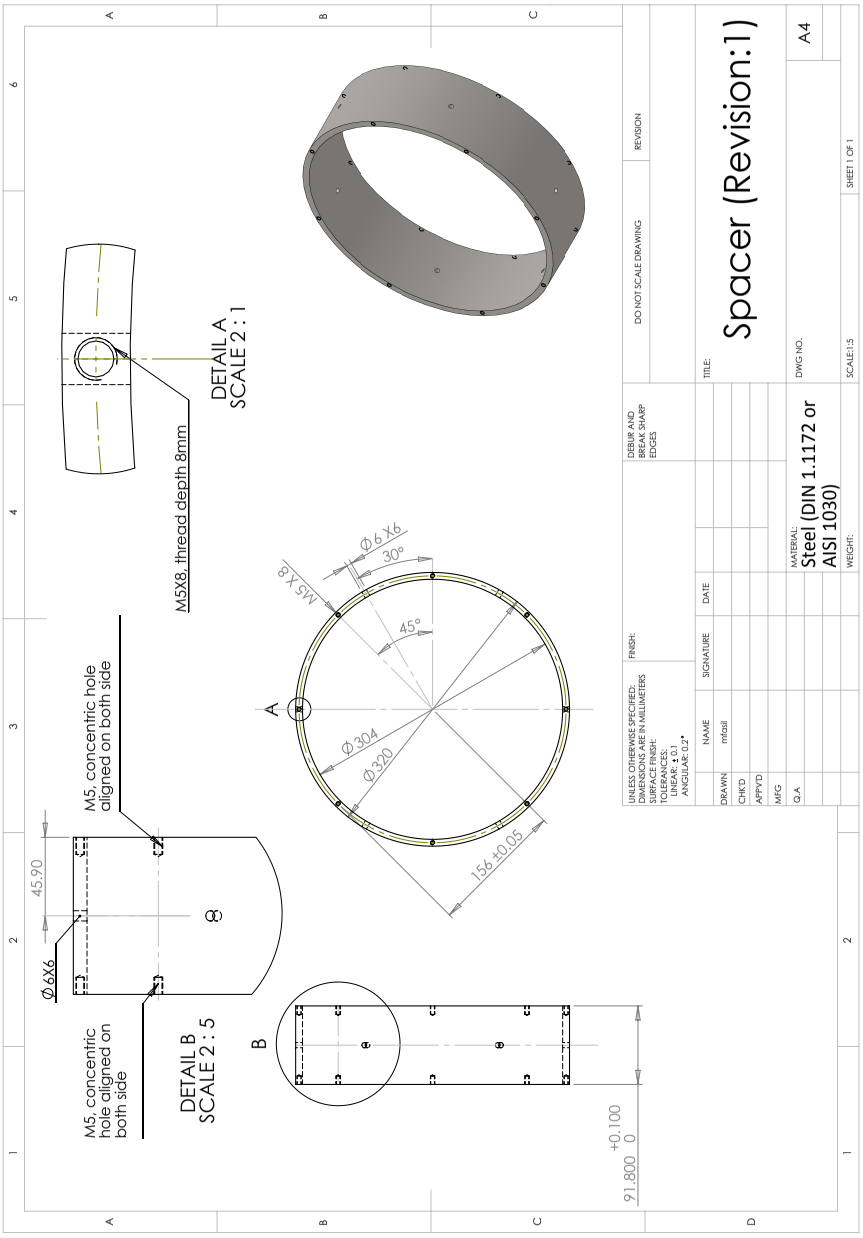
Spacer (Revision:1)
A4
Steel (DIN 1.1172 or AISI 1030)
DETAIL A
SCALE 2 : 1
DETAIL B
SCALE 2 : 5
M5X8, thread depth 8mm
M5, concentric hole aligned on both side
M5, concentric hole aligned on both side
Ø6X6
45.90
Ø6.X6
30°
45°
M5 X 8
Ø304
Ø320
156±0.05
91.800 +0.100 0
DO NOT SCALE DRAWING
REVISION
DEBUR AND BREAK SHARP-EDGES
UNLESS OTHERWISE SPECIFIED:
DIMENSIONS ARE IN MILLIMETERS
SURFACE FINISH:
TOLERANCES:
LINEAR: ±0.1
ANGULAR: 0.2°
FINISH:
NAME
SIGNATURE
DATE
DRAWN
mfadil
CHK'D
APPV'D
MFG
Q.A
MATERIAL:
WEIGHT:
TITLE:
DWG NO.
SCALE:1:5
SHEET 1 OF 1

Appendix F

Published and submitted papers

Published papers

1. M. Fasil, D. Plesner, J. H. Walther, N. Mijatovic, J. Holbøll, and B. B. Jensen, "Numerical and Experimental Investigation of Heat Flow in Permanent Magnet Brushless DC Hub Motor", SAE International. Journal of Alternative Powertrains, vol. 4, no. 1, October 2014.

2. M. Fasil, N. Mijatovic, B. B. Jensen, and J. Holbøll, "Performance Variation of Ferrite Magnet PMBLDC Motor With Temperature", IEEE Transactions on Magnetics, vol. 51, no. 12, December 2015.

3. M. Fasil, N. Mijatovic, B. Jensen, and J. Holbøll, "FE based design synthesis of axial flux PMBLDC Motors", IEEE Transactions on Applied Superconductivity, vol. PP, no. 4, June 2016.

4. M. Fasil, C. Antaloae, N. Mijatovic, B. B. Jensen, and J. Holbøll, "Improved dq-Axes Model of PMSM Considering Airgap Flux Harmonics and Saturation", IEEE Transactions on Applied Superconductivity, vol. 26, no. 4, June 2016.

5. M. Fasil, N. Mijatovic, B. Jensen, and J. Holbøll, "Nonlinear Dynamic Model of PMBLDC Motor Considering Core Losses", IEEE Transactions on Industrial Electronics, vol. 64, no. 12, December 2017.

Downloaded from SAE International by Muhammed Fasil Palakkunnu Veettil, Wednesday, October 01, 2014

2014-01-2900
Published 10/13/2014
Copyright © 2014 SAE International
doi:10.4271/2014-01-2900
saealtpow.saejournals.org

Numerical and Experimental Investigation of Heat Flow in Permanent Magnet Brushless DC Hub Motor

Muhammed Fasil, Daniel Plesner, Jens Honore Walther, Nenad Mijatovic, and Joachim Holbøll
Technical University of Denmark

Bogi Bech Jensen
University of the Faroe Islands

ABSTRACT

This paper investigates the heat dissipation in the hub motor of an electric two-wheeler using lumped parameter (LP), finite element (FE) and computational fluid dynamic (CFD) models. The motor uses external rotor permanent magnet brushless DC topology and nearly all of its losses are generated in the stator. The hub motor construction restricts the available conductive paths for heat dissipation from the stator to the ambient only through the shaft. In contrast to an internal rotor structure, where the stator winding losses are diffused via conduction, here convection plays a major role in loss dissipation. Therefore, a LP thermal model with improved convection modelling has been proposed to calculate the temperature of the components inside the hub motor. The developed model is validated with the FE thermal model and the test data. In addition, CFD tools has been used to accurately model the internal and the external flow as well as the convective heat transfer of the hub motor. Finally, an optimization study of the hub motor has been carried out using the CFD model to improve heat transfer from the stator.

CITATION: Fasil, M., Plesner, D., Walther, J., Mijatovic, N. et al., "Numerical and Experimental Investigation of Heat Flow in Permanent Magnet Brushless DC Hub Motor," *SAE Int. J. Alt. Power.* 4(1):2015, doi:10.4271/2014-01-2900.

INTRODUCTION

Major cities around the world are either implementing or considering the stringent environmental pollution regulations. This, along with the increasing price of fossil fuels and the growth of renewable energy has brought electric propulsion back to the market. The electric propulsion uses an electrical energy storage such as batteries or fuel cells, along with electric drives instead of an IC engine powertrain. Electric motor in an electric drivetrain can be incorporated in number of ways and hub motor, especially in direct drive configuration, offers a number of benefits such as improved efficiency, increased cabin space in four wheelers and weight reduction in two wheelers without affecting the ride and handling [1].

Figure 1. Exploded view of the motor (1. Endplate, 2. Rim, 3.Rotor core, 4. Magnet, 5. Winding, 6. Stator core, 7. Spider and 8. Non rotating shaft).

Downloaded from SAE International by Muhammed Fasil Palakkunnu Veettil, Wednesday, October 01, 2014

The hub motor investigated in this paper is taken from an electric two wheeler currently available in the market. The continuous rating of the motor is 750 W at 550 rpm and it has an external rotor radial flux permanent magnet brushless DC (PMBLDC) topology. The exploded view of the motor is shown in Fig. 1. The stator comprising of the stator core and the winding is attached to a non-rotating shaft via spider. The shaft is then connected to the two wheeler chassis. The wheel houses the rotor core and magnets and they are connected to the shaft via a set of endplates with bearing. An air gap of 0.5 mm separates the stator core and magnets.

A good thermal design of an electric motor not only helps to limit the temperature of its components within the thermal limit of their materials, but also allows the overall size reduction of motor [2]. A detailed thermal study is essential in case of the PMBLDC hub motor as nearly all of its losses are generated in the stator and their construction restricts available conductive paths for the heat dissipation to ambient only through the shaft. In contrast to an internal rotor structure, where the stator winding losses are diffused via conduction, here convection plays a major role in dissipating the losses.

In this work, a lumped parameter (LP) thermal model of PMBLDC hub motor is developed based on already available models [3, 4, 5, 6, 7]. The LP thermal model can be solved in minimum time and hence, it could be part of an electrical design program. This will helps the designer to evaluate the effects of change in ambient temperature and increased internal temperatures due to loading, on the motor performance. This is especially important in case of electric vehicle powertrain, as the motors are exposed to considerable temperature variation compared to the motors used in other applications. In addition, due to significant simplification, LP thermal model is computationally less demanding and could be used as a part of control algorithms to assess critical temperature rise in a real time and adjust control accordingly.

The developed LP model is validated with the finite element (FE) thermal model and the test data. The FE method can model more complex shapes and therefore predict more accurately than the LP thermal model. A sensitivity analysis of the LP thermal model has revealed that, the temperature of the components are highly influenced by the thermal resistance linked to the internal air and the motor casing. Subsequently, a computational fluid dynamic (CFD) model based study has been carried out to assess the internal and the external flow and the convective heat transfer. Further, an optimization study of the hub motor has been carried out using the CFD model to improve heat transfer from the stator.

LUMPED PARAMETER THERMAL MODEL

Losses in PMBLDC Motor

The resistive losses are generally the major component of power losses in PMBLDC motors and they are calculated as

$$P_r = mI_{ph}^2 R_{ph} \tag{1}$$

where m is the number of phases, I_{ph} is the RMS phase current and R_{ph} is the phase resistance of winding. The resistance varies with temperature and can be calculated from a known resistance at another temperature as [8]

$$R_{T2} = R_{T1}\left(\frac{234.5+T2}{234.5+T1}\right) \tag{2}$$

where R_{T1} and R_{T2} are resistances at temperatures $T1$ and $T2$ °C respectively. The hub motor considered here has coils with a turn diameter of 0.5 mm. Therefore, the ac effects such as skin, proximity and circulating current are not considered.

The stator core is made of insulated silicon steel laminations. Therefore, the magnetic flux variation due to the rotation of magnets generates eddy and hysteresis losses in laminations. These losses are estimated individually for stator teeth and yoke as the field variations in them are different [9]. The loss per unit mass due to hysteresis (P_h), eddy current in stator yoke (P_{ey}) and eddy current in stator tooth (P_{et}) are calculated as [9]

$$P_h = K_h f^{\alpha} B_m^{\beta} \tag{3}$$

$$P_{ey} = K_e \frac{8}{\pi} \frac{f^2 B_m^2}{\beta_m} \tag{4}$$

$$P_{et} = K_e \frac{4}{\pi} \frac{f^2 B_m^2}{\alpha_{tt}} \left[2 - \frac{\pi - \beta_m}{\alpha_{tt}}\right] \tag{5}$$

where f is the frequency of flux variation, B_m is the peak flux density, α_{tt} and β_m are the tooth arc and the pole width respectively in electrical radians, K_h, K_e, α and β are the curve fit constants calculated from the loss data of the laminations.

Besides the resistive losses and core losses, a PMBLDC motor will have electromagnetic losses in rotor core and in magnets. These are neglected in this study as they are found to be of very low value. The frictional loss in bearing and air friction loss are calculated using the standard formulas available in literature [4].

Downloaded from SAE International by Muhammed Fasil Palakkunnu Veettil, Wednesday, October 01, 2014

Thermal Network of Radial Flux PMBLDC Hub Motor

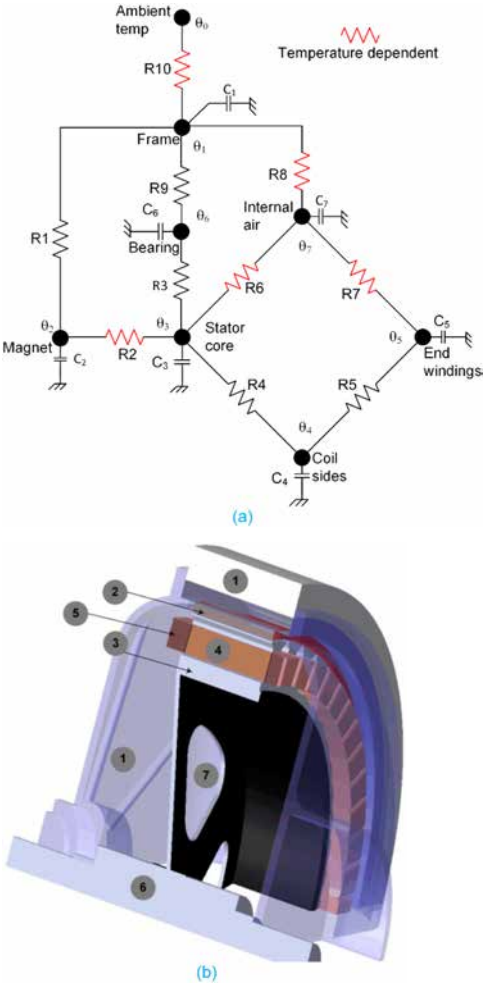

Figure 2. (a) Thermal network of PMBLDC hub motor and (b) position of nodes in motor.

The seven node thermal network of the PMBLDC hub motor is shown in fig. 2a; where θ_0 is the ambient temperature, θ_n is the nodal temperature rise from the ambient temperature, R_n is the thermal resistances between two nodes and C_n is the thermal capacities of the components near node *n*. Additionally, the thermal resistances that are function of temperature is highlighted in red color. The position of each node inside the motor is shown in fig. 2b. The nodes and the thermal resistance of the motor components are selected based on the specific characteristics such as temperature distribution, mechanical complexity and the material properties.

In general, the winding is the hottest part of the machine. A section of winding rests inside the slot (the node 4 in fig.2b) and remaining, known as overhang (the node 5 in fig.2b), is surrounded by the internal air. The heat from the winding is dissipated via slot walls to the stator core and also, via overhang to the internal air. This results in different thermal characteristics for the winding inside the slot and in the overhang; therefore modelled with two nodes. The temperature gradient inside the stator core for small machines are not very significant and hence, modelled with a single node. The motor uses a sintered Neodymium-Iron-Boron (NdFeB) magnets. The performance of the magnet is strongly influenced by the temperature and they could even get demagnetized if exposed to high temperature. Therefore, one node is assigned to the magnet. The rotor core, core housing and end plates are made of solid metals and they have good contact area. In order to simplify the modelling; only one node is assigned to these three components. Thermal and mass flow properties of air changes with the temperature. Therefore, accurate estimation of thermal resistance to the heat transfer via internal air requires its temperature and thus a node is assigned. The bearing temperature is a critical parameter that determines the life of electrical machines and hence a node is assigned to monitor the temperature of the bearing.

Thermal capacity of different components of motor are assigned to nearest nodes and represented in thermal network as capacitor connected to the nodes. Thermal capacity of an element consists of *n* components can be expressed as

$$C = \sum_{i=1}^{n} m_i c_i \tag{6}$$

where m_i and *c* are respectively the mass and the specific heat capacity of component *i*. Thermal resistance of components such as shaft, spider, magnet, rotor core and motor housing can be estimated using the expression for thermal resistance to conductive heat transfer as [8]

$$R = \frac{t}{kA} \tag{7}$$

where *t* is the effective length of heat flow path, *k* is the thermal conductivity of the material and *A* is the cross sectional area of the component. Thermal resistance of stator teeth, thermal resistance between slot and winding and thermal resistance between winding in the slot and in the overhang are calculated based on the approach described in [5]. The thermal resistance of bearing is calculated using the equivalent airgap assumption as described in [10].

Downloaded from SAE International by Muhammed Fasil Palakkunnu Veettil, Wednesday, October 01, 2014

Air Gap Heat Transfer

The air gap heat transfer in radial flux motors represents heat transfer between concentric cylinders. There are a number of literature discussing the stationary outer cylinder and rotating inner cylinder [2,7,11]. However in hub motors, the outer cylinder is rotating while the inner cylinder is stationary. In [12], authors addressed a smooth outer cylinder rotation with a stationary smooth inner cylinder for an air gap to diameter ratio of 0.05 and concluded that Nusselt number (N_u) is nearly one. Therefore, the flow is laminar and heat transfer via air gap is conductive. However, in this study when using Nusselt number equal to one, resulted in higher temperature of components. Authors in [13], studied the effect of slot on flow between concentric cylinders. They concluded that the flow is influenced by a geometrical parameter, hydraulic diameter (D_h) and can be calculated as

$$D_h = Q_s h_o + 2\frac{\pi\left(R_2^2 - R_1^2\right) + Q_s h_o w_o}{\pi(R_1 + R_2)} \tag{8}$$

where Q_s is the number of slot, h_o is depth of slot opening, w_o is the width of slot opening and R_1,R_2 are radius of inner and outer cylinder respectively. Further, Taylor number (T_a) which characterizes flow in annular region can be calculated using hydraulic diameter as [13]

$$Ta = \frac{\omega^2 R_1 \left(\frac{D_h}{2}\right)^3}{\upsilon^2} \tag{9}$$

where ω is the angular speed of rotation and υ is the kinematic viscosity of air. Subsequently, the Nusselt number for air gap region can calculated as [13]

$$6000 < Ta < 1.4 \times 10^6 : Nu = 0.132(Ta)^{0.3}$$

$$4 \times 10^6 < Ta < 2 \times 10^7 : Nu = 0.029(Ta)^{0.4} \tag{10}$$

The Nusselt number calculated for air gap region of hub motor at 350 rpm is found to be 5.75, much larger than the value discussed in [12]. The heat transfer coefficient (h) can be calculated using Nusselt number as

$$h = \frac{Nu\, k}{2(R_2 - R_1)} \tag{11}$$

Therefore, the equivalent thermal resistance of the air gap is

$$R2 = \frac{1}{hA} \tag{12}$$

where A is the inner surface area of the outer cylinder.

End Space Heat Transfer

The end space heat transfer includes heat flow from overhang winding to internal air, from stator core and spider to internal air and internal air to end plate. In [14], authors summarised number of studies and concluded that heat transfer coefficient follows a relation

$$h = k_1 + k_2 V^{k_3} \tag{13}$$

where k_1, k_2, k_3 are curve fit coefficients and V is the peripheral velocity.

Heat Transfer from Wheel to Ambient

When wheel with spokes rotate, it could create turbulence. Therefore, this study models the wheel as a disc in a turbulent flow. In [15], author has discussed the heat transfer from a disc under various flow condition and for this study the lowest value of Nusselt number corresponding to a turbulent flow has been used. The average heat transfer coefficient of wheel is given by

$$h = \frac{Nu\, k_{air}}{r_{wl}} \tag{14}$$

where k_{air} is thermal conductivity of air at ambient temperature and r_{wl} is the wheel radius. Thermal resistance of equivalent disc to ambient can be calculated using the eq.12.

Solving the Thermal Network

The thermal network in fig.2a can be solved to find the steady state temperature rise with respect to ambient as well as the temperature rise versus time. For a thermal network of n nodes, with each of them connected to the other via thermal resistances, the steady state relationship between heat generated at node i and nodal temperature rises can be expressed as [5]

$$P_i = \frac{\theta_i}{R_{i,i}} + \sum_{j=1}^{n} \frac{\theta_i - \theta_j}{R_{i,j}} \tag{15}$$

where P_i is the heat generated in node i, θ_i is the temperature rise at node i, $R_{i,i}$ is the thermal resistance between the node i and the ambient and $R_{i,j}$ is the thermal resistance between the node i and j. The eq.15 can be expanded to include heat generated in all node as

$$\begin{bmatrix} P_1 \\ P_2 \\ \vdots \\ P_n \end{bmatrix} = \begin{bmatrix} \sum_{i=1}^{n} \frac{1}{R_{1,i}} & -\frac{1}{R_{1,2}} & \cdots & -\frac{1}{R_{1,n}} \\ -\frac{1}{R_{2,n}} & \sum_{i=1}^{n} \frac{1}{R_{2,i}} & \cdots & -\frac{1}{R_{2,n}} \\ \vdots & \vdots & \ddots & \vdots \\ -\frac{1}{R_{n,1}} & -\frac{1}{R_{n,2}} & \cdots & \sum_{i=1}^{n} \frac{1}{R_{n,i}} \end{bmatrix} \begin{bmatrix} \theta_1 \\ \theta_2 \\ \vdots \\ \theta_n \end{bmatrix} \tag{16}$$

Downloaded from SAE International by Muhammed Fasil Palakkunnu Veettil, Wednesday, October 01, 2014

The above expression can be represented in vector form as

$$\boldsymbol{P} = \boldsymbol{G\theta} \tag{17}$$

where ***P*** is the loss vector containing the heat generated at each node, ***G*** is the thermal conductance matrix and ***θ*** is the temperature rise vector. Therefore, the steady state temperature rise can be calculated as

$$\boldsymbol{\theta} = \boldsymbol{G^{-1}P} \tag{18}$$

Time dependent or transient analysis of the thermal model helps to estimate the overload capacity of electrical machines. Transient study will help in optimizing the motor design in application such as electric vehicle; where load varies continuously. In transient analysis, system of equation for steady state analysis is modified to include the thermal capacity. When the thermal capacities are added, the eq.17 can modified as

$$\boldsymbol{P} = \boldsymbol{G\theta} + \boldsymbol{C}\frac{\partial \boldsymbol{\theta}}{\partial t} \tag{19}$$

where ***C*** is the thermal capacity matrix, which is defined as

$$\boldsymbol{C} = \begin{bmatrix} C_1 & 0 & \cdots & 0 \\ 0 & C_2 & \cdots & 0 \\ \vdots & \vdots & \ddots & \vdots \\ 0 & 0 & \cdots & C_n \end{bmatrix} \tag{20}$$

where C_n is the thermal capacity of node *n*. The eq.19 can be solved numerically by considering the temperature dependence of thermal resistance, thermal capacities and power losses.

FINITE ELEMENT THERMAL MODEL

In FE method, partial differential equations are solved numerically for the thermal network. The meshed FE model of PMBLDC hub motor is shown in fig.3. The model uses half sectional and geometrical symmetries to reduce the simulation time. Modelling and analysis is done via commercially available software. Losses are modelled by applying resistive and core loss densities to coil and stator core respectively. Internal convections in air gap and end space are modelled via experimentally derived empirical equations with geometrical dimension and thermal properties of cooling media as parameters [16]. Vertical plate and horizontal cylinder analogies are used to model the heat dissipation due to forced convection from motor casing. The bearing is modelled using an equivalent thermal gap as described in [10].

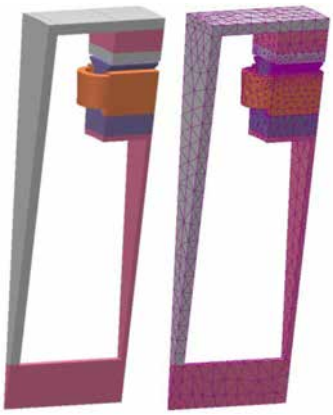

Figure 3. The half sectional model of PMBLDC hub motor using geometrical and its FE mesh.

THERMAL TESTING OF HUB MOTOR

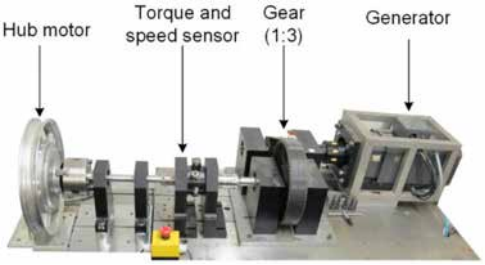

Figure 4. Thermal test set up of hub motor.

The experimental setup for thermal testing of the hub motor is shown in fig.4. Thermo couples are mounted inside the slot, on the winding overhang and on the stator core surface of hub motor to monitor the winding and core temperature. External casing temperature was monitored using a thermal camera. The motor is loaded to different load levels and the temperature rise from the ambient is captured. The temperatures are recorded for every one second and experiment is stopped when the temperature variation of winding over 10 minutes was less than 0.5 °C.

Lumped Parameter Model Validation with Finite Element and Test Data

Test has been conducted for three load step only due to a limitation on the test set up. The comparison of test, LP and FE steady state temperature of winding and core is shown in fig.5. The experimental and the simulated temperatures differ more under light load condition compared to higher load. This could be due to under estimation of constant losses such as core, windage and friction losses. As load increases, the ratio of winding losses to constant losses increases and the LP and

Downloaded from SAE International by Muhammed Fasil Palakkunnu Veettil, Wednesday, October 01, 2014

the FE predicted values are much closer to the test data. Overall the prediction by steady state LP model is within 10 °C of test data.

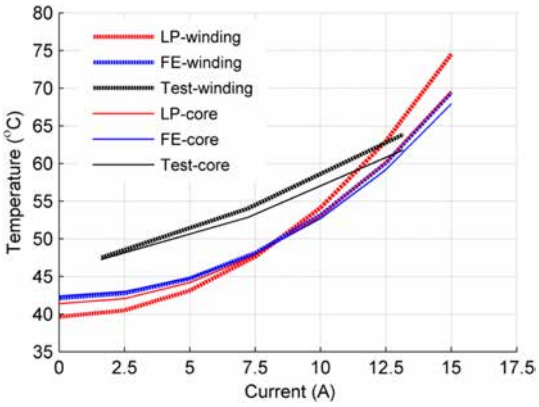

Figure 5. The steady state temperature variation of winding and stator core with load.

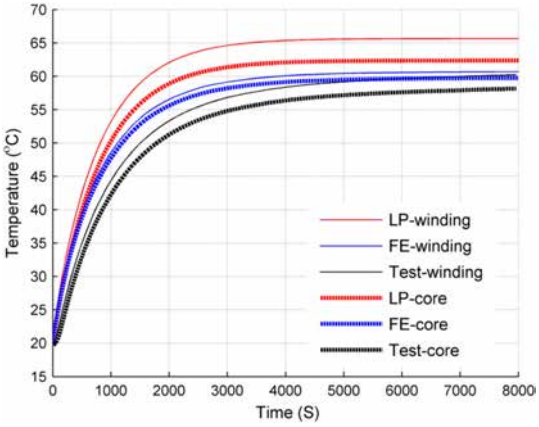

Figure 6. The temperature variation of winding and stator core with time for winding current of 13 A.

Time variation of winding and stator core temperature, when winding carries 13 A is plotted in fig.6. The mass of wheel rim and spoke is not considered in either LP or FE model, resulting in lower thermal capacities for both the models. This is reflected in lower settling time for both LP and FE model results. Under higher load condition LP models shows pessimistic results and therefore, magnets in a PMBLDC motor designed based on the model presented will operate at a lower temperature.

SENSITIVITY ANALYSIS OF LP THERMAL MODEL

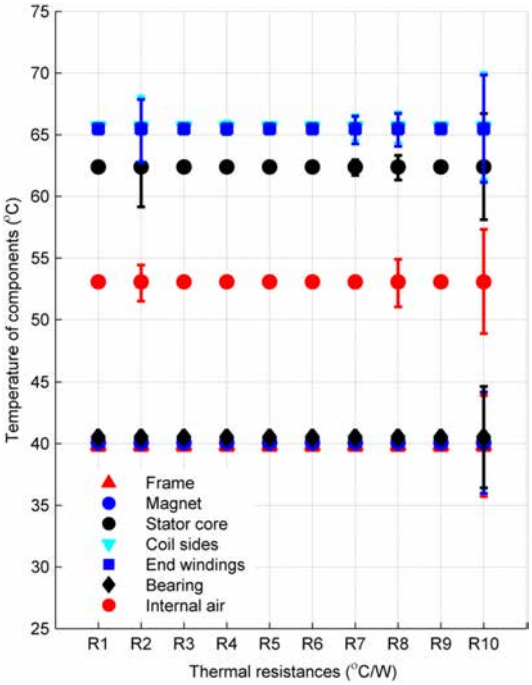

Figure 7. Sensitivity analysis of thermal resistances in a lumped parameter model of PMBLDC hub motor.

A sensitivity analysis has been carried out to evaluate, how an error in estimating the thermal resistance will influence the predicted temperature. The steady state nodal temperature has been evaluated by scaling each thermal resistance by factors 0.8 and 1.2, corresponding to lower and higher error respectively. The sensitivity analysis of LP model is carried out for a winding current of 13 A is shown in fig.7. The results shows that the changes in thermal resistances R2, R7, R8 and R10 have greater effects on temperature of components. Thermal resistances R2, R7 and R8 are related to internal air and any variations of them affects the temperature of the winding and the stator core. The accurate estimation of thermal resistance of motor casing is critical as the temperature of all motor components vary considerably with any error. Therefore, a CFD study has been carried out to model the heat transfer via internal air as well as the heat transfer from the outer casing.

Downloaded from SAE International by Muhammed Fasil Palakkunnu Veettil, Wednesday, October 01, 2014

COMPUTATIONAL FLUID DYNAMIC MODEL OF HUB MOTOR

The CFD analysis of hub motor has been carried out to study

- convective heat transfer via internal air
- heat dissipation from motor casing
- improvement of heat transfer via optimization

External Flow

The external flow simulation is primarily done to determine the local heat transfer coefficient over the exterior surface. This serves as a boundary condition for the internal analysis. Splitting the CFD study into two simulations will significantly lower the computational time when analyzing the internal heat transfer. The motor is placed inside a cavity to model the external flow. The outer boundaries are set to walls so that the system is closed. The walls have a constant temperature corresponds to ambient to remove the heat added. Furthermore, the walls are given a slip condition so that fluid momentum will not be dissipated at the walls. The heat is added to the model by applying a uniform temperature to the internal walls of motor. The rotational reference frame is used to model the rotation and implemented by splitting the fluid into a rotating and a stationary region. The generated mesh for external flow simulation is shown in fig.8. The effect of buoyancy is added by adding a body force to the momentum equations as

$$f = g(\rho - \rho_{ref}) \tag{21}$$

where g is acceleration due to gravity, ρ is the local density and ρ_{ref} is a reference density. The choice of turbulence model can be very important when studying fluid flow with CFD. Since each turbulence model has been verified for different flow cases, the difference between them can be significant. After a comparative study of different turbulence models the K-ε turbulence model has been selected.

Figure 8. The mesh for external flow simulation.

The heat transfer coefficient of the external surfaces of the motor with a rotational speed of 350 rpm and motor internal wall temperature of 50 °C is shown in fig.9. The ambient temperature considered in CFD modelling is 25 °C. The heat transfer coefficient is seen to be in the range of 0 to 200 W/m^2K, where the rim spokes and the outer rim presents the largest values, due to the higher local velocity.

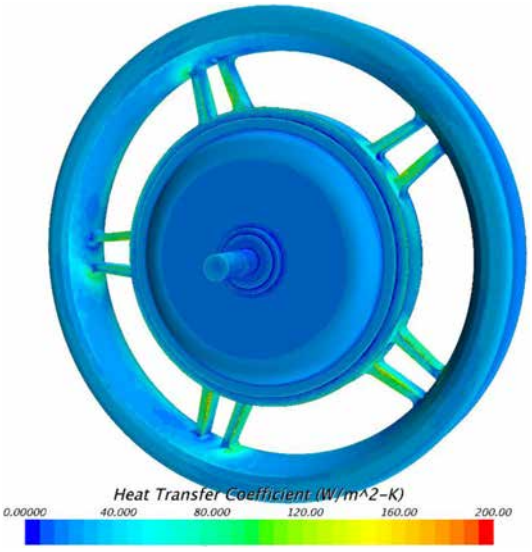

Figure 9. External heat transfer coefficient, with a rotational speed of 350 rpm at 50 °C internal motor wall temperature.

As the internal study is wished to be performed at various rotational speeds, the heat transfer coefficient is calculated for these speeds. The external components of hub motor are named as end plate1 (endplate with brake drum), end plate2 (endplate without brake drum) and rotor (the remaining components including rim and spokes). The rotational speed of the motor is varied from 100 to 1100 rpm in intervals of 150 rpm and the result is shown in fig.10 as the average heat transfer coefficients for the different parts.

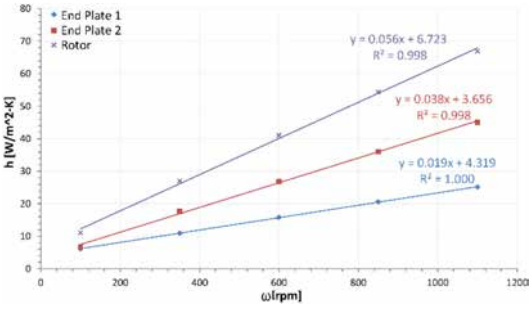

Figure 10. Average heat transfer coefficient for the different motor parts as a function of rotational speed at 50 °C motor internal wall temperature.

Downloaded from SAE International by Muhammed Fasil Palakkunnu Veettil, Wednesday, October 01, 2014

The variation of Nusselt number with rotational Reynolds number is shown in fig.11. The exponent for the end plates and the rotor are between 0.7 and 0.8. This implies that the heat transfer scales roughly equal to a flat plate as the Nusselt number for a turbulent flat plate follows the empirical correlation

$$Nu = 0.023Re^{0.8}Pr^{0.4} \quad (22)$$

where *Re* is Reynolds number *Pr* is Prandtl number.

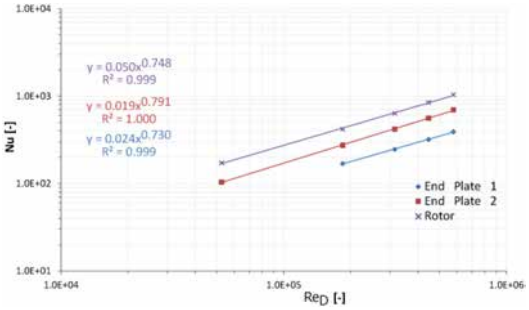

Figure 11. Average Nusselt number for the different motor parts as a function of Reynolds number at 50 °C motor internal wall temperature.

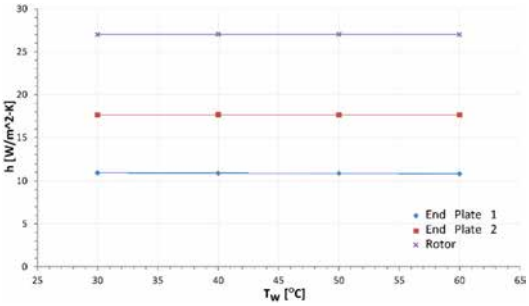

Figure 12. Average heat transfer coefficient for the different parts as a function of motor internal wall temperature. Speed of rotation = 350 rpm.

The influence of the motor internal wall temperature on the heat transfer is studied by varying the motor internal wall temperature in the range of 30 °C to 60 °C and the results are plotted in fig.12. The results of the varied internal wall temperature shows no correlation between the temperature and heat transfer coefficient. As seen in fig.10 the heat transfer coefficient was highly correlated by the rotational speed, which already indicates that the flow is dominated by viscous forces rather than buoyant forces from the density gradient. The varying temperature will also influence the local density, conductivity and viscosity, but these variations is seen to have no influence on the result.

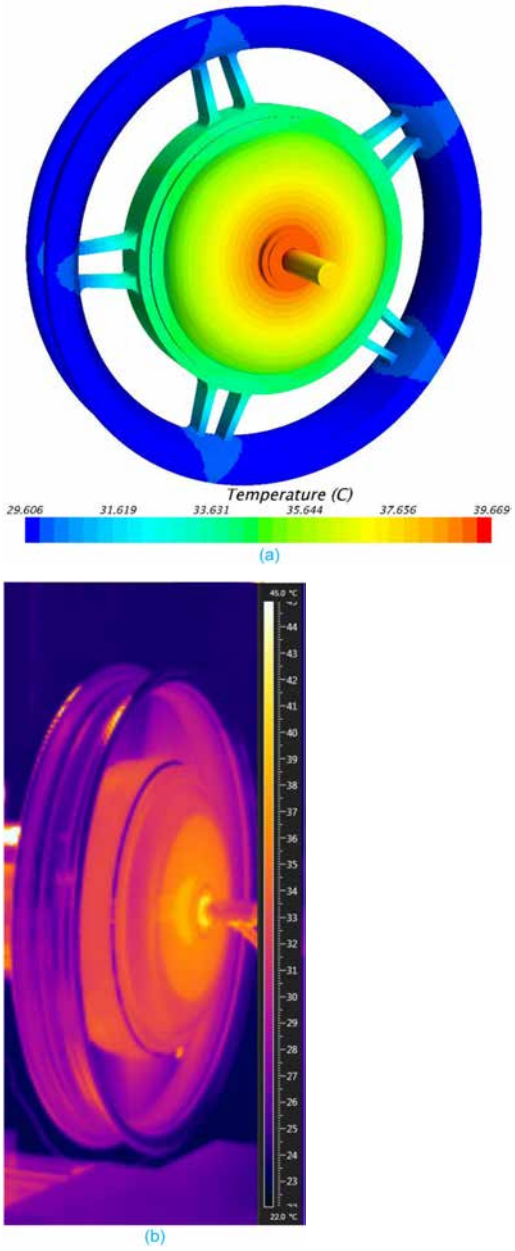

Figure 13. Exterior surface temperature (a) from CFD and (b) thermal image of motor, at 61 W winding loss and a rotational speed of 350 rpm

A comparison of CFD and experimental surface temperature variation of hub motor corresponding to a winding loss of 61 W is shown in fig.13. The temperature distribution is varying radially on the surface. Maximum temperatures occur close to

Downloaded from SAE International by Muhammed Fasil Palakkunnu Veettil, Wednesday, October 01, 2014

the center, mainly in the bearing. The accuracy of a thermal camera is typically within ±2 °C[17]. As many values for the CFD lie within this limit of the experimental, this proves good correlation between CFD and experiments for the external temperatures.

Internal Flow

The external flow model calculates the exterior boundary conditions of hub motor casing and these are applied to the internal flow modelling. A table containing the heat transfer coefficient from the external flow model is imported into the internal model where the values are mapped onto the new internal mesh. Based on the mesh convergence study a final base mesh size of 3.5 mm was selected and mesh size of different sections were specified with respect to base size. The meshed model used for convergence study is shown in fig.10. The model contains one third of the entire motor and the rim has not been considered as the internal flow is periodic by the six holes on the spider and the 51 windings, but the presence of the rim spokes makes the flow non periodic. K-ε turbulence model has been selected for modelling the internal flow also.

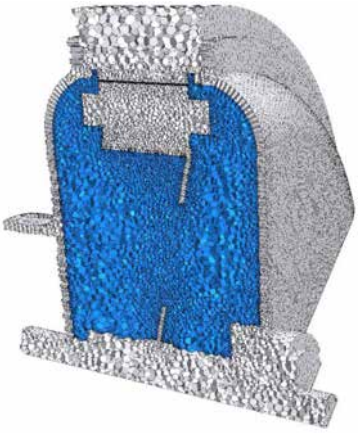

Figure 14. Meshed model for internal flow with polyhedral mesh of 3.5 mm base size.

The geometry created for the analysis is greatly simplified in different areas such as winding and bearing. The copper windings are replaced by a solid bulk as small strands of winding and the air gap between these would be nearly impossible to resolve in a mesh. A thermal resistance has been added in the interfaces to model these components and values are based on previous studies [10].

Internal flow has been simulated for different winding losses and fig. 15 shows the temperature distribution corresponding to a 30 W winding loss at a rotational speed of 350 rpm. The temperature varies in the domain with a minimum temperature of 27.32 °C and maximum of 55.25 °C. The highest temperature is found within the winding, as the heat is generated in this region. The presence of the thermal resistance between winding and stator slot is clearly visible as the discontinuity at the interface. The magnets temperature is 29.7 °C and they are being cooled by the rotating rim, which has the lowest average temperature of 27.8 °C. An overview of heat flow inside the motor is shown in the form of heat transfer network in fig.16. The heat has been transported by two paths. The heat generated in the stationary parts is dissipated by convection or transport it through the solids by conduction. Since the shaft cannot dissipate the amount of heat, it will have to go through the bearing by conduction or to the rotating parts by convection via air. This highlights the limitation of hub motor or external rotor configuration as the motor relies heavily on convection. From winding, 17 W gets dissipated by convection to the air inside the motor and 13 W dissipates by conduction to the stator core. The path of heat conduction continues to the stator core, where 10.1 W dissipates to the air and 2.58 W gets conducted to the spider. The only place stationary and rotating parts are in direct contact is through the bearings, and here the heat transfer is only 2.35 W, approximately 8% of the heat generated. The network show that heat dissipated to the ambient air goes mainly through the rim, with a heat transfer of 21.7 W. The end plates dissipate 3.25 W and 4.41 W for End Plate 1 and 2 respectively, while also conducting some heat to the rotor. The remaining heat of 0.67 W dissipated though the shafts.

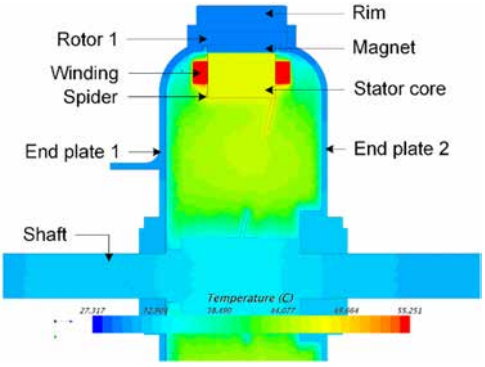

Figure 15. Temperature distribution corresponding to 30 W loss in winding at 350 rpm.

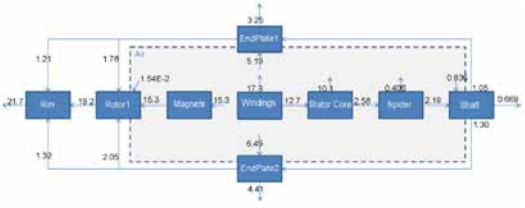

Figure 16. Heat flow corresponding 30 W loss in winding at 350 rpm

Downloaded from SAE International by Muhammed Fasil Palakkunnu Veettil, Wednesday, October 01, 2014

The tangential velocity distribution is shown in fig.17. The rotating walls creates an angular movement of the air inside the motor. The velocities vary from −0.19 to 3.76 m/s, and increases in the radial direction because of the increased wall velocity. The flow in the region close to the windings show that the fluid velocity outside its boundary layer is approximately 1.5 m/s. The local velocity is a critical value for the heat transfer coefficient as it increases shear friction and reduces the boundary layer. The rotational speed influences the convective heat transfer coefficients and the variation of ratio between conduction and convection with the speed is shown in fig.18. The conduction to convection ratio decreases with the increased speed, due to the increased role of convection. For 100 rpm the ratio is 0.95 and 0.85 for 30 W and 100 W respectively and decreases to 0.5 at 1100 rpm. The variation is also influenced by the loss, primarily at lower speeds.

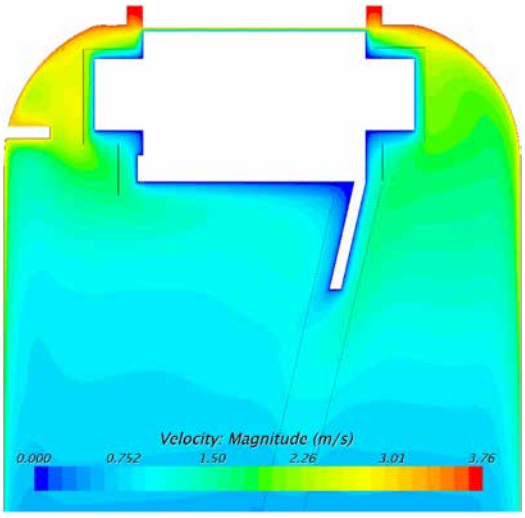

Figure 17. Tangential velocity distribution at 350 rpm.

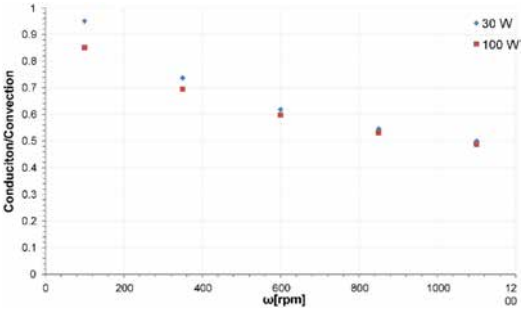

Figure 18. Conduction to convection ratio of the winding with varying rotational speed for different winding loss.

THERMAL OPTIMIZATION

Optimizing the heat transfer will consist of primarily optimizing the internal flow, which can be done in many ways, such as placing fins, adding a fan, reshape the geometry etc. As discussed in earlier sections, the convection is the dominating heat transfer mechanism in hub motors. Therefore, the focus should be on increasing the convective heat transfer coefficient of the windings and it can be done by increasing the local velocity or generate more turbulence, which increases the mixing. Several different shapes have been modelled to assess whether these have a potential of improving the heat transfer. To determine the thermal performance of these new designs a performance scalar is defined. This is defined as

$$\eta = \frac{T_{baseline} - T_{new}}{T_{baseline} - T_{ambient}} \quad (23)$$

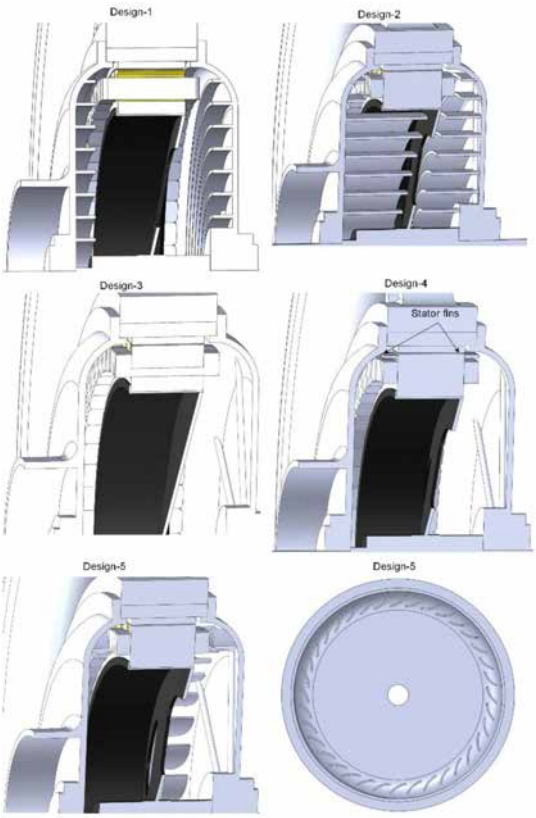

Figure 19. Proposed designs for heat improvement.

According to the first law of thermodynamics the lowest possible temperature in the motor would be the ambient temperature. This means that the performance scalar is independent of the load, where a reduction percentage would be dependent on the load and unit of temperature. The

Downloaded from SAE International by Muhammed Fasil Palakkunnu Veettil, Wednesday, October 01, 2014

proposed designs are shown in fig.19 and their thermal performance is shown in the bubble diagram in fig.20. The area of the bubbles represent their thermal performance, where a larger area means better performance. All design have same winding loss of 100 W at a rotational speed of 350 rpm. The baseline is also shown as the grey bubble, where the area is for visualization only as its performance is 0 by definition.

The first design consists of 15 concentric fins of depth 9 mm placed on the both end plates. The depth of the fins is increased to get much closer to the stator parts in design 2. The design 3 fills out the holes in the spider to improve conduction and increase surface area for convection. The design 4 adds fins to the stator core to increase the surface area. The final design proposed is adding curved fins to the end plates. This is done to increase mixing of the flow to enhance the heat transfer in the winding. Determining which design performs the best, is a choice between added mass or increased friction. Design 2 and 5 had a similar high thermal performance, but one did this by increasing mass and other increasing friction. The added friction is very small compare to other mechanical losses, such as bearing friction. The other proposals do not significantly improve heat transfer. The decreased temperature found for these are so minor that they are most likely within the uncertainties of the model. The design 5 has been selected to for optimization study as it has least mass penalty.

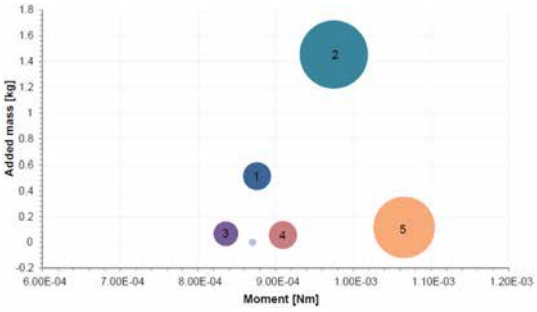

Figure 20. Bubble diagram of the performance of proposed designs, and their added mass and friction moment. The area of the bubbles relate to the thermal performance.

The four variables of the fin profile in design 5 are span (*a*), angle (*b*), thickness (*t*) and radius (*r*) from the center to the start of the fin and they are shown in fig.21. The distance to the winding (*d*) and the number of fins (*N*) are, the additional design parameters used for optimization study. The limits of each design parameters are shown in table 1. Increasing or decreasing some parameters past these limits could make the CAD generation fail, so conservative limits has been used to limit the amount of ill geometries created. Due to limitations of the CAD system in CFD program used in this study, fins are only added to one of the end plates. The resolution of each variable leads to a total of 6,782,490 combinations.

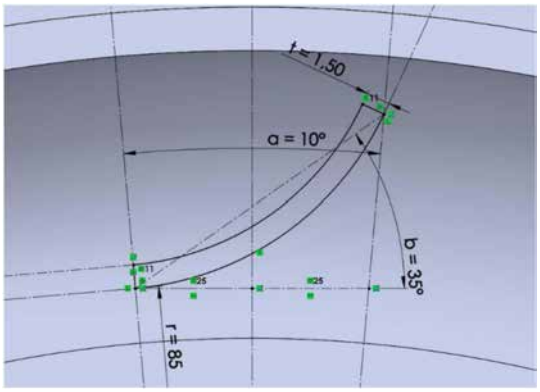

Figure 21. A sketch of the fin profile showing optimization variables

Optimizing the flow with the fins comes with a cost of increased air friction and mass. These three parameters will compete against each other as they are coupled; e.g. by having many fins will decrease temperatures, but increases both mass and friction. Therefore the optimization will be performed as a Pareto optimization. A Pareto optimization is a method where two or more objectives are optimized, and are competing against each other. Here the temperature is wished to be minimized, while the friction and mass are also wished to be decreased. The Pareto optimization will return a so called Pareto front, which consists of optimum solutions for each objective. The front can then be used to pick a design based on the weight of each objective. The results of optimization is shown in fig.22, with winding temperature and friction moment plotted for each design iteration. Optimum solutions are plotted as blue diamonds and non-optimum as red squares. The baseline model showed as green triangle. The mass optimization is not considered currently because having three objective will require significantly more runs and computational time. A solution is Pareto optimum if there is no solution which for e.g. the same moment can deliver lower temperature, and the other way around. The results shows that the cost of lowering the temperature rises rapidly past 119.5 °C.

Table 1. Design values and the optimization constraints

	Minimum	Maximum	Increment	Resolution
a	5°	10°	1°	6
b	10°	40°	1°	31
t	1 mm	3	0.5 mm	5
r	82 mm	90	0.5 mm	17
d	2 mm	8	0.5 mm	13
N	4	36	1	33

Downloaded from SAE International by Muhammed Fasil Palakkunnu Veettil, Wednesday, October 01, 2014

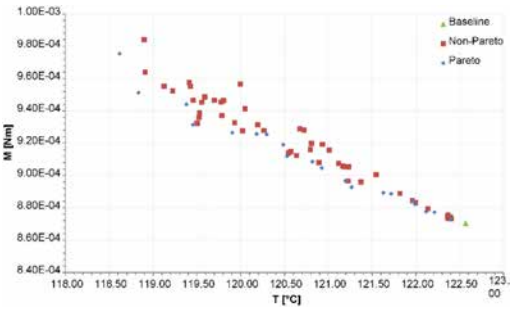

Figure 22. Results of the Pareto optimization study, with winding temperature and friction moment plotted for each design iteration.

CONCLUSION

The external rotor PMBLDC motor offers a unique solution for electric vehicles, in terms of space and weight requirement of the powertrain. This study investigates the heat dissipation in hub motors with the help of different methods, starting from using a lumped parameter model which can be incorporated in to a motor design program. Subsequently the finite element model has been presented; which offers more accuracy when complex geometries are involved. The steady state and transient results of the LP model has been compared to the FE results and the experimental data. The results are found to be within 10 °C. A sensitivity analysis of lumped parameter model revealed that any error in estimating the resistance associated with internal air or casing influences the results considerably. As the mechanism of heat transfer via internal air and from motor casing is convection; accurate study of it requires a computational fluid dynamic model.

The CFD model uses steady state approach using the K-ε turbulence model and the rotation is modelled using the rotating reference frame method. Before the modelling of internal heat transfer, boundary condition was determined for the external surfaces in contact with the ambient air. This was done by performing an external flow study to determine the heat transfer coefficients. The heat transfer coefficients showed to be only dependent on the rotational rate of the motor, meaning that buoyant forces was not important for the heat transfer. Subsequently, the internal flow analysis has been carried to out and identified the heat flow path from the windings. The tangential velocity distributions inside the motor has been discussed. It is found that the conduction to convection ratio decreases with the increased speed, due to the increased role of convection. Also, the ratio is influenced by the loss, especially at lower speeds.

Lastly an optimization study of the internal heat transfer was made to decrease temperatures. Five different designs were tested in the CFD model, where one showed the greatest potential without increasing considerable mass. This design was then picked up for further optimization by a multi objective Pareto optimization and the results shown that the cost of lowering the temperature rises rapidly past 119.5 °C.

REFERENCES

1. Anderson, M. and Harty, D., “Unsprung mass with in-wheel motors-myths and realities,” *10th International Symposium on Advanced Vehicle Control,(AVEC'10)*, 261-266, 2010.
2. Gazley, C., “Heat transfer characteristics of the rotational and axial flow between concentric cylinders,” *J. Heat Transfer*, 1958.
3. Camilleri, R., Howey, D.A., and McCulloch, M.D., “Thermal limitations in air-cooled axial flux in-wheel motors for urban mobility vehicles: A preliminary analysis,” *2012 Electrical Systems for Aircraft, Railway and Ship Propulsion*, IEEE, ISBN 978-1-4673-1372-8: 1-8, 2012, doi:10.1109/ESARS.2012.6387494.
4. Gieras, J.F., Wang, R.-J., and Kamper, M.J., “Axial flux permanent magnet brushless machines,” Springer, ISBN 1402082274, 2008, doi:10.1007/1-4020-2720-6.
5. Kylander, G., “Thermal modelling of small cage induction motors,” Chalmers University of Technology, 1995.
6. Lindstr, J., “Development of an Experimental Permanent-Magnet Motor Drive,” Chalmers University of Technology, ISBN 9171978038, 1999.
7. Wrobel, R., Mellor, P.H., McNeill, N., and Staton, D.A., Thermal Performance of an Open-Slot Modular-Wound Machine With External Rotor, *IEEE Trans. ENERGY Convers*. 25(2):403-411,2010, doi:10.1109/TEC.2010.2047041.
8. Hendershot, J. and Miller, T., “Design of brushless permanent-magnet machines,” 2010.
9. Deng Fang, “An improved iron loss estimation for permanent magnet brushless machines,” *IEEE Trans. Energy Convers*. 14(4):1391-1395, 1999, doi:10.1109/60.815078.
10. Staton, Dave, Boglietti Aldo, and Cavagnino Andrea. “Solving the more difficult aspects of electric motor thermal analysis.” In Electric Machines and Drives Conference, 2003. IEMDC'03. IEEE International, Vol. 2, pp. 747-755. IEEE, 2003. doi:10.1109/IEMDC.2003.1210320.
11. Howey, D.A., Childs, P.R.N., and Holmes, A.S., “Air-Gap Convection in Rotating Electrical Machines,” *IEEE Trans. Ind. Electron.* 59(3):1367-1375, 2012, doi:10.1109/TIE.2010.2100337.
12. Bjorklund, I. and Kays, W., “Heat transfer between concentric rotating cylinders,” *J. Heat Transfer* 81(D): 175-186, 1959.
13. Fénot, M., Bertin, Y., Dorignac, E., and Lalizel, G., “A review of heat transfer between concentric rotating cylinders with or without axial flow,” *Int. J. Therm. Sci.* 50(7):1138-1155, 2011, doi:10.1016/j.ijthermalsci.2011.02.013.
14. Staton, D. A., and Cavagnino Andrea. “Convection heat transfer and flow calculations suitable for analytical modelling of electric machines.” In IEEE Industrial Electronics, IECON 2006-32nd Annual Conference on, pp. 4841-4846. IEEE, 2006. doi:10.1109/IECON.2006.348143.
15. Wiesche, S. aus der, “Heat transfer from a rotating disk in a parallel air crossflow,” *Int. J. Therm. Sci.*, 2007.
16. ThermNet Help. Thermal analysis simulation software, Infolytica corportation.

ACKNOWLEDGMENTS

This research was supported by EU-FP7 NANOPYME Project (No. 310516)

All rights reserved. No part of this publication may be reproduced, stored in a retrieval system, or transmitted, in any form or by any means, electronic, mechanical, photocopying, recording, or otherwise, without the prior written permission of SAE International.

Positions and opinions advanced in this paper are those of the author(s) and not necessarily those of SAE International. The author is solely responsible for the content of the paper.

Performance Variation of Ferrite Magnet PMBLDC Motor With Temperature

Muhammed Fasil[1], Nenad Mijatovic[1], Bogi Bech Jensen[2], and Joachim Holboll[1]

[1]Department of Electrical Engineering, Technical University of Denmark, Kgs. Lyngby 2800, Denmark
[2]Department of Science and Technology, University of the Faroe Islands, Tórshavn FO-100, Faroe Islands

The price fluctuations of rare-earth (RE) metals and the uncertainty in their availability have generated an increased interest in ferrite magnet machines. The influence of temperature on the *B–H* characteristics of the ferrite magnet differs considerably from that of the RE magnet, and hence, requires a different approach when deciding their operating point. In this paper, the laboratory measured *B–H* curves of a ferrite magnet are used for estimating the possibility of demagnetization in a segmented axial torus (SAT) permanent magnet brushless dc (PMBLDC) motor. The *B–H* characteristics for different temperatures have been used to study the performance variation of the ferrite magnet SAT PMBLDC motor with temperature. A detailed analysis is carried out to ensure that the designed ferrite magnet motor is capable of delivering the specified torque throughout the operating speed, without any irreversible demagnetization of magnets. It has been shown that the ferrite magnet PMBLDC motor operation is influenced by the magnet temperature, and the maximum motor speed for a given load torque decreases as the magnet temperature drops.

***Index Terms*— Brushless machines, demagnetization, ferrites, permanent magnet (PM) machines, PMs.**

I. Introduction

IN RECENT years, there has been an uncertainty in the availability and the price of rare-earth (RE) metals used in high energy magnets [1]. This sets stage for renewed interest in the research of ferrite magnet machines [2]–[6] as ferrites are commonly available. The main challenges in substituting the RE magnet with the ferrite are its low remanence (B_r) and coercivity (H_c). Low B_r implies a lower magnetic loading and low H_c imparts restriction on the maximum electric loading to prevent demagnetization of the magnet, thus limiting the power density of the ferrite magnet machines. Most of the solutions proposed to address this limitation involve placing more magnets in rotor to enhance the air-gap flux density [7], [8].

Different aspects of magnet in operation, such as reversible and irreversible demagnetization as a result of armature reaction and temperature-induced operating point shift on the performance of permanent magnet (PM) machine, have been researched extensively for RE magnets [9]–[12]. In most of these situations, ferrite magnets behave different from RE magnets, because the coercivity of ferrite magnets increases with temperature; in other words, ferrite magnets have a positive temperature coefficient, and RE magnets have a negative temperature coefficient for coercivity. The remanence of both magnets decreases with temperature. Moreover, the knee point in the demagnetization characteristics appears at low temperature for ferrite magnets and at higher temperature for RE magnets. In applications such as direct drive hub motors, heat from magnets are dissipated rapidly to the surrounding because of their positioning in outer casing, and therefore, the possibility of high-temperature demagnetization when using RE magnets is less. In contrast, for ferrite magnets used in a similar motor configuration, the inrush current at start can be seen as a critical aspect from the magnet perspective, especially at low ambient temperatures, where the risk of demagnetisation is the highest.

Though the design of ferrite magnet machines is discussed extensively in [2]–[6], [8], [13], and [14], the performance variation of ferrite magnet PM brushless dc (PMBLDC) motors with temperature has not been examined in detail. Also, there is a lack of systematic approach presented for identifying the leeway for armature reaction with respect to irreversible demagnetization. The work presented in [15] discusses the effect of temperature on torque profile of a ferrite PMBLDC motor with the help of a finite-element (FE) electromagnetic and thermal model. Dorrell *et al.* [8] described a possible demagnetization due to a load line intersecting beyond the knee point of a ferrite magnet at low temperature. Petrov *et al.* [16] used the flux density distribution in magnets to estimate the level of demagnetization in a PM synchronous generator, and also calculated the performance variation with temperature. Sone *et al.* [6] used the *B–H* curve of a ferrite magnet corresponding to the lowest operating temperature to ensure that the field weakening operation is not causing any irreversible demagnetization in a PM synchronous motor. However, the authors did not evaluate the performance variation with temperature. Debruyne *et al.* [17] used the manufacturer supplied temperature coefficient of B_r and H_c of a ferrite magnet to evaluate the performance of a line-start PM machine for different operating temperatures.

This paper uses the laboratory measured *B–H* characteristics of a ferrite magnet to evaluate the margin of safety to irreversible demagnetization in a segmented axial torus (SAT) PMBLDC motor. In addition, the *B–H* characteristics of the ferrite magnet for different temperatures have been used to study the performance variation of the SAT PMBLDC motor with temperature.

Manuscript received February 26, 2015; revised May 22, 2015 and July 9, 2015; accepted July 12, 2015. Date of publication July 15, 2015; date of current version November 16, 2015. Corresponding author: M. Fasil (e-mail: mohammedfazil@gmail.com).

Color versions of one or more of the figures in this paper are available online at http://ieeexplore.ieee.org.

Digital Object Identifier 10.1109/TMAG.2015.2456854

0018-9464 © 2015 IEEE. Personal use is permitted, but republication/redistribution requires IEEE permission.
See http://www.ieee.org/publications_standards/publications/rights/index.html for more information.

TABLE I
PROPERTIES OF FERRITE MAGNET (GRADE:Y33BH) AS PER PRODUCT DATA SHEET

			Reversible coefficient	temperature
BH_{max} (kJ m^{-3})	B_r (T)	H_c (kA m^{-1})	$\%B_r$ (% °C^{-1})	$\%H_c$ (% °C^{-1})
33.25 ± 1.75	0.42 ± 0.1	247.5 ± 12.5	-0.2	$+0.3$

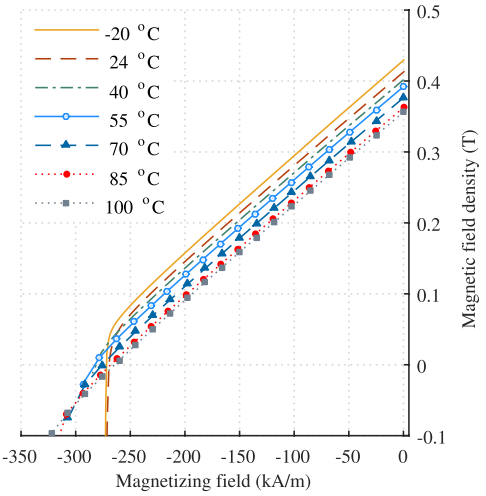

Fig. 1. Measured demagnetization characteristics of the ferrite magnet for different temperatures.

II. MEASURED B–H CHARACTERISTICS OF FERRITE MAGNET

This study has been carried out using a commercially available ferrite magnet, and the specification from the product data sheet is shown in Table I. The B–H characteristics of the ferrite magnet have been measured for temperatures starting from −20 °C to 100 °C. The second quadrant of the characteristics is shown in Fig. 1, and each data point is the average value of measurements on five samples. Each curve in Fig. 1, corresponding to a temperature, is traced from 300 to 500 data points. The only unexpected behavior observed is corresponding to the room temperature (24 °C) measurements, and the curve is found to have knee point earlier than that of −20 °C measurements. The second-quadrant knee point exists for all temperatures below 70 °C.

With regard to the PM machine design, the critical value of demagnetizing field that the magnet can be exposed to without any permanent loss in remanence can be found from the variation of differential permeability. Differential permeability is defined as the slop (dB/dH) of the B–H curve [18]. Differential permeability of the ferrite magnet material is plotted against the magnetizing field for different temperatures in Fig. 2. It is clear from the figure that the dB/dH remains constant until 250 kA m^{-1}, and its values at lower temperatures are changing initially. Therefore, it can be concluded that the ferrite magnet used in this paper can safely withstand a demagnetizing field or an armature reaction field up to 250 kA m^{-1}.

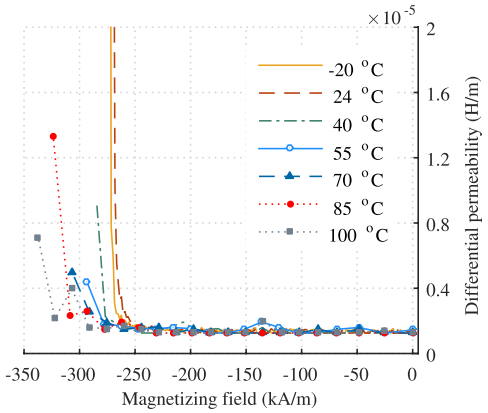

Fig. 2. Differential permeability variation with magnetizing field of the ferrite magnet.

Fig. 3. Schematic of the ferrite magnet SAT PMBLDC motor. 1: end cover. 2: rotor yoke. 3: magnets. 4: stator winding. 5: stator core. 6: wheel rim.

III. SEGMENTED AXIAL TORUS PERMANENT MAGNET BRUSHLESS DC MOTOR

A SAT PMBLDC motor with a ferrite magnet as rotor poles is designed to study the extent of demagnetization under severe armature reaction. The schematic of the SAT PMBLDC motor is shown in Fig. 3. The SAT motor topology [19]–[21] is a variation of torus slotted north–south axial flux motor (AFM) topology, and has no stator yoke. The magnetically separated teeth can be wound separately before assembly, and this ensures high fill factor and short end turn resulting in an efficiency improvement [22]. This add to improved a torque density that comes with the AFM topology [21]. A pole/slot combination of $P = Ns \pm 2$ has been selected to reduce the cogging torque [23]. In addition, a single-layer winding is opted as they are more suitable for the BLDC motor operation [23]. The specification and main geometrical

TABLE II
SPECIFICATION AND GEOMETRICAL DIMENSIONS OF THE FERRITE MAGNET SAT PMBLDC MOTOR

Parameter	Value
The rated voltage	48 V
The rated power output	700 W
The rated torque	20 N m
Outer diameter of the motor	275 mm
Diameter ratio	0.45
Axial length of the motor	65.5 mm
Number of poles	16
Number of slots	18
Gross slot fill factor	0.5
Thickness of magnet poles	7.5 mm
Length of air gap	0.4 mm
Number of turns per coil	30
Diameter of a coil turn	2.68 mm

dimensions of the motor are listed in Table II. The motor will be used in an electric two-wheeler with the maximum speed of 32 km h^{-1}. In order to attain the maximum speed of vehicle, the motor should produce a torque of 12 N m at 330 r/min.

IV. ESTIMATION OF DEMAGNETIZATION LEVEL OF FERRITE MAGNET IN OPERATING CONDITION

As explained in Section II, the ferrite magnet is more susceptible to demagnetization at lower temperatures, and for this reason, the B–H curve of the ferrite magnet at −20 °C is used for demagnetization study. The 3-D FE static analysis is carried out for two values of peak armature currents 20 and 200 A, corresponding to the full load and ten times the full load, respectively. Ruoho and Arkkio [10] proved that both antiparallel and perpendicular field components to the direction of magnetization are necessary to accurately estimate the level of demagnetization. Therefore, $|H|$ and not $|B|$ field distribution is used in this paper. Furthermore, Kim *et al.* [24] and Higashi *et al.* [25] concluded that the edges and the area of PM exposed to air gap are more susceptible to demagnetization than the inner volume. The demagnetizing field acting on the entire magnet disk is shown in Figs. 4(a) and 5(a), and the field on a single pole is shown in Figs. 4(b) and 5(b). At ten times the rated current, 48 % of magnet volume is experiencing a demagnetizing field value more than 250 kA m^{-1}, and hence nearly half of the magnet disk will be demagnetized. It is clear from the figures that at rated current levels only a small volume of magnet located in the interpolar region will experience $|H|$ field approaching a critical value of 250 kA m^{-1} for the presented design.

V. PERFORMANCE VARIATION OF PMBLDC MOTOR WITH TEMPERATURE

Besides the shift in knee point, the remanence also varies with temperature for the ferrite magnet, as shown in Fig. 1. The B_r value diminishes by more than 10% when temperature rises

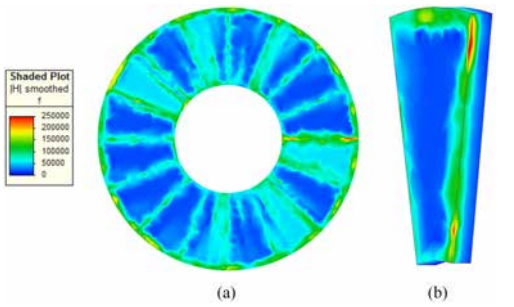

Fig. 4. Demagnetizing field distribution for an armature current of 20 A in (a) 16-pole disk and (b) pole.

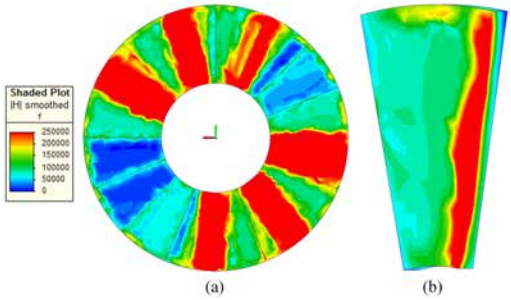

Fig. 5. Demagnetizing field distribution for an armature current of 200 A in (a) 16-pole disk and (b) pole.

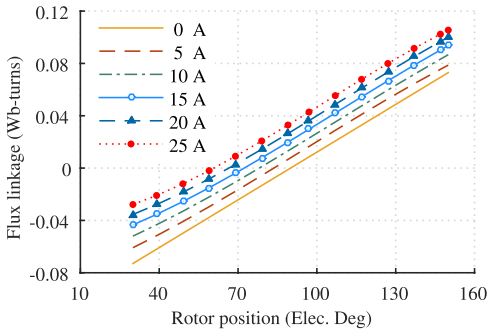

Fig. 6. Variation of flux linkage of a phase with rotor position for different armature currents at a magnet temperature of −20 °C.

from −20 °C (the lowest ambient temperature considered) to a steady-state magnet temperature under load (assumed to be between 55 °C and 70 °C), and this variation will have an impact on the motor performance. A series of static FE analysis is carried out to find the flux linkage of a phase as a function of the rotor position and the armature current, and the results are shown in Fig. 6 for a magnet temperature of −20 °C. As the rotor rotates, flux linkage variations will induce an electromotive force (EMF) in the winding, and the instantaneous EMF induced per phase (e_{ph}) can be

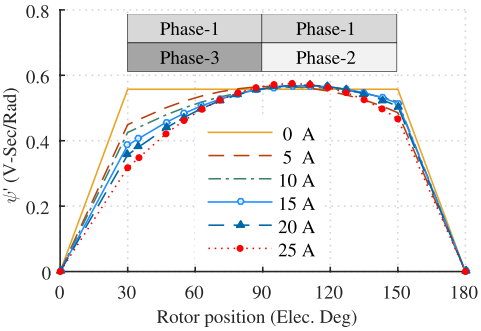

Fig. 7. Variation of ψ' with the rotor position for different armature currents at a magnet temperature of −20 °C.

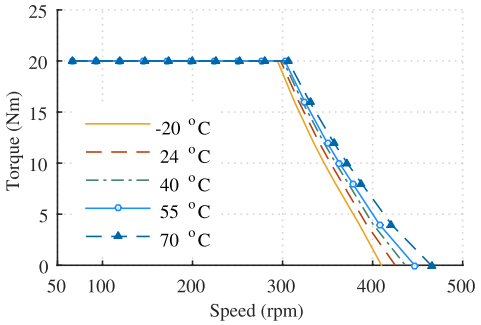

Fig. 9. Torque delivered at shaft versus speed curves of the ferrite magnet PMBLDC motor for different magnet temperatures.

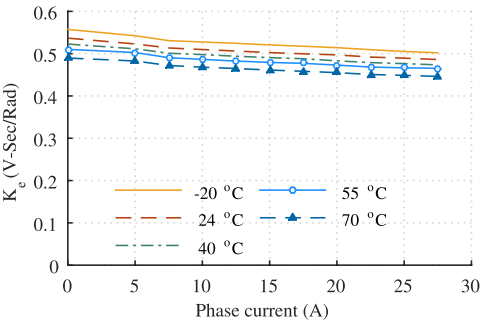

Fig. 8. Variation of the average EMF constant with the armature current for different magnet temperatures.

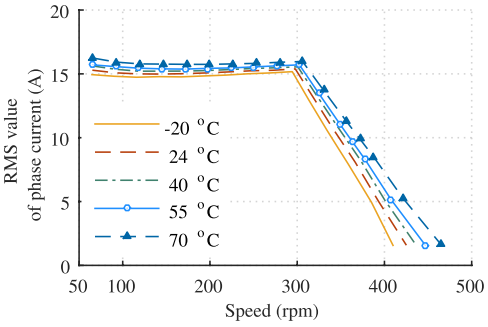

Fig. 10. RMS value of the phase current versus the speed curves of the ferrite magnet PMBLDC motor for different magnet temperatures.

calculated as

$$e_{\text{ph}} = \frac{d\psi}{dt} = \frac{d\psi}{d\theta} \times \frac{d\theta}{dt} = \psi' \times \omega \tag{1}$$

where ψ is the flux linkage per phase, θ is the rotor position, and ω is the angular velocity. The variation of ψ' with a rotor position for different armature currents is shown in Fig. 7. In three-phase PMBLDC motor, only two phases conduct at the same time. Therefore, Phase-1 and Phase-3 conduct for 30 to 90 elec. deg and Phase-1 and Phase-2 conducts for 90 to 150 elec. deg, as shown in Fig. 7. The average EMF generated per phase of a PMBLDC motor (E_{ph}) can be expressed as

$$E_{\text{ph}} = K_e \times \omega \tag{2}$$

where K_e is the EMF constant of a PMBLDC motor. The EMF constant can be derived from the flux linkage variation by comparing (1) and (2) as

$$K_e = \text{mean}(\psi'). \tag{3}$$

The variation of EMF constant with the armature current for different temperatures, plotted in Fig. 8, shows the effect temperature on K_e.

A dynamic model of the three-phase PMBLDC motor is developed based on models presented in [26]–[29]. The model uses a 3-D lookup table of EMF constants as a function of the rotor position and the armature current to calculate the rotational EMF at a magnet temperature. The phase inductances obtained from the FE model of the motor are included in the model, to account for the effect of transformer EMF. The model neglects the temperature variation of winding resistance as the maximum possible change in winding loss for the temperature range considered here is <10 W. The core loss value of 35 W in the rotor yoke and the stator teeth is calculated by applying Steinmetz equation to the flux density distribution obtained from the FE model of the SAT PMBLDC motor.

The torque versus speed characteristics of the designed motor obtained from the simulation of a dynamic model are shown in Fig. 9. It is found that the motor operation beyond the base speed varies considerably with the magnet temperature and the maximum motor speed for a given load torque decreases with colder magnets. Still, the presented design will meet the torque requirement for accelerating the vehicle to the maximum speed throughout the range of temperature considered in this paper. The rms value of the phase current of the machine plotted against the speed of the motor is shown in Fig. 10. The weakened magnet field due to drop in remanence at higher temperature implies a reduced back EMF, which results in higher current throughout

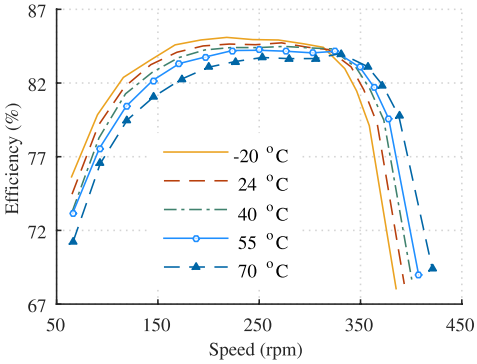

Fig. 11. Efficiency versus speed curves of the ferrite magnet PMBLDC motor for different magnet temperatures.

the speed range considered. The increased current at higher temperature gives rise to higher copper losses and reduced efficiency, as shown in Fig. 11. This trend reverses beyond the base speed as the torque increases with temperature for a given speed. This results in higher output power and, hence, an improved efficiency in spite of drawing more current.

The impact of temperature dependence of the ferrite magnet motor on system performance requires the accurate modeling of power converters and controllers. The motor discussed is designed for a low cost powertrain of electric two-wheelers, and in such applications, closed-loop controls are not usually implemented due to cost constraints. Nevertheless, the presented study with the consideration of the motor alone can give controller designers a better outlook into the performance variation with temperature beyond the base speed, which will be helpful in designing a control strategy for mitigating perceived speed changes to the user.

VI. Conclusion

The interest in the ferrite magnet machines appears to be increasing. As discussed in this paper, the ferrite magnet machines are more susceptible to irreversible demagnetization due to armature reaction at lower temperature. Moreover, the ferrite magnet motor performance, especially beyond the constant torque operation varies considerably with a magnet temperature. As the temperature of the ferrite magnets drops, remanent flux density increases, and knee point moves more toward the operating region of magnets in machines. From the motor design perspective, as demonstrated in this paper, designer has to ensure that the designed ferrite magnet motor is capable of delivering the specified torque throughout the operating speed, without any irreversible demagnetization of magnets.

The temperature-dependant characteristics of ferrites have to be considered when designing ferrite magnet machines for applications, such as an electric powertrain, where they are exposed to ambient temperature changes and field weakening operation spans across large operating speeds. This paper is carried out on the PMBLDC motor, and can be extended to other type of ferrite magnet machines also.

Acknowledgment

This work was supported by EU-FP7 NANOPYME Project (No. 310516) [30]. The authors would like to thank the Instituto de Magnetismo Aplicado, Spain, for measuring the B-H characteristics of magnets.

References

[1] P. C. Dent and M. H. Walmer, "Supply chain sustainability—Rare earth materials," in *Proc. IEEE Int. Vac. Electron. Conf. (IVEC)*, May 2010, pp. 57–58.

[2] M. M. Rahman, K.-T. Kim, and J. Hur, "Design and optimization of neodymium-free SPOKE-type motor with segmented wing-shaped PM," *IEEE Trans. Magn.*, vol. 50, no. 2, Feb. 2014, Art. ID 7021404.

[3] M. R. Mohammad, K.-T. Kim, and J. Hur, "Design and analysis of a spoke type motor with segmented pushing permanent magnet for concentrating air-gap flux density," *IEEE Trans. Magn.*, vol. 49, no. 5, pp. 2397–2400, May 2013.

[4] H.-W. Kim, K.-T. Kim, Y.-S. Jo, and J. Hur, "Optimization methods of torque density for developing the neodymium free SPOKE-type BLDC motor," *IEEE Trans. Magn.*, vol. 49, no. 5, pp. 2173–2176, May 2013.

[5] P. Sekerak, V. Hrabovcova, J. Pyrhonen, L. Kalamen, P. Rafajdus, and M. Onufer, "Comparison of synchronous motors with different permanent magnet and winding types," *IEEE Trans. Magn.*, vol. 49, no. 3, pp. 1256–1263, Mar. 2013.

[6] K. Sone, M. Takemoto, S. Ogasawara, K. Takezaki, and H. Akiyama, "A ferrite PM in-wheel motor without rare earth materials for electric city commuters," *IEEE Trans. Magn.*, vol. 48, no. 11, pp. 2961–2964, Nov. 2012.

[7] K. Atallah and J. Wang, "A rotor with axially and circumferentially magnetized permanent magnets," *IEEE Trans. Magn.*, vol. 48, no. 11, pp. 3230–3233, Nov. 2012.

[8] D. G. Dorrell, M.-F. Hsieh, and A. M. Knight, "Alternative rotor designs for high performance brushless permanent magnet machines for hybrid electric vehicles," *IEEE Trans. Magn.*, vol. 48, no. 2, pp. 835–838, Feb. 2012.

[9] T. Sebastian, "Temperature effects on torque production and efficiency of PM motors using NdFeB magnets," *IEEE Trans. Ind. Appl.*, vol. 31, no. 2, pp. 353–357, Mar./Apr. 1995.

[10] S. Ruoho and A. Arkkio, "Partial demagnetization of permanent magnets in electrical machines caused by an inclined field," *IEEE Trans. Magn.*, vol. 44, no. 7, pp. 1773–1778, Jul. 2008.

[11] S. Ruoho, J. Kolehmainen, J. Ikaheimo, and A. Arkkio, "Interdependence of demagnetization, loading, and temperature rise in a permanent-magnet synchronous motor," *IEEE Trans. Magn.*, vol. 46, no. 3, pp. 949–953, Mar. 2010.

[12] C. Kral, R. Sprangers, J. Waarma, A. Haumer, O. Winter, and E. Lomonova, "Modeling demagnetization effects in permanent magnet synchronous machines," in *Proc. 19th Int. Conf. Elect. Mach. (ICEM)*, Sep. 2010, pp. 1–6.

[13] H.-S. Kim, Y.-M. You, and B.-I. Kwon, "Rotor shape optimization of interior permanent magnet BLDC motor according to magnetization direction," *IEEE Trans. Magn.*, vol. 49, no. 5, pp. 2193–2196, May 2013.

[14] S.-M. Jang, H.-J. Seo, Y.-S. Park, H.-I. Park, and J.-Y. Choi, "Design and electromagnetic field characteristic analysis of 1.5 kW small scale wind power generator for substitution of Nd–Fe–B to ferrite permanent magnet," *IEEE Trans. Magn.*, vol. 48, no. 11, pp. 2933–2936, Nov. 2012.

[15] O. Craiu, N. Dan, and E. Badea, "Numerical analysis of permanent magnet DC motor performances," *IEEE Trans. Magn.*, vol. 31, no. 6, pp. 3500–3502, Nov. 1995.

[16] I. Petrov, M. Polikarpova, and J. Pyrhonen, "Rotor surface ferrite magnet synchronous machine for generator use in a hybrid application—Electromagnetic and thermal analysis," in *Proc. 39th Annu. Conf. IEEE Ind. Electron. Soc. (IECON)*, Nov. 2013, pp. 3090–3095.

[17] C. Debruyne *et al.*, "Evaluation of the efficiency of line-start permanent-magnet machines as a function of the operating temperature," *IEEE Trans. Ind. Electron.*, vol. 61, no. 8, pp. 4443–4454, Aug. 2014.

[18] S. H. Minnich, M. V. K. Chari, and J. Berkery, "Operational inductances of turbine-generators by the finite-element method," *IEEE Trans. Power App. Syst.*, vol. PAS-102, no. 1, pp. 20–27, Jan. 1983.

[19] T. J. Woolmer and M. D. McCulloch, "Analysis of the yokeless and segmented armature machine," in *Proc. IEEE Int. Electr. Mach. Drives Conf.*, vol. 1. May 2007, pp. 704–708.

[20] W. Fei, P. C. K. Luk, and K. Jinupun, "A new axial flux permanent magnet segmented-armature-torus machine for in-wheel direct drive applications," in *Proc. IEEE Power Electron. Specialists Conf.*, Jun. 2008, pp. 2197–2202.

[21] F. Giulii Capponi, G. De Donato, and F. Caricchi, "Recent advances in axial-flux permanent-magnet machine technology," *IEEE Trans. Ind. Appl.*, vol. 48, no. 6, pp. 2190–2205, Nov./Dec. 2012.

[22] T. J. Woolmer and M. D. McCulloch, "Axial flux permanent magnet machines: A new topology for high performance applications," in *Proc. IET Hybrid Vehicle Conf*, Coventry, U.K., Dec. 2006, pp. 27–42.

[23] S. M. Jafari-Shiadeh and M. Ardebili, "Analysis and comparison of axial-flux permanent-magnet brushless-DC machines with fractional-slot concentrated-windings," in *Proc. 4th Annu. Int. Power Electron., Drive Syst., Technol. Conf.*, Feb. 2013, pp. 72–77.

[24] K.-C. Kim, S.-B. Lim, D.-H. Koo, and J. Lee, "The shape design of permanent magnet for permanent magnet synchronous motor considering partial demagnetization," *IEEE Trans. Magn.*, vol. 42, no. 10, pp. 3485–3487, Oct. 2006.

[25] T. Higashi *et al.*, "Development of rare earth-saving magnet using localized diffusion method," *SAE Int. J. Alternative Powertrains*, vol. 2, no. 2, pp. 394–400, Apr. 2013.

[26] C. C. Chan, W. Xia, J. Z. Jiang, K. T. Chan, and M. L. Zhu, "Permanent magnet brushless drives," *IEEE Ind. Appl. Mag.*, vol. 4, no. 6, pp. 16–22, Nov./Dec. 1998.

[27] J. Gan, K. T. Chau, C. C. Chan, and J. Z. Jiang, "A new surface-inset, permanent-magnet, brushless DC motor drive for electric vehicles," *IEEE Trans. Magn.*, vol. 36, no. 5, pp. 3810–3818, Sep. 2000.

[28] O. A. Mohammed, S. Liu, and Z. Liu, "A phase variable model of brushless dc motors based on finite element analysis and its coupling with external circuits," *IEEE Trans. Magn.*, vol. 41, no. 5, pp. 1576–1579, May 2005.

[29] M. Fazil and K. R. Rajagopal, "Nonlinear dynamic modeling of a single-phase permanent-magnet brushless DC motor using 2-D static finite-element results," *IEEE Trans. Magn.*, vol. 47, no. 4, pp. 781–786, Apr. 2011.

[30] *Nanopyme Project Website*. [Online]. Available: http://nanopyme-project.eu, accessed Dec. 16, 2014.

Finite-Element Model-Based Design Synthesis of Axial Flux PMBLDC Motors

M. Fasil, N. Mijatovic, B. B. Jensen, and J. Holboll

***Abstract*—This paper discusses the design synthesis of a permanent-magnet brushless dc (PMBLDC) machine using a finite-element (FE) model. This work differentiates itself from the past studies by following a synthesis approach, in which many designs that satisfy the performance criteria are considered instead of a unique solution. The designer can later select a design, based on comparing parameters of the designs, which are critical to the application that the motor will be used for. The presented approach makes it easier to define constraints for a design synthesis problem. A detailed description of the setting up of an FE-based design synthesis problem, starting from the definition of design variables, the FE model of the machine, how the design synthesis is carried out, and to how a design is finalized from a set of designs that satisfy the performance criteria, is included in this paper. The proposed synthesis program is demonstrated by designing a segmented axial torus PMBLDC motor for an electric two-wheeler.**

***Index Terms*—Axial flux machines, electrical machine design synthesis, finite-element model, integer constrained genetic algorithm, PMBLDC motor, segmented stator tooth.**

I. Introduction

PERMANENT magnet (PM) brushless machines offer higher efficiency and power density compared to machines that require externally supplied field current [1]. Radial flux (RF) and axial flux (AF) are the two major configurations of PM rotating machines. AF machines offer higher torque density compared to RF motors for low-speed application such as an in-wheel motor for electric two-wheelers, where the axial length of the machine is restricted by the limited space available [2], [3]. Many approaches exist to synthesize an optimized design of AF machines [4]–[9].

This work implements an FE based design synthesis approach by developing a design program for a segmented axial torus (SAT) permanent magnet brushless DC (PMBLDC) machine. The SAT motor topology [10]–[13] is a variation of SSDR-NS (single stator dual rotor north-south) axial flux motor topology [14] and has no stator yoke. Exploded view of the SAT PMBLDC hub motor is shown in Fig. 1. A SAT PMBLDC motor with a voltage rating of 48 V and produces 20 N m at 340 rpm is designed to demonstrate the design program.

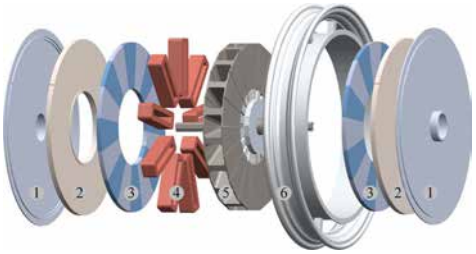

Fig. 1. Exploded view of the SAT PMBLDC motor: 1, end cover; 2, rotor yoke; 3, magnets; 4, stator winding; 5, stator; and 6, wheel rim.

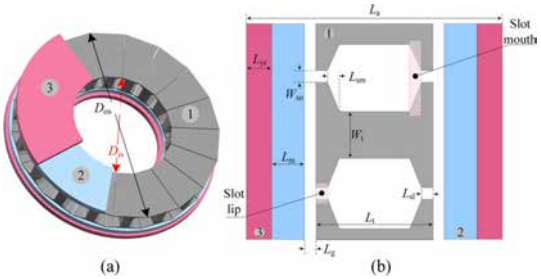

Fig. 2. Variables that define the geometry of the SAT PMBLDC motor: 1, segmented stator; 2, magnets; and 3, rotor. (a) Cutaway model. (b) Sectional view of the inner periphery. The definition of each variable is given in the Appendix.

II. FE Model-Based Design Synthesis

The design synthesis program presented here has two parts. The first part is an FE based design tool that will estimate the motor dimensions based on a given specification and constraints. The second part is a search program that will use the design tool to identify designs satisfying the performance criteria specified by the designer. This section will explain design variables of SAT PMBLDC motor, FE based design tool, and search program.

A. Design Variables of the SAT PMBLDC Motor

The set of dimensions that define the geometry of the SAT PMBLDC motor, excluding the winding is shown in Fig. 2. The

Manuscript received October 19, 2015; accepted March 1, 2016. Date of publication March 3, 2016; date of current version March 16, 2016. This work was supported by the EU-FP7 NANOPYME Project under Grant 310516. *(Corresponding author: M. Fasil.)*

M. Fasil, J. Holboll, and N. Mijatovic are with the Department of Electrical Engineering, Technical University of Denmark, 2800 Kongens Lyngby, Denmark (e-mail: mfasil@elektro.dtu.dk; nm@elektro.dtu.dk; jh@elektro.dtu.dk).

B. B. Jensen is with the Department of Science and Technology, University of the Faroe Islands, 100 Tórshavn, Faroe Islands (e-mail: bogibj@setur.fo).

Color versions of one or more of the figures in this paper are available online at http://ieeexplore.ieee.org.

Digital Object Identifier 10.1109/TASC.2016.2537743

1051-8223 © 2016 IEEE. Personal use is permitted, but republication/redistribution requires IEEE permission.
See http://www.ieee.org/publications_standards/publications/rights/index.html for more information.

TABLE I
DESIGN VARIABLES OF THE SAT PMBLDC MOTOR

Specification	Primary	Secondary
Rated voltage	Number of stator slots	Width of stator tooth
Rated power	Number of rotor poles	Depth of rotor yoke
Rated speed	Length of airgap	Diameter of a coil turn
	Outer diameter of stator	Number of turns/coil
	Gross slot fill factor	Axial length of tooth
	Width of slot opening	Axial length of motor
	Depth of slot lip	
	Depth of slot mouth	
	Depth of magnet	
	Magnet overhang	
	Diameter ratio of stator	
	Max. current density	
	Ratio of pole arc to pole pitch	
	Max. rotor yoke flux density	
	Max. stator tooth flux density	

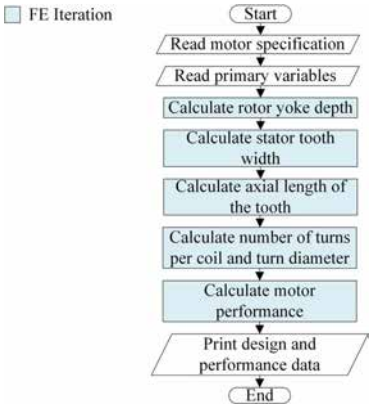

Fig. 3. Flowchart of the design tool showing the different stages in the estimation of secondary variables and the motor performance.

dimensions as seen from the inner periphery of the motor are indicated in Fig. 2(b). The design variables of SAT PMBLDC motor can be grouped into three sets: specification, primary, and secondary variables as listed in Table I. The primary variables are those design parameters that can be changed independently, without affecting the value of other primary variables. For example, the length of airgap can be changed alone to generate different designs. The secondary variables are calculated by the design tool for given values of specification and primary variables. It is important to note that some variables can be either primary or secondary. For example, if the axial length of the machine is a design constraint, then the outer diameter of the stator can be a secondary variable.

B. FE Model-Based Design Tool

When developing a design program for newer machine topologies, the use of FE models helps to avoid the time required for development of lumped parameter or analytical models. Though, the FE model provides accurate solutions, it requires longer time for solving each design iteration compared to the other two models. The design tool is shown in Fig. 3 in the form of a flowchart, which will give an overview of different stages involved in the calculation of secondary variables and the motor performance.

In the first stage, the rotor yoke depth is calculated iteratively using a stator-less three-dimensional (3D) static FE model of a SAT PMBLDC motor. Iteration starts with a minimum rotor yoke depth, and the depth will be increased in each iteration. Iterations stop when the maximum flux density inside the rotor yoke is below the value of flux density constraint. Similarly, the program calculates stator tooth width by gradually increasing tooth width of the FE model from a minimum value. Iteration stops when the maximum tooth flux density is below the value set by the constraint. During this stage, the axial length of the tooth is set as twice the depth of slot lip and mouth together. The program records average airgap flux density at the end of this stage, B_{g0} for future calculations. The EMF generated in the phase winding of a PMBLDC motor because of the rotor movement can be expressed as [15]

$$\begin{aligned} E_{\rm ph} &= P\phi Z\frac{N_r}{60} \\ &= B_g\frac{\pi}{4}\left(D_{\rm os}^2 - D_{\rm is}^2\right)\frac{2N_cN_s}{2\times 3}\frac{N_r}{60} \\ &= \frac{N_r}{60}\frac{N_s}{3}\frac{\pi}{4}\left(D_{\rm os}^2 - D_{\rm is}^2\right)B_gN_c \end{aligned} \tag{1}$$

where, P is the number of rotor poles, ϕ is the flux per pole, Z is the number of conductors in series per phase, N_r is the rated speed of machine, B_g is the average airgap flux density, N_c is the number of turns per coil, N_s is the number of stator slots. The rated output power of a three-phase PMBLDC motor is given by

$$\begin{aligned} P_r &= 2E_{\rm ph}I_{\rm ph} \\ &= 2\left[\frac{N_r}{60}\frac{N_s}{3}\frac{\pi}{4}\left(D_{\rm os}^2 - D_{\rm is}^2\right)B_gN_c\right]\left(\frac{\pi}{4}D_{\rm ct}^2J\right) \\ &= \left[\frac{N_s}{3\times 4}B_gJ\left(D_{\rm os}^2 - D_{\rm is}^2\right)\frac{2\pi N_r}{60}\right]\left(N_c\frac{\pi}{4}D_{\rm ct}^2\right) \\ &= \left[\frac{N_s}{12}JB_g\left(D_{\rm os}^2 - D_{\rm is}^2\right)\omega_r\right](K_{\rm sff}\times \text{Slot area}) \end{aligned} \tag{2}$$

where, $D_{\rm ct}$ is the diameter of a coil turn, J is the current density of a coil turn, and $K_{\rm sff}$ is the gross slot fill factor. Therefore, the slot area can be calculated as from (2) as

$$\text{Slot area} = \frac{12T_r}{K_{\rm sff}N_sJB_g\left(D_{\rm os}^2 - D_{\rm is}^2\right)} \tag{3}$$

where, T_r, is the rated torque of the machine. The axial length of the tooth can be calculated from the area of stator slot [refer Fig. 2(b)], and the flowchart of Fig. 4 shows iterative steps implemented to calculate the axial length of the tooth. In the next stage, the design tool will calculate the number of turns per coil and the diameter of a turn iteratively using back EMF equation (1) as shown in the flowchart of Fig. 5. The design generation concludes by calculating the motor performance data such as input current, efficiency, losses, etc. using the FE model of the

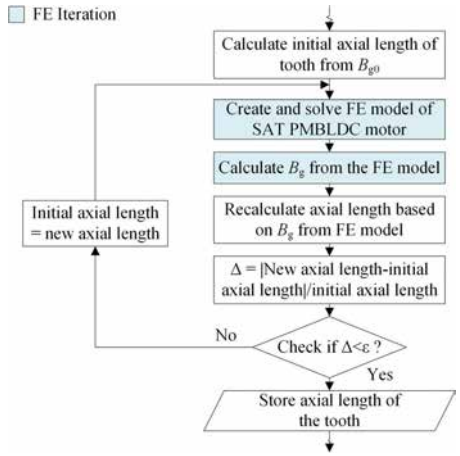

Fig. 4. Flowchart for calculating the axial length of the stator tooth iteratively using the FE model of the SAT PMBLDC motor. ε is the tolerance for convergence.

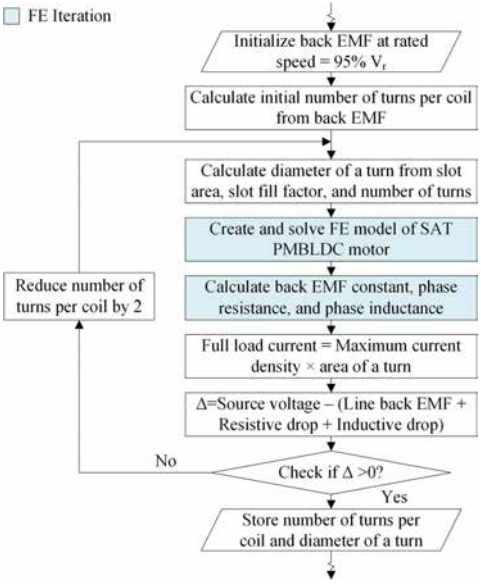

Fig. 5. Flowchart for calculating the number of turns of the coil and the diameter of a turn iteratively using the FE model of the SAT PMBLDC motor.

developed design. The design tool is implemented using Excel-VBA and commercial FE software package, MagNet.

C. Search Program

The search program finds designs that meet performance targets set by the designer. The objective function of the search program uses the design tool described in Section II-B, and the search program is implemented using integer constrained genetic algorithm available in MATLAB. The integer constrained algorithm helps to define discrete realistic set of values for primary variables. All intermediate points of the optimization process are recorded, and the search program is stopped when there is no major improvement in the value of the objective function.

TABLE II
SPECIFICATION OF THE SAT PMBLDC MOTOR POWERTRAIN FOR THE ELECTRIC TWO-WHEELER

Parameter	Value
Maximum mass of vehicle including load	130 kg
Maximum speed of vehicle	30 km h^{-1}
Time to reach maximum speed	20 s
Rated speed of motor	340 rpm
Rated torque of motor	20 N m
Rated voltage of battery	48 V

TABLE III
PRIMARY VARIABLES OF THE SAT PMBLDC MOTOR, EXCLUDING OPTIMIZATION VARIABLES, AND THEIR VALUES

Variable name	Value
Number of slots-poles	18–16
Length of airgap	0.4 mm
Outer diameter of stator	260 mm
Gross slot fill factor	50%
Width of slot opening	1 mm
Depth of slot lip	2 mm
Depth of slot mouth	2 mm
Current density of coil	4.5 A mm^{-2}
Ratio of pole arc to pole pitch	1
Max. flux density of rotor yoke	1.2 T
Max. flux density of stator tooth	1.6 T

III. DESIGN SYNTHESIS OF THE SAT PMBLDC MOTOR FOR THE ELECTRIC TWO-WHEELER POWERTRAIN

A SAT PMBLDC in-wheel motor for a battery operated two-wheeler has been designed using the FE based synthesis program. The specification of the powertrain, shown in Table II, has been identified using the methodology described by Ehsani *et al.* [16].

The number of primary variables that require optimization has been reduced considerably by following the design guidelines of PMBLDC motor [17] and values of these variables are listed in Table III. The airgap length is decided based on the manufacturing tolerances. The maximum possible outer diameter of the motor for a 14 inch wheel is selected to limit the axial length. The SAT topology allows a higher fill factor than the 30 to 40% used in classical machines. The sections around the slot opening are made sufficiently thick based on FE studies of the motor to avoid the saturation in these areas. As the motor is not force-cooled, a current density of less than 5 A mm^{-2} is selected. The machine will be using bonded rare earth magnets with a remanence of 0.58 T and a coercivity of 330 kA mm^{-1}. The ease of assembly of magnets was given higher priority than the cost saving via magnet material reduction; hence a pole arc to pole pitch ratio of one is selected. Solid soft-iron is used

TABLE IV
PRIMARY VARIABLES USED AS OPTIMIZATION VARIABLES IN THE DESIGN SYNTHESIS OF THE SAT PMBLDC MOTOR AND THEIR RANGE

Variable name	Range
Depth of magnet	7 mm to 10 mm in steps of 0.5 mm
Magnet overhang	0%, 5%, 10%
Diameter ratio of stator	45% to 60% in steps of 2.5%

Fig. 6. FE model of the SAT PMBLDC motor used in the design synthesis of the in-wheel motor.

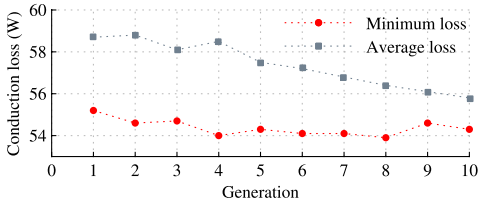

Fig. 7. Results of the FE-based design synthesis of the SAT PMBLDC in-wheel motor using the genetic algorithm.

to make the rotor yoke; therefore, the maximum flux density is set to 1.2 T to reduce the core loss. The cold rolled silicon steel lamination of grade M-36 is used to make the stator tooth, and a maximum flux density 1.6 T is achievable in this material without considerable core loss.

The three remaining primary variables: depth of the magnet (L_m), ratio of magnet overhang to radial length of the stator (h), and diameter ratio of the stator (λ_d) are optimized to generate SAT PMBLDC motor designs. The discrete set of values for these parameters are shown in Table IV. The SAT PMBLDC motor topology has a lower core loss compared to topologies with stator yoke [18]. In addition, the low flux density threshold selected for the rotor yoke and the stator tooth will help to reduce core losses generated in them. Therefore, the synthesis program is devised to identify the designs with low conduction losses $(P_{\rm cu})$, with the assumption that the core loss variation among these designs will be negligible.

The 3D FE model of SAT PMBLDC motor utilizing the geometrical symmetry, excluding the elements of air volume, used in the design synthesis of the in-wheel motor is shown Fig. 6. Only one coil belong to each phase is modeled and the phase back EMF is calculated with the help of winding factor presented by Ishak *et al.* [19]. The synthesis took 73.6 hours and generated 551 designs. The result of genetic algorithm optimization is shown in Fig. 7. The design synthesis is stopped at tenth generation because there was no significant change in minimum loss from the fourth generation onwards. Moreover, the average loss is moving towards the minimum loss shows the convergence.

TABLE V
MINIMUM LOSS DESIGNS FROM THE DESIGN SYNTHESIS OF THE SAT PMBLDC IN-WHEEL MOTOR

	Design #						
Parameters	63	88	124	143	158	270	410[a]
$L_{\rm m}$ (mm)	7.5	9.5	8	7	7	7.5	7
h (%)	0	10	5	0	5	10	0
$\lambda_{\rm d}$ (%)	50	52.5	50	47.5	45	47.5	45
$L_{\rm yr}$ (mm)	7	7	7	8	8	8	8
$W_{\rm t}$ (mm)	11.3	11.9	11.3	10.8	10.2	10.8	10.2
$N_{\rm c}$	24	24	24	28	22	22	28
$D_{\rm ct}$ (mm)	2.8	2.8	2.8	2.6	2.8	2.9	2.5
$L_{\rm t}$ (mm)	32.4	30.6	32.2	32.6	33.4	32.6	32.8
$L_{\rm a}$ (mm)	62.2	64.4	63	63.4	63.9	64.4	63.6
I (A)	28.0	28.4	28.2	23.4	28.5	29.4	22
$P_{\rm cu}$ (W)	56.8	56.1	57.2	56.3	55.2	55.8	54

[a] Design #410 is selected because it is the one with the lowest current, and a powertrain motor with a lower current at rated load will improve the range of the electric vehicle.

TABLE VI
GEOMETRICAL VARIABLES OF THE SAT PMBLDC MOTOR AND THEIR DEFINITION

No.	Variable	Variable definition
1.	$D_{\rm os}$	Outer diameter of stator
2.	$D_{\rm is}$	Inner diameter of stator
3.	$L_{\rm g}$	Axial length of airgap
4.	$W_{\rm so}$	Width of slot opening
5.	$L_{\rm sl}$	Depth of slot lip
6.	$L_{\rm sm}$	Depth of slot mouth
7.	$L_{\rm m}$	Depth of magnet
8.	$L_{\rm yr}$	Depth of rotor yoke
9.	$W_{\rm t}$	Width of stator tooth
10.	$L_{\rm t}$	Axial length of stator tooth
11.	$L_{\rm a}$	Axial length of motor

The minimum loss designs from the design synthesis that satisfy geometrical constraints are listed in Table V. The SAT PMBLDC motor is designed for battery operated two-wheeler, and a motor with a lower current (I) at rated load will improve the range of the vehicle. Therefore, design #410 is selected because it is the one with the lowest rated current.

IV CONCLUSION

An FE based design synthesis approach is demonstrated by developing a design program for SAT PMBLDC motor. Even though, the time taken for each design iteration with FE model is considerably more compared to analytical or lumped parameter models; accurate results can be achieved with significantly less program development time. The developed program is demonstrated by designing a traction motor for an electric two-wheeler.

APPENDIX

The variables defining the geometry of the SAT PMBLDC motor are shown in Table VI.

REFERENCES

[1] T. J. E. Miller, *Brushless Permanent-Magnet and Reluctance Motor Drives*. New York, NY, USA: Oxford Univ. Press, 1989.

[2] A. Cavagnino, M. Lazzari, F. Profumo, and A. Tenconi, "A comparison between the axial flux and the radial flux structures for PM synchronous motors," *IEEE Trans. Ind. Appl.*, vol. 38, no. 6, pp. 1517–1524, Nov. 2002.

[3] J. F. Gieras, R.-J. Wang, and M. J. Kamper, *Axial Flux Permanent Magnet Brushless Machines* Dordrecht, The Netherlands: Kluwer, 2005.

[4] M. Aydin and T. Lipo, "Design and 3D electromagnetic field analysis of non-slotted and slotted TORUS type axial flux surface mounted permanent magnet disc machines," in *Proc. IEEE IEMDC Cat. No.01EX485*, 2001, pp. 645–651.

[5] T. F. Chan and L. L. Lai, "An axial-flux permanent-magnet synchronous generator for a direct-coupled wind-turbine system," *IEEE Trans. Energy Convers.*, vol. 22, no. 1, pp. 86–94, Mar. 2007.

[6] N. Rostami, M. R. Feyzi, J. Pyrhonen, A. Parviainen, and V. Behjat, "Genetic algorithm approach for improved design of a variable speed axial-flux permanent-magnet synchronous generator," *IEEE Trans. Magn.*, vol. 48, no. 12, pp. 4860–4865, Dec. 2012.

[7] A. Mahmoudi, S. Kahourzade, N. A. Rahim, and W. P. Hew, "Design, analysis, and prototyping of an axial-flux permanent magnet motor based on genetic algorithm and finite-element analysis," *IEEE Trans. Magn.*, vol. 49, no. 4, pp. 1479–1492, Apr. 2013.

[8] Y.-P. Yang, Y.-P. Luh, and C.-H. Cheung, "Design and control of axial-flux brushless DC wheel motors for electric vehicles—Part I: Multiobjective optimal design and analysis," *IEEE Trans. Magn.*, vol. 40, no. 4, pp. 1873–1882, Jul. 2004.

[9] F. Chuang, "Optimization for reduction of torque ripple in an axial flux permanent magnet machine," *IEEE Trans. Magn.*, vol. 45, no. 3, pp. 1760–1763, Mar. 2009.

[10] T. Woolmer and M. McCulloch, "Analysis of the yokeless and segmented armature machine," in *Proc. IEEE Int. Elect. Mach. Drives Conf.*, May 2007, vol. 1, pp. 704–708.

[11] W. Fei, P. C. K. Luk, and K. Jinupun, "A new axial flux permanent magnet segmented-armature-torus machine for in-wheel direct drive applications," in *Proc. IEEE Power Electron. Spec. Conf.*, Jun. 2008, pp. 2197–2202.

[12] F. Giulii Capponi, G. De Donato, and F. Caricchi, "Recent advances in axial-flux permanent-magnet machine technology," *IEEE Trans. Ind. Appl.*, vol. 48, no. 6, pp. 2190–2205, Nov. 2012.

[13] H. Vansompel, P. Sergeant, L. Dupre, and A. Van den Bossche, "Axial-flux PM machines with variable air gap," *IEEE Trans. Ind. Electron.*, vol. 61, no. 2, pp. 730–737, Feb. 2014.

[14] S. Kahourzade, A. Mahmoudi, H. W. Ping, and M. N. Uddin, "A comprehensive review of axial-flux permanent-magnet machines," *Can. J. Elect. Comput. Eng.*, vol. 37, no. 1, pp. 19–33, 2014.

[15] P. Campbell, "Principles of a permanent-magnet axial-field d.c. machine," in *Proc. Inst. Elect. Eng.*, Dec. 1974, pp. 1489–1494.

[16] M. Ehsani, K. Rahman, and H. Toliyat, "Propulsion system design of electric and hybrid vehicles," *IEEE Trans. Ind. Electron.*, vol. 44, no. 1, pp. 19–27, Feb. 1997.

[17] J. Hendershot and T. Miller, *Design of Brushless Permanent-Magnet Machines*. Oxford, U.K.: Clarendon, 2010.

[18] T. J. Woolmer and M. McCulloch, "Axial flux permanent magnet machines: A new topology for high performance applications," in *Proc. IET Hybrid Veh. Conf.*, Coventry, U.K., 2006, pp. 27–42.

[19] D. Ishak, Z. Zhu, and D. Howe, "Comparison of PM brushless motors, having either all teeth or alternate teeth wound," *IEEE Trans. Energy Convers.*, vol. 21, no. 1, pp. 95–103, Mar. 2006.

Improved dq-Axes Model of PMSM Considering Airgap Flux Harmonics and Saturation

M. Fasil, C. Antaloae, N. Mijatovic, B. B. Jensen, and J. Holboll

***Abstract*—In this paper, the classical linear model of a permanent-magnet synchronous motor (PMSM) is modified by adding d- and q-axis harmonic inductances so that the modified model can consider nonlinearities present in an interior permanent magnet (IPM) motor. Furthermore, a method has been presented to assess the effect of saturation and cross-saturation on constant torque curves of a PMSM. Two IPM motors with two different rotor topologies and different specifications are designed to evaluate the effect of saturation on synchronous and harmonic inductances and on the operating points of the machines.**

***Index Terms*—Field weakening, harmonic inductances, interior permanent magnet machine, permanent magnet synchronous machine, saturation.**

I. Introduction

PERMANENT magnet synchronous machines (PMSM) are a popular choice in electric powertrain because of benefits such as high power density, high torque density and wide constant power operation [1]. The classical model of PMSM neglects non-linearities caused by the higher order airgap flux harmonics (greater than second) and the saturated magnetic flux path [2]. This was not an issue in earlier versions of PMSM drives as they were mostly using surface permanent magnet (SPM) machines. The large effective airgap of SPM machines limits the influence of armature reaction on machine parameters. The applications like drives for traction require extended constant power operation and interior permanent magnet (IPM) machines, which utilizes reluctance torque along with magnet torque, are more suitable compared to SPM machines [3]–[6]. The IPM machines have a narrow airgap and, therefore, the armature current influences the amplitude of harmonic fluxes, the saturation level, core losses, and dq-axes inductances [7].

Several studies have been carried out to estimate the effect of saturation on parameters of IPM machines and to improve the accuracy of classical dq-axes model of PMSM [8]–[11]. In [12], the authors presented a comparison between the classical dq-axes model and the finite element (FE) model of an IPM machine. In their study, an error of less than 10% in core-loss at base speed has increased to more than 75% at four times the base speed. The authors proposed adding harmonic inductance to dq-axes model of IPM machine and this helps to model the increased core loss in field weakening mode. The authors used same inductances, which was obtained by dividing the sum of magnitudes of all higher order flux linkage harmonics with the magnitude of phase current, to both d and q equivalent circuits. Even though, the model was closer to test results compared to the classical model, considerable deviations were observed.

In this work, the model presented in [12] was modified by considering harmonic fluxes that are resolved into d-axis and q-axis to calculate harmonic inductances of d and q equivalent circuits. In addition, the effect of saturation on operating point of IPM machine when it is operating under maximum torque per ampere (MTPA) control has been studied. Two IPM machines with different rotor topologies, shown in Fig. 1, are designed to demonstrate the proposed concepts.

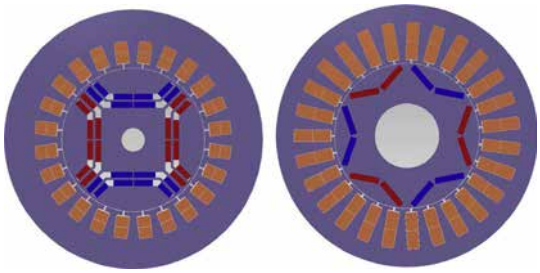

(a) (b)

Fig. 1. IPM topologies used for calculating dq-axis equivalent circuit parameters. (a) Two-layer-angled barrier magnets. (b) Embedded variable orientation magnets.

II. The dq-Axes Model of PMSM Considering Harmonic Inductances

The flowchart shown in Fig. 2, describes the procedure for calculating the fundamental (or synchronous) and harmonic components of dq-axes inductances, considering saturation and cross-saturation. The d-axis and q-axis harmonic components of flux linkages, ψ_{dn} and ψ_{qn} can be obtained from the Fourier analysis of airgap flux density distribution as [13]

$$\psi_{\mathrm{dn}} = B_{\mathrm{dn}} \frac{DL_{\mathrm{stk}}}{p} k_{\mathrm{wn}} T_{\mathrm{ph}}; \quad \psi_{\mathrm{qn}} = B_{\mathrm{qn}} \frac{DL_{\mathrm{stk}}}{p} k_{\mathrm{wn}} T_{\mathrm{ph}} \quad (1)$$

Manuscript received October 19, 2015; accepted January 27, 2016. Date of publication February 5, 2016; date of current version February 24, 2016. This work was supported by the EU-FP7 NANOPYME Project under Grant 310516. *(Corresponding author: M. Fasil.)*

M. Fasil, N. Mijatovic, and J. Holboll are with the Department of Electrical Engineering, Technical University of Denmark, 2800 Lyngby, Denmark (e-mail: mfasil@elektro.dtu.dk; nm@elektro.dtu.dk; jh@elektro.dtu.dk).

C. Antaloae is with AVL Powertrain U.K. Ltd., Coventry CV4 7EZ, U.K. (e-mail: ciprian.antaloae@avl.com).

B. B. Jensen is with the Department of Science and Technology, University of the Faroe Islands, 100 Torshavn, Faroe Islands (e-mail: bogibj@setur.fo).

Color versions of one or more of the figures in this paper are available online at http://ieeexplore.ieee.org.

Digital Object Identifier 10.1109/TASC.2016.2524021

1051-8223 © 2016 IEEE. Personal use is permitted, but republication/redistribution requires IEEE permission.
See http://www.ieee.org/publications_standards/publications/rights/index.html for more information.

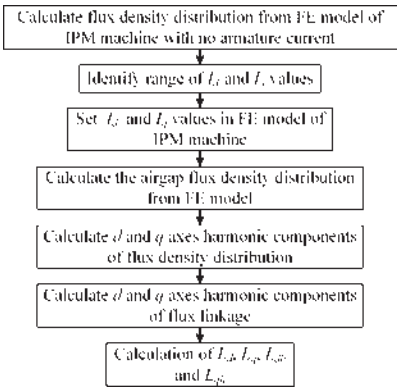

Fig. 2. Flowchart to calculate fundamental and harmonic inductances from the FE model of the IPM machine.

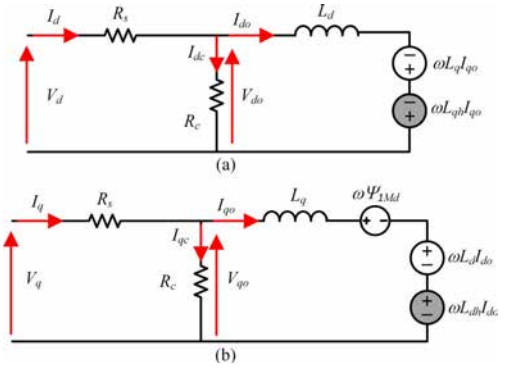

Fig. 3. Modified dq-axis equivalent circuit of the IPM machine. (a) d-axis equivalent circuit. (b) q-axis equivalent circuit.

where $B_{\rm dn}$ and $B_{\rm qn}$ are values of real and imaginary parts of the nth harmonic component of flux density distribution under load, D is the outer diameter of the airgap, $L_{\rm stk}$ is the stack length of the machine, p is the number of pole pairs of the machine, $k_{\rm wn}$ is nth harmonic winding factor and $T_{\rm ph}$ is the number of turns in series per phase. The d-axis and q-axis synchronous inductances are calculated as

$$L_d = \frac{\psi_{1\rm Md} - \psi_{d1}}{I_d}; \quad L_q = \frac{\psi_{q1}}{I_q} \tag{2}$$

where $\psi_{1\rm Md}$ is the fundamental component of the d-axis flux linkage due to the magnet flux alone. The effect of all higher order harmonics of flux linkage is represented by harmonic inductances, $L_{\rm dh}$ and $L_{\rm qh}$ and they can be calculated as

$$L_{\rm dh} = \sum_{i=5,7,\ldots}^{\infty} \frac{\psi_{d0i} - \psi_{\rm di}}{I_d}; \quad L_{\rm qh} = \sum_{i=5,7,\ldots}^{\infty} \frac{\psi_{\rm qi}}{I_q} \tag{3}$$

where ψ_{d0i} is the ith harmonic flux linkage due to magnet flux alone. The modified dq-axis equivalent circuits of IPM machine considering harmonic inductances are shown in Fig. 3. In Fig. 3, R_s is the phase resistance, R_c is the core loss resistance [12], $I_{\rm dc}$ and $I_{\rm qc}$ are core loss components and $I_{\rm do}$ and $I_{\rm qo}$ are torque producing components of I_d and I_q. In steady state, voltage relationship for the circuit can be expressed as

$$V_{\rm do} = -\omega L_q I_{\rm qo} - \omega L_{\rm qh} I_{\rm qo} \tag{4}$$

$$V_{\rm qo} = \omega \Psi_{1\rm Md} + \omega L_d I_{\rm do} + \omega L_{\rm dh} I_{\rm do} \tag{5}$$

$$V_d = I_d R_s + V_{\rm do} \tag{6}$$

$$V_q = I_q R_s + V_{\rm qo}. \tag{7}$$

III. Estimating the Effect of Saturation and Cross-Saturation on Constant Torque Curves of IPM Machine

The saturation of steel laminations changes values of dq-axes inductances, and causes considerable deviation between analytically predicted and measured performances of IPM machines [14]. Thus, the operating point of IPM machines can shift considerably with saturation, especially at higher load levels. A flowchart to estimate the shift in constant torque curves of an IPM machine in an $I_d I_q$-plane is shown in Fig. 4. The method uses torque equation to identify synchronous inductances from a lookup table corresponding to a set of I_d, I_q values. Torque expression itself is a function of I_d, I_q and synchronous inductances and therefore, an iterative procedure is required.

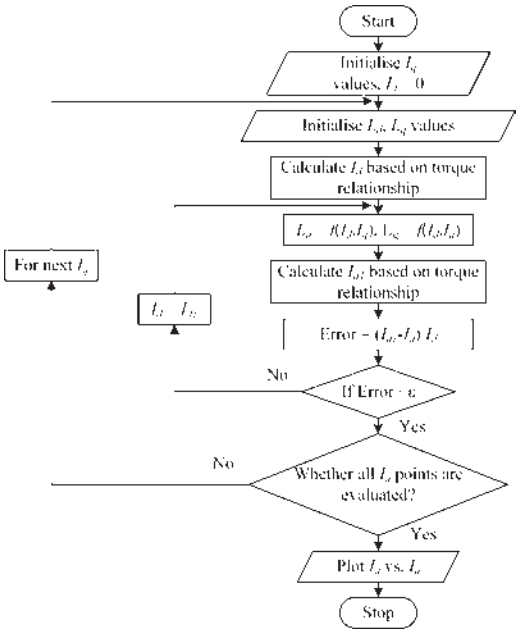

Fig. 4. Flowchart for estimating the effect of saturation and cross-saturation on constant torque curves of the IPM machine (where ε is a predefined error limit).

TABLE I
OVERVIEW OF SPECIFICATION AND dq-AXIS EQUIVALENT CIRCUIT PARAMETERS OF IPM MACHINES

Parameters	Design 1	Design 2
Rotor topology	two layer angled barrier	embedded
Rated power (kW)	125	75
Number of pole pairs	2	3
Number of slots	24	27
Rated speed (rpm)	3275	3055
Full load torque (Nm)	364	233
Full load RMS line voltage (V)	315	308
Full load RMS phase current (A)	319	220
Outer diameter of stator (mm)	276	300
Stack length of stator (mm)	193	281
Magnet flux linkage (Wb-turns)	0.24	0.167
Phase resistance of winding (mΩ)	6.09	1.9
d-axis inductance at full load (mH)	0.34	0.47
q-axis inductance at full load (mH)	0.79	1.39
Core loss at full load (W)	830	3240
Core loss resistance (Ω)	119.55	29.28

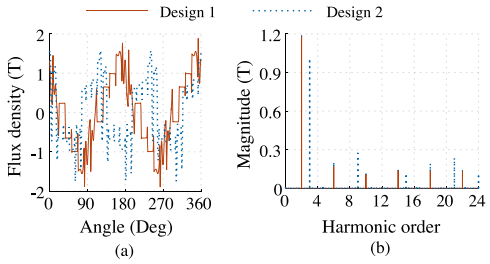

Fig. 5. Airgap flux density distributions and its harmonics when a current of 283 A applied at an advancing angle 45° to the design 1 and a current of 194 A applied at an advancing angle 45° to the design 2. (a) Airgap flux density distributions. (b) Flux density harmonics.

IV. CALCULATION OF MODIFIED dq-AXIS EQUIVALENT CIRCUIT PARAMETER FOR IPM MOTOR DESIGNS

An overview of the specification and dq-axes circuit parameters of the two motors designed using the commercial design program, MotorSolve™, are listed in the Table I. Airgap flux density distributions and its harmonics when a current of 283 A applied at an advancing angle 45° to the design 1 and a current of 194 A applied at an advancing angle 45° to the design 2 is shown in Fig. 5. Flux density plots of these machines for different I_d and I_q values are shown in Figs. 6 and 7. Harmonic inductances are calculated for harmonic orders starting from 5 to 21. The variation of d and q synchronous and harmonic inductances are shown in Figs. 8 and 9, and it is clear from these figures that harmonic inductance magnitudes are of the same order of synchronous inductances for the machines considered here. The value of synchronous inductances is decreasing as demagnetizing-I_d and I_q values are increased for two layer angled barrier rotor topology. The saturation levels of barriers (located in d-axis flux path) are highly sensitive to both I_d and I_q as shown in Fig. 6 (b) and (c). As a result a widely spread plot of d-axis inductance variation is observed as shown in Fig. 8(a). From, Figs. 6(b) and 8(b), it is clear that the effect of cross-saturation on L_q is less pronounced for angled barrier IPM

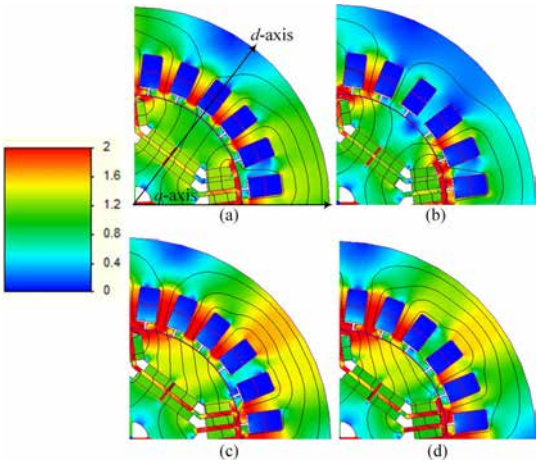

Fig. 6. Flux density (T) plots for design 1 for different I_d and I_q values. (a) $I_d = -40$ A, $I_q = 40$ A, (b) $I_d = -280$ A, $I_q = 40$ A, (c) $I_d = -40$ A, $I_q = 280$ A, and (d) $I_d = -280$ A, $I_q = 280$ A.

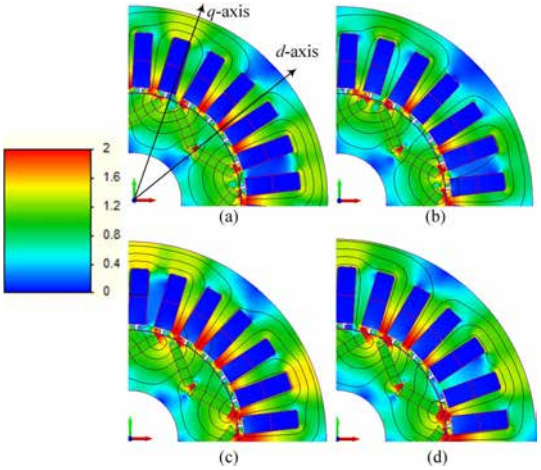

Fig. 7. Flux density (T) plots for design 2 for different I_d and I_q values. (a) $I_d = -27.5$ A, $I_q = 27.5$ A, (b) $I_d = -220$ A, $I_q = 27.5$ A, (c) $I_d = -27.5$ A, $I_q = 220$ A, and (d) $I_d = -220$ A, $I_q = 220$ A.

motor design. For embedded rotor topology, the gap between magnets located in q-axis is the only section of q-axis flux path in rotor that is highly saturated and the saturation level of this area is depended more on I_d than I_q, resulting in L_q and $L_{\rm qh}$ plots that are more or less constant with variations of I_q.

When the motor operates under MTPA control, the operating points will be the intersections of MTPA curve and constant torque curves. The MTPA curve for the proposed model under saturation is obtained by joining minimum current points of constant torque curves (corresponding to 50%, 75% and 100% of the rated torque, T_r) as shown in Fig. 10. The estimated full load torque of the design 1 shows an improvement of 4% and that of the design 2 shows an improvement of 7%

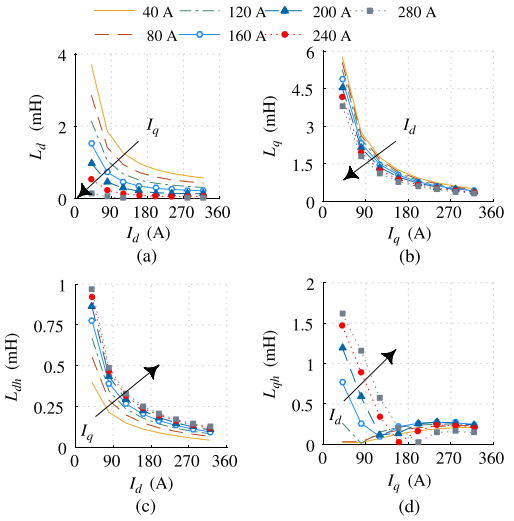

Fig. 8. Effect of saturation and cross-saturation on synchronous and harmonic inductances of a 125-kW 4-pole two-layer-angled barrier IPM machine. In this plot, I_d generates a demagnetizing field.

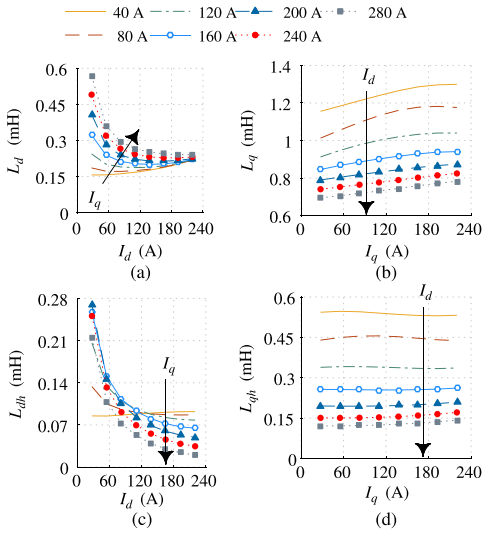

Fig. 9. Effect of saturation and cross-saturation on synchronous and harmonic inductances of a 75-kW 6-pole embedded IPM machine. In this plot, I_d generates a demagnetizing field.

when saturation of the flux path and harmonic inductances are accounted in the dq-axes model of the machine.

V. Conclusion

IPM motors have higher content of airgap flux harmonics than surface magnet machines and their operation in the field weakening mode can cause the saturation of magnetic flux paths. This study proposed to add harmonic inductances to the classic dq-axes model of PMSM to accurately model the effect of the higher harmonic flux content of IPM motors. The analysis of two IPM machines concluded that the impact of saturation and cross-saturation on synchronous and harmonic inductances are highly influenced by the rotor topology of IPM machines. It has been found that discrepancy between models with and without higher order harmonic parameters can be as high as 7%.

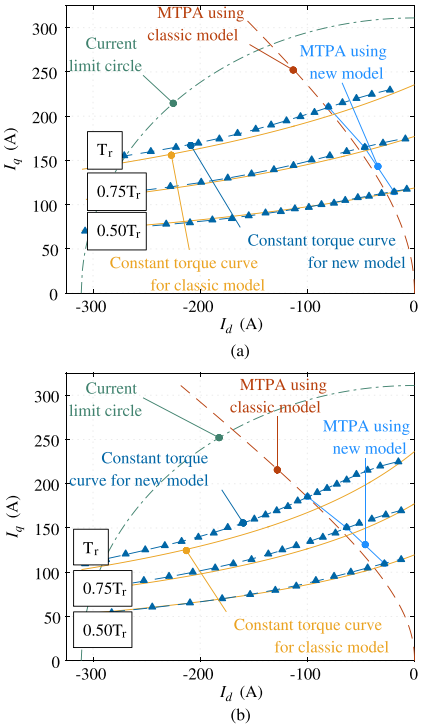

Fig. 10. Effect of saturation and space harmonics on MTPA control. (a) 125-kW 4-pole two-layer-angled barrier IPM machine. (b) 75-kW 6-pole embedded IPM machine.

Acknowledgment

The authors would like to thank AVL Powertrain Ltd., UK for their help in carrying out the research.

References

[1] Z. Q. Zhu and D. Howe, "Electrical machines and drives for electric, hybrid, and fuel cell vehicles," *Proc. IEEE*, vol. 95, no. 4, pp. 746–765, Apr. 2007.

[2] J. Hendershot and T. Miller, *Design of Brushless Permanent-Magnet Machines*. Oxford, U.K.: Clarendon Press, 2010.

[3] W. Soong and T. Miller, "Field-weakening performance of brushless synchronous AC motor drives," *Proc. Inst. Elect. Eng.—Elect. Power Appl.*, 1994, pp. 331–340. [Online]. Available: http://digital-library.theiet.org/content/journals/10.1049/ip-epa_19941470

[4] T. Jahns, "Component rating requirements for wide constant power operation of interior PM synchronous machine drives," in *35th Conf. Rec. IEEE IAS Annu. Meeting World Conf. Ind. Appl. Elect. Energy*, 2000, vol. 3, pp. 1697–1704. [Online]. Available: http://ieeexplore.ieee.org/lpdocs/epic03/wrapper.htm?arnumber=882109

[5] A. Vagati, G. Pellegrino, and P. Guglielmi, "Comparison between SPM and IPM motor drives for EV application," in *Proc. IEEE 12th ICEM*, Sep. 2010, pp. 1–6. [Online]. Available: http://ieeexplore.ieee.org/xpl/articleDetails.jsp?arnumber=5607911&nav igation=1

[6] M. A. Rahman, "History of interior permanent magnet motors [History]," *IEEE Ind. Appl. Mag.*, vol. 19, no. 1, pp. 10–15, Jan. 2013.

[7] N. C. Kar, S. Hamidifar, and M. Kazerooni, "Analytical modelling and parametric sensitivity analysis for the PMSM steady-state performance prediction," *IET Elect. Power Appl.*, vol. 7, no. 7, pp. 586–596, Aug. 2013.

[8] H. Chen, D. Li, R. Qu, Z. Zhu, and J. Li, "An improved analytical model for inductance calculation of interior permanent magnet machines," *IEEE Trans. Magn.*, vol. 50, no. 6, pp. 1–8, Jun. 2014.

[9] X. Chen, J. Wang, B. Sen, P. Lazari, and T. Sun, "A high-fidelity, computationally efficient model for interior permanent magnet machines considering the magnetic saturation, spatial harmonics and iron loss effect," *IEEE Trans. Ind. Electron.*, vol. 62, no. 7, pp. 4044–4055, Jul. 2015.

[10] Z. Li and H. Li, "MTPA control of PMSM system considering saturation and cross-coupling," in *Proc. 15th ICEMS*, 2012, pp. 1–5.

[11] G. Y. Sizov, D. M. Ionel, and N. A. O. Demerdash, "Modeling and parametric design of permanent-magnet AC machines using computationally efficient finite-element analysis," *IEEE Trans. Ind. Electron.*, vol. 59, no. 6, pp. 2403–2413, Jun. 2012.

[12] B.-H. Lee *et al.*, "Modeling of core loss resistance for d–q equivalent circuit analysis of IPMSM considering harmonic linkage flux," *IEEE Trans. Magn.*, vol. 47, no. 5, pp. 1066–1069, May 2011.

[13] N. Bianchi and S. Bolognani, "Magnetic models of saturated interior permanent magnet motors based on finite element analysis," in *33rd Conf. Rec. IEEE IAS Annu. Meeting*, 1998, vol. 1, pp. 27–34.

[14] T. M. Jahns, G. B. Kliman, and T. W. Neumann, "Interior permanent-magnet synchronous motors for adjustable-speed drives," *IEEE Trans. Ind. Appl.*, vol. IA-22, no. 4, pp. 738–747, Jul. 1986.

Nonlinear Dynamic Model of PMBLDC Motor Considering Core Losses

Muhammed Fasil, Nenad Mijatovic, *Senior Member, IEEE*, Bogi Bech Jensen, *Senior Member, IEEE*, and Joachim Holboll, *Senior Member, IEEE*

***Abstract*—The phase variable model is used commonly when simulating a motor drive system with a three-phase permanent magnet brushless dc (PMBLDC) motor. The phase variable model neglects core losses and this affects its accuracy when modeling fractional-slot machines. The inaccuracy of phase variable model of fractional-slot machines can be attributed to considerable armature flux harmonics, which causes an increased core loss. This study proposes a nonlinear phase variable model of PMBLDC motor that considers the core losses induced in the stator and the rotor. The core-loss model is developed based on the detailed analysis of the flux path and the variation of flux in different components of the machine. A prototype of fractional slot axial flux PMBLDC in-wheel motor is used to assess the proposed nonlinear dynamic model.**

***Index Terms*—Axial flux machines, brushless dc (BLDC) machines, dynamic model, nonlinear model, segmented axial torus (SAT) motor.**

I. Introduction

UNLIKE the 2-D flux path of radial flux machines, the main flux in axial flux (AF) machines has a 3-D path. Therefore, these machines have to be analysed using techniques like magnetic equivalent circuit [1]–[3] or 3-D finite element (FE) method [4] that consider 3-D fluxes for obtaining accurate results. The time required to solve the 3-D model of a machine makes simulating a system such as electric vehicles that include models of power electronic converter and load along with AF machines impractical. Therefore, simulating a system with AF permanent magnet brushless dc (PMBLDC) motor requires a motor model with a solution time similar to the models of other components of the system, such as linear phase variable model [5], [6], nonlinear phase variable model [7], [8], and average value two axes model [9], [10]. All the three models mentioned neglect core-loss modeling.

Manuscript received August 6, 2016; revised November 26, 2016 and April 2, 2017; accepted April 30, 2017. Date of publication June 7, 2017; date of current version October 24, 2017. This work was supported by the EU-FP7NANOPYME Project under Grant 310516. *(Corresponding author: Muhammed Fasil.)*

M. Fasil, N. Mijatovic, and J. Holboll are with the Department of Electrical Engineering, Technical University of Denmark, Kongens Lyngby 2800, Denmark (e-mail: mfasil@elektro.dtu.dk; nm@elektro.dtu.dk; jh@elektro.dtu.dk).

B. B. Jensen is with the Department of Science and Technology, University of the Faroe Islands, Tórshavn 100, Faroe Islands (e-mail: bogibj@setur.fo).

Color versions of one or more of the figures in this paper are available online at http://ieeexplore.ieee.org.

Digital Object Identifier 10.1109/TIE.2017.2711536

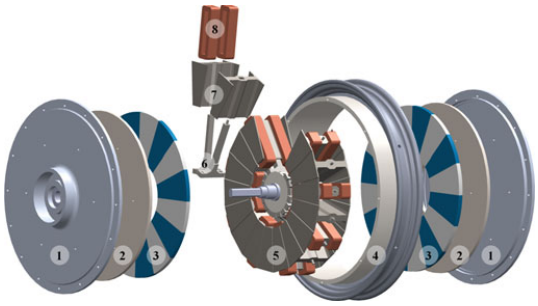

Fig. 1. Schematic of the SAT PMBLDC in-wheel motor (1. End cover, 2. rotor yoke, 3. magnet poles, 4. wheel rim with spacer, 5. stator, 6. tooth holder, 7. segmented tooth, and 8. coils).

There is an increased interest in fractional-slot winding machines because of the benefits such as high power density, high efficiency, low cogging torque, and fault tolerance [11], [12]. The fractional-slot machines have considerable rotor losses due to the rich presence of sub- and super-space harmonic components of armature flux that are not in synchronism with the rotor [13], [14]. Because of higher value of core loss in fractional-slot machines compared to integral-slot machines, the lack of core loss calculation in PMBLDC motor models could introduce considerable error in the performance simulation of fractional-slot PMBLDC machines.

In this work, a core-loss model of a segmented axial torus (SAT) PMBLDC motor is developed and incorporated into the nonlinear phase variable model of PMBLDC motor. The proposed model is evaluated using a prototype of SAT PMBLDC in-wheel motor to investigate the further areas of development of the proposed model.

II. SAT PMBLDC In-Wheel Motor

A SAT PMBLDC in-wheel motor with ferrite magnets as rotor poles is designed and fabricated to power an electric two-wheeler. The schematic of the SAT PMBLDC motor is shown in Fig. 1. The SAT motor topology is a variation of torus slotted north–south AF motor topology and has no stator yoke [15], [16]. The magnetically separated teeth can be wound separately before assembly and this ensures high fill factor and short end turn resulting in an efficiency improvement [17].

0278-0046 © 2017 IEEE. Personal use is permitted, but republication/redistribution requires IEEE permission.
See http://www.ieee.org/publications_standards/publications/rights/index.html for more information.

TABLE I
RATING AND DIMENSIONS OF THE SAT PMBLDC MOTOR

Parameter	Value
The rated voltage	48 V
The rated power output	700 W
The rated torque	20 Nm
Outer diameter of the motor	275 mm
Diameter ratio	0.45
Axial length of the motor	95.8 mm
Number of stator slots-rotor poles	18–16
Thickness of magnet poles	7.5 mm
Length of air gap	2 mm
Number of turns per coil	30

The specification and main geometrical dimensions of the motor are listed in Table I.

III. CORE LOSSES IN SAT PMBLDC MOTORS

The time variation of flux density in components such as stator core, magnets, magnet retaining ring, and rotor yoke generate core losses in permanent magnet (PM) machines. Core losses can be classified as hysteresis loss, eddy current loss, and excess loss [18]. This study considers only the hysteresis and the eddy current losses. The SAT PMBLDC motor is a stator-yokeless topology, and ferrite magnets are nonconducting magnets. Therefore, the flux density variation generates losses only in the segmented stator tooth and the solid rotor yoke of the motor. The FE analysis of the SAT PMBLDC motor showed a considerable variation in the maximum value of flux densities in the tooth-tip and the remaining part of the stator tooth (the section of the tooth excluding the tooth-tip will be addressed as tooth henceforth). Therefore, the tooth-tip and the tooth are considered as two different components for loss modeling. In this paper, the magnetic losses associated with the current building up and the pulse width modulation switching of the stator current are neglected. The following part of this section will formulate expressions for calculating core losses in the stator tooth, the tooth-tip, and the rotor yoke of a SAT PMBLDC motor.

A. Core Losses in Stator Tooth-Tip

In a PM machine, the armature flux will distort the tooth flux density distribution generated by the PMs. The unexcited and the excited flux density distributions on a pair of tooth faces of the SAT PMBLDC motor is shown in Fig. 2. From Fig. 2, it is clear that the armature current not only distorts the no-load field distribution of tooth-tips but also increases the maximum flux density. The flux density variation of the two stator tooth-tips, one with coil and one without coil, with rotor position is shown in Fig. 3. The flux density variations are captured from a series of static FE simulations. In each simulation step, the rotor is rotated by an angle and a pair of phases are excited with a constant current to produce a positive motoring torque. The tooth-tip flux densities inside the tooth tip volume are sampled at three points of a plane located at the midpoint of the tooth-tip thickness. The captured flux density variations can be simplified as shown in Fig. 4 to fit the core-loss model for electrical machines with

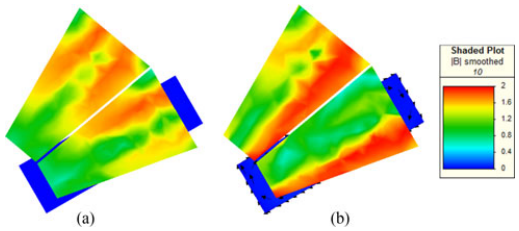

Fig. 2. Flux density distribution on stator tooth faces of the SAT PMBLDC motor. (a) No-load. (b) When the armature carries a current of 15 A.

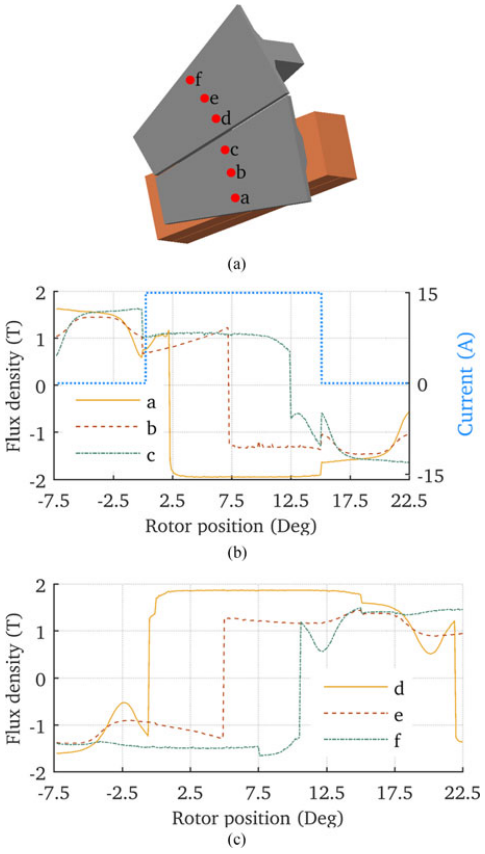

Fig. 3. Flux density variation inside the tooth tip with rotor position for six points in a plane located at the middle of a tooth-tip of the SAT PMBLDC motor, when armature carries a current of 15 A. (a) Position of flux density sampling points in the stator. (b) Flux density variation in a tooth with current carrying coil. (c) Flux density variation in a tooth without coil.

nonsinusoidal excitation, proposed by Slemon and Liu [19]. The simplified flux density waveform accounts the peak flux density and the rotor displacement over which the flux density variation occurs. The simplified flux density waveform changes the polarity over angle α_{tt}, the mean pole transition angle in electrical

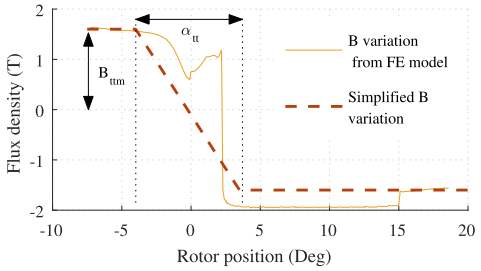

Fig. 4. Tooth-tip flux density variation and the simplified tooth-tip flux density variation of the SAT PMBLDC motor.

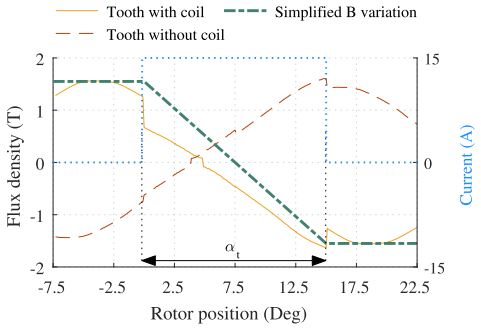

Fig. 5. Flux density variation with rotor position for a tooth with coil and a tooth without coil of the SAT PMBLDC motor, when the armature carries a current of 15 A.

radians. The tooth-tip core loss per unit mass corresponding to the simplified flux density waveform is given by [19]

$$p_{tt} = K_h f^{\alpha} B_{ttm}^{\beta} + \frac{4}{\pi} K_e \frac{f^2 B_{ttm}^2}{\alpha_{tt}} \quad (1)$$

where K_h, α, β, and K_e are the constants obtained from the curve fitting of core loss data measured for a toroidal stack of steel laminations with sinusoidal excitation, f is the frequency of flux density variation, and B_{ttm} is the peak value of flux density at the tooth-tip.

B. Core Losses in Stator Tooth

The flux density variation with rotor position for a tooth with coil and a tooth without coil of the SAT PMBLDC motor is shown in Fig. 5. The flux density variations are captured at the geometrical centre of the tooth because the tooth has a uniform flux density across its cross section. The coils are carrying a current of 15 A. The armature current affects only a peak during one cycle of tooth flux density variation and the effect on the affected peak is less pronounced as shown in Fig. 5. Therefore, the tooth flux density variation with the armature current is not considered. The tooth core loss can be calculated using the model of Slemon and Liu [19] with the help of the simplified flux density variation shown in Fig. 5. The tooth core loss per

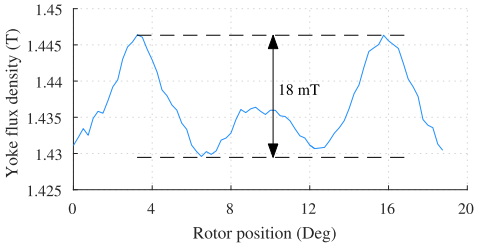

Fig. 6. Rotor yoke flux density variation of the SAT PMBLDC motor with rotor position under no-load.

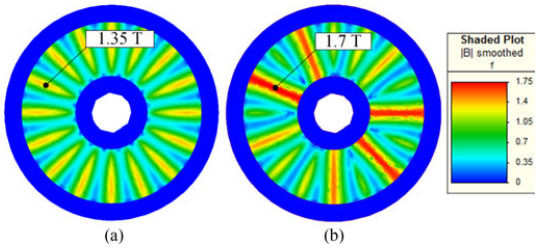

Fig. 7. Rotor yoke flux density of the SAT PMBLDC motor. (a) No-load. (b) When armature carries a current of 20 A.

unit mass is given by [19]

$$p_t = K_h f^{\alpha} B_{tm}^{\beta} + \frac{4}{\pi} K_e \frac{f^2 B_{tm}^2}{\alpha_t} \quad (2)$$

where B_{tm} is the peak value of the tooth flux density, and α_t is $2\pi/3$, the phase current conduction angle in electrical radians.

C. Core Losses in Solid Rotor Yoke

There are two reasons for the flux variation in the rotor yoke with time. The change in the reluctance seen by the rotor magnets as they move past the slot openings, and the relative speed between the armature flux and the rotor yoke. The designed motor has a 1 mm slot opening and this narrow slot opening creates only a minor flux density variation in the rotor yoke, as shown in Fig. 6. Therefore, the core loss generated in the rotor yoke due to slot opening is neglected because the reluctance seen by magnets remains nearly constant as the rotor rotates.

The armature flux will generate both hysteresis and eddy current loss in a solid rotor yoke of a PMBLDC motor. The rotor yoke flux density of the SAT PMBLDC motor at no-load and when the armature carries a current of 20 A is shown in Fig. 7. Comparing no-load and load flux density distributions in yoke, it is clear that the armature flux enhances some of the no-load peaks and diminishes the others. The sections of the rotor yoke that experience the maximum flux density will have a loss corresponding to a minor hysteresis loop formed about the operating point defined by the no-load flux density 1.35 T. The area of the minor loop will increase with armature current. However, Bottauscio *et al.* in their work shown that the hysteresis loss will be a smaller fraction of the total rotor

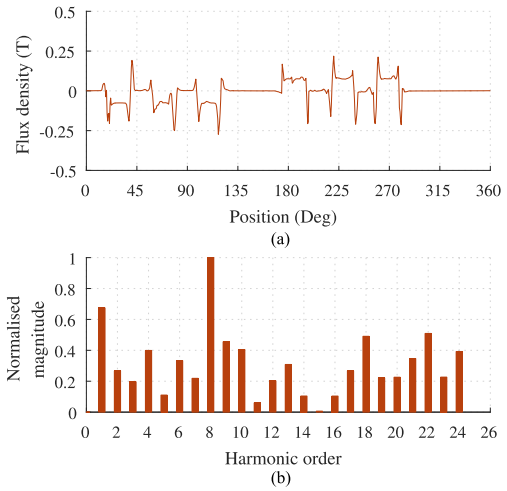

Fig. 8. Airgap flux density harmonics of the SAT PMBLDC motor, when armature carries a current of 15 A, and the magnet flux is set to zero. (a) Flux density over a 360° contour. The contour used is a circle with radius equal to the mean stator radius and located at the middle of the mechanical airgap. (b) Normalized magnitude of airgap flux density harmonics.

losses [20], and hence, the rotor yoke hysteresis loss is not considered in this work.

The eddy current loss generated in the solid conducting rotor yoke of a PM motor by armature harmonic fluxes can be calculated using either an FE model [21] or an analytical model [22]. The studies comparing both models found that the results obtained from the analytical model are within the acceptable limits of results of the FE model [23], [24]. A 3-D-FE model of a SAT PMBLDC motor will take considerably longer simulation time because of the small element size required for the accurate simulation of eddy current distribution in a solid conducting yoke [23], [25]. Therefore, this work uses an analytical approach using a three-layer model proposed by Lawrenson *et al.* and Oberretl [26], [27].

The airgap flux density variation of the SAT PMBLDC motor and its normalised harmonics are shown in Fig. 8. The airgap flux density variation of Fig. 8 is generated by setting the magnet flux to zero and the armature current to 15 A. The flux density variation of Fig. 8 is rich in harmonics because of the fractional-slot concentrated winding employed in the machine. Though, the phase windings of PMBLDC motors are spatially separated from each other by 120° electrical; they carry currents that have a phase difference of 180° electrical. As a result, rotating armature flux is not formed in PMBLDC motors, and the armature flux is either stationary or pulsating depending upon whether the winding carries a constant current or a varying current. Consequently, the velocity of the stationary armature flux density wave of a PMBLDC motor with respect to its rotor is the rotational speed of the machine.

The linear velocity of the armature flux density wave of a PMBLDC motor with respect to its rotor is given by

$$v = 2\pi n R_{\mathrm{Ymean}} \tag{3}$$

where n is the rotational speed of the machine in revolutions per second, and R_{Ymean} is the mean radius of the rotor yoke. The wave length, λ_i of the ith harmonic of flux density wave is given by

$$\lambda_i = \frac{2\pi R_{\mathrm{Ymean}}}{i}. \tag{4}$$

The angular frequency of the ith harmonic of flux density wave is given by

$$\omega_i = \frac{2\pi v}{\lambda_i}. \tag{5}$$

Substituting (3) and (4) to (5)

$$\omega_i = 2\pi \times 2\pi n R_{\mathrm{Ymean}} \times \frac{i}{2\pi R_{\mathrm{Ymean}}} = 2\pi n i. \tag{6}$$

The skin depth of ith harmonic of flux density wave is given by

$$\delta_i = \sqrt{\frac{2\rho_{\mathrm{Fe}}}{\mu_{\mathrm{Fe}}\omega_i}} \tag{7}$$

where ρ_{Fe} is the resistivity, and μ_{Fe} is the average permeability of the rotor yoke material, which is normally made of solid soft iron in PMBLDC motors. Substituting (6) to (7)

$$\delta_i = \sqrt{\frac{\rho_{\mathrm{Fe}}}{i\pi\mu_{\mathrm{Fe}} n}}. \tag{8}$$

The eddy current loss generated in a rotor yoke due to ith harmonic of flux density wave can be calculated as [22], [28]

$$P_{\mathrm{Lrye}i} = \frac{|B_i|^2 v^2 \delta_i}{4\rho_{\mathrm{Fe}}} \times A_{\mathrm{ry}} \tag{9}$$

where $|B_i|$ is the magnitude of ith harmonic of the armature flux density wave and A_{ry} area of the rotor yoke face. Substituting (3) and (8) to (9)

$$P_{\mathrm{Lrye}i} = |B_i|^2 R_{\mathrm{Ymean}}^2 A_{\mathrm{ry}} \sqrt{\frac{\pi^3}{i\rho_{\mathrm{Fe}}\mu_{\mathrm{Fe}}}} \times n^{1.5}. \tag{10}$$

The total eddy current loss generated due to armature flux density wave corresponding to a motor speed of n is given by

$$P_{\mathrm{Lrye}} = n^{1.5} \times R_{\mathrm{Ymean}}^2 A_{\mathrm{ry}} \sqrt{\frac{\pi^3}{\rho_{\mathrm{Fe}}\mu_{\mathrm{Fe}}}} \sum_{i=1}^{\infty} \frac{|B_i|^2}{\sqrt{i}}. \tag{11}$$

The second term of (11) is independent of the rotational speed of the PMBLDC motor and can be expressed as a function of source current i_{s} as

$$f_{\text{yoke eddy loss}}\{i_{\mathrm{s}}\} = R_{\mathrm{Ymean}}^2 A_{\mathrm{ry}} \sqrt{\frac{\pi^3}{\rho_{\mathrm{Fe}}\mu_{\mathrm{Fe}}}} \sum_{i=1}^{\infty} \frac{|B_i|^2}{\sqrt{i}}. \tag{12}$$

Therefore, (11) can be written as

$$P_{\mathrm{Lrye}} = n^{1.5} \times f_{\text{yoke eddy loss}}\{i_{\mathrm{s}}\}. \tag{13}$$

Rotor yoke eddy current loss in a PMBLDC motor with more than one rotor yoke can be calculated as

$$P_{\mathrm{Lrye}} = n_{\mathrm{y}} n^{1.5} \times f_{\text{yoke eddy loss}}\{i_{\mathrm{s}}\} \tag{14}$$

where, n_{y} is the number of rotor yokes in the motor. The (14) can be expressed in terms of the operating frequency of the

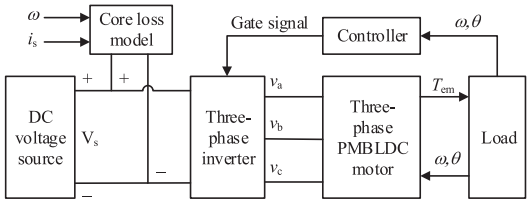

Fig. 9. Block diagram of nonlinear dynamic model of three-phase PMBLDC motor.

motor similar to equations for core losses in the stator tooth-tip (1) and the stator tooth (2) as

$$P_{\mathrm{Lrye}} = n_{\mathrm{y}} \left(\frac{f}{p}\right)^{1.5} \times f_{\text{yoke eddy loss}}\{i_{\mathrm{s}}\} \tag{15}$$

where p is the number of pole pairs of PMBLDC motor.

IV. Nonlinear Dynamic Model of Three-Phase PMBLDC Motor

A block diagram of the proposed nonlinear dynamic model of three-phase PMBLDC motor is shown in Fig. 9. It consists of dc voltage source, a three-phase inverter, a PMBLDC motor, a load, a controller, and a core-loss model. The model is implemented in MATLAB-Simulink. This section discusses the implementation of individual blocks of the dynamic model of a PMBLDC motor drive.

A. Three-Phase PMBLDC Motor Model

The motor model solves the voltage equations and the torque equation of the motor. The SAT PMBLDC motor has an alternate tooth winding. The tooth without coil will have fluxes from the two nearby coils. However, the flux from one coil will not link with other coil. Therefore, mutual coupling of coils is not present in SAT PMBLDC motor. The voltage equation of a phase is given by [29]

$$\begin{aligned} v &= iR + L\frac{di}{dt} + e \\ &= iR + L\frac{di}{dt} + \frac{d\psi(\theta, i)}{d\theta}\omega \\ &= iR + L\frac{di}{dt} + \psi'(\theta, i)\omega \end{aligned} \tag{16}$$

where v is the applied phase voltage, i is the phase current, R is the phase resistance, L is the phase inductance, e is the phase back EMF, ψ is the flux linkage of a phase as a function of the rotor position in mechanical degree, θ and the phase current, ψ' is the derivative of ψ, and ω is the angular velocity of the rotor. The flux linkage is obtained from a series of static 3-D FE simulations. The instantaneous electromagnetic torque of the motor, T_{em} can be expressed as

$$T_{\mathrm{em}} = \psi'_{\mathrm{a}}(\theta, i_{\mathrm{a}})i_a + \psi'_{\mathrm{b}}(\theta, i_{\mathrm{b}})i_b + \psi'_{\mathrm{c}}(\theta, i_{\mathrm{c}})i_c + T_{\mathrm{cg}}(\theta) \tag{17}$$

where $T_{\mathrm{cg}}(\theta)$ is the cogging torque as a function of the rotor position. The implementation of voltage equations and torque

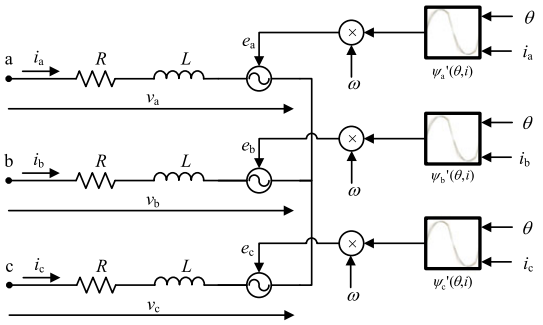

Fig. 10. Model for solving the voltage equation of a three-phase PMBLDC motor.

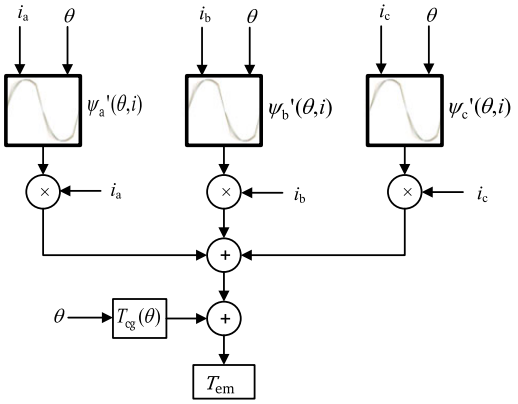

Fig. 11. Model for solving the torque equation of a three-phase PMBLDC motor.

equation of a three-phase PMBLDC motor is shown in Figs. 10 and 11, respectively. Both the models uses a 2-D look-up table of the flux linkage derivative as a function of phase current and rotor position, calculated from a series of static FE simulations, to model the nonideal back EMF waveform and the effect armature reaction on it.

B. Core-Loss Model

The loss model incorporates hysteresis and eddy current losses in the stator core and eddy current loss in the rotor yoke into the nonlinear phase variable model of a PMBLDC motor. If M_{stt} is the mass of all tooth-tips and M_{st} is the mass of all tooth, the total core losses generated in the stator core can be calculated from (1) and (2) as

$$\begin{aligned} P_{\mathrm{cs}} = {} & K_{\mathrm{h}} f^{\alpha} \left(M_{\mathrm{stt}} B_{\mathrm{ttm}}^{\beta} + M_{\mathrm{st}} B_{\mathrm{tm}}^{\beta}\right) \\ & + \frac{4}{\pi} K_{\mathrm{e}} f^2 \left(\frac{M_{\mathrm{stt}} B_{\mathrm{ttm}}^2}{\alpha_{\mathrm{tt}}} + \frac{M_{\mathrm{st}} B_{\mathrm{tm}}^2}{\alpha_{\mathrm{t}}}\right). \end{aligned} \tag{18}$$

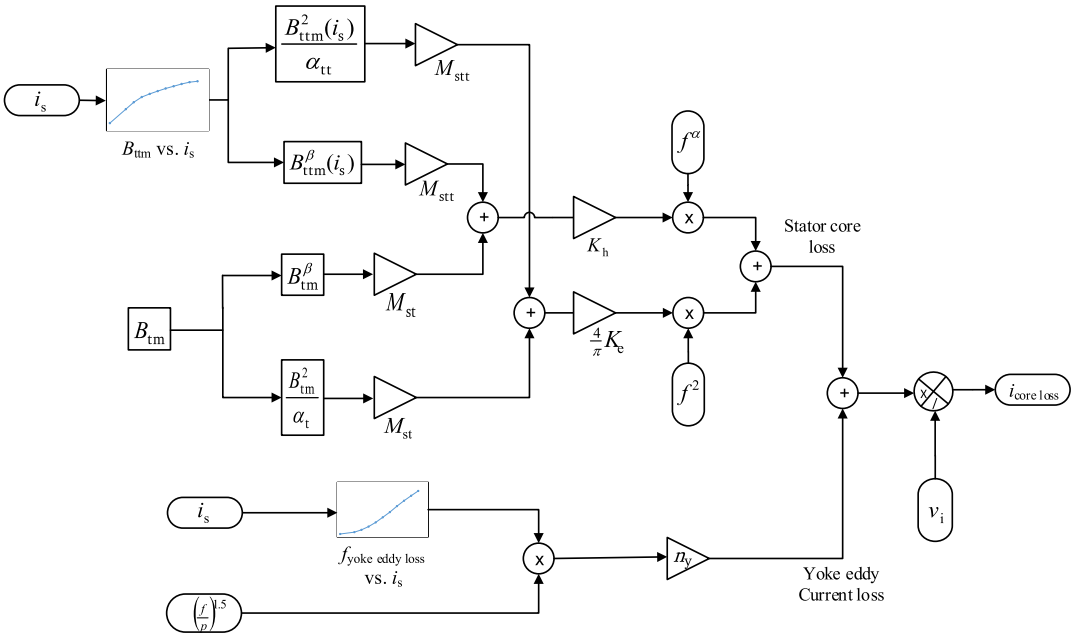

Fig. 12. Core-loss model of a PMBLDC motor.

Total core loss can be obtained by adding (15) and (18)

$$P_c = n_y \left(\frac{f}{p}\right)^{1.5} \times f_{\text{yoke eddy loss}}\{i_s\} + K_h f^{\alpha}\left(M_{stt}B^{\beta}_{ttm} + M_{st}B^{\beta}_{tm}\right) + \frac{4}{\pi}K_e f^2\left(\frac{M_{stt}B^2_{ttm}}{\alpha_{tt}} + \frac{M_{st}B^2_{tm}}{\alpha_t}\right). \quad (19)$$

The core loss equation (19) of a PMBLDC motor is solved using the model shown in Fig. 12. The core-loss model uses two look-up tables, one for the peak tooth-tip flux density and another one for the rotor yoke eddy current loss function. The look-up table of peak tooth-tip flux density versus armature current can be generated from the same set of FE models used to calculate the variation of flux linkage with rotor position and armature current. The look-up table of the rotor yoke eddy current loss function is obtained by solving FE models of a PMBLDC motor without magnet flux for different armature current. Though, removing magnet flux will enhance the magnitude of stator flux density harmonics by lowering the saturation level of the flux path, the approach will help to capture low amplitude subharmonic components, which can penetrate deep into the yoke and induce most of the losses [21], [22], [30]. The core-loss model calculates the core loss component of the current, and in a Simulink model, this current will be drawn from the voltage source via a block named controlled current source, connected across the voltage source.

C. Power Electronic Converter Model

A standard three bridge converter from the Simulink library is used in the model. Furthermore, a controller is modeled to generate the gate pulses for the converter based on the rotor position so that a positive shaft torque is produced.

D. Load Model

The electromagnetic torque developed in the motor has to work against the load torque, inertia of rotating components, and moving friction. The equation governing the load behaviour can be written as

$$T_{em} = T_L + j\frac{d\omega}{dt} + b\omega \quad (20)$$

where T_L is the load torque, j is the moment of inertia of rotating parts of the motor and the load, and b is the constant of moving friction.

V. Simulated and Experimental Results

The dynamic model proposed in this work is used to simulate the SAT PMBLDC motor prototype driving a constant torque load in a test bench. A comparative study of results of the simulation and the testing is presented to assess the model and to identify areas of improvements in the dynamic modeling of the PMBLDC motor.

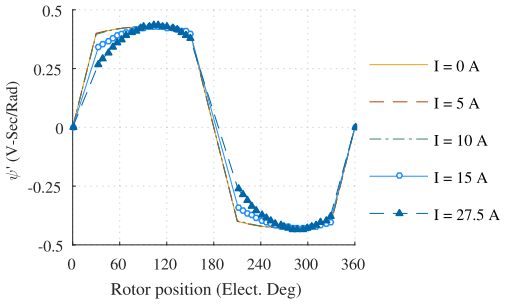

Fig. 13. Variation of the flux-linkage-derivative with rotor position for different phase current obtained from a series of static FE simulations of the ferrite magnet SAT PMBLDC motor prototype.

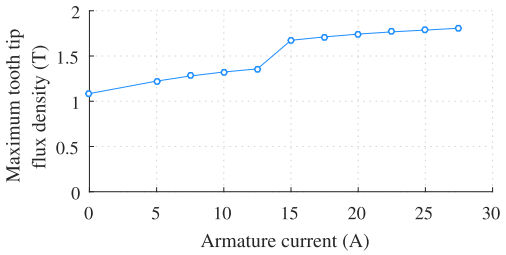

Fig. 14. Variation of the peak value of the tooth-tip flux density with armature current obtained from the FE simulation of the SAT PMBLDC motor.

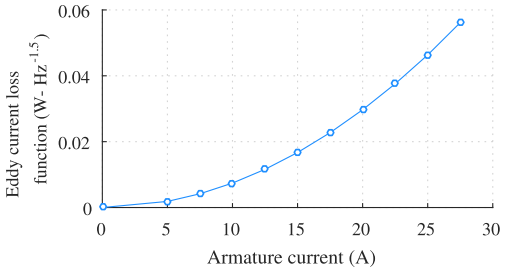

Fig. 15. Values of yoke eddy current loss function of the SAT PMBLDC motor design for different armature current.

A. Nonlinear Dynamic Model Parameters

The variation of flux-linkage-derivative of the motor with rotor position for different values of phase current is shown in Fig. 13. The simulated peak tooth-tip flux density variation of the prototype motor with armature current is shown in Fig. 14, and the change in the curve from 15 A can be attributed to saturation of stator laminations. The change of rotor yoke eddy current loss function with armature current is shown in Fig. 15. Cogging torque of the motor is not considered because the FE analysis of a reduced sized model found that the peak-to-peak value of cogging torque is only 16 mN m. The phase resistance

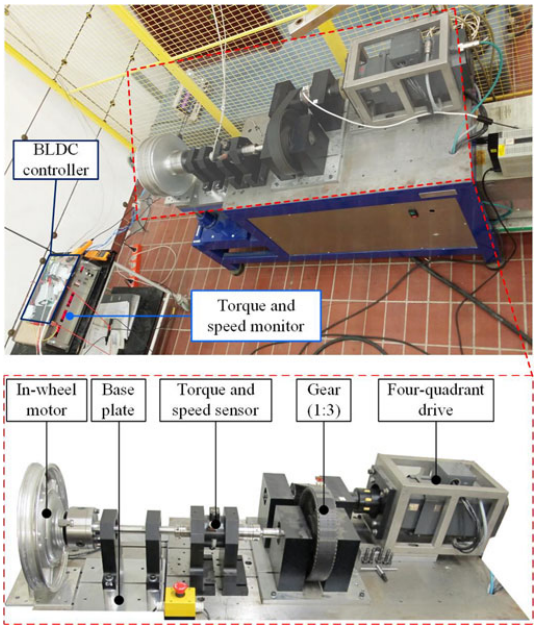

Fig. 16. Experimental setup to measure the performance of the SAT PMBLDC in-wheel motor.

value of 56 mΩ and the phase inductance value of 1.8 mH, obtained from the FE model, are used in the simulation.

B. Experimental Setup for Testing SAT PMBLDC Motor

The test setup to measure the performance of SAT PMBLDC in-wheel motor is shown in Fig. 16. The test bench consists of a four-quadrant drive, speed reduction gears, torque and speed sensor, a monitor to record torque and speed, a BLDC motor controller, and a dc power supply. The four-quadrant drive is configured to work as a generator, and it can act as a constant torque load to the motor.

C. Discussion

The variation of the flux-linkage-derivative with rotor position is used to estimate the line back EMF at 340 rpm. The calculated line back EMF is plotted in Fig. 17 along with the waveform obtained from the back EMF test of the motor. The deviation of the test back EMF waveform from the FE simulated back EMF waveform can be attributed to manufacturing variations of the motor compared to the assembly simulated in the FE software. The major variations observed in the prototype are in widths of slot openings, in dimensions of interpolar gaps, and in thickness of magnets.

The phase current waveforms obtained from the dynamic modeling and the testing of the prototype motor is plotted in Fig. 18. The waveform corresponds to a load torque of 10 Nm at a speed of 300 rpm. The efficiency map obtained from the test and the simulation of the prototype ferrite magnet SAT PMBLDC

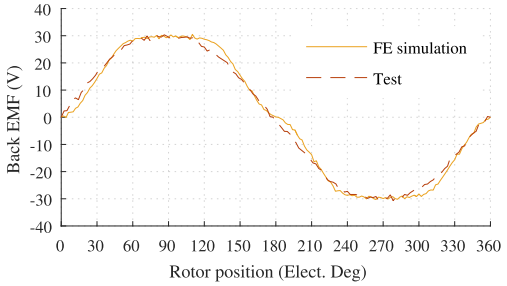

Fig. 17. Test and the FE simulated line back EMF waveforms of the prototype ferrite magnet SAT PMBLDC motor.

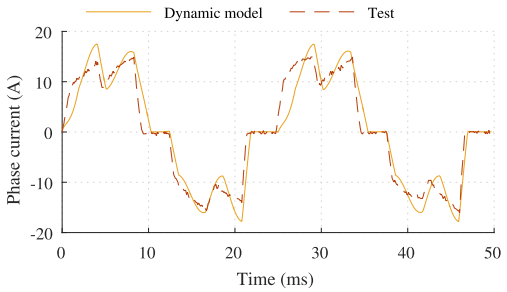

Fig. 18. Test and simulated phase current waveforms of the SAT PMBLDC motor.

motor is shown in Fig. 19. The simulated current waveform closely follows that of the test. However, there is considerable variation in maximum efficiencies and distributions of efficiency bands of the dynamic model and the test data. The reasons for the difference between the simulated and the tested efficiency maps of the ferrite magnet prototype have been explored, and they are as follows.

1) The simplified windage and friction loss model used in the dynamic model cannot expect to be accurate, especially when the motor is operating with an efficiency more than 90%. The windage loss characterization of the PMBLDC motor requires a detailed study using nonmagnetic dummy rotors and computational fluid dynamic models [31], [32]. The lack of mechanical loss characterization prevents the extraction of electromagnetic losses other than the conduction loss from the test data. The segregation of losses will help to improve the overall accuracy of the dynamic model by individually validating each loss model and thus improving the loss models used in the study.
2) The prototype motor uses a commercial controller, and the detailed operation and the component layout of the controller were not available. The dynamic model of the PMBLDC motor discussed in this work uses a basic six-pulse inverter. Using an in-house developed PMBLDC motor controller would help to model and validate the switching and conduction losses in the controller.

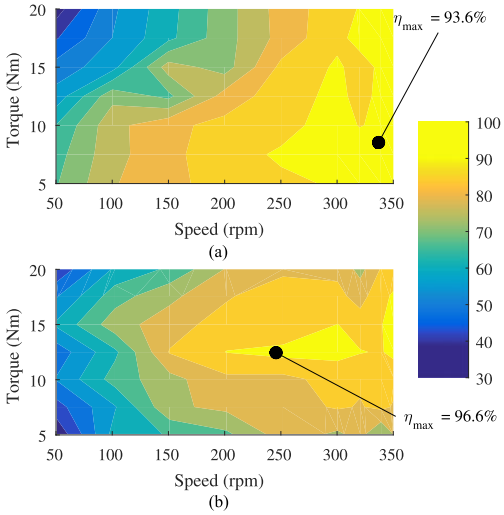

Fig. 19. Efficiency map of the SAT PMBLDC motor. (a) From the dynamic model. (b) From the testing.

3) The prototype motor has a considerable vibration between 310 rpm and 330 rpm only when connected to the test bench, and the readings of the torque and the speed from the sensors were oscillating substantially during this speed range.

VI. Conclusion

This work discusses the development of a core-loss model and incorporating it into the nonlinear phase variable model of three-phase PMBLDC motor. The model is developed for SAT motor topology. A theoretical study has been presented in which the core loss is modeled as a function of peak flux densities of flux paths, the armature current, and the speed of the machine. The model captures nonlinearities in core losses of the stator and the solid rotor yoke with the help of two look-up tables derived from the static FE model of the machine. The first look-up table relates the maximum tooth tip flux density and the armature current, and the second look-up table relates eddy current in the rotor yoke and the armature current.

A comparative study of the results of the dynamic modeling and the test results of a SAT PMBLDC motor is carried out. The motor was operating with an efficiency of more than 90%, and the accuracy with which all electromagnetic and mechanical losses are modeled is critical to estimate the system performance accurately at this level of efficiency. Therefore, it is concluded that a loss segregation study is required to complete the validation of core-loss model.

References

[1] Y. Kano, T. Kosaka, and N. Matsui, "A simple nonlinear magnetic analysis for axial-flux permanent-magnet machines," *IEEE Trans. Ind. Electron.*, vol. 57, no. 6, pp. 2124–2133, Jun. 2010.

[2] G. De Donato, F. G. Capponi, and F. Caricchi, "No-load performance of axial flux permanent magnet machines mounting magnetic wedges," *IEEE Trans. Ind. Electron.*, vol. 59, no. 10, pp. 3768–3779, Oct. 2012.
[3] R. Ni, G. Wang, X. Gui, and D. Xu, "Investigation of d and q-axis inductances influenced by slot-pole combinations based on axial flux permanent-magnet machines," *IEEE Trans. Ind. Electron.*, vol. 61, no. 9, pp. 4539–4551, Sep. 2014.
[4] B. Xia, J.-X. Shen, P. C.-K. Luk, and W. Fei, "Comparative study of air-cored axial-flux permanent-magnet machines with different stator winding configurations," *IEEE Trans. Ind. Electron.*, vol. 62, no. 2, pp. 846–856, Feb. 2015.
[5] T. M. Jahns, "Torque production in permanent-magnet synchronous motor drives with rectangular current excitation," *IEEE Trans. Ind. Appl.*, vol. IA-20, no. 4, pp. 803–813, Jul. 1984.
[6] C.-T. Pan and E. Fang, "A phase-locked-loop-assisted internal model adjustable-speed controller for BLDC motors," *IEEE Trans. Ind. Electron.*, vol. 55, no. 9, pp. 3415–3425, Sep. 2008.
[7] O. Mohammed, S. Liu, and Z. Liu, "A phase variable model of brushless dc motors based on finite element analysis and its coupling with external circuits," *IEEE Trans. Magn.*, vol. 41, no. 5, pp. 1576–1579, May 2005.
[8] L. Queval and H. Ohsaki, "Nonlinear ABC-model for electrical machines using N-D lookup tables," *IEEE Trans. Energy Convers.*, vol. 30, no. 1, pp. 316–322, Mar. 2015.
[9] K. Tabarraee, J. Iyer, and J. Jatskevich, "Average-value modeling of brushless DC motors With trapezoidal back-EMF," in *Proc. IEEE Int. Symp. Ind. Electron.*, Jun. 2011, pp. 531–537.
[10] M. Jagiela, T. Garbiec, J. Gwozdz, and J. Kolodziej, "Fast steady-state field-circuit model for SMPM-BLDC motors driven from 120 Deg and 180 Deg quasi-square wave inverters," *IEEE Trans. Magn.*, to be published.
[11] A. EL-Refaie, "Fractional-slot concentrated-windings synchronous permanent magnet machines: Opportunities and challenges," *IEEE Trans. Ind. Electron.*, vol. 57, no. 1, pp. 107–121, Jan. 2010.
[12] G. De Donato, F. G. Capponi, G. A. Rivellini, and F. Caricchi, "Integral-Slot versus fractional-slot concentrated-winding axial-flux permanent-magnet machines: Comparative design, FEA, and experimental tests," *IEEE Trans. Ind. Appl.*, vol. 48, no. 5, pp. 1487–1495, Sep. 2012.
[13] E. Fornasiero, N. Bianchi, and S. Bolognani, "Slot harmonic impact on rotor losses in fractional-slot permanent-magnet machines," *IEEE Trans. Ind. Electron.*, vol. 59, no. 6, pp. 2557–2564, Jun. 2012.
[14] A. Masmoudi and A. Masmoudi, "3-D analytical model with the end effect dedicated to the prediction of PM eddy-current loss in FSPMMs," *IEEE Trans. Magn.*, vol. 51, no. 4, pp. 1–11, Apr. 2015.
[15] T. Woolmer and M. McCulloch, "Analysis of the yokeless and segmented armature machine," in *Proc. IEEE Int. Elect. Mach. Drives Conf.*, May 2007, vol. 1, pp. 704–708.
[16] F. G. Capponi, G. De Donato, and F. Caricchi, "Recent advances in axial-flux permanent-magnet machine technology," *IEEE Trans. Ind. Appl.*, vol. 48, no. 6, pp. 2190–2205, Nov./Dec. 2012.
[17] T. J. Woolmer and M. McCulloch, "Axial flux permanent magnet machines: A new topology for high performance applications," in *Proc. IET Hybrid Veh. Conf.*, 2006, vol. 2006, pp. 27–42.
[18] G. Bertotti, "General properties of power losses in soft ferromagnetic materials," *IEEE Trans. Magn.*, vol. 24, no. 1, pp. 621–630, Jan. 1988.
[19] G. Slemon and X. Liu, "Core losses in permanent magnet motors," *IEEE Trans. Magn.*, vol. 26, no. 5, pp. 1653–1655, Sep. 1990.
[20] O. Bottauscio, G. Pellegrino, P. Guglielmi, M. Chiampi, and A. Vagati, "Rotor loss estimation in permanent magnet machines with concentrated windings," *IEEE Trans. Magn.*, vol. 41, no. 10, pp. 3913–3915, Oct. 2005.
[21] N. Bianchi, D. Durello, and A. Fasolo, "Relationship between rotor losses and size of permanent-magnet machines," *IEEE Trans. Ind. Appl.*, vol. 49, no. 5, pp. 2015–2023, Sep. 2013.
[22] R. Di Stefano and F. Marignetti, "Electromagnetic analysis of axial-flux permanent magnet synchronous machines with fractional windings with experimental validation," *IEEE Trans. Ind. Electron.*, vol. 59, no. 6, pp. 2573–2582, Jun. 2012.
[23] R.-J. Wang and M. Kamper, "Calculation of eddy current loss in axial field permanent-magnet machine with coreless stator," *IEEE Trans. Energy Convers.*, vol. 19, no. 3, pp. 532–538, Sep. 2004.
[24] D. Liu, A. Jassal, H. Polinder, and J. Ferreira, "Validation of eddy current loss models for permanent magnet machines with fractional-slot concentrated windings," in *Proc. IEEE Int. Elect. Mach. Drives Conf.*, May 2013, pp. 678–685.
[25] J. Pyrhonen, H. Jussila, Y. Alexandrova, P. Rafajdus, and J. Nerg, "Harmonic loss calculation in rotor surface permanent magnets-new analytic approach," *IEEE Trans. Magn.*, vol. 48, no. 8, pp. 2358–2366, Aug. 2012.
[26] P. Lawrenson, P. Reece, and M. Ralph, "Tooth-ripple losses in solid poles," *Proc. Inst. Elect. Eng.*, vol. 113, no. 4, pp. 657–662, Apr. 1966.
[27] K. Oberretl, "Eddy current losses in solid pole shoes of synchronous machines at no-load and on load," *IEEE Trans. Power App. Syst.*, vol. PAS-91, no. 1, pp. 152–160, Jan. 1972.
[28] H. Polinder, M. Hoeijmakers, and M. Scuotto, "Eddy-current losses in the solid back-iron of PM machines for different concentrated fractional pitch windings," in *Proc. IEEE Int. Elect. Mach. Drives Conf.*, May 2007, vol. 1, pp. 652–657.
[29] T. J. E. Miller, *Brushless Permanent-Magnet and Reluctance Motor Drives*. London, U.K.: Oxford Univ. Press, 1989.
[30] L. Alberti, E. Fornasiero, and N. Bianchi, "Impact of the rotor yoke geometry on rotor losses in permanent-magnet machines," *IEEE Trans. Ind. Appl.*, vol. 48, no. 1, pp. 98–105, Jan. 2012.
[31] F. Deng, "An improved iron loss estimation for permanent magnet brushless machines," *IEEE Trans. Energy Convers.*, vol. 14, no. 4, pp. 1391–1395, 1999.
[32] R. Wrobel, G. Vainel, C. Copeland, T. Duda, D. Staton, and P. H. Mellor, "Investigation of mechanical loss components and heat transfer in an axial-flux PM machine," *IEEE Trans. Ind. Appl.*, vol. 51, no. 4, pp. 3000–3011, Jul. 2015.

Authors' photographs and biographies not available at the time of publication.

www.elektro.dtu.dk

Department of Electrical Engineering
Centre for Electric Technology (CET)
Technical University of Denmark
Elektrovej, Building 325
DK-2800, Kgs. Lyngby
Denmark

Tel: (+45) 45 25 38 00
Fax: (+45) 45 93 16 34
Email: info@elektro.dtu.dk